Project No. 10-951

Design, Testing and Modeling of the Direct Reactor Auxiliary Cooling System for AHTRs

Reactor Concepts

Dr. Xiaodong Sun
Ohio State University

In collaboration with:
Oak Ridge National Laboratory

Brian Robinson, Federal POC
Piyush Sabharwall, Technical POC

NEUP Nuclear Energy University Programs
U.S. Department of Energy

Final Report
10-951

Design, Testing and Modeling of the Direct Reactor Auxiliary Cooling System for AHTRs

Award Identification Number:
Blanket Master Contract No. 42898, Release No. 25

Period of Performance: 10/01/2010 to 12/31/2014

Principal Investigators
Xiaodong Sun, Richard Christensen, and Thomas Blue

Collaborators
Graydon Yoder and Dane Wilson

Submitted by

Qiuping Lv, Xiaodong Sun, Richard Christensen, and Thomas Blue
Nuclear Engineering Program
The Ohio State University
201 West 19th Avenue, Columbus, OH 43210

and

Graydon Yoder and Dane Wilson
Oak Ridge National Laboratory
P.O.Box 2008, Oak Ridge, TN 37831

Supported by

Nuclear Energy University Programs
The Department of Energy

May 8, 2015

THE OHIO STATE UNIVERSITY
NUCLEAR ENGINEERING PROGRAM
THERMAL HYDRAULICS LABORATORY

NEUP-10-951
NON-PROPRIETARY REPORT

FINAL REPORT

DESIGN, TESTING, AND MODELING OF THE DIRECT REACTOR AUXILIARY COOLING SYSTEM FOR AHTRS

---

by

Qiuping Lv, Xiaodong Sun, Richard Christensen, and Thomas Blue

The Ohio State University

and

Graydon Yoder and Dane Wilson

Oak Ridge National Laboratory

May 8, 2015

Prepared for

Nuclear Energy University Programs
The U.S. Department of Energy

Nuclear Engineering Program, The Ohio State University
201 West 19th Avenue, Columbus, OH 43210

Project Objective:

The principal objective of this research is to test and model the heat transfer performance and reliability of the Direct Reactor Auxiliary Cooling System (DRACS) for AHTRs. In addition, component testing of fluidic diodes is to be performed to examine the performance and viability of several existing fluidic diode designs. An extensive database related to the thermal performance of the heat exchangers involved will be obtained, which will be used to benchmark a computer code for the DRACS design and to evaluate and improve, if needed, existing heat transfer models of interest. The database will also be valuable for assessing the viability of the DRACS concept and benchmarking any related computer codes in the future. The experience of making a liquid fluoride salt test facility available, with lessons learned, will greatly benefit the development of the Fluoride Salt-cooled High-temperature Reactor (FHR) and eventually the AHTR programs.

Background:

The project became active on July 26 2010, but the actual work started in September 2010. During the performance period (10/01/2010 to 12/31/2014) of this project, we conducted a literature review of the AHTR and FHR designs and proposed a prototypic design of the DRACS capable of removing 200 kW decay heat for a 20-MWth FHR. In addition, we performed a detailed scaling analysis and developed a scaling methodology for the DRACS to study its performance under both transient and steady-state conditions. Starting from the core scaling, we obtained the convection time ratio in the primary loop, with which we proceeded to accomplish the scaling for the entire DRACS system. Based on the scaling results, we developed a design of a scaled-down low-temperature test facility and a design of a scaled-down high-temperature test facility, the latter of which is currently under construction. The low-temperature test facility is currently in operation, and two representative accident scenarios, namely, the DRACS startup and the pump trip scenario, have been simulated in this facility. In both scenarios, natural circulations are successfully established, demonstrating the passive decay heat removal capability of the DRACS concept. Meanwhile, a MATLAB computer code has been developed to predict the thermal performance of the DRACS system. A preliminary validation of this MATLAB code has been performed, using available experimental data that are as closely relevant as possible. The code predictions show good agreement with the experimental data, which demonstrates promise in the code's capability in predicting the thermal performance of the DRACS system. This computer code will be eventually validated by the experimental data obtained from the two test facilities.

Progresses to Date:

1. Literature review and identify/develop an up-to-date DRACS design

In the literature, although the DRACS concept has been proposed for AHTRs/FHRs as one means of passively removing the reactor decay heat, there is no detailed, quantitative design available yet for a test-scale FHR (thermal power being on the order of 20 MWth). Therefore, as a first step, we performed a literature review of test-scale FHR designs, fluidic diode designs, and DHX and NDHX designs. Based on the literature review, a prototypic DRACS design for the 16-MWth pebble bed core designed by UC Berkeley was developed, which is capable of removing 200 kW decay heat. This design employs FLiBe and FLiNaK as the primary and secondary salts, and air as the ultimate sink, respectively. Shell-and-tube type heat exchangers, featuring small pressure drops as well as mature design and manufacturing technologies, were adopted for the DHX and NDHX designs. As an important component in restricting the heat loss during core normal operation and launching the DRACS upon accidents, a fluidic diode was employed and a vortex diode design was adapted since it has been tested with water by previous researchers. An annular air chimney, made from reinforced concrete, was also carefully designed to ensure sufficient air flow during the DRACS operation. This prototypic DRACS design, with its performance confirmed (by scaling up the results from the high-temperature DRACS test facility), will be important in demonstrating the viability of the DRACS concept for FHRs.

2. Scaling analysis

We have performed a detailed scaling analysis for the DRACS to understand its performance under both transient and steady-state conditions. By non-dimensionalizing the governing equations, namely, the continuity equation, the energy balance equations, and the integral momentum equations, we obtained the key non-dimensional numbers that characterize the thermal performance of the DRACS system. Similarity laws, based on the non-dimensionalized governing equations and the non-dimensional numbers, were proposed. In addition, we also developed a scaling methodology for the DRACS, which consists of the core and the loop scaling. Starting from the core scaling, we obtained the convection time ratio in the primary loop, with which we proceeded to accomplish the scaling for the entire DRACS system. The scaling analysis not only strengthens our understanding of the DRACS thermal performance, but also is essential in providing guidance for the designs of the scaled-down test facilities.

3. Design and performance evaluation code

To help with the design and thermal performance evaluation of the DRACS system, we have been developing a computer code based on the MATLAB platform. To date, code versions for the low-temperature DRACS test facility (LTDF) and the high-temperature DRACS test facility (HTDF) have been developed. The code is based on one-dimensional formulation and its principle is to solve the energy balance and integral momentum equations governing the DRACS system. By axially discretizing the entire system, the energy balance equation is applied to each cell while the integral momentum equation applied to each loop. The temperature distribution along the loop, mass flow rates in each loop, and correspondingly the performance of entire system can be predicted for both steady-state and transient conditions. In addition, the pump trip process has been incorporated into the code, which is of significant importance to the study of the flow reversal phenomenon in the DRACS primary loop. When the flow reversal occurs, it is likely that the primary coolant temperature will increase considerably in a short period of time. The inclusion of the pump trip process enables to better understand the temperature evolution of the coolants during the transient. After the experiments are performed and testing data are made available from the test facilities, the codes will be benchmarked/validated against the experimental results. Finally, the thermal performance of the prototypic DRACS design will be re-evaluated using the validated code. The validated code could be potentially applied to DRACS design for commercial FHRs.

4. Scaled-down test facilities

Based on the prototypic DRACS design and the scaling analysis results, two scaled-down DRACS test facilities have been designed.

4.1. Low-temperature DRACS test facility

The three natural circulation/convection loops in the DRACS are coupled through two heat exchangers, namely, the DHX and NDHX. The coupling among the loops is very important to determine the overall system thermal performance and fluid flow characteristics. The LTDF is proposed to mainly examine the loop couplings, as well as providing design and operation experience for the subsequent high-temperature DRACS test facility, which will be more challenging. The LTDF employs water as both the primary (pressurized to 1.0 MPa) and secondary coolants. The LTDF is currently in operation, and two representative accident scenarios, namely, the DRACS startup and the pump trip scenario, have been simulated in this facility. In both scenarios, natural circulations are successfully established, demonstrating the passive decay heat removal capability of the DRACS concept. More experiments with various operation conditions in terms of the core power, flow resistance, and air inlet temperature are being performed.

4.2. High-temperature DRACS test facility

The main purpose of having the HTDF is to help design and evaluate the DRACS performance as to its capability of removing the decay heat under a similar condition to the prototypic. Molten fluoride salts, FLiNaK and KF-ZrF_4, have been selected as the primary and secondary coolants, respectively. Experimental data from the HTDF will be used to evaluate the thermal performance of the heat exchangers, as well as that of the entire system. The data will also be used to benchmark/validate the heat transfer and pressure drop correlations/models that are used in the DRACS design and the MATLAB code. To date, the design of the HTDF has been accomplished, and all the components including the salts have been purchased. During the last quarter, we completed the majority of the power controlling and monitoring system for the HTDF, and started assembling the HTDF. We plan to complete the construction of the HTDF and the preprocessing of the salts, and start performing experiments on the HTDF in the following semester. Regarding the instrumentation for the HTDF, high-temperature ultrasonic flowmeters from Flexim have been purchased for the flow rate measurement. For the pressure/differential pressure measurements, indirect ways based on regular differential pressure transducers have been adopted. The viability of these instruments will be demonstrated in the HTDF.

Effect has been made in laying out the two test facilities, mainly due to the constrained space in our laboratory. A solution has been found, with which the two test facilities will coexist in our laboratory. In addition, a platform to support the two test facilities has been carefully designed. A stress analysis indicates that the platform will be strong enough to support even the heaviest salt pump (estimated at 2,151 lbs).

5. Computational Fluid Dynamics (CFD) study of the vortex diode

As an essential component, the fluidic diode switches the DRACS from core normal operation mode to decay heat removal mode when accidents occur. For the HTDF, a vortex diode has been proposed. To obtain a design that will exhibit desired pressure drops at the prescribed flow rates for both the forward and reverse flow directions, a parametric CFD study of a series of vortex diodes has been performed. Correlations for the forward and reverse Euler numbers (i.e., pressure drop coefficients) were developed, which were used in the design of the vortex diode for the HTDF.

The vortex diodes that have been studied for application to HTDF employ diverging/converging nozzles, which are considered not general or representative. In addition, in the previous study, the Reynolds number covers a rather narrow range from 711 to 4,789. For applications in larger-scale FHRs and some other industries, the Reynolds number can reach higher values. In view of this, we have performed a parametric CFD study for a more general set of vortex diodes over a wider range of Reynolds numbers (Re < 30,000). These vortex diodes employ straight inlet and outlet nozzles. The CFD study is beneficial to our understanding of the flow and pressure drop characteristics in a vortex diode. In addition, it is found from the literature that there has been a lack of useful correlations for the forward and reverse Euler numbers for vortex diodes, especially for fluoride salt applications. Correlations for the Euler numbers are being developed based on the CFD study, which will be helpful for any design purposes.

Status:

Task 1.1: Expand the literature review of the AHTR and FHR designs and obtain a prototypic design that DOE would like to further study (Ohio State Responsible).

1. Task Status: Completed

The Advanced High-Temperature Reactor (AHTR) combines two existing technologies, i.e., coated particle fuel and liquid salt coolant (Forsberg, 2005; Bardet et al., 2008). In the current AHTR design, a Direct Reactor Auxiliary Cooling System (DRACS), a passive system relying on natural convection/circulation process, is proposed as part of the ultimate heat sink for decay heat removal.

A schematic drawing of the DRACS adopted in our work is shown in Fig. 1.1.1 (Holcomb et al., 2009). There are three natural convection/circulation loops, i.e., the primary salt loop from a reactor core to a DRACS Heat Exchanger (DHX), to a fluidic diode, and then back to the reactor core (primary loop); the secondary salt loop from the DHX to a Natural Draft Heat Exchanger (NDHX), and then back to the DHX (secondary loop); and the surrounding air convection between the NDHX and environment (third loop). The performance of each loop/subsystem is dependent upon not only itself, but also the other two. The close coupling among these subsystems results in a major challenge in designing and evaluating the DRACS.

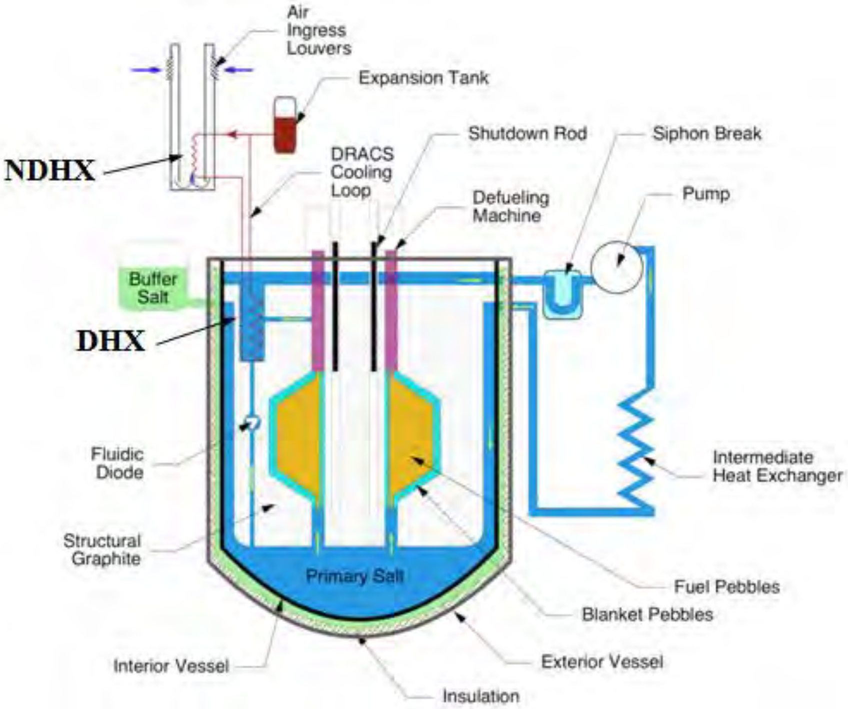
Air Ingress Louvers
Expansion Tank
Shutdown Rod
Siphon Break
NDHX
DRACS Cooling Loop
Defueling Machine
Pump
Buffer Salt
DHX
Fluidic Diode
Intermediate Heat Exchanger
Structural Graphite
Primary Salt
Fuel Pebbles
Blanket Pebbles
Interior Vessel
Exterior Vessel
Insulation

Fig. 1.1.1. Schematic drawing of the DRACS with the primary heat transport system (Holcomb et al., 2009)

In the current study, a detailed modular design of the DRACS for a 20-MWth FHR is developed. As a starting point, the DRACS is designed to remove 1% of the nominal power, i.e., the decay heat rate being 200 kW.

Selection of Salts

The first step in our DRACS design process is the determination of the working fluids. The determination of the working fluids is based on considerations of the physical, nuclear, and chemical properties of various salts. In addition, considerable experience was obtained with the fluoride salts from the Molten Salt Reactor (MSR) program in Oak Ridge National Laboratory (ORNL). We applied the criteria established by Grimes (1967 and 1970) for selecting candidates of primary and secondary salt coolants in MSR applications. It requires that the salt:

1. has a small thermal neutron capture cross section (<1 barn),
2. exhibits chemical stability at T > 800 ºC,
3. is stable under intense radiation,
4. melts at useful temperatures (< 525 ºC) and is not volatile, and
5. is compatible with high-temperature alloys and graphite.

When the secondary salt coolant for the secondary loop is considered, Criteria 1 and 3 may be relaxed. In addition, it is safer to adjust the freezing temperature requirement in Criterion 4 to an even lower value.

Different types of fluoride salts have been investigated, including alkali fluorides (such as LiF-KF, LiF-RbF, LiF-NaF-KF), ZrF_4 salts (such as LiF-ZrF_4, NaF- ZrF_4), and BeF_2 salts (such as LiF-BeF_2, LiF-NaF-BeF_2). As suggested by Williams et al. (2006), FLiBe (^{7}LiF-BeF_2, 66-34 in mol%) enriched with more than 99.995% ^{7}Li (which provides a large moderating ratio and small coolant parasitic capture probability) was selected as the primary coolant. FLiNaK (LiF-NaF-KF, 46.5-11.5-42 in mol%) was chosen as the secondary salt due to its good heat transfer capability, low melting point, and low cost. Table 1.1.1 summarizes the properties of the primary and secondary coolants.

Table 1.1.1 Summary of properties of FLiBe and FLiNaK (T in Kelvin)

	Melting point (ºC)	Density (kg/m^3)	Specific heat (J/Kg-K)	Viscosity (cP)	Thermal conductivity (W/m-K)
FLiBe	458	2280-0.4884(T-273)	2380	0.116exp(3755/T)	0.0005T+32/33-0.34
FLiNaK	454	2530-0.73(T-273)	1883	0.04exp(4170/T)	0.0005T+32/41.3-0.34

The mass flow rate ($\dot{m}$) of the working coolant in the loop is calculated as:

$$\dot{m} = \frac{\dot{Q}}{\overline{c}_p \Delta T}, \tag{1.1.1}$$

where $\dot{Q}$ is the decay heat rate. $\overline{c}_p$ and ΔT are the average specific heat at constant pressure of the salt and temperature difference between the hot and cold state of the salt or air.

The driving force overcoming the total pressure loss (ΔP) is generated from the density variation due to temperature difference of the salt or air and vertical distance as:

$$\Delta P = \Delta \rho g H, \tag{1.1.2}$$

where H is the vertical distance between the thermal centers of the DHX and reactor core in the primary loop, or that between NDHX and DHX thermal centers in the secondary loop, or the louver height in the third loop. Here, $\Delta\rho$ is the density difference between the hot salt (or air) and cold salt (or air) in a certain loop and g is the gravitational acceleration. Contributions to the total pressure loss in the primary loop are due to the flow through the reactor core, shell side of the DHX, fluidic diode, and connecting pipes, including elbows. In the secondary loop, the pressure drops take place on tube side of the DHX, tube bundles in the NDHX, connecting pipes, and all elbows. In the third loop, the pressure loss is mainly due to the air flow across the tube bundles of the NDHX, and frictional pressure drop along the chimney, as well as the form loss.

Selection of Core Design and its Pressure Drop Calculation

Several core designs have been proposed in the literature for AHTRs, including a 16-MWth annular pebble bed reactor core proposed by University of California at Berkeley (UCB), the FHR-16 test reactor (Peterson, 2009). This reactor is adopted for this study, as detailed dimensions of this design are available as shown in Fig. 1.1.2(a). To estimate the pressure loss through the core, we conceptually divided the core into 6 sections from bottom to top, with a diverging entrance region and a converging exit region, as shown in Fig. 1.1.2(b).

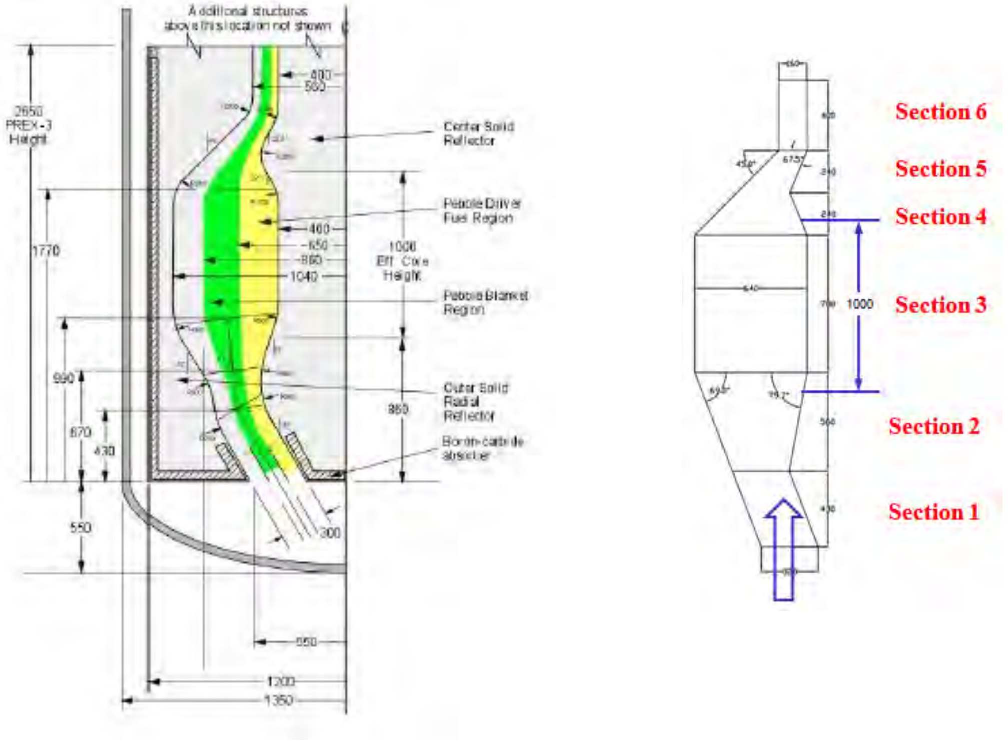
Additional structures above this location not shown
2650 PREX-3 Height
1770
990
670
430
550
400
560
400
650
860
1040
1000 Eff. Core Height
860
300
550
1200
1350
Center Solid Reflector
Pebble Driver Fuel Region
Pebble Blanket Region
Outer Solid Radial Reflector
Boron-carbide absorber
Section 6
Section 5
Section 4
1000
Section 3
Section 2
Section 1

(a) (b)

Fig. 1.1.2. (a) The pebble bed reactor core used in FHR-16 (Peterson, 2009) and (b) simplified sketch of the reactor core

The bulk temperature rise of FLiBe (the primary salt) across the core when the decay power is balanced by the DRACS heat removal capability can be estimated. Due to lack of the information on the decay power curve for the core design shown in Fig. 1.1.2(a), we employed the decay power equation for the light water reactors (LWRs), given as (Todreas and Kazimi, 1989):

$$\frac{P}{P_o} = 0.1\left[\left(\tau - \tau_s + 10\right)^{-0.2} - \left(\tau + 10\right)^{-0.2} + 0.87\left(\tau + 2\times 10^7\right)^{-0.2} - 0.87\left(\tau - \tau_s + 2\times 10^7\right)^{-0.2}\right], \quad (1.1.3)$$

where P, P_o, τ, and τ_s are the decay power, reactor power, time after reactor startup, and reactor operating time, respectively. The unit of time is second. It was found that the reactor power decreases to 1% after about 2.08×10^4 seconds (5.8 hours) and the increase in the bulk temperature of FLiBe is around 70 °C. The temperatures of FLiBe when it enters and exits the core under normal operation are designed to be 600 and 704 °C, respectively. We therefore assumed that 705 and 750 °C are respectively the temperatures of FLiBe in and out of the core when the DRACS is capable of removing 200 kW decay heat in accident.

Pebbles in the reactor core are categorized into fuel and blanket pebbles with an outer diameter (OD) of 30 mm. The pressure drop over the packed pebble bed is calculated following the Ergun relation (de Zwaan et al., 2007):

$$\Delta P = \frac{1-\varepsilon}{\varepsilon^3}\left(170\frac{\mu A}{\dot{m} d_p}(1-\varepsilon) + 1.75\right)\frac{L}{d_p \rho}\left(\frac{\dot{m}}{A}\right)^2 . \quad (1.1.4)$$

Here, ε, μ, ρ and $\dot{m}$ denote the volume fraction, dynamic viscosity, density, and mass flow rate of the fluid (FLiBe in the current analysis), respectively; L and A are the height and cross sectional area of the reactor core; d_p is the pebble OD. When the DRACS functions (i.e., the reactor is scrammed), the velocity of FLiBe decreases rapidly to less than 1 mm/s in the main region of the core. It results in a calculated pressure drop in the core, including the form loss, being 13 Pa, which is significantly smaller than that at the normal operating condition. It is noteworthy that the power provided in this core design (16 MWth) is lower than our proposed power level (20 MWth). This issue will be discussed later.

Selection of Fluidic Diode and its Pressure Drop Calculation

In the primary loop, a fluidic diode is employed as the passive flow control device. It avoids parasitic heat loss during normal operation by preventing a large amount of primary coolant from flowing upward through the DHX (reverse flow through the flow diode). In the event of a loss of forced flow coupled with a loss of shutdown cooling, natural circulation will reverse the flow in the DHX and the fluidic diode will operate in the forward direction (downward in Fig. 1.1.1) such that the primary coolant experiences much smaller resistance.

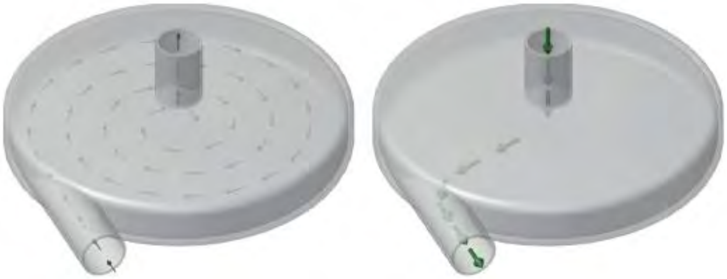

Fig. 1.1.3. Reverse and forward directions in a vortex diode

The performance of the fluidic diode greatly depends on the design parameters. We utilized a classic vortex diode (shown in Fig. 1.1.3), which has the design parameters listed in Table 1.1.2. The pressure loss is calculated based on the relations between the Reynolds number and resistance coefficient obtained by Chikazawa et al. (2009) from experiments, as plotted in Fig. 1.1.4. Here, the Reynolds number (Re) and resistance coefficient (ε) are respectively defined as:

Table 1.1.2 Parameters of the vortex diode

Diameter of vortex room	326.7 mm
Height of vortex room	130.7 mm
Diameter of vertical nozzle	36.0 mm
Tangential nozzle height	131.0 mm
Tangential nozzle width	12.8 mm

$$\mathrm{Re} = \frac{Vd}{\nu}, \tag{1.1.5}$$

$$\varepsilon = \frac{\Delta p}{0.5\rho V^2}, \tag{1.1.6}$$

where V, d, ν, and ρ are the flow velocity at the upper vertical nozzle at the vortex chamber ceiling, diameter of the upper vertical nozzle, kinetic viscosity and density of the fluid, respectively. When the capability of the DRACS is 200 kW, corresponding to the highest and lowest temperatures of FLiBe at 750 and 705 °C, respectively, the Reynolds number of FLiBe evaluated at the average temperature of FLiBe is 1.21×10^4, which is beyond the points shown in Fig. 1.1.4. However, it may be appropriate to assume that the resistance coefficient does not change dramatically when the Reynolds number changes from 1.0×10^5 to 1.21×10^4 after we examined the trend in Fig. 1.1.4. Therefore, the resistance coefficient could be taken between 0.3 and 0.35 when Reynolds number is around 1.21×10^4. It results in a pressure drop ranging from 254 to 296 Pa in our study. Additional pressure drop due to form loss is 44 Pa. We could further reduce the pressure loss by increasing the dimensions of the fluidic diode if needed.

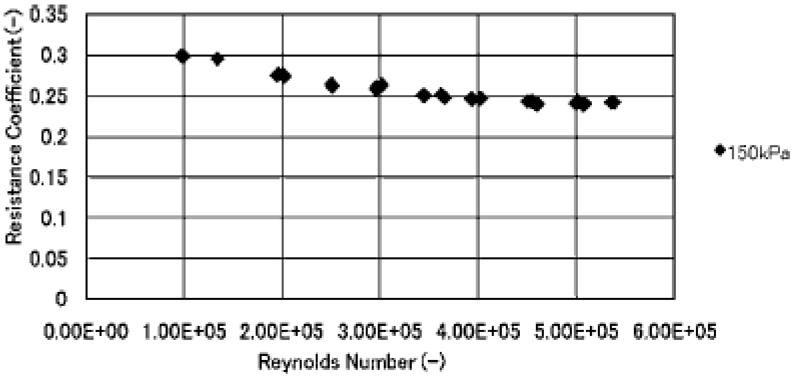

Fig. 1.1.4. Relations between the Reynolds number and resistance coefficient (forward flow) (Chikazawa et al., 2009)

Designs of DHX and its Pressure Drop Calculation

To date, a Matlab code based on the Delaware Method (Hewitt, 1992), which is well established for designing shell-and-tube heat exchanger, has been developed at Ohio State University for the designs of DHX and NDHX. Here, Hastelloy N, a nickel-base alloy, was selected as the structure material of both DHX and NDHX as it has good oxidation resistance to hot fluoride salts at high temperatures up to 871 ^{o}C (1600 ^{o}F). The thermal conductivities of Hastelloy N at different temperatures are provided in Table 1.1.3

Table 1.1.3 Thermal conductivities of Hastelloy N (Haynes international, Inc., 2002)

Temperature (^{o}C)	200	300	400	500	600	700
Thermal conductivity (W/m-K)	13.1	14.4	16.5	18.0	20.3	23.6

A one-pass shell and one-pass tube type heat exchanger was designed for the DHX, where FLiBe (hot fluid) and FLiNaK (cold fluid) were on the shell and tube sides of the DHX, respectively. As aforementioned, the highest and lowest temperatures of FLiBe are 750 and 705 ^{o}C, respectively when the capability of the DRACS is 200 kW. In addition, we assumed that the tube side (FLiNaK) outlet temperature is 680 ^{o}C based on the consideration of the DHX effectiveness, as well as leaving a sufficient margin above the melting point of FLiNaK. The tube side inlet temperature (FLiNaK) was considered as a variable, and we obtained different designs of DHX with different inlet temperature of FLiNaK.

The standard BWG 18 tubes with outer diameter (OD) of 15.875 mm and tube thickness of 1.245 mm were selected. They were arranged in a triangular pattern, with a pitch-to-diameter ratio of 1.4. Four baffles with a cut of 25% were used to increase the heat transfer capability. Figures 1.1.5 and 1.1.6 show the variations of the tube length and primary loop height with the tube side inlet temperature for three different tube numbers, i.e., 141, 196, and 261. A tradeoff among the tube number, tube length and primary loop height calls for the design with 196 tubes and tube inlet temperature of 630 ^{o}C, leading to a tube length of 1.21 m and shell inner diameter of 350 mm. The working conditions of the coolants are summarized in Table 1.1.4.

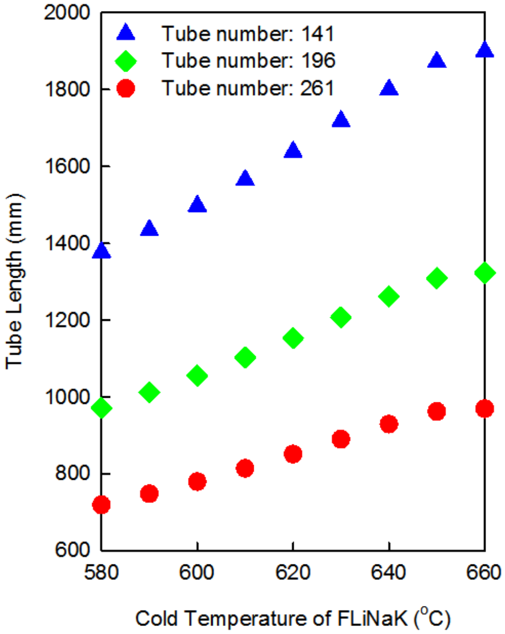

Fig. 1.1.5. Relation between the tube length and tube side inlet temperature

Table 1.1.4 Working conditions of selected salts

		Primary salt	Secondary salt
Chemical formula		FLiBe	FLiNaK
DHX		Shell side	Tube side
Temperature (°C)	high	750	680
	low	705	630
Mass flow rate (kg/s)		1.84	2.12

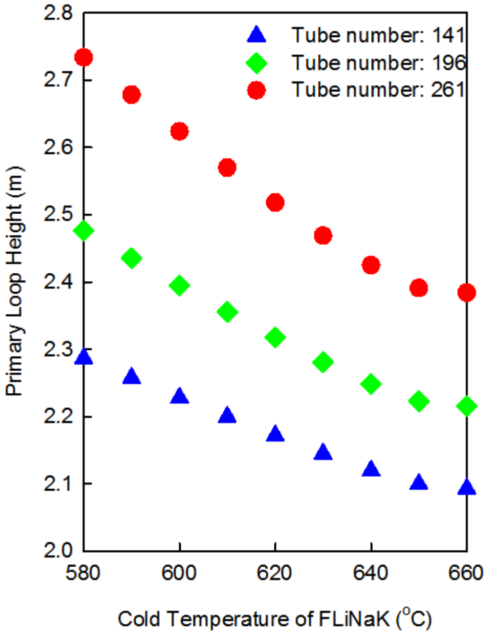

Fig. 1.1.6. Relation between the primary loop height and tube side inlet temperature

Designs of NDHX and Air Chimney and Pressure Drop Calculations

The secondary salt (FLiNaK) flows inside the straight tube bundles of the NDHX while air flows across the tube bundles, as illustrated in Fig. 1.1.7. For the NDHX design, we used the same dimensions for the tubes as those in the DHX design and arranged them in a triangular pattern with a pitch-to-diameter ratio of 2. The NDHX was placed at the bottom of the air chimney with 4 louvers, as shown in Fig. 1.1.7. The louvers were assumed half open in the calculations to ensure that the louver has enough controlling capability on the DRACS performance.

It was found that with increment in the number of tube rows, the resulting louver height increased significantly (due to the increased pressure drop through the rows of tubes). Therefore, only two rows of tubes were used in our design. The air inlet temperature was selected to be 40 °C to be conservative. The air outlet temperature was determined by investigating its influence on the louver height and tube length. It was calculated that the air outlet temperature should be higher than 90 °C if we desire the louver height to be below a reasonable height. On the other hand, the higher air outlet temperature demands longer tubes for all the cases with different number of tubes per row, as shown in Fig. 1.1.8. Using more tubes per row helps to reduce the tube length, but the width of each row is also increased correspondingly. We finally decided to employ 50 tubes per row, which yielded a tube length closer to the row width. With all above considerations, the air outlet temperature was chosen to be 100 °C, leading to the tube length of 1.93 m and air chimney of 10.43 m.

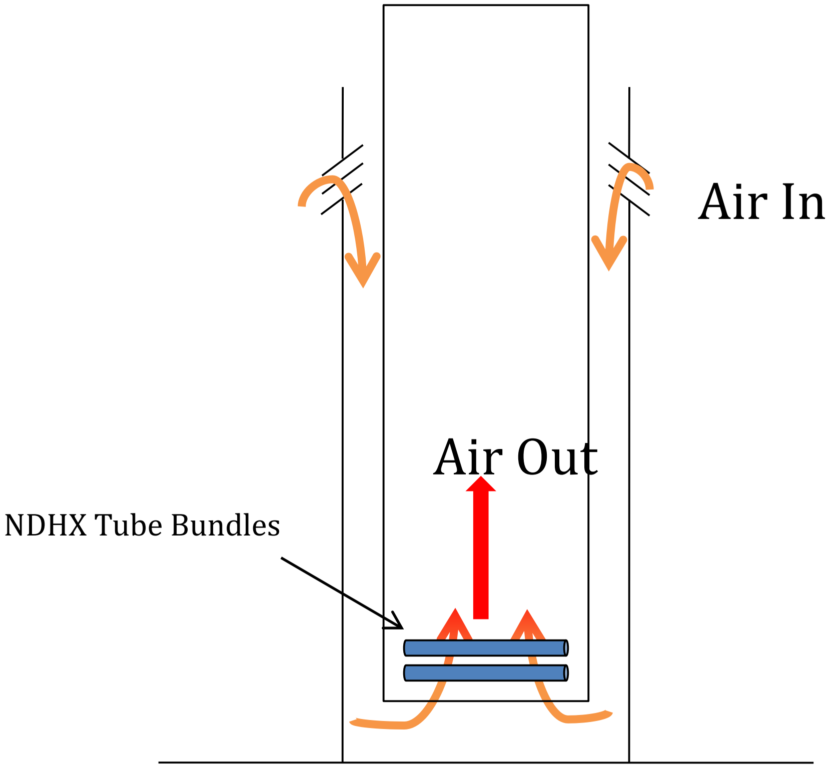
Air In
Air Out
NDHX Tube Bundles

Fig. 1.1.7. Air chimney with the NDHX at the bottom

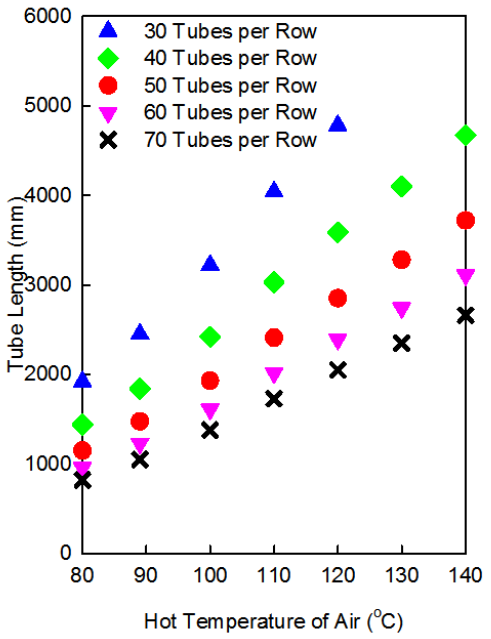

Fig. 1.1.8. Relation between the tube length and the air outlet temperature

Summary of Prototypic Design

Based on the aforementioned studies, the total pressure loss in the core region for the UCB FHR-16 core design is about 13 Pa, which is considerably small compared to the values due to other components in the primary loop such as the DHX ((~ 122 Pa) and fluidic diode (~ 330 Pa), as summarized in Table 1.1.5. Therefore, the pressure loss in the core region plays a minor role in the total pressure loss of the primary loop. This confirms that the use of the core dimensions from the UCB FHR-16 design to estimate the pressure loss in the reactor core is reasonable. Also, pipes with inner diameter (ID) of 15 cm were chosen for the piping systems in both primary and secondary loops.

To overcome the total pressure drop of ~ 491 Pa in the primary loop, the required vertical thermal center-to-center distance from the DHX to the core is approximately 2.28. The total pressure loss of the secondary loop is about 150 Pa, which mainly comes from the tube side of the DHX (96 Pa). It requires a 0.42-m thermal center-to-center distance from the NDHX to DHX and a 10.43-m high louver system. For the secondary loop, although a loop height of 0.42 m is sufficient to overcome the pressure drops along the loop, this height does not take into account of the physical layout of the reactor, especially the reactor pool, which might impose some other constraints on the loop height due to the fact that the DHX would be submerged in the pool. To date, there has not been any test FHR built yet. The only known effort in designing and building a test-scale FHR is due to Massachusetts Institute of Technology under an Integrated Research Project (Forsberg et al., 2014). Before a final design of the test FHR is accomplished, the pebble bed reactor core adopted in our previous DRACS prototype will be retained. This pebble bed core, as shown in Fig. 1.1.9, was the yield from a nuclear engineering design class at UC Berkeley. The detailed dimensions of the core were given, which were utilized in the calculation of the pressure drop over the core. However, a complete pool design for this pebble bed core, which would affect the layout and height of the DRACS secondary loop, was never accomplished. Due to this, we have referred to the SmAHTR design (Greene, 2010) by ORNL to reach a relatively more realistic layout for the DRACS secondary loop. The SmAHTR design features a total thermal power of 125 MWth, which is much larger than that of the pebble bed core. However, the physical size of the SmAHTR core, as seen from the comparison in Fig. 1.1.9, is comparable to that of the pebble bed core. Referring to the SmAHTR pool design will provide us some idea of the layout for the DRACS secondary loop.

Table 1.1.5 Pressure losses and heights of the primary and secondary loops

Primary Loop Pressure Drop (Pa)					Required Height (m)
Core	DHX shell side	Fluidic diode	Piping + connections	Total	
13	122	330	~ 16	~ 491	2.28
Secondary Loop Pressure Drop (Pa)					Required Height (m)
DHX tube side	NDHX tube side	Piping + connections	Total		
28	96	~ 26	~ 150		0.42

By referring to the SmAHTR pool design, the layout of the DRACS secondary loop has been proposed as illustrated in Fig. 1.1.10. The DHX will be submerged in the pool salt by 0.5 m, above which will be 0.5 m clearance for an inert gas. After exiting the DHX, the piping is routed in a zigzag shape to avoid interference with any equipment above the reactor. The NDHX is elevated from the chimney bottom by 0.5 m to enable the air flow to turn around by 180 degree. With such a loop layout, the height of the secondary loop has been intentionally increased from

0.42 to 2.3 m, including half of the DHX length. The high and low temperatures in the DRACS secondary loop have been selected based on the optimization of the DHX and NDHX designs, which will be maintained. With the total power fixed, the flow and pressure drops along the secondary loop will be the same as before. Due to the increased loop height, however, there will be an extra buoyancy of approximately 630 Pa induced in the secondary loop, which should be accommodated by adding extra throttling.

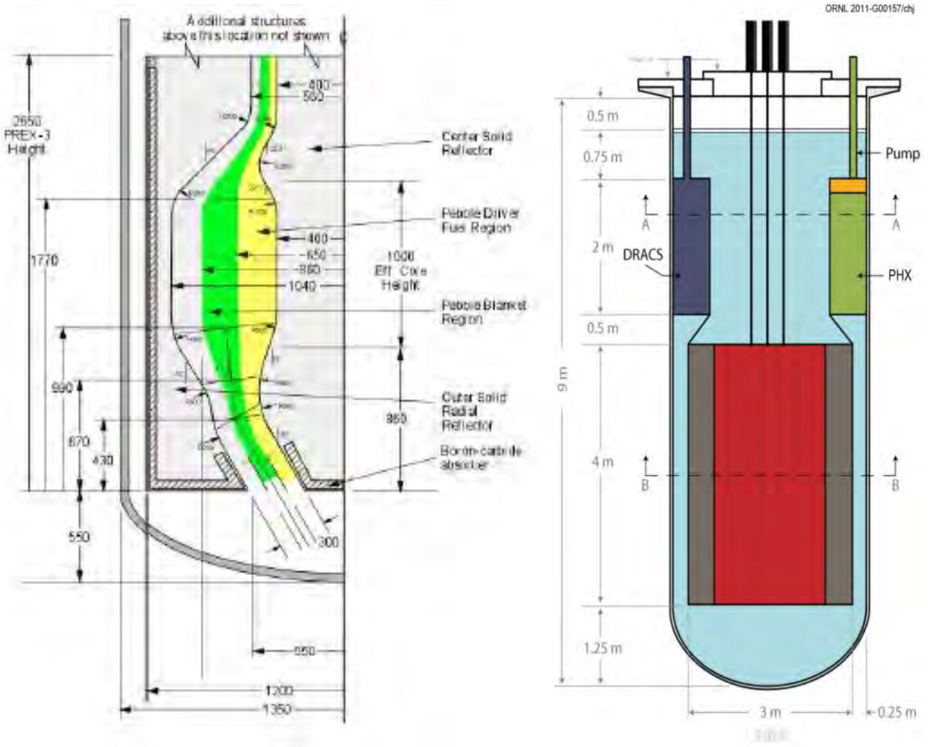
Additional structures above this location not shown
400
550
2650 PREX-3 Height
Center Solid Reflector
Pebble Driver Fuel Region
400
650
880
1040
1770
1000 Eff. Core Height
Pebble Blanket Region
990
Outer Solid Radial Reflector
860
670
430
Boron-carbide absorber
550
300
550
1200
1350
ORNL 2011-G00157/chj
0.5 m
0.75 m
Pump
A
A
2 m
DRACS
PHX
0.5 m
9 m
4 m
B
B
1.25 m
3 m
0.25 m

(a)

(b)

Fig. 1.1.9. (a) The FHR-16 pebble bed core (Peterson, 2009) and (b) SmAHTR core (Greene, 2010)

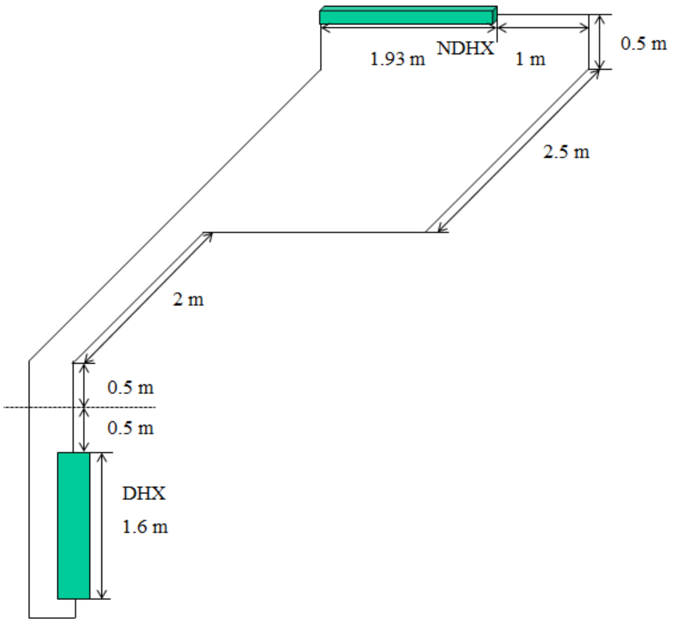
NDHX
1.93 m
1 m
0.5 m
2.5 m
2 m
0.5 m
0.5 m
DHX
1.6 m

Fig. 1.1.10. Layout of the DRACS secondary loop

In conclusion, the DRACS secondary loop height has been increased to 2.3 m, considering the constraints imposed by the physical layout of the reactor. The final design of the prototypic DRACS capable of removing 200 kW decay heat is shown in Fig. 1.1.11, with the design parameters summarized in Table 1.1.6.

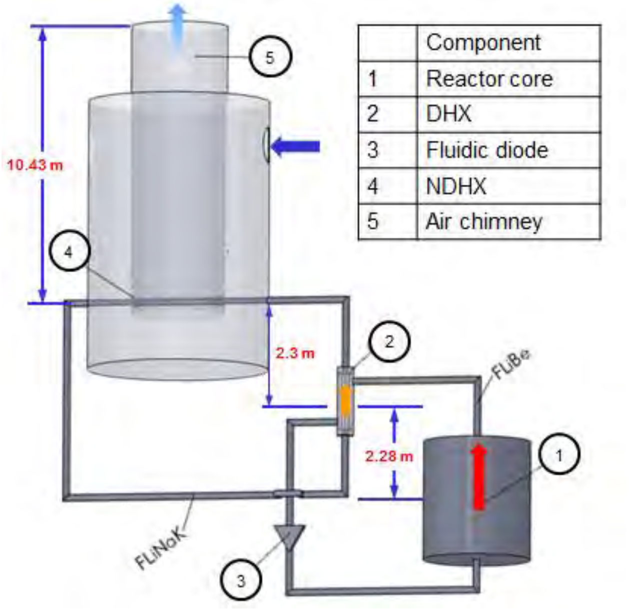
5
10.43 m
4
2.3 m
2
FLiBe
2.28 m
1
FLiNaK
3

	Component
1	Reactor core
2	DHX
3	Fluidic diode
4	NDHX
5	Air chimney

Fig. 1.1.11. Prototypic design of the DRACS

Table 1.1.6 Temperatures and mass flow rates of working fluids

	FLiBe	FLiNaK	Air
T_{hot} (°C)	750	680	100
T_{cold} (°C)	705	630	40
$\dot{m}$ (kg/s)	1.84	2.12	3.31

References:

Bardet, P., Blandford, E., Fratoni, M., Niquille, A., Greenspan, E., and Peterson, P.F., "Design, Analysis and Development of the Modular PB-AHTR," *Proc. of ICAPP'08*, Anaheim, CA, June 8-12, 2008.

Chikazawa, Y., Aizawa, K., Shiraishi, T., and Sakata, H., "Experimental Demonstration of Flow Diodes Applicable to a Passive Decay Heat Removal System for Sodium-Cooled Reactors," *Journal of Nuclear Science and Technology*, **46**(4), pp. 321-330, 2009.

de Zwaan, S.J., Boer, B., Lathouwers, D., and Kloosterman, J. L., "Static Design of A Liquid-Salt-Cooled Pebble Bed Reactor," *Annals of Nuclear Energy*, **34**, pp. 83-92, 2007.

Forsberg, C.W., "The Advanced High-Temperature Reactor: High-Temperature Fuel, Liquid Salt Coolant, and Liquid-Metal-Reactor Plant," *Progress in Nuclear Energy*, **47**(1-4), pp. 32-43, 2005.

Forsberg, C.W., Hu, L., Peterson, P.F., and Sridharan, K., "Fluoride-Salt-Cooled High-Temperature Reactor (FHR) for Power and Process Heat Final Project Report," MIT-ANP-TR-157, December 2014.

Greene, S.R., et al., "Pre-Conceptual Design of a Fluoride-Salt-Cooled Small Modular Advanced High-Temperature Reactor (SmAHTR)", ORNL/TM-2010/199, Oak Ridge National Laboratory, Oak Ridge, TN, 2010.

Grimes, W.R., "Chemical Research and Development for the Molten-Salt Breeder Reactor," ORNL/TM-1853, Oak Ridge National Laboratory, Oak Ridge, TN, 1967.

Grimes, W.R., "Molten Salt Reactor Chemistry," *Nuclear Applications and Technology* **8**(2), pp. 137–155, 1970.

Hastelloy N alloy, website of Haynes international, Inc., 2002.

Hewitt, G.F., *Handbook of Heat Exchanger Design*, chapter 3.3, Begell House, Inc., Wallingford, 1992.

Holcomb, D.E., Cetiner, S.M., Flanagan, G.F., Peretz, F.J., Yoder, G.L., Jr., "An Analysis of Testing Requirements for Fluoride Salt-cooled High Temperature Reactor Components," ORNL/TM-2009/297, Oak Ridge National Laboratory, November, 2009.

Peterson, P.F., "Modular Pebble-Bed AHTR Design Review," University of California, Berkeley, Design Status Update, October 7, 2009.

Williams, D.F., Toth, L.M., Clarno K.T., "Assessment of Candidate Molten Salt Coolants for the Advanced High-Temperature Reactor (AHTR)," ORNL.TM-2006/12, Oak Ridge National Laboratory, Oak Ridge, TN, 2006.

Todreas, N.E. and Kazimi, M.S., *Nuclear Systems I Thermal Hydraulic Fundamentals*, pp. 67, Taylor & Francis, 1989.

2. Issues/Concerns
To date, a final design of the fluidic diode has been completed. No issues are anticipated.

Task 1.2: Perform a review of the potential heat exchanger candidates for the DRACS and identify the heat exchanger types for the DRACS (Ohio State Responsible).

1. Task Status: Completed
Refer to Task 1.1

2. Issues/Concerns
None

Task 1.3: Develop a scaling analysis approach (Ohio State Responsible).

1. Task Status: Completed

Governing Equations

We conducted a scaling analysis to investigate the performance of the DRACS at both transient and steady-state conditions. In the similarity analysis, we applied Boussinesq approximation, which states that the fluid is incompressible except in the buoyancy term in the momentum equation. The density is therefore given as

$$\rho = \rho_0\{1-\beta(T-T_0)\}, \tag{1.3.1}$$

where subscript 0 stands for the reference constant value; ρ, β, and T are the density, thermal expansion coefficient, and temperature.

With this assumption, we obtained the one-dimensional governing equations as (Ishii and Kataoka, 1984; Vijayan and Austregesilo, 1994):
Continuity equation:

$$u_i a_i = u_r a_0, \tag{1.3.2}$$

Integral momentum equation:

$$\rho \frac{\mathrm{d}u_r}{\mathrm{d}t}\sum_i \frac{a_0}{a_i} l_i = g\rho \oint \beta\left(T - T_0\right)dz - \frac{\rho u_r^2}{2}\sum_i \left(\frac{fl}{d}+K\right)_i \left(\frac{a_0}{a_i}\right)^2, \tag{1.3.3}$$

Fluid energy equation for i^{th} section:

$$\rho c_p \left\{\frac{\partial T}{\partial t} + u\frac{\partial T}{\partial z}\right\} = \frac{4h}{d}\left(T_s - T\right), \tag{1.3.4}$$

Solid energy equation for i^{th} section:

$$\rho_s c_{ps} \frac{\partial T_s}{\partial t} - k_s \nabla^2 T_s - \dot{q}_s = 0, \tag{1.3.5}$$

Boundary condition between fluid and structure for i^{th} section:

$$-k_s \frac{\partial T_s}{\partial y} = h\left(T_s - T\right). \tag{1.3.6}$$

Here, subscripts i, r, and s are the ith component, representative variable, and solid structure, respectively. In addition, t, u, a, l, g, f, K, d, c_p, h, k, and $\dot{q}$ are the time, velocity, flow area, axial length, gravitational acceleration, friction factor, form loss factor, hydraulic diameter, heat capacity, heat transfer coefficient, conductivity, and volumetric heat generation, respectively. y and z denote the transverse and axial coordinates, respectively. We chose the steady-state values in each loop as reference values and defined the dimensionless parameters, as summarized in Table 1.3.1. Here, the hydraulic diameter d and conduction depth δ are respectively defined as $d = 4a / \xi$ and $\delta = a_s / \xi$, where ξ is the wetted perimeter.

We then obtained the non-dimensional conservation equations as:

$$U_i A_i = U_r, \tag{1.3.7}$$

$$\frac{dU_r}{d\tau}\left(\sum_i \frac{L_i}{A_i}\right) = \mathrm{R}\oint \theta\, dZ - \frac{U_r^2}{2}\left(\sum_i \frac{\mathrm{F}_i}{A_i^2}\right), \tag{1.3.8}$$

$$\frac{\partial \theta_i}{\partial \tau} + \frac{U_r}{A_i}\frac{\partial \theta_i}{\partial Z} = \mathrm{St}_i(\theta_{si} - \theta_i), \tag{1.3.9}$$

$$\frac{\partial \theta_{si}}{\partial \tau} - \mathrm{T}^* \nabla_i^{*2} \theta_{si} - \mathrm{Q}_{si} = 0, \tag{1.3.10}$$

$$\frac{\partial \theta_{si}}{\partial Y_i} = \mathrm{Bi}_i\left(\theta_i - \theta_{si}\right). \tag{1.3.11}$$

The dimensionless numbers in the above equations are defined below:

Richardson number: $\mathrm{R} \equiv \dfrac{\beta g \Delta T_0 l_0}{u_0^2}$,

Friction number: $\mathrm{F}_i \equiv \left(\dfrac{fl}{d} + K\right)_i$,

Stanton number: $\mathrm{St}_i \equiv \left(\dfrac{4hl_0}{\rho c_p u_0 d}\right)_i$,

Time ratio number: $\mathrm{T}_i^* \equiv \left(\dfrac{\alpha_s}{\delta^2}\dfrac{l_0}{u_0}\right)_i$, Heat source number: $\mathrm{Q}_{si} \equiv \left(\frac{\dot{q}_s l_0}{\rho_s c_{ps} u_0 \Delta T_0} \right)_i$,

Biot number: $\mathrm{Bi}_i \equiv \left(\frac{h\delta}{k_s} \right)_i$.

Table 1.3.1 Reference values and dimensionless parameters

	Reference values	Dimensionless parameters
Velocity	u_0: steady-state fluid velocity in the pipe (in primary or secondary loop)	$U_i = u_i / u_0$ $U_r = u_r / u_0$
Length	l_0 : vertical distance between thermal centers of DHX & core in primary loop or that between thermal centers of NDHX & DHX in secondary loop	$L_i = l_i / l_0$ $Z = z / l_0$
	δ : conduction depth	$\nabla^{*2} = \delta^2 \nabla^2$ $Y = y / d$
Area	a_0 : cross-sectional area of the pipe (in primary or secondary loop)	$A_i = a_i / a_0$
Time	l_0 / u_0	$\tau = t u_0 / l_0$
Temperature	ΔT_0 : temperature difference of primary salt in primary loop or that of secondary salt in secondary loop in steady state	$\theta = \left(T - T_0\right) / \Delta T_0$

Scaling Similarity Criteria

The similarity criteria between the prototype and model were established based on the aforementioned non-dimensional governing equations, i.e., Eqs. (1.3.7) - (1.3.11). They are summarized as follows:

$$\left(\sum_i L_i / A_i \right)_R = 1, \tag{1.3.12}$$

$$\left(\sum_i \mathrm{F}_i / A_i^2 \right)_R = \left[\sum_i \left(f_i \frac{l_i}{d_i} + K_i \right) / \left(a_i / a_0 \right)^2 \right]_R = 1, \tag{1.3.13}$$

$$\mathrm{R}_R = \left(\beta \Delta T_0 l_0 / u_0^2 \right)_R = 1, \tag{1.3.14}$$

$$A_{iR} = \left(a_i / a_0 \right)_R = 1, \tag{1.3.15}$$

$$\mathrm{St}_{iR} = \left(h l_0 / \rho c_p u_0 d \right)_{iR} = 1, \tag{1.3.16}$$

$$\mathrm{Bi}_{iR} = \left(h\delta / k_s \right)_{iR} = 1, \tag{1.3.17}$$

$$\mathrm{T}_{iR}^{*} = \left(\alpha_s l_0 / \delta^2 u_0\right)_{iR} = 1, \tag{1.3.18}$$

$$\mathrm{Q}_{siR} = \left(\dot{q}_s l_0 / \rho_s c_{ps} u_0 \Delta T_0\right)_{iR} = 1. \tag{1.3.19}$$

Here, the subscript R denotes the ratio between the model and the prototype. Equations (1.3.12) - (1.3.14) are the requirements considering the entire primary/secondary loop, while the rest are applied to each component in the primary/secondary loop. It is noted that the summations in Eqs. (1.3.12) and (1.3.13) provide weaker restrictions. A more restrictive relation applied to the individual component in the loop can be provided. For instance, Eq. (1.3.12) can be replaced by considering the axial geometrical similarity, given as:

$$L_{iR} = \left(l_i / l_0\right)_R = 1. \tag{1.3.20}$$

Considering the steady-state momentum and energy conservations of the entire primary/secondary loop, we got the ratios for the reference velocity and temperature difference as following:

$$\left(u_0\right)_R = \left(\frac{\beta l_0 \dot{Q}}{\rho c_p a_0}\right)_R^{1/3}, \tag{1.3.21}$$

$$\left(\Delta T_0\right)_R = \left(\frac{\dot{Q}}{\rho c_p u_0 a_0}\right)_R. \tag{1.3.22}$$

The requirement of the Richardson number is satisfied automatically if Eqs. (1.3.21) and (1.3.22) are used.

Table 1.3.2 summarizes the design parameters in the prototype and model (experiment), as well as some constraints in our experiment. For the primary loop scaling, we had two equations, i.e. Eqs. (1.3.21) and (1.3.22), but 5 unknowns, $\left(u_0\right)_R$, $\left(l_0\right)_R$, $\left(a_0\right)_R$, $\left(\Delta T_0\right)_R$, and $\left(\dot{Q}\right)_R$. To close the equations, three assumptions had to be made. Due to the power and space that are accessible in our experiment, we started with some assumptions on the power and loop height ratios, as listed in the last column of Table 1.3.2. So far, the only component that has been finalized in our prototypic design is the pebble bed reactor core while designs of other components are relatively flexible. Therefore, it is reasonable to provide the third assumption by performing core scaling analysis.

According to the time ratio scale in Eq. (1.3.18), the convection time ratio is formulated as:

$$\left(\frac{l_0}{u_0}\right)_R = \left(\frac{k_s \rho_s c_{ps}}{h^2}\right)_R. \tag{1.3.23}$$

We determined the convection time ratio in the primary loop based on the information on the structure material of the heat source and heat transfer coefficient, both in the prototype and experiment. This enables us to complete the core and primary loop scaling, as illustrated in Figs. 1.3.1 and 1.3.2. The product of the loop height ratio and pipe area ratio (which is the volume ratio) can be calculated either by using Eq. (1.3.19) with specified core geometry or from the loop scaling analysis. The heat source number matches if the evaluated values of this product from the two approaches are the same.

Table 1.3.2 Design parameters in the prototype and model

Parameters		Value in prototype	Value in experiment	Ratio
Q		200 kW	2 ~ 50 kW	0.01 ~ 0.25
l_0	Primary loop	2.28 m	< 2 m	< 0.88
	Secondary loop	0.42 m	If the same height	1.0
u_0	Primary loop	0.0541 m/s		
	Secondary loop	0.0586 m/s		
l_0/u_0	Primary loop	42.2 s	If real time simulation: 42.2 s	1.0
	Secondary loop	7.2 s	If real time simulation: 7.2 s	1.0
ΔT_0	Primary loop	45°C		
	Secondary loop	50°C		

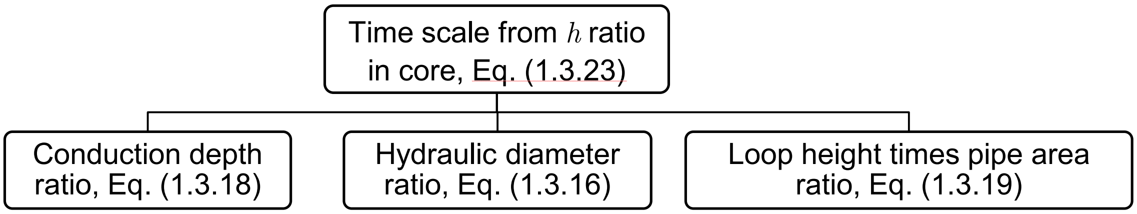
Time scale from h ratio in core, Eq. (1.3.23)
Conduction depth ratio, Eq. (1.3.18)
Hydraulic diameter ratio, Eq. (1.3.16)
Loop height times pipe area ratio, Eq. (1.3.19)

Fig. 1.3.1. Flowchart for the core scaling

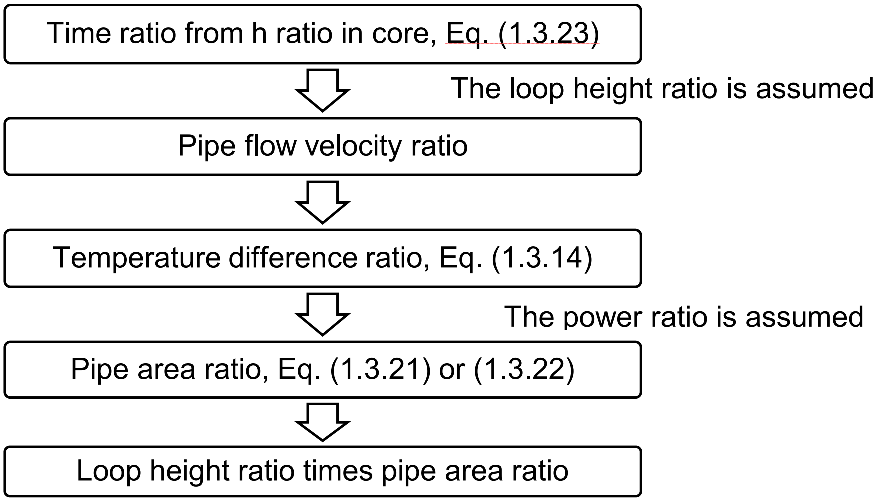
Time ratio from h ratio in core, Eq. (1.3.23)
The loop height ratio is assumed
Pipe flow velocity ratio
Temperature difference ratio, Eq. (1.3.14)
The power ratio is assumed
Pipe area ratio, Eq. (1.3.21) or (1.3.22)
Loop height ratio times pipe area ratio

Fig. 1.3.2. Flowchart for the primary loop scaling

For the secondary loop scaling, the same set of equations were applied, but the number of unknowns was reduced to 3 instead of 5 compared to the primary loop scaling. The reason is that one unknown, $\left(\dot{Q}\right)_R$, which is the heat removed by the secondary loop, is the same as that removed by the primary loop if the heat loss is negligible. In addition, the primary and secondary loops are the coupled through the DHX. The time ratio between the two loops will be the same if the thickness of the tubes of the DHX is considerably small compared to the tube diameter, which means that there is little storage energy in the structure. As a result, only loop height ratio was assumed for the secondary loop scaling. The process for the primary loop scaling (Figs. 1.3.1 and 1.3.2) can then be applied to the secondary loop as well.

As the heat transfer and pressure losses inside the DHX and NDHX are important, Eqs. (1.3.16) - (1.3.18), as well as the requirement of the friction number, are applied to DHX and NDHX, respectively. The fluidic diode in the primary loop exhibits negligible heat loss, but experiences significant pressure drop, which indicates that only the requirement of the friction number needs to be enforced on the fluidic diode. Upon the completion of the component scaling, Eqs. (1.3.12) and (1.3.13) are examined for the entire primary and secondary loops, respectively. If these requirements are not met, some compromise will need to be made in the scaling of some components.

Core Scaling Analysis

As discussed, the scaling process started with the convection time ratio in the primary loop, which is related to the convective heat transfer coefficient of the reactor core and structure properties of the reactor fuel.

We conducted a literature review of the heat transfer correlations in pebble bed and found out that most of them were valid under high Reynolds number cases. Here, we followed the discussions conducted by Karabales et al. (1971) for mass transfer correlations applicable to the low Reynolds number. We employed their correlations in the heat transfer analysis by analogising the Sherwood number to the Nusselt number and the Schmidt number to the Prandtl number. The heat transfer in the pebble bed could be natural, mixed, or forced convection, depending on its Reynolds number and Grashof number, which are respectively defined as:

$$\mathrm{Re} \equiv \frac{D_p G}{\mu}, \tag{1.3.24}$$

$$\mathrm{Gr} \equiv \frac{g\beta \triangle T D_p^3}{\nu^2}. \tag{1.3.25}$$

Here, D_p, $\triangle T$, G, μ and ν are the pebble diameter, temperature increase, mass flux, dynamic viscosity, and kinematic viscosity of the fluid, respectively. The heat transfer correlations for different flow regimes were given by Karabales et al. (1971) as:

Mixed convection:

$$\begin{cases} \text{Laminar: } \mathrm{Nu} = \left[\left\{ 0.46 \left(\mathrm{Gr}\,\mathrm{Pr} \right)^{1/4} \right\}^6 + \left\{ 4.58\,\mathrm{Re}^{1/3}\,\mathrm{Pr}^{1/3} \right\}^6 \right]^{1/6}, & (1.3.26) \\ \text{Turbulent: } \mathrm{Nu} = \left[\left\{ 0.112 \left(\mathrm{Gr}\,\mathrm{Pr} \right)^{1/3} \right\}^2 + \left\{ 2.39\,\mathrm{Re}^{0.56}\,\mathrm{Pr}^{1/3} \right\}^2 \right]^{1/2}, & (1.3.27) \end{cases}$$

Forced convection:

$$\mathrm{Nu} = \left[\left\{ 4.58\,\mathrm{Re}^{1/3}\,\mathrm{Pr}^{1/3} \right\}^6 + \left\{ 2.39\,\mathrm{Re}^{0.56}\,\mathrm{Pr}^{1/3} \right\}^6 \right]^{1/6}. \tag{1.3.28}$$

Figure 1.3.3 provides the relations between the Reynolds number and Grashof number when the flow transitions from the mixed to forced convection. The Reynolds number and Grashof number when the capability of the DRACS is 200 kW are 3.9 and 4.6E5, respectively, leading to a mixed laminar condition. The Nusselt number is 22.1 based on Eq. (1.3.26), and the heat transfer coefficient is 832 W/m^2-K when FLiBe is used as the primary coolant.

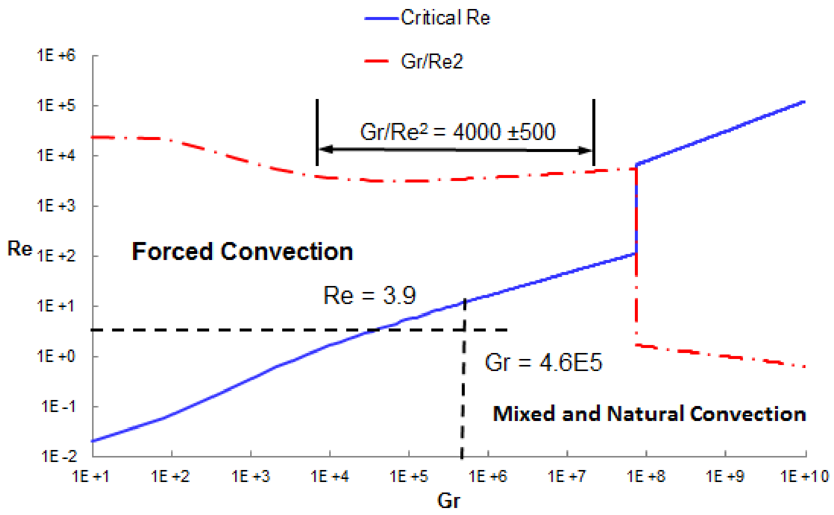

Fig. 1.3.3. Relations between the critical Reynolds number and Grashof number

Figure 1.3.4 shows the fuel pebble in the prototypic design proposed by Peterson (2009). This fuel pebble is smaller in size compared to conventional fuel pebble (3 cm vs. 6 cm in diameter). TRISO particles are embedded in the spherical shell with high-density graphite as the binder. The low-density graphite in the center of the pebble can adjust the overall density. The detailed dimension information on the pebble and the TRISO particle is listed in Table 1.3.3.

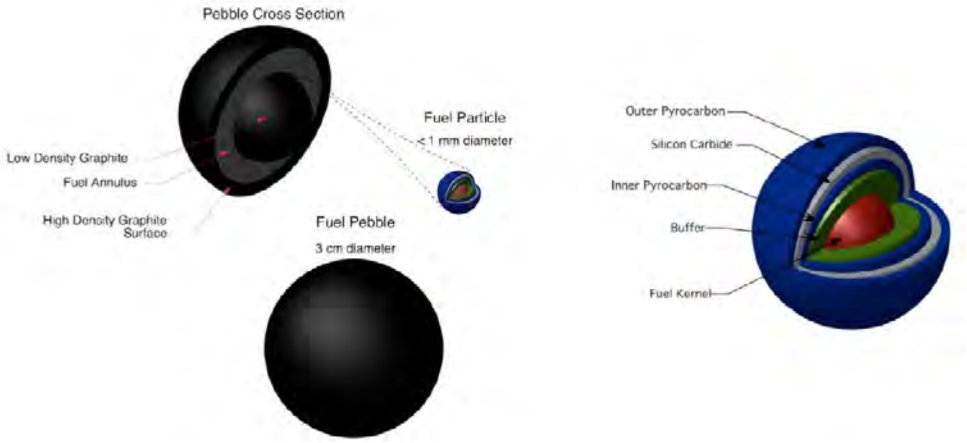
Pebble Cross Section
Low Density Graphite
Fuel Annulus
High Density Graphite Surface
Fuel Particle
<1 mm diameter
Fuel Pebble
3 cm diameter
Outer Pyrocarbon
Silicon Carbide
Inner Pyrocarbon
Buffer
Fuel Kernel

Fig. 1.3.4. The structure of a fuel pebble and TRISO particle (Peterson, 2009)

The TRISO particle has been well studied, and the material properties are readily available. The properties of different materials constructing a TRISO particle were summarized by Gougar et al. (2010). It is found that, the physical properties, such as specific heat capacity, density, and thermal conductivity, highly depend on the temperature. The thermal conductivity is also a function of the received neutron fluence. However, there have been limited studies on the matrix graphite, namely, the high-density graphite coating and the filling graphite in the fuel spherical shell. In the current study, we adopted the same matrix graphite as used in High Temperature Gas-Cooled Reactors (HTGRs).

Table 1.3.3 Dimensions of the fuel pebble and the TRISO particle (Griveau, 2007)

<table>
<tr><td colspan="6">Fuel pebble</td></tr>
<tr><td>Graphite kernel radius</td><td>Fuel zone outer radius</td><td>Coating thickness</td><td>Total number of TRISO</td><td colspan="2">Volumetric fraction of TRISO</td></tr>
<tr><td>0.992 cm</td><td>1.25 cm</td><td>0.25 cm</td><td>2144</td><td colspan="2">20%</td></tr>
<tr><td colspan="6">TRISO particle</td></tr>
<tr><td>Layer</td><td>Fuel kernel</td><td>Porous carbon</td><td>Pyrocarbon</td><td>SiC</td><td>Pyrocarbon</td></tr>
<tr><td>Radius (mm)</td><td>0.251</td><td>0.3425</td><td>0.3824</td><td>0.4177</td><td>0.4577</td></tr>
</table>

Two HTGR concepts have been developed: one is the pebble bed design adopted by Germany, China, and South Africa, and the other is the prismatic design adopted by the USA and Japan. Different fabricating processes of the fuel elements have be illustrated and compared by Barrachin et al. (2010). Despite the difference in the fabrication technology, the matrix graphite in the fuel pebble or the prismatic compact has the same composition, namely, 64% natural graphite, 16% synthetic graphite, and 20% thermosetting resin. We therefore assumed that the matrix graphite has the same properties despite its fabrication process. The properties of the matrix graphite depend on the temperature. The thermal conductivity of the matrix graphite also decreases with the increased neutron fluence that has been irradiated. The un-irradiated matrix graphite has thermal conductivity of 62 W/m-K at the room temperature (Sato et al., 1993) and 35 W/m-K at 1000 °C (Tang et al., 2002). The thermal conductivity of the un-irradiated matrix graphite at an arbitrary temperature between 25 and 1000 °C is obtained by linear interpolation. The change of the thermal conductivity with the received neutron fluence for the matrix graphite was obtained by Ahlf et al. (1990), as shown in Fig. 1.3.5.

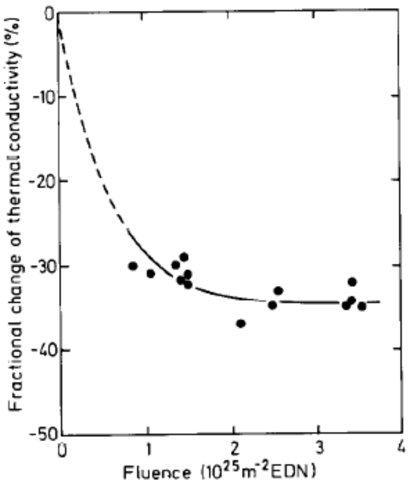

Fig. 1.3.5. Fractional change of thermal conductivity of matrix graphite with fluence at 1123-1213 K (Ahlf et al., 1990)

The temperature information was based on the simulations performed by Griveau (2007), who modelled the temperature evolution inside the pebble bed reactor during the loss of forced coolant accident (LOFC) transient. From Fig. 1.3.6, an average temperature of 750 °C (1023 K) inside the fuel was assumed in our analysis. The properties of every structure material at 750 °C are given in Table 1.3.4 under different fluence conditions. In what follows, we will discuss how to evaluate the effective properties of the entire pebble.

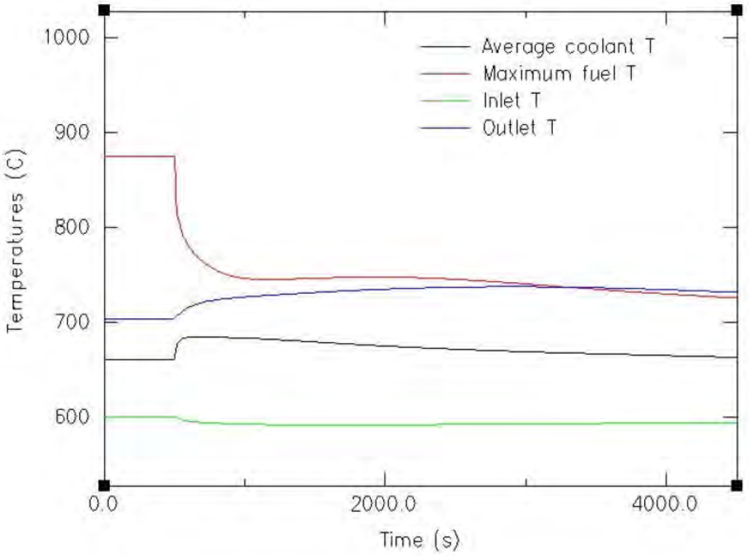

Fig. 1.3.6. Temperatures variation during the LOFC transient (Griveau, 2007)

Table 1.3.4 Properties of the structure materials of a pebble

Fluence (E25 n/m^2)		0	0.1	0.2	0.5	1	3--8
k (W/m-K)	UO_2	3.26	3.26	3.26	3.26	3.26	3.26
	Porous carbon	1.44	1.38	1.32	1.19	1.04	0.64
	Pyrocarbon	4.42	4.24	4.07	3.66	3.18	1.97
	SiC	19.48	19.23	19.00	18.28	17.15	10.15
	Matrix graphite	41.9	40.0	38.2	33.9	30.1	27.6
	Effective	36.5	33.1	30.8	26.7	23.7	21.0
c_p (J/kg-K)	UO_2	289					
	Porous carbon	645					
	Pyrocarbon	2175					
	SiC	1200					
	Matrix graphite	1772					
	Effective	1635					
ρ (kg/m^3)	UO_2	10750					
	Porous carbon	970					
	Pyrocarbon	1900					
	SiC	4210					
	Matrix graphite	1740					
	Effective	1894					

We used volumetric average to evaluate the effective density, and mass-weighted average to evaluate the effective specific heat capacity. The determination of the effective thermal conductivity was a little complicated and consisted of two steps. First of all, we used the empirical German relationship (Gao and Shi, 2002) for the homogeneous fuel spherical shell:

$$k_{shell} = 1.2768\left(\frac{-0.3906E-4T+0.06892}{DOSIS+1.931E-4T+0.105}+1.228E-4T+0.042\right), \tag{1.3.29}$$

where k_{shell} is the effective thermal conductivity of the fuel spherical shell in W/cm-K; T is the temperature in °C; $DOSIS$ is the neutron fluence in E25 n/m^2. Secondly, a volume-based harmonic average was made over the fuel spherical shell and the high-density graphite coating by considering that the two layers are in series and the total thermal resistance should be the summation of the individual ones. The effective thermal conductivity of the entire pebble, k_{pebble}, was thus calculated as:

$$k_{pebble} = \frac{k_{shell}V_{shell} + k_{matrix}V_{matrix}}{V_{shell} + V_{matrix}}. \tag{1.3.30}$$

The effective properties of the entire pebble are also provided in Table 1.3.4.

The next step is to determine the core and coolants for the experiment. For the low-temperature test facility, we will use surrogates (Dowtherm A or water) as the coolants. For the high-temperature facility, FLiNaK will be used as both the primary and secondary salts. Electrical heater bundles in circular vessel will be utilized to simulate the prototypic core in both test facilities. With the core and coolants specified, we can apply similar analysis to above to obtain the heat transfer coefficient and properties of the structure material of the heater rods in the experiment, based on which, the convection time ratio can be obtained from Eq. (1.3.23). The scaling strategy in forms of the flow chart shown in Figs. 1.3.1 and 1.3.2 enables us to complete the scaling of the entire system.

References:

Ahlf, J., Conrad, R., Cundy, M., and Scheurer, H., “Irradiation experiments on high temperature gas-cooled reactor fuels and graphites at the high flux reactor petten”, *Journal of Nuclear Materials*, **171**, pp. 31-36, 1990.

Barrachin, M., et al., “High Temperature Gas Cooled Reactor Fuels and Materials,” IAEA-TECDOC-1645-CD, IAEA, VIENNA, 2010.

Gao, Z., and Shi, L., “Thermal Hydraulic Calculation of the HTR-10 for the Initial and Equilibrium Core”, Nucl. Eng. and Des., **218**, pp. 51-64, 2002.

Gougar, H. et al., "Prismatic Coupled Neutronics/Thermal Fluids Transient Benchmark of the MHTGR-350 MW Core Design," 2010.

Griveau, A., "Modeling and Transient Analysis for the Pebble Bed Advanced High Temperature Reactor (PB-AHTR)", UCBTH-07-001, University of California at Berkeley, Berkeley, CA, 2007.

Ishii, M. and Kataoka, I., “Scaling Laws for Thermal-Hydraulic System under Single Phase and Two-Phase Natural Circulation,” *Nuclear Engineering and Design*, **81**, pp. 411-425, 1984.

Karabelas, A. J., Wegner, T. H., and Hanratty, T. J., "Use of Asymptotic Relations to Correlate Mass Transfer Data in Packed Beds", *Chemical Engineering Science*, **26**, pp. 1581-1589, 1971.

Peterson, P.F., “Modular Pebble-Bed AHTR Design Review,” University of California, Berkeley, Design Status Update, October 7, 2009.

Sato, S., et al., “Fracture mechanical properties and neutron irradiation effects of fuel compacts for the HTTR”, *Nuclear Engineering and Design*, **141**, pp. 395-408, 1993.

Tang, C., et al., “Design and manufacture of the fuel element for the 10 MW high temperature gas-cooled reactor”, *Nuclear Engineering and Design*, **218**, pp. 91-102, 2002.

Vijayan, P.K. and Austregesilo, H., “Scaling Laws for Single-phase Natural Circulation Loops,” *Nuclear Engineering and Design*, **152**, pp. 331-347, 1994.

2. Issues/Concerns
None

Task 1.4: Review relevant heat transfer and pressure drop correlations/model for the DRACS application (Ohio State Responsible).

1. Task Status: Completed
Refer to Task 1.1-1.3

2. Issues/Concerns
None

Task 1.5: Develop a computer code for DRACS performance evaluation (Ohio State Responsible).

1. Task Status: In progress; to be validated against OSU experimental data

To obtain a better understanding of the performance of the DRACS design as well as to guide the test facility design, we plan to conduct numerical simulations of DRACS using both RELAP5 and a computer code (both in Matlab and Simulink) that is being developed at Ohio State University.

The computer code to evaluate the performance of the prototypic DRACS design is being developed first. The principle behind this code is to solve the energy balance equations and integrated momentum equations, with some simplifications as follows:
i. A linear temperature gradient of the fluids in longitudinal direction was assumed in the core, DHX (both shell and tube sides), and NDHX (both shell and tube sides). The heat loss in the piping systems and the fluidic diode was assumed negligible;
ii. For the structures of the core, DHX, and NDHX, a lumped temperature was respectively assumed;
iii. The total friction pressure drop in each loop was calculated using an effective friction coefficient based on the steady state;
iv. Specific heat and thermal expansion coefficient of the fluids were assumed constant and assigned with their corresponding steady-state values;
v. For preliminary calculations, all the heat transfer coefficients were assumed to be linear with the corresponding mass flow rates;
vi. The mass of the fluids in the core, DHX, and NDHX was assumed constant.

Among them, the assumption v oversimplifies the problem, which will distort the transient simulation. More reasonable dynamic response functions of the heat exchangers will be implemented in the later work. Based on aforementioned assumptions, by integrating the energy balance equations over the core, DXH, and NDHX, we obtained the following eight equations:

Core:

$$h_c(T_c - \frac{T_1^h + T_1^c}{2})A_c + c_{pc} m_c \frac{dT_c}{dt} = \dot{Q} \tag{1.5.1}$$

$$c_{p1} m_{1c} \frac{d}{dt}\left(\frac{T_1^h + T_1^c}{2}\right) + c_{p1}\dot{m}_1\left(T_1^h - T_1^c\right) = h_c(T_c - \frac{T_1^h + T_1^c}{2})A_c \tag{1.5.2}$$

DHX:

$$h_{Ds}(\frac{T_1^h + T_1^c}{2} - T_D)A_{Ds} = h_{Dt}(T_D - \frac{T_2^h + T_2^c}{2})A_{Dt} + c_{pD} m_D \frac{dT_D}{dt} \tag{1.5.3}$$

$$-c_{p1} m_{1D} \frac{d}{dt}\left(\frac{T_1^h + T_1^c}{2}\right) + c_{p1}\dot{m}_1\left(T_1^h - T_1^c\right) = h_{Ds}(\frac{T_1^h + T_1^c}{2} - T_D)A_{Ds} \tag{1.5.4}$$

$$c_{p2} m_{2D} \frac{d}{dt}\left(\frac{T_2^h + T_2^c}{2}\right) + c_{p2}\dot{m}_2\left(T_2^h - T_2^c\right) = h_{Dt}(T_D - \frac{T_2^h + T_2^c}{2})A_{Dt} \tag{1.5.5}$$

NDHX:

$$h_{Nt}(\frac{T_2^h + T_2^c}{2} - T_N)A_{Nt} = h_{Ns}(T_N - \frac{T_3^h + T_3^c}{2})A_{Ns} + c_{pN} m_N \frac{dT_N}{dt} \tag{1.5.6}$$

$$-c_{p2} m_{2N} \frac{d}{dt}\left(\frac{T_2^h + T_2^c}{2}\right) + c_{p2}\dot{m}_2\left(T_2^h - T_2^c\right) = h_{Nt}(\frac{T_2^h + T_2^c}{2} - T_N)A_{Nt} \tag{1.5.7}$$

$$c_{p3} m_{3N} \frac{d}{dt}\left(\frac{T_3^h + T_3^c}{2}\right) + c_{p3}\dot{m}_3\left(T_3^h - T_3^c\right) = h_{Ns}(T_N - \frac{T_3^h + T_3^c}{2})A_{Ns} \tag{1.5.8}$$

Here, subscripts c, D, N, s, t, 1, 2, and 3 denote the core, DHX, NDHX, shell side, tube side, primary salt, secondary salt, and air, respectively; superscripts h and c denote the hot and cold temperature, respectively. In addition, h, A, T, c_p, m, and $\dot{m}$ stand for the heat transfer coefficient, heat transfer area, temperature, specific heat, total mass, and mass flow rate, respectively.

Except T_3^c which is set to be 40 °C, all the other temperatures and the mass flow rates are the variables. As can be seen, there are 11 unknowns, i.e., T_1^h, T_1^c, T_2^h, T_2^c, T_3^h, T_c, T_D, T_N, $\dot{m}_1$, $\dot{m}_2$, and $\dot{m}_3$, but only 8 equations, i.e., Eqs. (1.5.1) - (1.5.8). The equation system is closed by considering the other three integrated momentum equations:

$$\frac{d\dot{m}_1}{dt}\sum_i \frac{l_i}{a_i} = g\rho_{0,1}\beta_1 H_1(T_1^h - T_1^c) - \frac{f_1}{2\rho_1 A_1^2}\dot{m}_1^2 \tag{1.5.9}$$

$$\frac{d\dot{m}_2}{dt}\sum_i \frac{l_i}{a_i} = g\rho_{0,2}\beta_2 H_2(T_2^h - T_2^c) - \frac{f_2}{2\rho_2 A_2^2}\dot{m}_2^2 \tag{1.5.10}$$

$$\frac{d\dot{m}_3}{dt}\sum_i \frac{l_i}{a_i} = g\rho_{0,3}\beta_3 H_3(T_3^h - T_3^c) - \frac{f_3}{2\rho_3 A_3^2}\dot{m}_3^2 \tag{1.5.11}$$

where ρ, β and g are the density and thermal expansion coefficient of the working fluid, and the gravitational acceleration, respectively. l and a denote the length and area for the ith component in the loop; H is the height of the corresponding loop; and f stands for the effective friction coefficient, which is evaluated from the steady-state solutions.

Before employing the decay power function, we first tested the code during a LOFC (loss of forced coolant) accident with a constant decay power of 200 kW. The code was executed for 10^4 and 10^5 s, respectively. The temperatures and the mass flow rates of the fluids are given in Figs. 1.5.1 and 1.5.2, respectively. As can be seen, all these temperatures approach the values we designed, which indicates that the expected steady state will be successfully established. However, because of the oversimplified dynamic response functions used for the heat exchangers, the duration of the transient, as well as the temperature evolution during the transient was not well predicted.

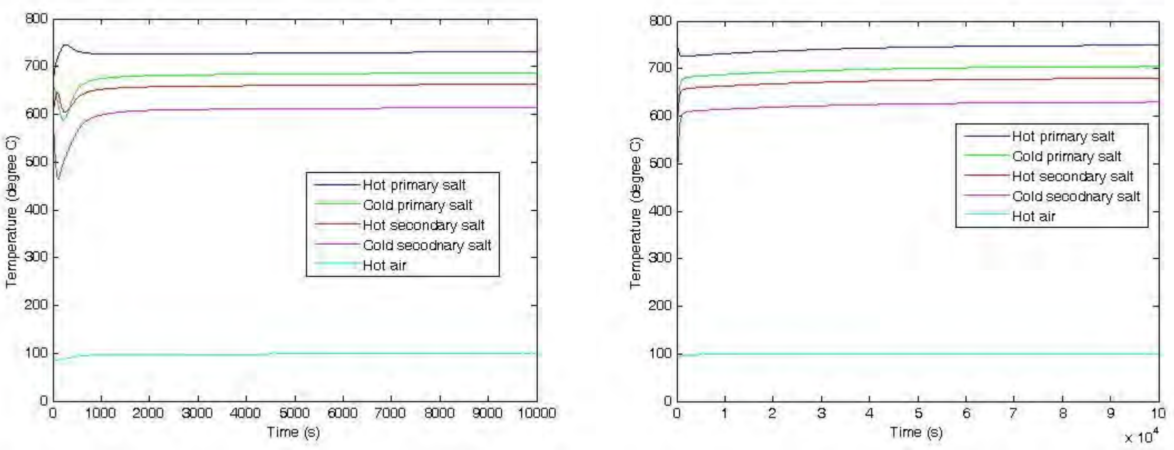

(a) (b)

Fig. 1.5.1. Temperatures of the fluids during the transient with a constant decay power of 200 kW for up to: (a) $t = 10^4$ s and (b) $t = 10^5$ s

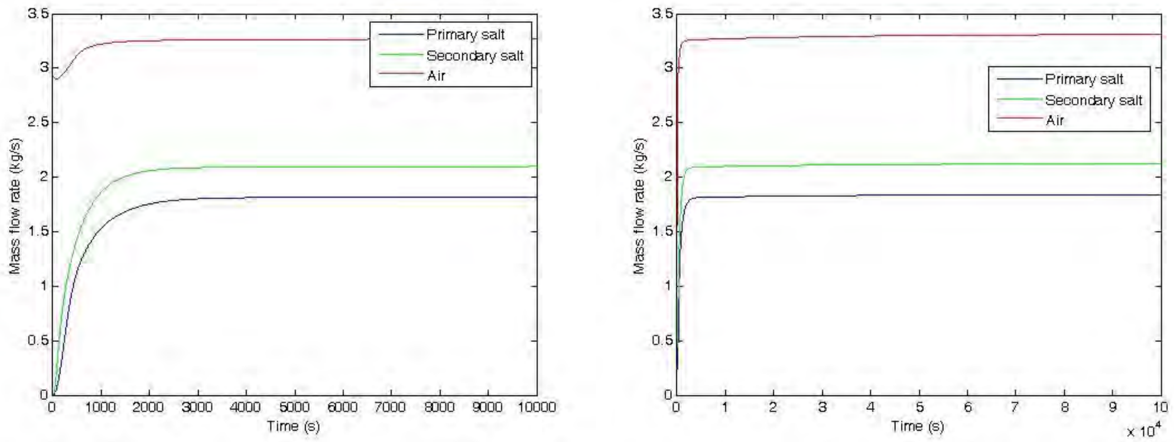

(a) (b)

Fig. 1.5.2. Mass flow rates of the fluids during the transient with a constant decay power of 200 kW for up to: (a) $t = 10^4$ s and (b) $t = 10^5$ s

As stated before, the assumption v regarding the heat transfer coefficients oversimplifies the problem, leading to distortion of the transient simulation. In regard of this, we first introduced more accurate heat transfer models for the DHX and NDHX, which are the same as those used in the heat exchanger design code. For shell-and-tube heat exchangers, the heat transfer coefficient is a function of the fluid inlet and outlet temperatures, structure temperature, and mass flow rate. Specifically, the shell-side heat transfer coefficient is based on that for ideal cross flow over tube banks:

$$h_s = J_c J_l J_b J_r J_s h_i, \tag{1.5.12}$$

where J_c, J_l, J_b, J_r, and J_s are the correction factors for the effect of baffle cut, leakage flow, bypass flow, adverse temperature gradient associated with laminar flow, and unequal baffle spacing. These correction factors depend on the heat exchanger geometry and the flow regime (J_r), and are detailed in the Heat Exchanger Design Handbook (Hewitt, 1992). h_i is the heat transfer coefficient for ideal cross flow over tube banks:

$$h_i = j_i c_{p,s} G_s (\mathrm{Pr}_s)^{-2/3} \left(\frac{\mu_s}{\mu_{s,w}} \right)^{0.14}, \tag{1.5.13}$$

where $c_{p,s}$, G_s, Pr_s, and μ_s are the heat capacity, mass flux, Prandtl number, and viscosity of the shell-side fluid, respectively. The tube wall effect is accounted for by considering $\mu_{s,w}$, which is the viscosity of the shell-side fluid at the tube wall temperature. The heat transfer factor j_i is obtained as follows:

$$j_i = a_1 \left(\frac{1.33}{L_{tp} / D_t} \right)^{a} \mathrm{Re}^{a_2}, \tag{1.5.14}$$

$$a = \frac{a_3}{1 + 0.14 \mathrm{Re}^{a_4}}, \tag{1.5.15}$$

where L_{tp} and D_t are the tube pitch and outer diameter, respectively. The values of a_1, a_2, a_3, and a_4 corresponding to different Reynolds number Re are listed in Table 1.5.1 (Hewitt, 1992).

Table 1.5.1 Empirical coefficients for calculation of j_i (Hewitt, 1992)

Re	a_1	a_2	a_3	a_4
10^5 - 10^4	0.321	-0.388	1.450	0.519
10^4 - 10^3	0.321	-0.388		
10^3 - 10^2	0.593	-0.477		
10^2 - 10	1.360	-0.657		
< 10	1.400	-0.667		

For the tube side, Hausen correlation was adopted for the laminar flow (Re < 2000):

$$h_t = \frac{k_t}{D_{ti}} \left\{ 3.65 + \frac{0.0668 \mathrm{Re}_t \mathrm{Pr}_t (D_{ti} / L_{ti})}{1 + 0.04 \left[\mathrm{Re}_t \mathrm{Pr}_t (D_{ti} / L_{ti}) \right]^{2/3}} \right\} \left(\frac{\mu_t}{\mu_{t,w}} \right)^{0.14}, \tag{1.5.16}$$

where k_t, μ_t, Re_t, and Pr_t are the thermal conductivity, viscosity, Reynolds number, and Prandtl number of the tube-side fluid, respectively; $\mu_{t,w}$ is the viscosity of the tube-side fluid estimated at the tube wall temperature; D_{ti} and L_{ti} are the tube inner diameter and length, respectively. Sieder-Tate correlation was used for the turbulent flow (Re > 10000):

$$h_t = 0.023 \frac{k_t}{D_{ti}} \mathrm{Re}_t^{0.8} \mathrm{Pr}_t^{1/3} \left(\frac{\mu_t}{\mu_{t,w}} \right)^{0.14} . \tag{1.5.17}$$

For transition flow, a linear interpolation was made between Eqs. (1.5.16) and (1.5.17).

Furthermore, we replaced the constant power by the decay power equation for LWRs, given as Eq. (1.1.3) in the updated code.

The initial temperatures of the hot and cold primary salt were chosen the same as the temperatures of the primary slat at steady state under normal operation, i.e., 704 °C and 600 °C, respectively. For the secondary salt, a uniform initial temperature was assumed as 618 °C. The air inlet temperature was assumed to be 40 °C in order to be conservative. The fluids were all assumed near-stationary in the beginning of the transient.

With the more accurate heat transfer models for DHX and NDHX, as well as the decay power profile, the evolutions of the temperatures and mass flow rates of the primary and secondary salts, and the air are given in Fig. 1.5.3. As can be seen, both the temperatures and mass flow rates of the fluids peak at around 5.6 h, which is understandable since the heat removal capability of the DRACS catches up with the decay power at 5.8 h after reactor shutdown as discussed in Task 1.1. In addition, the peak values of the temperatures and the mass flow rates, shown in Fig. 1.5.3, coincide with the designed values of the DRACS (which are the values in the bracket in Fig. 1.5.3). This coincidence somewhat demonstrates the validity of our code.

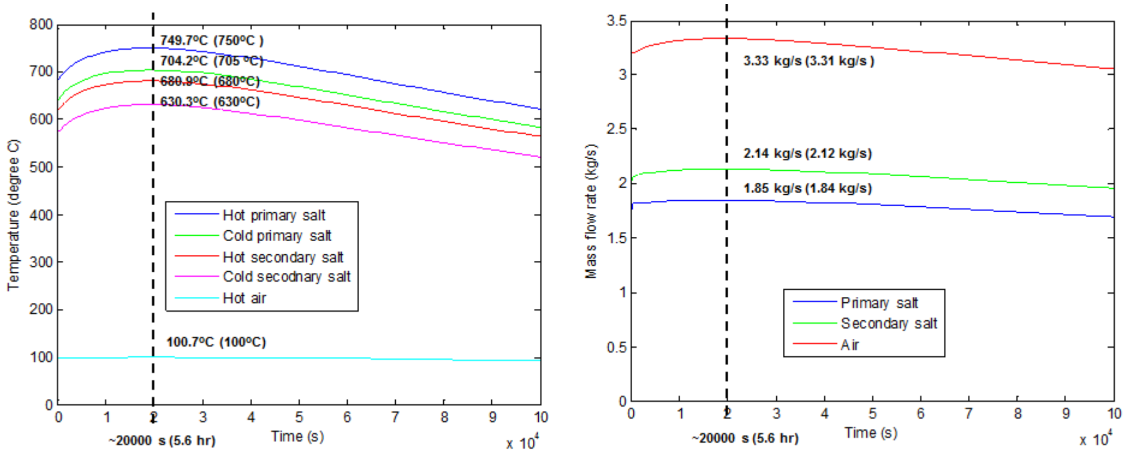

(a) (b)

Fig. 1.5.3. Information of the fluids during the transient for up to: t = 10^5 s: (a) Temperatures and (b) mass flow rates

We also examined the effect of the air inlet temperature on the performance of the DRACS with our code. The results of fluid temperatures and mass flow rates for air inlet temperature of 20, 40, and 60 °C are shown in Figs. 1.5.4 and 1.5.5. As can be seen, the overall trend of the temperatures and mass flow rates development is not affected by the air inlet temperature. However, the peaks of the temperature and mass flow rate are reached earlier for lower air inlet temperature. In addition, lower air inlet temperature tends to decrease the peak values of the temperatures, but slightly increase the peak values of the mass flow rates. The results of the peaking time, temperatures, and mass flow rates for different air inlet temperature are summarized in Table 1.5.2.

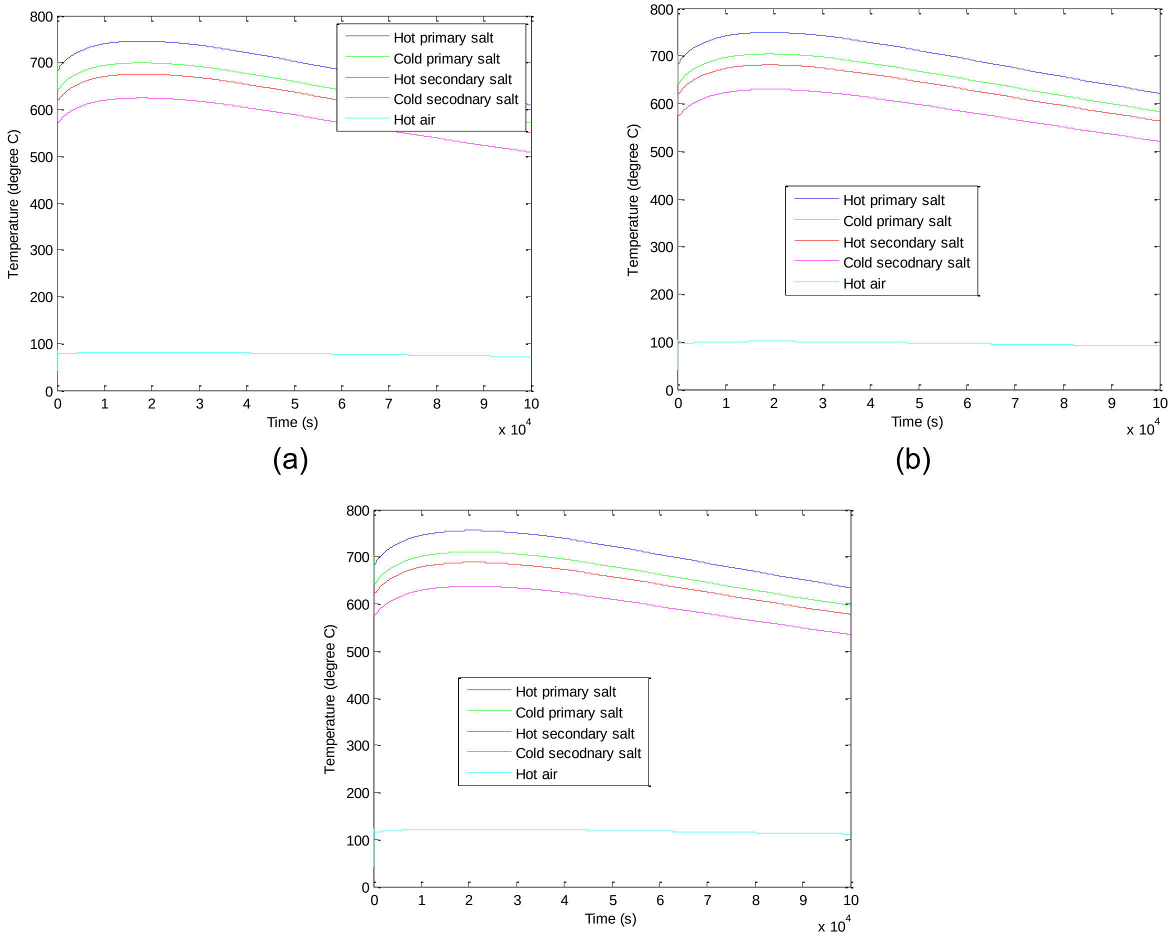

(a)

(b)

(c)

Fig. 1.5.4. Temperatures of the fluids during the transient for air inlet temperature of (a) 20 ^{o}C, (b) 40 ^{o}C, and (c) 60 ^{o}C

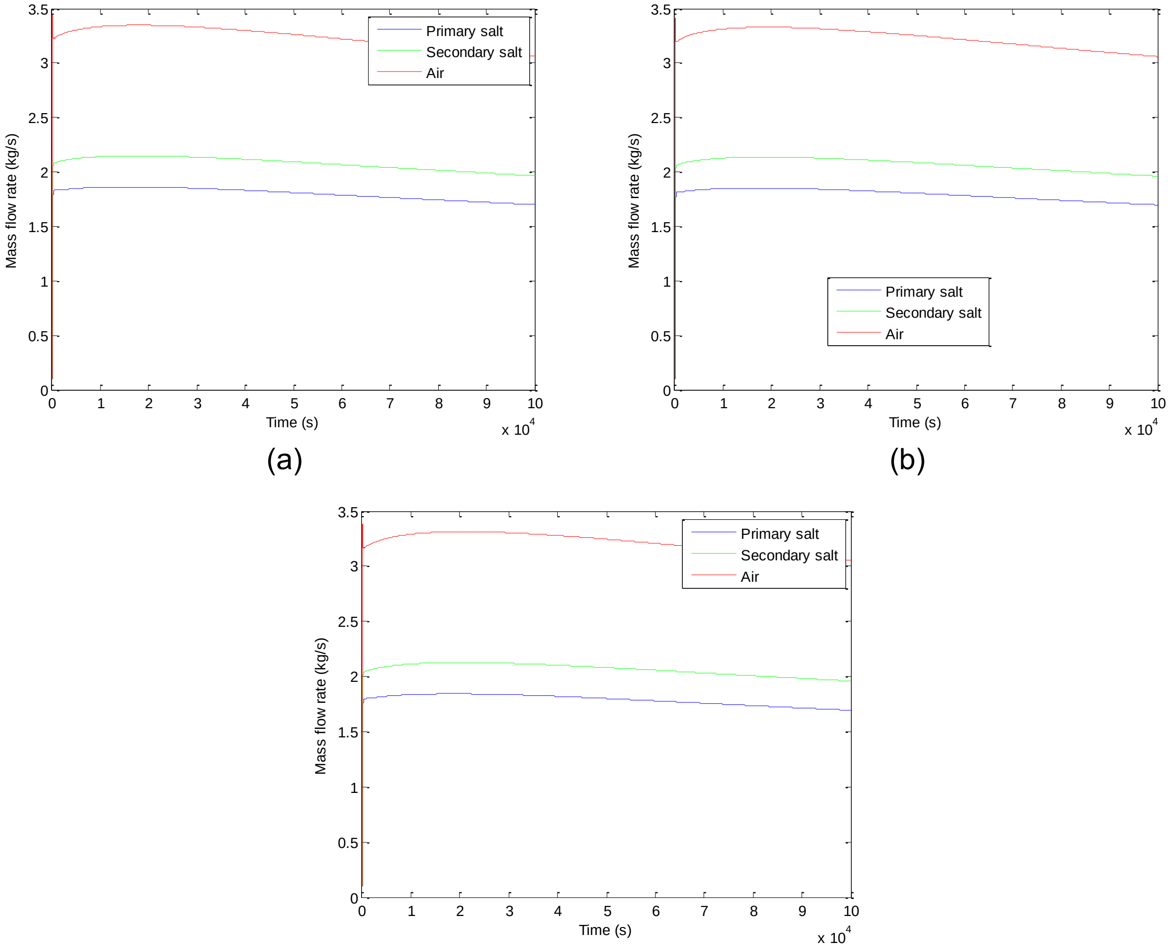

(a)

(b)

(c)

Fig. 1.5.5. Mass flow rates of the fluids during the transient for air inlet temperature of (a) 20 °C, (b) 40 °C, and (c) 60 °C

Table 1.5.2 Performance of the DRACS for different air inlet temperatures

Air inlet temperature	20 °C	40 °C	60 °C
t_{peak} (s)	1.75×10^4	2.0×10^4	2.1×10^4
$T_{1,hot}$ (°C)	745.8	749.7	755.8
$T_{1,cold}$ (°C)	699.7	704.2	710.7
$T_{2,hot}$ (°C)	675.8	680.9	688.1
$T_{2,\mathrm{cold}}$ (°C)	624.6	630.3	638.0
$T_{3,hot}$ (°C)	81.4	100.7	121.1
$\dot{m}_1$ (kg/s)	1.86	1.85	1.84
$\dot{m}_2$ (kg/s)	2.15	2.14	2.13
$\dot{m}_3$ (kg/s)	3.35	3.33	3.31

A low-temperature DRACS test facility (LTDF) that is designed to understand the interactions and coupling among the three natural circulation/convection loops is now under construction. It utilizes three electric heaters, with a total power of 2 kW, to simulate the core. Water has been selected as both the primary and secondary coolant, due to its availability and good thermal conductivity. Commercial shell-and-tube-, and finned tube heat exchangers have been used as the DHX and NDHX, respectively. To better understand the thermal performance of the LTDF, a MATLAB code has been developed based on the code previously developed for the prototypic DRACS design. Improvements have been made in the code formulation, heat transfer models, and friction resistance models. Experimental data obtained from the LTDF later on will be used to benchmark the code.

In the code for the prototypic DRACS design, the core inlet and outlet temperatures were assumed to be the same as the DHX shell-side outlet and inlet temperatures, respectively. Similarly, the DHX tube-side inlet and outlet temperatures were assumed to be the same as the NDHX tube-side outlet and inlet temperatures, respectively; and the NDHX air-side outlet temperature was assumed to be the same as the chimney outlet temperature. These assumptions are indeed true for the DRACS steady state. However, during the transient when the temperatures are still evolving, there is a time lag in temperature evolution between the outlet of a component and the inlet of the subsequent component. Therefore, the temperature variation along the connecting pipes and chimney has been also taken into account in the new code.

The principle is the same as before, i.e., to solve the energy balance equations and integrated momentum equations. Two assumptions have been made, which are:

i. The Boussinesq assumption applies, i.e., the density of the fluid is assumed to be constant except in the buoyance term in the integrated momentum equation;

ii. Heat loss from the entire LTDF is negligible.

For the LTDF, the temperature variations of the coolants are confined within a few tens degrees, which can be seen from Table 1.6.3. The corresponding density changes for the coolants are insignificant, which justifies the first assumption. Besides, the heat loss from the LTDF to the environment has also been investigated. It was found that, with 2-inch fiberglass pipe insulations, the heat loss from the LTDF is around 63 W, accounting for 3% of the total power of the facility. The aforementioned assumptions appear reasonable, which however will reduce the computation time significantly.

Finite volume method was applied by axially dividing the main components, as well as the connecting pipes, into subsections. For the core, DHX shell and tube sides, and NDHX tube side, each was axially divided into 5 equally long subsections. For the NDHX air side, because air flows across only two layers of finned tubes, one section was assumed for the entire air side. For the connecting pipes in the primary loop, as shown in Fig. 1.7.1, the two horizontal pipes connected to the core inlet and outlet, and the vertical pipe connected to the DHX shell-side inlet were divided to 5 equal subsections each. For the vertical pipe connected to the DHX shell-side outlet, it was first divided into 2 sections, one having the same length as the one connected to the DHX shell-side inlet, the other having the same length as the core height. The segmented vertical pipe was further divided into 5 equal subsections each, in which way, the primary hot and cold legs have the same number of subsections. For the secondary loop, the two main horizontal pipes, one to the left of DHX tube-side inlet and the other to the right of the NDHX tube-side inlet, and the two vertical pipes were divided into 5 equal subsections each. Finally, the air chimney as shown in Fig. 1.7.4 was equally divided into 5 subsections. There are totally 146 subsections for the LTDF, over which the energy balance equation was integrated. The temperature of each subsection will be solved for. Based on the aforementioned assumptions, these integrated energy balance equations are formulated as:

Core:

$$h_c(T_c - T_{1c})A_c + c_{pc} m_c \frac{\mathrm{d}T_c}{\mathrm{d}t} = \dot{Q} \tag{1.5.18}$$

$$c_{p1} m_{1c} \frac{\mathrm{d}T_{1c}}{\mathrm{d}t} + c_{p1}\dot{m}_1\left(T_{1c}^{out} - T_{1c}^{in}\right) = h_c(T_c - T_{1c})A_c - h_{cv}(T_{1c} - T_{cv})A_{cv} \tag{1.5.19}$$

$$h_{cv}(T_{1c} - T_{cv})A_{cv} = c_{pcv} m_{cv} \frac{\mathrm{d}T_{cv}}{\mathrm{d}t} \tag{1.5.20}$$

DHX:

$$h_{Ds}(T_{1D} - T_D)A_{Ds} = h_{Dt}(T_D - T_{2D})A_{Dt} + c_{pD} m_D \frac{\mathrm{d}T_D}{\mathrm{d}t} \tag{1.5.21}$$

$$c_{p1} m_{1D} \frac{\mathrm{d}T_{1D}}{\mathrm{d}t} + c_{p1}\dot{m}_1\left(T_{1D}^{out} - T_{1D}^{in}\right) = h_{Ds}(T_D - T_{1D})A_{Ds} - h_{Dv}(T_{1D} - T_{Dv})A_{Dv} \tag{1.5.22}$$

$$h_{Dv}(T_{1D} - T_{Dv})A_{Dv} = c_{pDv} m_{Dv} \frac{\mathrm{d}T_{Dv}}{\mathrm{d}t} \tag{1.5.23}$$

$$c_{p2} m_{2D} \frac{\mathrm{d}T_{2D}}{\mathrm{d}t} + c_{p2}\dot{m}_2\left(T_{2D}^{out} - T_{2D}^{in}\right) = h_{Dt}(T_D - T_{2D})A_{Dt} \tag{1.5.24}$$

NDHX:

$$h_{Nt}(T_{2N} - T_N)A_{Nt} = h_{Ns}(T_N - T_{3N})A_{Ns} + c_{pN} m_N \frac{\mathrm{d}T_N}{\mathrm{d}t} \tag{1.5.25}$$

$$c_{p2} m_{2N} \frac{\mathrm{d}T_{2N}}{\mathrm{d}t} + c_{p2}\dot{m}_2\left(T_{2N}^{out} - T_{2N}^{in}\right) = h_{Nt}(T_N - T_{2N})A_{Nt} \tag{1.5.26}$$

$$c_{p3} m_{3N} \frac{\mathrm{d}T_{3N}}{\mathrm{d}t} + c_{p3}\dot{m}_3\left(T_{3N}^{out} - T_{3N}^{in}\right) = h_{Ns}(T_N - T_{3N})A_{Ns} \tag{1.5.27}$$

Primary, secondary pipes and chimney:

$$c_{pi}m_{ip}\frac{\mathrm{d}T_{ip}}{\mathrm{d}t}+c_{pi}\dot{m}_{i}\left(T_{ip}^{out}-T_{ip}^{in}\right)=h_{ipv}(T_{ip}-T_{ipv})A_{ipv} \tag{1.5.28}$$

$$h_{ipv}(T_{ip}-T_{ipv})A_{ipv}=c_{pipv}m_{ipv}\frac{\mathrm{d}T_{ipv}}{\mathrm{d}t} \tag{1.5.29}$$

Here, subscripts c, D, N, p, v, s, t, 1, 2, and 3 denote the simulated core, DHX, NDHX, pipe/chimney, vessel, shell side, tube side, primary water, secondary water, and air, respectively; subscript i can take a value of 1, 2, or 3, representing one of the three circulation loops; superscripts out and in denote the outlet and inlet temperature for a specific cell. In addition, h, A, T, c_p, m, and $\dot{m}$ stand for the heat transfer coefficient, heat transfer area, temperature, specific heat, total mass, and mass flow rate, respectively.

It should be noted that, the core vessel, DHX shell, and all the piping systems have been taken into account for energy storage during the transient, which will mitigate the coolants' temperature increase. The number of equations obtained from energy balance is the same as that of temperature unknowns that need to be solved for. However, there are three more unknowns, i.e., the mass flow rates of the primary and secondary coolant, and air, calling for three more equations. The three integrated momentum equations provide the closure:

$$\frac{\mathrm{d}\dot{m}_1}{\mathrm{d}t}\sum_i\frac{l_i}{a_i}=g\rho_{o,1}\beta_1\sum_i(\pm)H_iT_i-\Delta P_1(\dot{m}_1) \tag{1.5.30}$$

$$\frac{\mathrm{d}\dot{m}_2}{\mathrm{d}t}\sum_i\frac{l_i}{a_i}=g\rho_{o,2}\beta_2\sum_i(\pm)H_iT_i-\Delta P_2(\dot{m}_2) \tag{1.5.31}$$

$$\frac{\mathrm{d}\dot{m}_3}{\mathrm{d}t}\sum_i\frac{l_i}{a_i}=g\rho_{o,3}\beta_3\sum_i(\pm)H_iT_i-\Delta P_3(\dot{m}_3) \tag{1.5.32}$$

where ρ , β and g are the density and thermal expansion coefficient of the working fluid, and the gravitational acceleration, respectively. l, a and H denote the length, area, and height for the ith component in the loop. Any horizontal component will not contribute to the buoyance, the height of which is taken as zero. For any component located in the hot fluid section, the sign in the buoyancy term is positive, otherwise negative. In addition, ΔP stands for the entire loop pressure loss, which depends on the loop flow rate, and will be discussed in detail in the following discussion.

Heat transfer in the simulated core, DHX, and NDHX is the most important in determining the thermal performance of the DRACS. The simulated core, as shown in Fig. 1.6.1, consists of three electric heaters. Heat transfer correlations proposed by Mohanty and Sahoo (1986, 1987) for a 7-rod bundle were adopted, mainly due to the limited study for 3-rod bundle configurations. During a postulated transient with no initial flows in the DRACS, the flow through the core will stay as laminar flow, for which the Nusselt numbers for the two sub-channels in the simulated core are constant. An area-weighted average was made between the heat transfer coefficients in the two sub-channels, yielding an overall heat transfer coefficient of 100.04 W/m^2-K for the core.

For the DHX shell and tube sides, and NDHX tube side, heat transfer models used in the present code are the same as those used in the previous code for the prototypic DRACS design, i.e., Eqs. (1.5.12) - (1.5.17). In the LTDF, finned tube heat exchanger has been used for the NDHX, which is different from the bare tube design in the prototypic DRACS design. Therefore, for the NDHX air side, Briggs and Young correlation for cross flow over finned tube has been used:

$$h_{air} = 0.134\frac{k_{air}}{d_r}\left(\frac{d_r\rho_{air}V_{\max}}{\mu_{air}}\right)^{0.68}\mathrm{Pr}_{air}^{1/3}\left(\frac{H}{s}\right)^{-0.2}\left(\frac{Y}{s}\right)^{-0.12} \tag{1.5.33}$$

where k_{air}, μ_{air}, and $\mathrm{Pr}_{\mathrm{air}}$ are the thermal conductivity, viscosity, and Prandtl number of air, respectively; V_{max} denotes the maximum air velocity across the finned tubes; d_r, H, Y, and s are the bare tube outer diameter, fin height, fin thickness, and fin spacing, respectively.

As mentioned earlier, the core vessel, DHX shell, and all the piping systems have been considered for energy storage. For the piping systems, the same correlations as those for the DHX and NDHX tube side were used, i.e., Eqs. (1.5.12) - (1.5.17). For the core, an imaginary annulus between the core vessel and the rod bundle was assumed. As the flow through the core stays as laminar during the transient, the Nusselt number for laminar flow in an annular duct proposed by Lee and Kuo (1998) was employed, which is a constant of 7.52 for the present case. For the DHX, because the clearance between the shell and tube bundle is much smaller than the shell inner diameter, and also the flow in the clearance is mainly along the periphery of the shell inner surface, a heat transfer model for flow between parallel plates was adopted. Laminar flow is retained in the aforementioned clearance, and a constant Nusselt number of 7.54 (Todreas and Kazimi, 1990) corresponding to a constant boundary temperature condition was used.

It was noted that, the heat transfer correlations for the DHX shell side and NDHX air side would give vanishing values when the corresponding fluids are stationary. However, heat can still be transferred to the shell-side fluid or air by conduction, even if there is no flow. Therefore, a Nusselt number of a value 2 has been selected for the DHX shell side and NDHX air side when there is no flow, analogous to the heat conduction from a sphere to a stagnant fluid.

In the present code, an overall loop pressure loss model has been developed for each of the three natural circulation loops, based on the contributions from various components to the total pressure loss. By introducing the loop pressure loss models, the pressure loss characteristic in each loop is retained, while the computation time is significantly reduced. For the primary loop, at the nominal steady-state conditions, pressure losses from various contributors are summarized in Table 1.5.3. As can be seen, almost 91% of the total pressure loss comes from the throttling valve and the form loss. According to Eq. (1.7.1), the pressure loss in the throttling valve can be modeled as proportional to the second order of mass flow rate, which is the same for the form loss. Therefore, the total pressure loss in the primary loop was modeled as:

$$\Delta P_1(\dot{m}_1) = A\dot{m}_1^2 \tag{1.5.34}$$

Table 1.5.3 Pressure losses over the main components in the primary loop

	Pressure Loss (Pa)
Core	0.02
DHX Shell Side	4.5
Primary Pipe	4.9
Form Loss	~ 5.3
Throttling Valve	~ 92.1

For the secondary loop, the pressure losses over the various components at steady state are summarized in Table 1.5.4. As can be seen, around 17% pressure loss exists due to the pipe, while the rest mainly comes from the throttling valve and the form losses. As the flow inside the secondary loop pipe stays in laminar regime, in which the friction factor is inversely proportional to the mass flow rate. Therefore, the friction loss in the pipe is proportional to the mass flow rate, and the total loop pressure loss was modeled as:

$$\Delta P_2(\dot{m}_2) = B\dot{m}_2 + C\dot{m}_2^2 \tag{1.5.35}$$

Table 1.5.4 Pressure losses over the main components in the secondary loop

	Pressure Loss (Pa)
DHX Tube Side	0.5
NDHX Tube Side	0.2
Secondary Pipe	9.6
Form Loss	~ 7.3
Throttling Valve	~ 37.3

For the air-chimney, which is illustrated in Fig. 1.7.4, the contributions to the total pressure loss at steady state are summarized in Table 1.5.5. As can be seen, the friction in the small pipe, form loss, and acceleration loss are the main contributors, the latter two of which can be modeled as proportional to the second order of mass flow rate. However, the air flow in the duct at the steady state becomes turbulent, in which the friction coefficient is inversely proportional to $\dot{m}^{-1/4}$ according to the Blasius relation (Todreas and Kazimi, 1990). Therefore, the total pressure loss in the air loop is modeled as:

$$\Delta P_3(\dot{m}_3) = D\dot{m}_3^{1.75} + E\dot{m}_3^2 \tag{1.5.36}$$

Table 1.5.5 Pressure losses over the main components in the air loop

	Pressure Loss (Pa)
Friction in small pipe	0.2448
Friction in large pipe	1.946E-4
NDHX air side	0.1554
Acceleration loss	0.4351
Form loss	1.7498

The proportionality constants in these loop pressure loss models, i.e., A, B, C, D, and E, were determined from the pressure losses and mass flow rates at the nominal steady state of the LTDF, which are shown in Tables 1.5.3 - 1.5.5, and Table 1.6.3.

The code was executed with a constant heating power of 2.05 kW and various initial conditions. In the experiment, the LTDF will probably be started at room temperature, and with zero initial flows. The results corresponding to uniform initial temperatures of 20°C and zero initial flows are shown in Figs. 1.5.6 - 1.5.9. As can be seen, both the coolant temperatures and mass flow rates asymptotically approach a constant value. A closer observation reveals that the steady-state mass flow rates and hot-cold-leg temperature differences are quite close to the design values which are listed in Table 1.6.3. However, the absolute values of the temperatures deviate from the designed values, which is probably because of the difference between the purchased heat exchangers and designed ones as seen from Tables 1.7.3 and 1.7.5. In addition, the initial conditions which determine the initial energy storage in the LTDF may also affect the steady-state coolants' temperatures. The evolution of the coolants' temperatures and mass flow rates during the beginning of the transient are also shown in Figs. 1.5.6 - 1.5.9 (b). Due to the connecting pipes/chimney, there is a lag in temperature evolution between the core outlet and DHX shell-side inlet, the DHX shell-side outlet and core inlet, etc. As time elapses, this lag decreases. Because the primary water will be heated up immediately after the heaters are turned on, the primary mass flow rate develops quickly from time zero. However, the secondary water will not receive heat until the hot primary water propagates to the DHX shell side, which is the reason why the secondary mass flow rate stays as zero for about 200 s in the beginning. The same reasoning applies to the air mass flow rate trend.

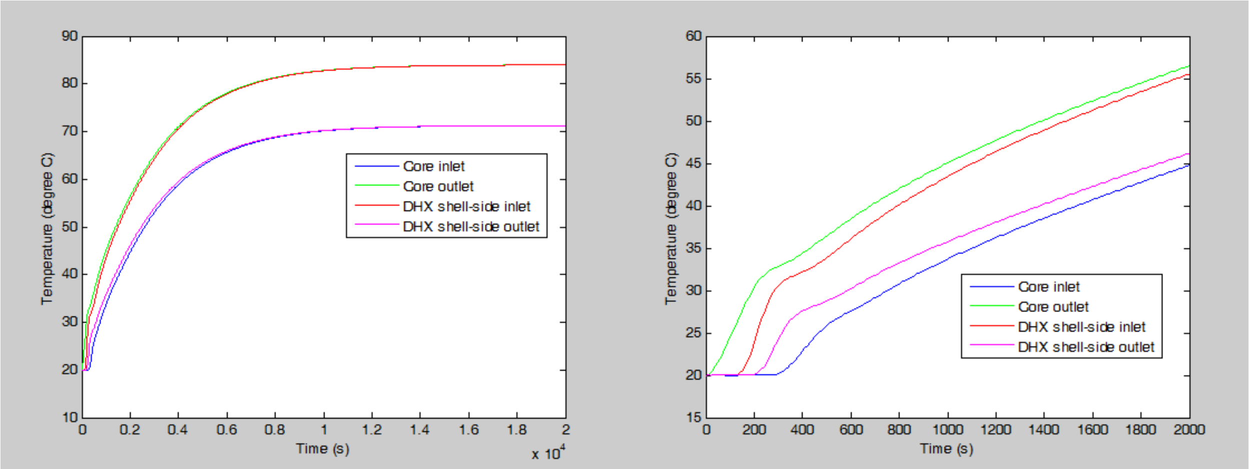

(a) (b)

Fig. 1.5.6. Temperatures in primary loop during the transient for up to: (a) t = 20,000 s and (b) t = 2,000 s

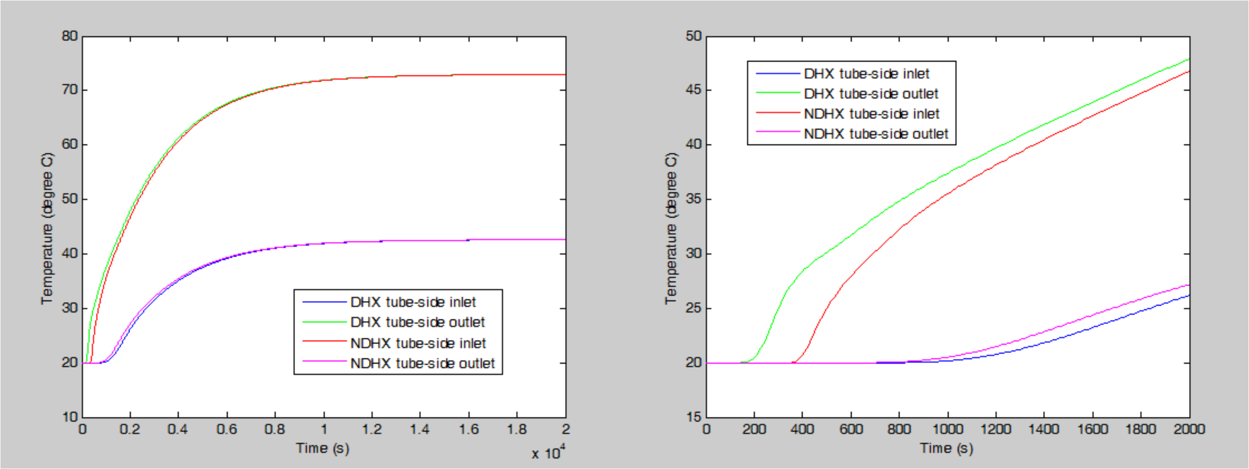

(a) (b)

Fig. 1.5.7. Temperatures in secondary loop during the transient for up to: (a) t = 20,000 s and (b) t = 2,000 s

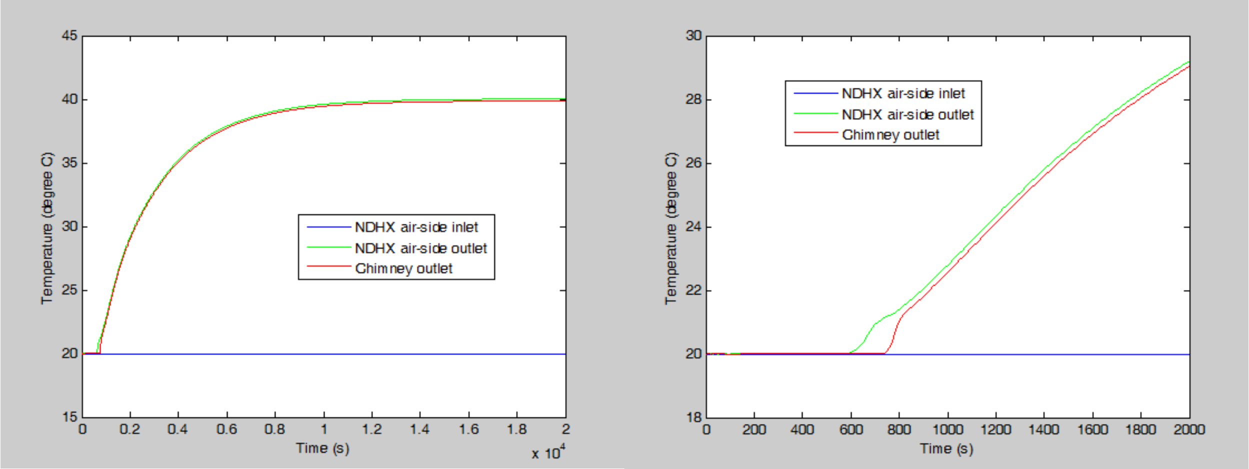

(a) (b)

Fig. 1.5.8. Temperatures in air loop during the transient for up to: (a) t = 20,000 s and (b) t = 2,000 s

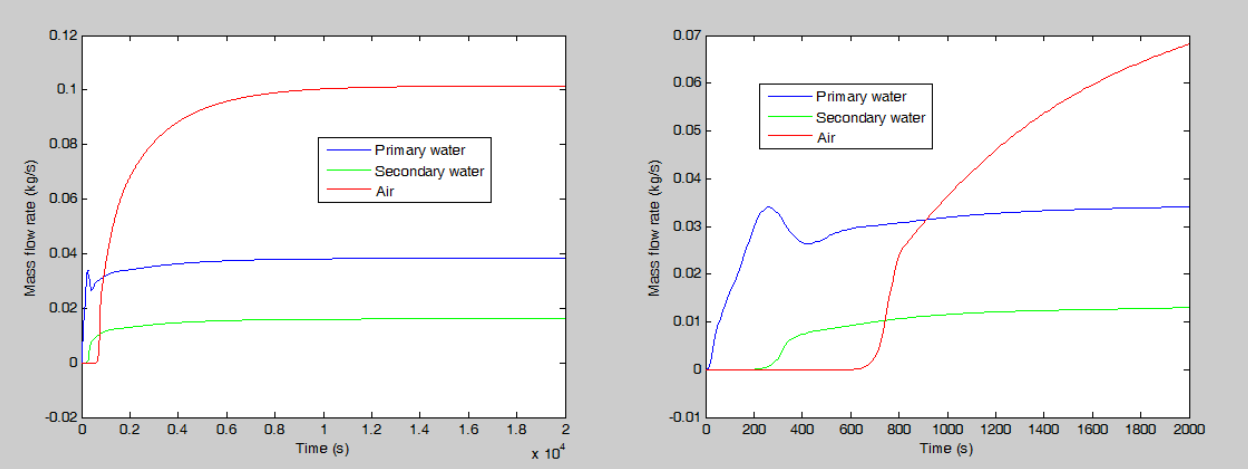

(a) (b)

Fig. 1.5.9. Mass flow rates during the transient for up to: (a) t = 20,000 s and (b) t = 2,000 s

In the prototypic DRACS, the system will start functioning with initial conditions determined from the normal steady-state operation of the reactor, instead of the previously assumed initial conditions. Besides, as mentioned earlier, the initial conditions may also affect the DRACS steady-state conditions. Therefore, the code was ran with a different set of initial conditions, in which the initial temperatures of the heater sheath, DHX tubes, NDHX tubes, chimney wall, primary water, secondary water, and air were assumed to be 120, 50, 35, 30, 60, 40, and 30°C, respectively. The initial coolant flow rates were still assumed to be zero. There are no special reasons for assigning initial conditions as such. We simply wanted to examine how the LTDF performance would be affected by the initial conditions. The results with the elevated initial temperatures are illustrated in Figs. 1.5.10 - 1.5.13. As can be seen, the lag in temperature evolution between the core outlet and DHX shell-side inlet, the DHX shell-side outlet and core inlet, etc., still exists due to the connecting pipes/chimney. Because of the initial temperature gradient from the core to the ambience, water in the DHX shell side, as well as that in the NDHX tube side are cooled down, while air in NDHX is heated up from the very beginning of the transient, which can be seen from Figs. 1.5.10 - 1.5.12 (b). As a result, density difference is initiated in all three loops from the time point of zero, which is why the mass flow rates develop faster than the previous case as seen from Fig. 1.5.13. In addition, comparison between Figs. 1.5.6 - 1.5.9 and Figs. 1.5.10 - 1.5.13 reveals that, the steady state approached in present case is quite close to that in previous case, which is mainly because of the more quickly developed mass flow rates. Although initial energy stored in the LTDF in present case is higher, heat transfer is also better due to the more quickly developed mass flow rates, which leads to a steady state close to that in previous case. Based on this finding, we may conclude that the deviation in the absolute values of the coolants' temperatures is mainly because of the difference between the purchased heat exchangers and designed ones.

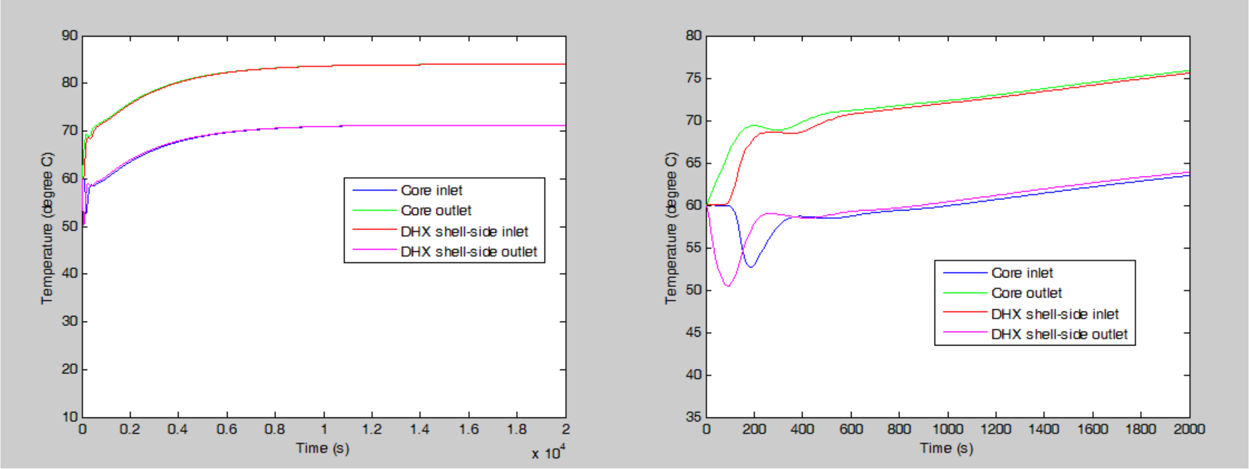

(a) (b)

Fig. 1.5.10. Temperatures in primary loop during the transient with elevated initial temperatures for up to: (a) t = 20,000 s and (b) t = 2,000 s

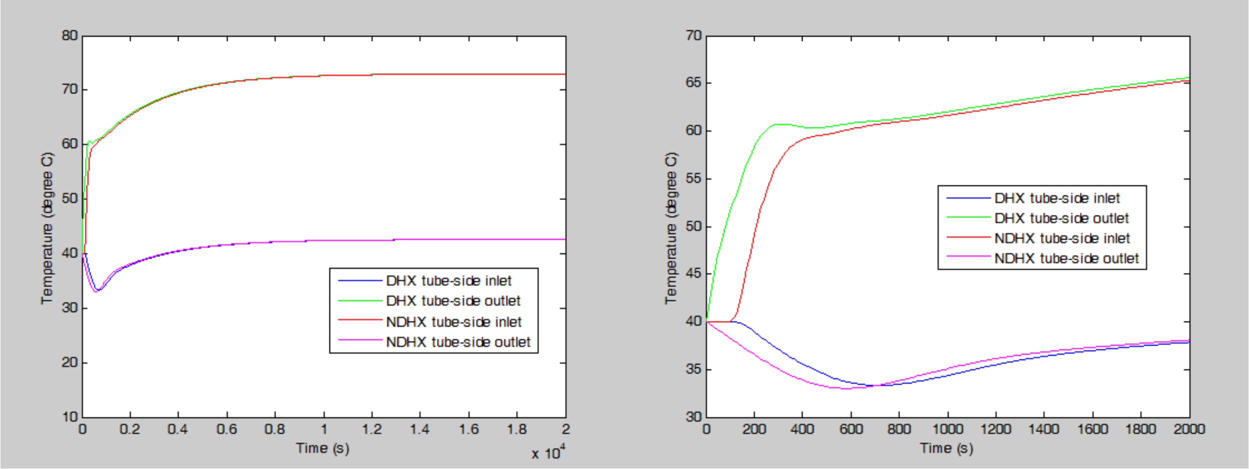

(a) (b)

Fig. 1.5.11. Temperatures in secondary loop during the transient with elevated initial temperatures for up to: (a) t = 20,000 s and (b) t = 2,000 s

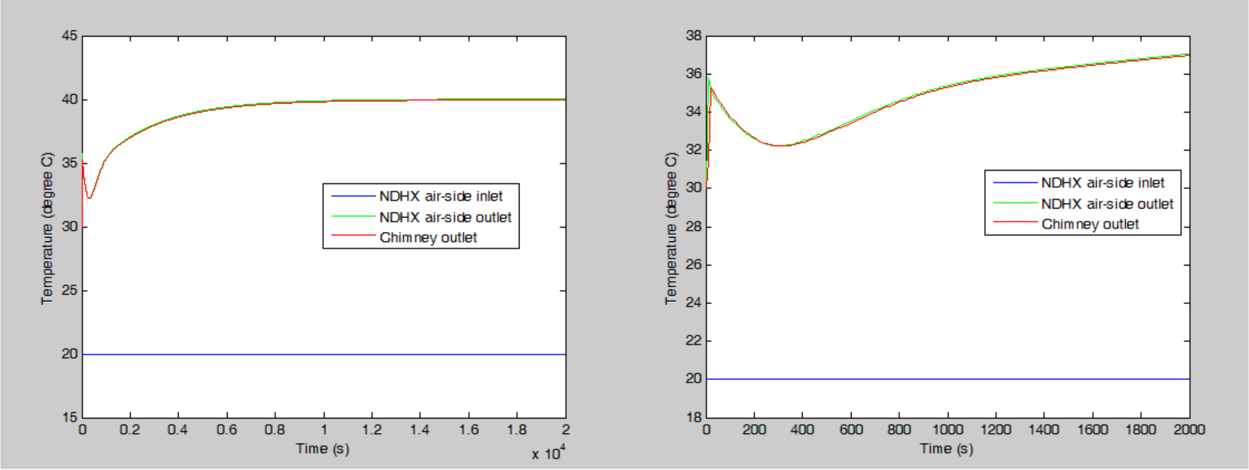

(a) (b)

Fig. 1.5.12. Temperatures in air loop during the transient with elevated initial temperatures for up to: (a) t = 20,000 s and (b) t = 2,000 s

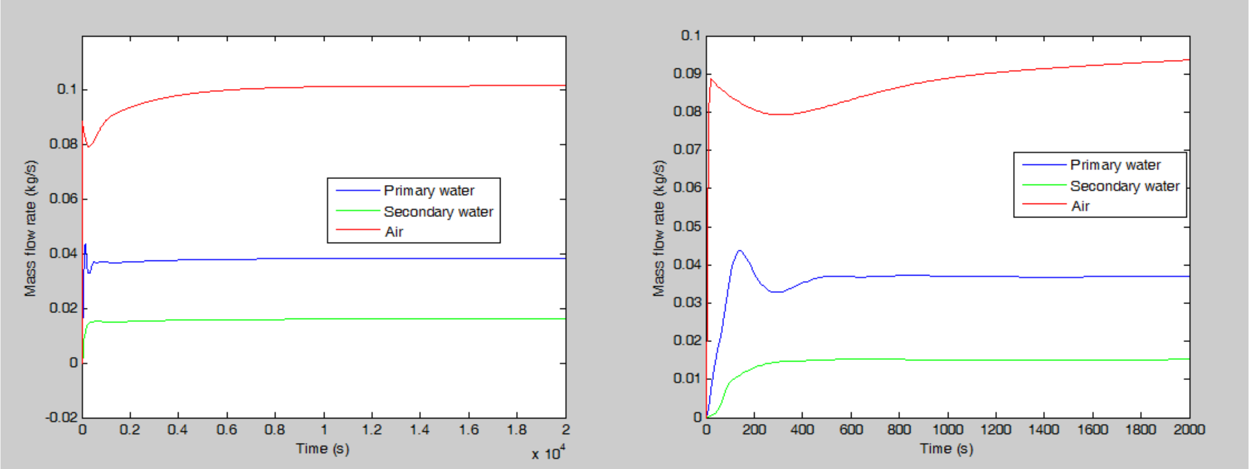

(a) (b)

Fig. 1.5.13. Mass flow rates during the transient with elevated initial temperatures for up to: (a) t = 20,000 s and (b) t = 2,000 s

In our study, the effect of energy storage in the core vessel, DHX shell, and all the piping systems on the LTDF performance has also been examined. In the third run of the code, all the vessels and pipings were neglected, while the initial conditions remained the same as in the first case. The results without considering the vessels and pipings are shown in Figs. 1.5.14 - 1.5.17. The effect of energy storage in the vessels and pipings in suppressing the coolants' temperature increase during the transient is easily seen by comparing Figs. 1.5.14 - 1.5.16 (b) with Figs. 1.5.6 - 1.5.8 (b). In addition, the mass flow rates of the coolants develop slightly faster than the first case, due to the absence of energy absorbing by the vessels and pipings. However, it seems from Figs. 1.5.14 - 1.5.17 (a), that the steady state of the LTDF is almost not influenced by the ignoring the structural materials. This is partly because of the much lower heat capacity of the structural materials compared with the coolants. In addition, as concluded from the second case, the LTDF steady state is more related to the capacity of the heat exchangers, instead of the energy storage in the system.

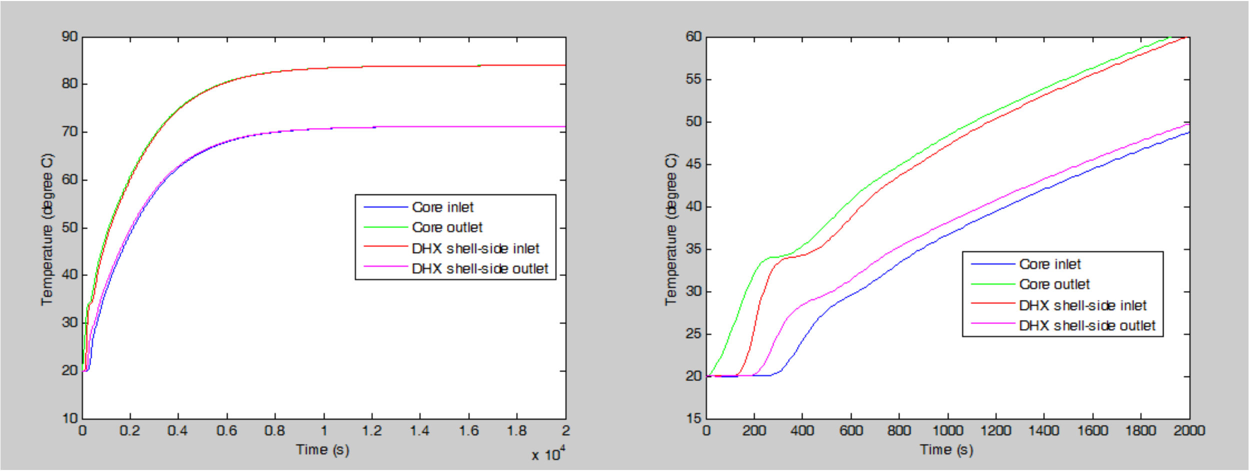

(a) (b)

Fig. 1.5.14. Temperatures in primary loop during the transient without considering the vessels and pipings for up to: (a) t = 20,000 s and (b) t = 2,000 s

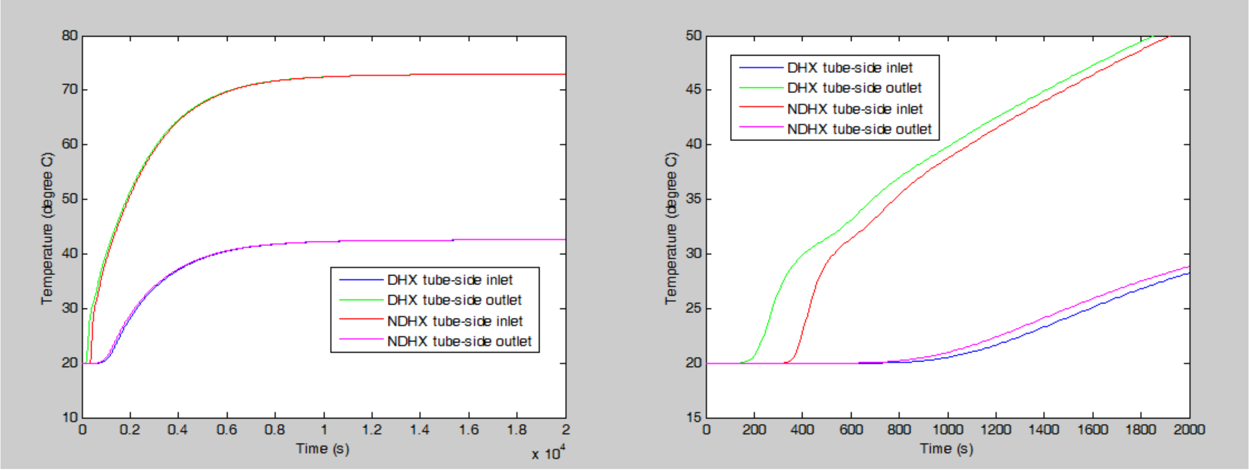

(a) (b)

Fig. 1.5.15. Temperatures in secondary loop during the transient without considering the vessels and pipings for up to: (a) t = 20,000 s and (b) t = 2,000 s

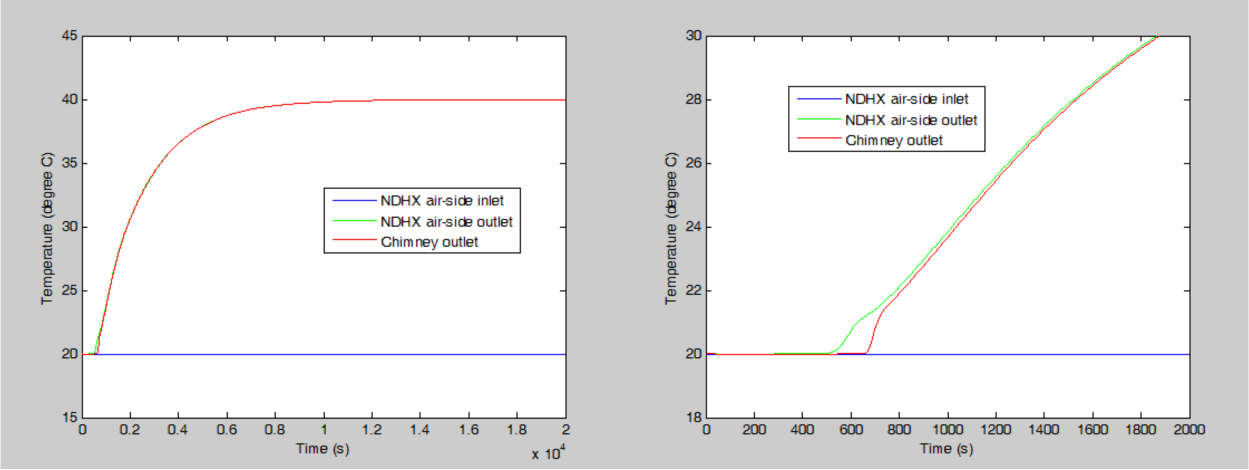

(a) (b)

Fig. 1.5.16. Temperatures in air loop during the transient without considering the vessels and pipings for up to: (a) t = 20,000 s and (b) t = 2,000 s

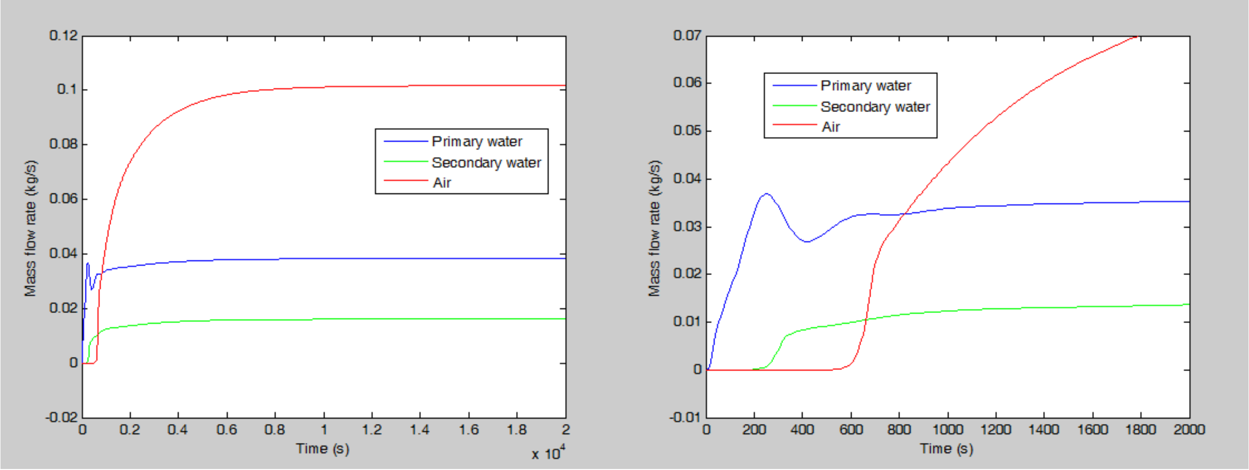

(a) (b)

Fig. 1.5.17. Mass flow rates during the transient without considering the vessels and pipings for up to: (a) t = 20,000 s and (b) t = 2,000 s

Simulation of Pump Trip Process in the LTDF

In the DRACS prototype, after the pump shutdown (accompanied by reactor shutdown), the forced flow through the core, as well as the parasitic bypass flow through the DRACS gradually decreases to zero. Due to the fluid heating in the core, buoyancy starts to build up in the DRACS primary loop. At some point, the flow through the DRACS will be reversed. Eventually a natural circulation will gradually develop and be established in the DRACS primary loop. The LTDF that is being built employs a vertical incline circulation pump, which makes it possible to experimentally investigate the pump trip process (and the flow reversal in the DRACS). In the previous MATLAB code for the LTDF, the pump trip process was not taken into account. In the following discussion, a new version of the MATLAB code that incorporates the pump trip process is presented, along with the simulation results.

In the new code, one additional loop (pump loop) in which the pump is installed is added, as shown schematically in Fig. 1.5.18. As before, this additional loop was divided into subsections, and a bulk temperature was assumed for each subsection. Energy balance equation was applied to each subsection. One complexity that has been caused due to the introduction of the pump loop lies in the flows. In the earlier code, only one closed DRACS primary loop was considered. However, with the pump loop introduced, we have three parallel loops, which are denoted as DRACS loop, core loop, and pump loop in Fig. 1.5.18. At any moment, two closed circulations exist in the three loops. Shown in Fig. 1.5.18 are the two circulations in the pump and core loop, and pump and DRACS loop.

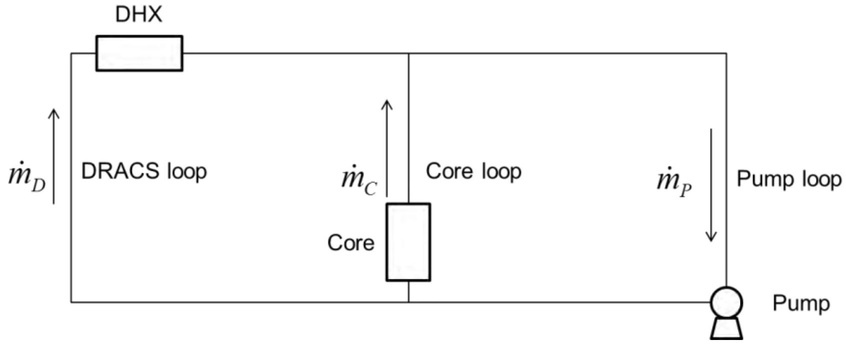

Fig. 1.5.18. The pump loop, core loop, and DRACS loop (flow situation 1)

To solve for the temperatures of the pump loop subsections and the flow rates, the governing equations need to be identified. The energy balance equations for each subsection, the continuity equation, and the integral momentum equations provide these governing equations. The energy balance equations are the same as those used in the previous MATLAB code (Eqs. (1.5.28) and (1.5.29)). The continuity equation dictates that:

$$\dot{m}_P = \dot{m}_C + \dot{m}_D \tag{1.5.37}$$

where $\dot{m}_P$, $\dot{m}_C$, and $\dot{m}_D$ are the flows through the pump loop, core loop, and DRACS loop, respectively. The integral momentum equation is applied to the two closed circulations shown in Fig. 1.5.18. It should be noted that, due to the involvement of the pump which has rotational part, the integral momentum equation will be slightly different from those used in the previous code. The integral momentum equation for the circulation in the pump-core loop is first considered, and the equation for the other circulation loop (pump-DRACS loop) will be similar. The integral momentum equation over the pump-core loop can be written as:

$$\frac{\mathrm{d}\dot{m}_P}{\mathrm{d}t}\left(\sum_i \frac{l_i}{a_i}\right)_P + \frac{\mathrm{d}\dot{m}_C}{\mathrm{d}t}\left(\sum_i \frac{l_i}{a_i}\right)_C = \frac{F}{A} + g\rho_{o,1}\beta_1\sum_i(\pm)H_iT_i - \Delta p_P(\dot{m}_P) - \Delta p_C(\dot{m}_C) \tag{1.5.38}$$

Here, l_i, a_i, H_i, and T_i are the axial length, flow area, height (if horizontal, the height is zero), and temperature of each subsection, respectively. g, $\rho_{o,1}$, and β_1 are the gravitational acceleration, fluid density and fluid thermal expansion coefficient, respectively. Δp_P and Δp_C are the pressure drops (friction and form loss) in the pump loop and core loop, respectively. F is the force exerted by the pump onto the discharged water, and A is the flow area at the discharger of the pump. If we also apply Newton's second law to the pump, we can obtain:

$$FR = -I\frac{\mathrm{d}\omega}{\mathrm{d}t} = -IC\frac{\mathrm{d}\dot{m}_P}{\mathrm{d}t} \tag{1.5.39}$$

where R is the radius of the pump impeller; I is the pump inertia, including the impeller inertia and the motor inertia; and ω is the pump angular speed. In above derivation, it has been assumed the pump discharge is proportional to the angular speed, and C is the proportionality constant. Plugging Eq. (1.5.39) into Eq. (1.5.38) gives:

$$\frac{\mathrm{d}\dot{m}_P}{\mathrm{d}t}\left[\left(\sum_i \frac{l_i}{a_i}\right)_P + \frac{IC}{RA}\right] + \frac{\mathrm{d}\dot{m}_C}{\mathrm{d}t}\left(\sum_i \frac{l_i}{a_i}\right)_C = g\rho_{o,1}\beta_1 \sum_i (\pm) H_i T_i - \Delta p_P(\dot{m}_P) - \Delta p_C(\dot{m}_C) \qquad (1.5.40)$$

As can be seen, the above equation is quite similar to the integral momentum equation previously used (Eq. (1.5.30)). The main difference is the term of $\frac{IC}{RA}$, which accounts for the inertial of the pump. With the pump inertial involved, the flow rates will take more time to vary.

Similarly, for the pump-DRACS loop, the integral momentum equation can be derived as:

$$\frac{\mathrm{d}\dot{m}_P}{\mathrm{d}t}\left[\left(\sum_i \frac{l_i}{a_i}\right)_P + \frac{IC}{RA}\right] + \frac{\mathrm{d}\dot{m}_D}{\mathrm{d}t}\left(\sum_i \frac{l_i}{a_i}\right)_D = g\rho_{o,1}\beta_1 \sum_i (\pm) H_i T_i - \Delta p_P(\dot{m}_P) - \Delta p_D(\dot{m}_D) \qquad (1.5.41)$$

Due to the heating of the fluid in the core, the flow through the core always stays upward, however, flow reversal can happen in both the DRACS loop and pump loop. With flow reversal in the DRACS loop and pump loop, there are two other flow situations, as shown in Figs. 1.5.19 and 1.5.20. Due to the heat sink (DHX) in the DRACS loop, flow reversal will first occur in the DRACS loop. At a later time, flow reversal will also occur in the pump loop, due to the cold fluid entering the core from the DRACS loop. Because there is now heat sink in the pump loop, as can be imagined, there will be no flow in the pump loop at the final steady state.

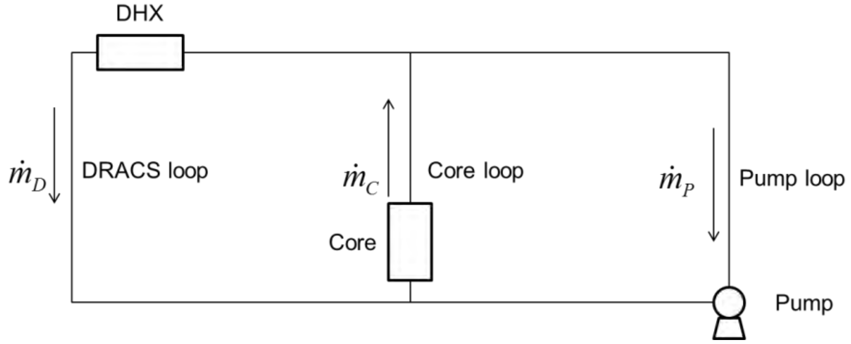

Fig. 1.5.19. Flow situation 2: flow reversal in the DRACS loop

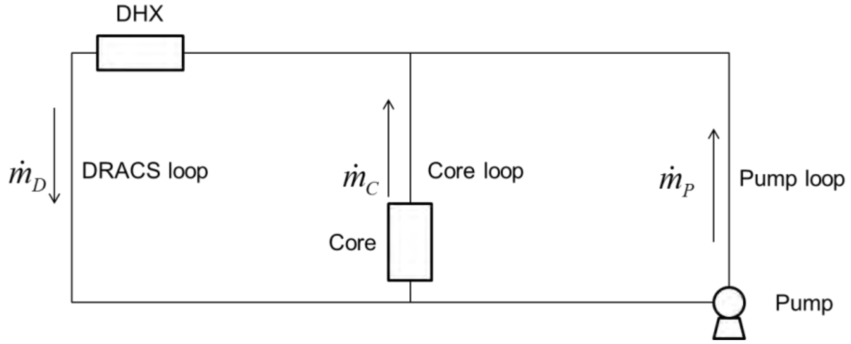

Fig. 1.5.20. Flow situation 3: flow reversal in the pump loop

When flow reversal occurs in the DRACS loop and pump loop, the integral momentum

equations are formulated as:
Flow situation 1:

$$\frac{\mathrm{d}\dot{m}_P}{\mathrm{d}t}\left[\left(\sum_i \frac{l_i}{a_i}\right)_P + \frac{IC}{RA}\right] + \frac{\mathrm{d}\dot{m}_C}{\mathrm{d}t}\left(\sum_i \frac{l_i}{a_i}\right)_C = g\rho_{o,1}\beta_1 \sum_i (\pm) H_i T_i - \Delta p_P(\dot{m}_P) - \Delta p_C(\dot{m}_C) \tag{1.5.42}$$

$$\frac{\mathrm{d}\dot{m}_C}{\mathrm{d}t}\left(\sum_i \frac{l_i}{a_i}\right)_C - \frac{\mathrm{d}\dot{m}_D}{\mathrm{d}t}\left(\sum_i \frac{l_i}{a_i}\right)_D = g\rho_{o,1}\beta_1 \sum_i (\pm) H_i T_i - \Delta p_C(\dot{m}_C) - \Delta p_D(\dot{m}_D) \tag{1.5.43}$$

Flow situation 2:

$$\frac{\mathrm{d}\dot{m}_C}{\mathrm{d}t}\left(\sum_i \frac{l_i}{a_i}\right)_C - \frac{\mathrm{d}\dot{m}_D}{\mathrm{d}t}\left(\sum_i \frac{l_i}{a_i}\right)_D = g\rho_{o,1}\beta_1 \sum_i (\pm) H_i T_i - \Delta p_C(\dot{m}_C) - \Delta p_D(\dot{m}_D) \tag{1.5.44}$$

$$-\frac{\mathrm{d}\dot{m}_P}{\mathrm{d}t}\left[\left(\sum_i \frac{l_i}{a_i}\right)_P + \frac{IC}{RA}\right] - \frac{\mathrm{d}\dot{m}_D}{\mathrm{d}t}\left(\sum_i \frac{l_i}{a_i}\right)_D = g\rho_{o,1}\beta_1 \sum_i (\pm) H_i T_i - \Delta p_P(\dot{m}_P) - \Delta p_D(\dot{m}_D) \tag{1.5.45}$$

It should be noted that, Eq. (1.5.37) always holds if we assign negative values to the flow rates when flow reversal occurs.

In the new code, the heat transfer models for the DHX and NDHX are the same as those used in previous code. However, for the core, the flow through it will be turbulent following the pump shutdown. For turbulent flow through rod bundles, Sahoo and Mohanty (1991) found that the Dittus-Boelter correlation could predict the heat transfer coefficient well, which is written as (Todreas, 1990):

$$\mathrm{Nu} = 0.023\,\mathrm{Re}^{0.8}\,\mathrm{Pr}^{0.4} \tag{1.5.46}$$

where Nu, Re, and Pr are the Nusselt number, Reynolds number, and Prandtl number, respectively. When the flow through the core is laminar, the same correlation as in the previous code is used.

Taking the pump loop into account will not affect the secondary and air loops, and therefore, the loop pressure drop models (Eqs. (1.5.35) and (1.5.36)) adopted in the previous code are still applicable. For the DRACS loop, the previously developed model (Eq. (1.5.34)) still applies after the flow reversal. Before the flow reversal when the flow is still upward, the flow through the DRACS loop (parasitic flow) will be quite restricted. In addition, the main pressure drop in the DRACS loop will still be that in the valve. Therefore Eq. (1.5.34) is also applicable for the upward DRACS flow.

For the core loop, the pressure drop is due to the friction in the pipe, friction in the core and the form loss. For the pipe, correlations of Darcy friction factor for different flow regimes are used (Todreas, 1990):

For Re < 2300,

$$f = \frac{64}{\mathrm{Re}} \tag{1.5.47}$$

For 30,000 < Re < 1,000,000

$$f = 0.184\,\mathrm{Re}^{-0.2} \tag{1.5.48}$$

For Re < 30,000

$$f = 0.316\,\mathrm{Re}^{-0.25} \tag{1.5.49}$$

When the flow is in the laminar-to-turbulent transition regime, a linear interpolation is taken between Eqs. (1.5.47) and (1.5.49). For the core, the friction factor correlation developed by Sahoo and Mohanty (1991) for rod bundles is used, which is:

$$f = 0.332\,\mathrm{Re}^{-0.25} \tag{1.5.50}$$

For the pump loop, the main pressure drop is the friction in the pipe and the form loss. Eqs. (1.5.47) – (1.5.49) can be used to calculate the friction pressure drop in the pump loop. For all the form losses, form loss coefficients tabulated in (Todreas, 1990) can be used to estimate the values.

To demonstrate the flow reversal phenomenon in the fluidic diode associated with the pump coast down, a case similar to one of the previously investigated cases was examined, in which a uniform initial temperature of 20°C throughout the system was assumed. For the initial bypass flow through the fluidic diode in the reverse flow direction, it was selected to be the same as that in the forward flow direction of the fluidic diode during DRACS normal operation, i.e., 0.0376 kg/s. For the initial major flow through the core, it was determined by looking at the ratio of the flow through the core during core normal operation to that during DRACS normal operation in the prototype. This ratio can be determined from the core inlet and outlet temperatures and the operating powers for the two different operation situations, which are summarized in Table 1.5.6. The flow ratio was thus determined as:

$$\frac{\dot{m}_{normal}}{\dot{m}_{accident}} = \left(\frac{P}{c_p \Delta T}\right)_{normal} \Bigg/ \left(\frac{P}{c_p \Delta T}\right)_{accident} = 43.27 \tag{1.5.51}$$

The core flow ratio between the core normal operation and the DRACS normal operation in the LTDF experiment was assumed to the same as that in the prototype, i.e., 43.27, resulting in an initial major core flow of 1.627 kg/s. For the secondary and air loops, the initial flow rates were assumed to be zero.

Table 1.5.6 Operating temperatures and powers during core normal operation and DRACS normal operation (accidents) in the prototype

	Normal Operation	Accident
Core inlet temperature (°C)	600	705
Core outlet temperature (°C)	704	750
Power	20 MW	200 kW

The improved code was run with above mentioned initial conditions for up to 20,000 seconds, with the results shown in Figs. 1.5.21 – 1.5.24. From Fig. 1.5.21, it can be clearly seen that flow reversal occurs in the fluidic diode at around 640 seconds. In addition, the overall trends of the three flow rates after the flow reversal are kind of similar to those shown in Fig. 1.5.17. With pump costdown, the secondary flow starts to develop before the flow reversal happens, which is because secondary water is already heated up when the flow through the fluidic diode is still upward (reverse flow direction). Comparing Figs 1.5.22 – 1.5.24 with Figs. 1.5.14- 1.5.16, it is seen that, the temperatures during transient with pump coastdown are quite different from those without considering pump coastdown, However, the long-term temperatures at the steady state for the two cases are the same. This is because there is no heat sink in the pump loop, and there will be eventually no flow through the pump. It behaves like there is no such pump loop, making the long-temperatures unchanged.

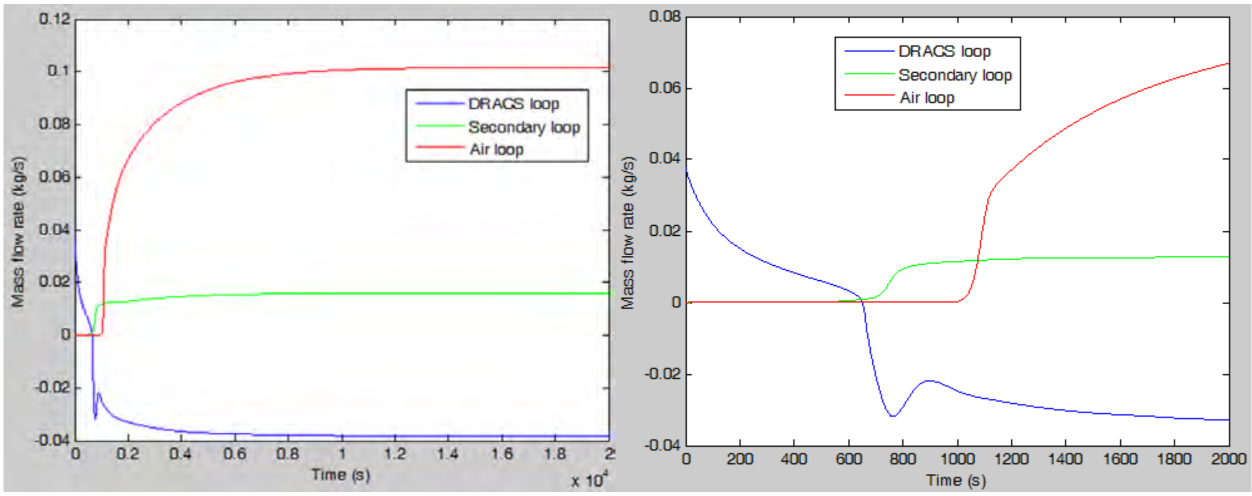

(a) (b)

Fig. 1.5.21. Mass flow rates during the transient with pump coastdown for up to: (a) t = 20,000 s and (b) t = 2,000 s

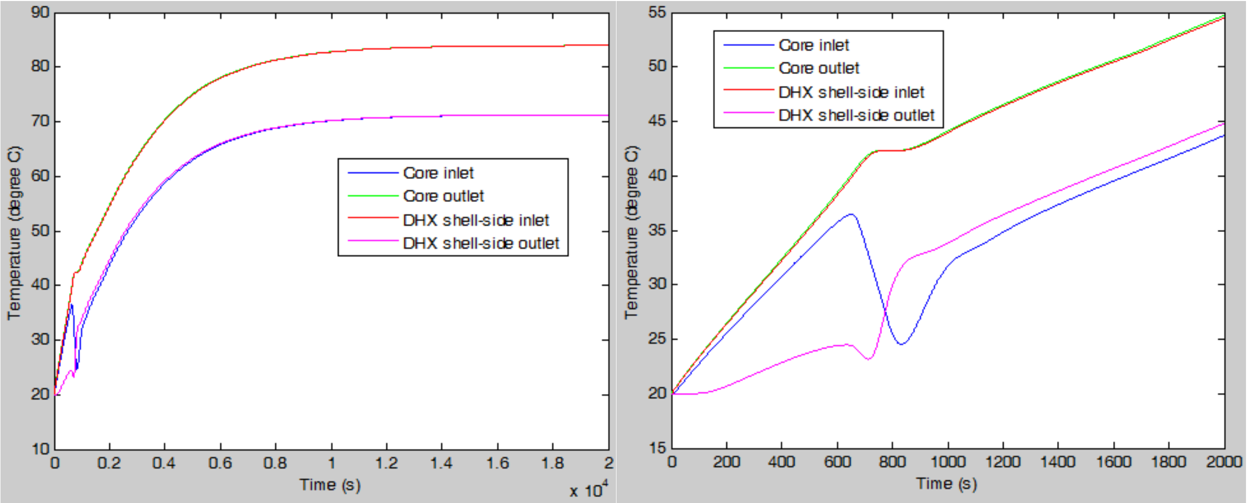

(a) (b)

Fig. 1.5.22. Temperatures in primary loop during the transient with pump coastdown for up to: (a) t = 20,000 s and (b) t = 2,000 s

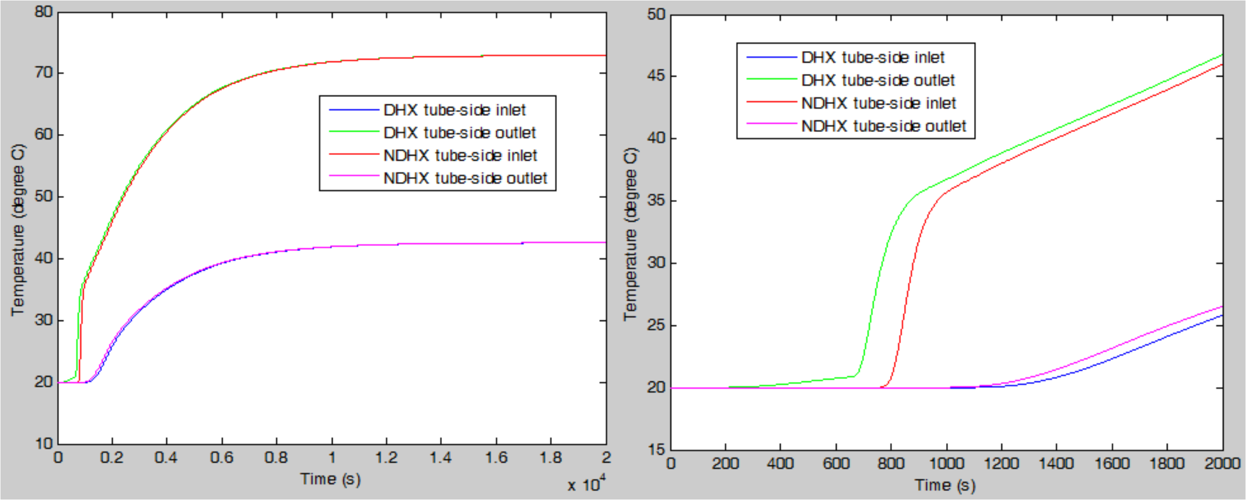

(a) (b)

Fig. 1.5.23. Temperatures in secondary loop during the transient with pump coastdown for up to: (a) t = 20,000 s and (b) t = 2,000 s

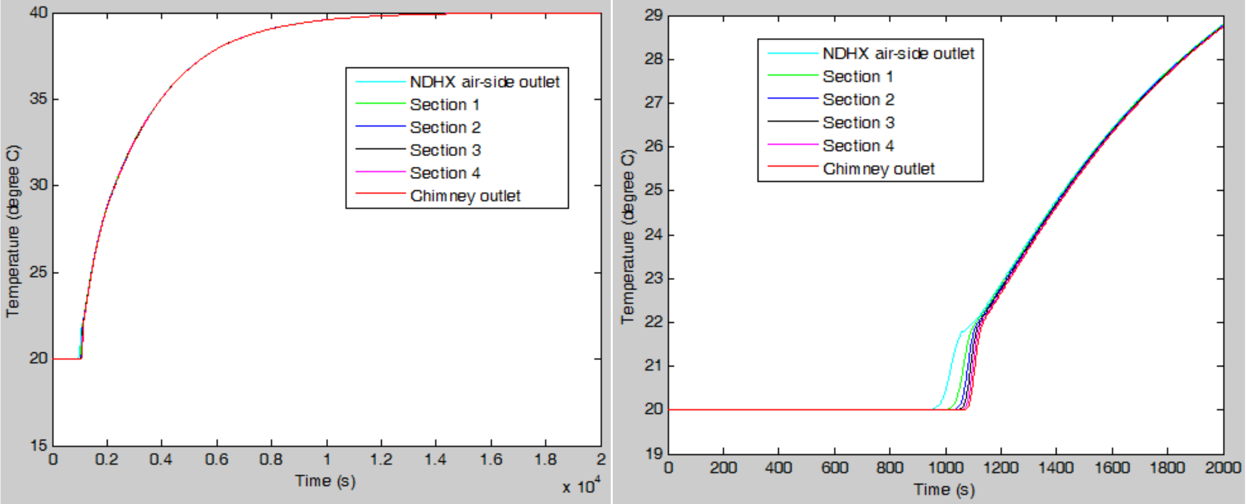

(a) (b)

Fig. 1.5.24. Temperatures in air loop during the transient with pump coastdown for up to: (a) t = 20,000 s and (b) t = 2,000 s

The above results have been based on an estimated value of 9E5 m^{-1} for the pump inertia term (*IC/RA*), mainly because we could not obtain the detailed dimensions of the pump, as well as the pump inertia. The pump inertia was estimated as:

$$I = \frac{1}{2} m R^2 \tag{1.5.52}$$

where the total mass of the pump of around 80 lbs was used for *m*, and the impeller chamber radius of 5.6 inch was used for *R*. The pump discharge proportionality constant, *C*, was estimated using the nominal pump speed of 3500 rpm and discharge rate of 1.627 kg/s. *A* was based on the pipe inner diameter of 4.09 cm. It should be noted that, the above approximation overestimated the pump inertia term (*IC/RA*), because the rotatory part has mass less than 80 lbs, and the motor has radius less than the chamber radius. Due to the uncertainty in the pump inertia term, we have also examined the effect this term on the flow reversal process. Five different values for the pump inertia term were examined, with the previously estimated value the highest and the lowest value of 5,000 m^{-1}. The results are shown in Fig. 1.5.25. As can be see, with less pump inertia, the flow reversal tends to occur earlier, which is quite understandable. In addition, when the pump inertia decreases to 5,000 m^{-1}, its effect on the flow reversal becomes insignificant, which because the inertia of the water in the pump loop starts to dominate.

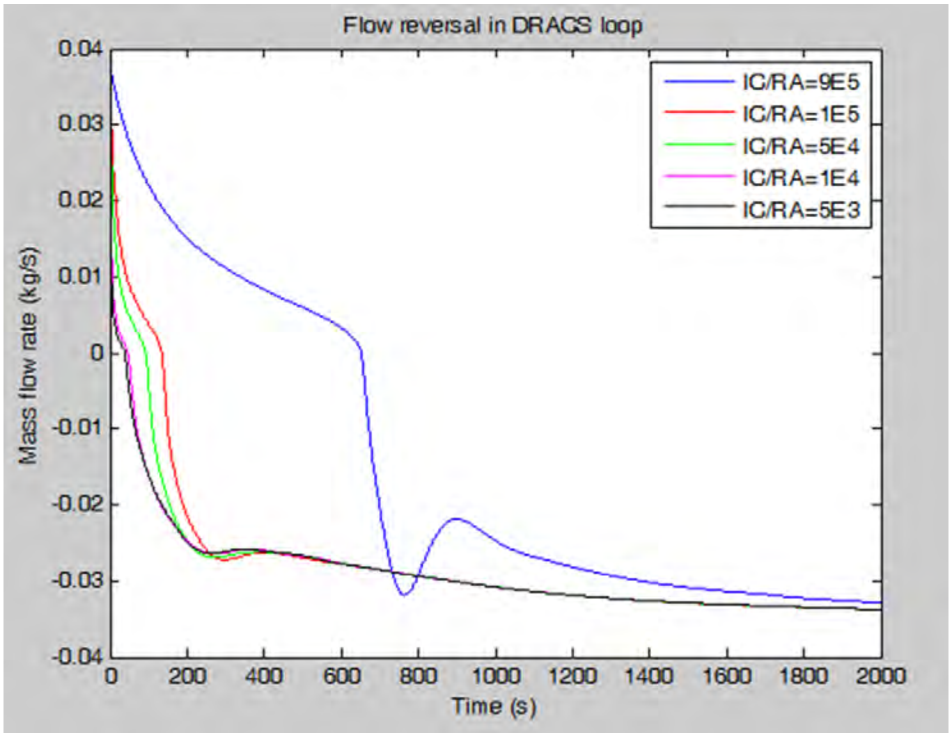

Fig. 1.5.25. Effect of the pump inertia term on the flow reversal

Preliminary Validation of the MATLAB Code

A preliminary validation of the developed MATLAB code by using available experimental data that are as closely relevant as possible has been performed before the experimental data from the DRACS test facilities are available. In the following discussion, a preliminary code benchmark is performed by applying the code to a natural circulation loop from the literature (Hallinan et al., 1986; Hallinan et al., 1985) and comparing the code predictions with the corresponding experimental data. The code predictions show good agreement with the experimental data, which demonstrates promise in the code's capability in predicting the thermal performance of the DRACS system.

The single-phase natural circulation loop modeled in the present work is shown schematically in Fig. 1.5.26 (Hallinan et al., 1986; Hallinan et al., 1985). The rectangular loop is constructed from Kimax tubes with an inner diameter of 76.2 mm and a wall thickness of 4.8 mm. The loop features a height of 1.5 m and a width of 1.49 m. In addition, the loop is insulated with three layers of 25.4-mm thick Johns-Manville insulation pipes.

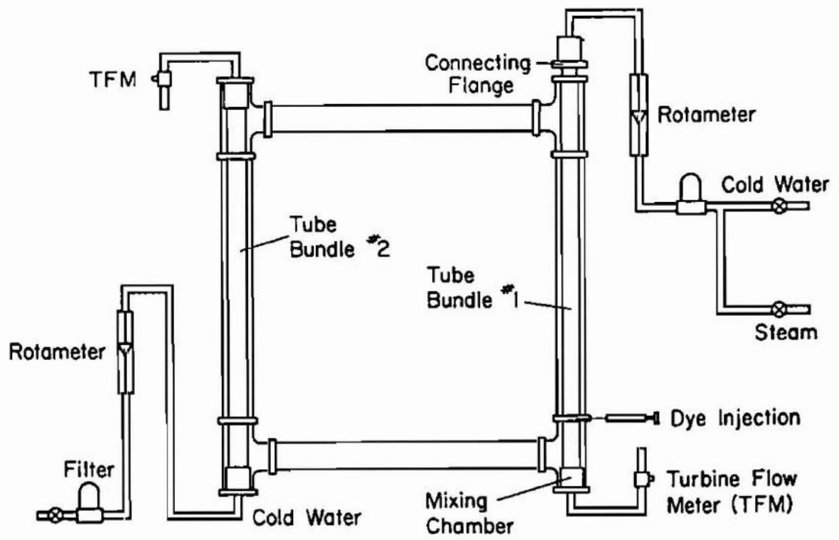

Fig. 1.5.26. Schematic of the modeled natural circulation loop (Hallinan et al., 1986)

Two tube bundles are located in the vertical legs, providing a means of heat addition to and removal from the loop. Tube Bundle # 1 in the source leg, shown in Fig. 1. 5.26, provides heat to the loop water through circulating hot water inside the tubes. The hot water is supplied by mixing steam with cold water from chillers. Heat is removed from the loop by the chilled water flowing inside Tube Bundle # 2. The cooling water is supplied at a temperature of 14 ± 1°C. The inlets and outlets to each of the tube bundles can be interchanged to allow both co-current and countercurrent flow arrangements in the tube bundles. Copper tubes are used for the two bundles to improve heat transfer. The geometrical information of the two tube bundles can be found in Table 1.5.7.

Table 1.5.7 Dimensions of the tube bundles (Hallinan et al., 1986)

	Bundle # 1	Bundle # 2
Number of tubes	21	7
OD of tubes (mm)	9.55	19.05
Tube thickness (mm)	1.59	1.02
Length of bundle (m)	1.65	1.58
Type of array	Rectangular	Triangular
Pitch-to-diameter ratio	1.33	1.25

The principle of the code is the same as before, i.e., to solve the energy balance equations for the four loop legs and the integral momentum equation for the entire loop. The Boussinesq approximation has been adopted, which states that the density of the fluid is assumed as a constant except for the buoyancy term in the momentum equation. In addition, other physical properties of the fluid are assumed to be constant, which is justified by the small temperature variations observed from the experimental data in the literature, ranging from 20 to 45°C (Hallinan et al., 1986). The values of these physical properties are evaluated based on the average of the high and lower temperatures of the circulating fluid at the quasi-steady state.

Finite volume method is applied by axially dividing the loop into a total of 252 cells, including the heating (hot) and cooling water, circulating water, bundle tubes, and loop pipes. The mesh size is determined based on the finding by Hallinan and Viskanta (1986) in their numerical study that a mesh size of 0.08 m (21 cells per leg) for the modeled loop will lead to grid-independent solutions. Energy balance equation is integrated over each of the cells. For each cell, a bulk mean temperature is assumed and will be solved for. Based on the aforementioned assumptions, these integrated energy balance equations are formulated as:

The tube bundles:

$$c_{pi} m_i \frac{\mathrm{d}T_i}{\mathrm{d}t} + c_{pi} \dot{m}_i \left(T_i^{out} - T_i^{in} \right) = h_i A_i \left(T_b - T_i \right) \tag{1.5.53}$$

$$c_{pb} m_b \frac{\mathrm{d}T_b}{\mathrm{d}t} = h_i A_i \left(T_i - T_b \right) - h_f A_f \left(T_b - T_f \right) \tag{1.5.54}$$

$$c_{pf} m_f \frac{\mathrm{d}T_f}{\mathrm{d}t} + c_{pf} \dot{m}_f \left(T_f^{out} - T_f^{in} \right) = h_f A_f \left(T_b - T_f \right) - h_p A_p \left(T_f - T_p \right) \tag{1.5.55}$$

$$c_{pp} m_p \frac{\mathrm{d}T_p}{\mathrm{d}t} = h_p A_p \left(T_f - T_p \right) - \frac{L_p}{THR} \left(T_p - T_a \right) \tag{1.5.56}$$

The horizontal legs:

$$c_{pf} m_f \frac{\mathrm{d}T_f}{\mathrm{d}t} + c_{pf} \dot{m}_f \left(T_f^{out} - T_f^{in} \right) = -h_p A_p \left(T_f - T_p \right) \tag{1.5.57}$$

$$c_{pp} m_p \frac{\mathrm{d}T_p}{\mathrm{d}t} = h_p A_p \left(T_f - T_p \right) - \frac{L_p}{THR} \left(T_p - T_a \right) \tag{1.5.58}$$

Here, subscripts *i*, *f*, *b*, *p,* and *a* denote the heating/cooling water, circulating water, bundle wall, loop pipe wall, and ambient air, respectively; superscripts *out* and *in* denote the fluid outlet and inlet temperatures for a specific cell. In addition, *h, A, L, T,* c_p*, m*, and $\dot{m}$ stand for the heat transfer coefficient, heat transfer area, cell length, temperature, specific heat, total mass, and mass flow rate, respectively. It should be noted that the heat loss from the loop to the ambient air is accounted for by the last term in Eqs. (1.5.56) and (1.5.58), where *THR* is the total thermal resistance for heat transfer from the loop pipe wall to the ambient air and can be calculated as:

$$THR = \frac{1}{2\pi k_{ins}} \ln\left(\frac{R_{inso}}{R_{insi}} \right) + \frac{1}{2\pi R_{inso} h_{natural}} \tag{1.5.59}$$

where k_{ins}, R_{inso}, R_{insi}, and $h_{natural}$ denote the insulation thermal conductivity, insulation outer diameter, insulation inner diameter, and heat transfer coefficient for natural convection on the surface of the insulation. It is found that the thermal conductivity of the used insulation material is as low as 0.035 W/m-K (Johns-Manville) and that the natural convection heat transfer coefficient estimated based on Morgan correlations (Morgan, 1975) is typically larger than unity even for a temperature difference of 1°C. Therefore, the second term on the right hand side of Eq. (1.5.59) is much smaller than the first term, and is neglected in the present analysis.

The number of equations obtained from the energy balance is the same as that of the temperature unknowns that need to be solved for. However, there is more unknown showing in the energy balance equations, i.e., the mass flow rate of the circulating water due to N.C. The integral momentum equation over the loop provides the closure:

$$\frac{\mathrm{d}\dot{m}_f}{\mathrm{d}t} \sum_i \frac{l_i}{a_i} = g\rho\beta \sum_i \left(\pm \right) H_i T_i - \frac{\dot{m}_f^2}{2\rho} \sum_i \frac{1}{a_i^2} \left(f \frac{l}{D_h} + K \right) \tag{1.5.60}$$

where ρ, β and g are the density and thermal expansion coefficient of the circulating water, and the gravitational acceleration, respectively. *l, a, H* and D_h denote the length, flow area, height, and hydraulic diameter of the *i*th cell in the loop. Any horizontal cell will not contribute to the buoyancy, the height of which is taken as zero. For any cell located in the source leg, the sign in the buoyancy term is positive, otherwise negative. In addition, *f* and *K* stands for the friction pressure drop and form loss, respectively.

Correlations for the heat transfer and pressure drop are required for the solution of aforementioned equation systems. Steady-state correlations for heat transfer and pressure drop have been identified from the literature and adopted in the present work. For heat transfer from the tube bundles to the circulating water, correlations exactly for the two tube bundles in question have been developed by Gruszczynski and Viskanta (1983) and Hallinan and Viskanta (1985). For the 7-tube bundle shown in Table 1.5.7, the Nusselt number can be calculated from:

$$\mathrm{Nu} = 0.081\,\mathrm{Re}^{0.8}\mathrm{Pr}^{0.43} \text{ (parallel-flow)} \tag{1.5.61}$$

$$\mathrm{Nu} = 0.067\,\mathrm{Re}^{0.8}\mathrm{Pr}^{0.43} \text{ (counter-flow)} \tag{1.5.62}$$

For the 21-tube bundle, the Nusselt number can be estimated by:

$$\mathrm{Nu} = 0.051\,\mathrm{Re}^{0.8}\mathrm{Pr}^{0.43} \text{ (parallel-flow)} \tag{1.5.63}$$

$$\mathrm{Nu} = 0.026\,\mathrm{Re}^{0.93}\mathrm{Pr}^{0.43} \text{ (counter-flow)} \tag{1.5.64}$$

where Pr and Re are the Prandtl number and Reynolds number, respectively.

It should be noted that the above correlations are applicable for 80 < Re < 500. For Re > 500, no correlations are available for the Nusselt number. However, for the cases simulated in the present work, the quasi-steady-state Re of the circulating water will not considerably exceed 500. Therefore, the above correlations have been adopted for Re > 80 in the current work. When the circulating water is stagnant, to account for the heat transfer through conduction, a Nusselt number of value 2 has been selected, analogous to the heat conduction from a sphere to a stagnant fluid. For Re < 80, a linear interpolation is made between 2 and the Nusselt number predicted by Eqs. (1.5.61) – (1.5.64).

For heat transfer inside the bundle tubes and that between the circulating water and the loop pipe, Hausen correlation (Wolverine) and Sieder-Tate correlation (Todreas, 1989) are utilized for the laminar (Re < 2,000) and turbulent (Re > 10,000) flow, respectively:

$$\mathrm{Nu} = 3.66 + \frac{0.0668\,\mathrm{Re}\,\mathrm{Pr}(D_h / L)}{1 + 0.04\left[\mathrm{Re}\,\mathrm{Pr}(D_h / L)\right]^{2/3}} \tag{1.5.65}$$

$$\mathrm{Nu} = 0.023\,\mathrm{Re}^{0.8}\,\mathrm{Pr}^{1/3}\left[1 + \left(D_h / L\right)^{0.7}\right] \tag{1.5.66}$$

where D_h, and L are the thermal hydraulic diameter and length of the tube/pipe, respectively. It should be noted that the entrance effect on heat transfer has been considered.

For the total pressure drop in the loop, instead of accounting for the friction and form losses in each leg, an effective total flow resistance has been employed, which is defined as:

$$R = \sum_i \frac{1}{a_i^2}\left(f\frac{l}{D_h} + K\right) \tag{1.5.67}$$

A correlation for the effective flow resistance specifically for the modeled loop has been developed by Hallinan and Viskanta (1985), which is written as:

$$RA^2 = 8050/\mathrm{Re} + 1.467 \tag{1.5.68}$$

where A and Re are the flow area and Reynolds number in the source leg, respectively. It is apparent that the first term on the right hand side of Eq. (1.5.68) accounts for the friction loss while the second term accounts for the form loss. In addition, based on the format of the dependence of the resistance on the Re, this correlation should be only applied to laminar flow. Because the quasi-steady-state flows for the simulated cases in the present paper remain in laminar region, it is assumed that Eq. (1.5.68) is applicable.

Two start-up cases that were experimentally studied by Hallinan and Viskanta (1986) are simulated, in which the loop water is initially stagnant and at the room temperature. In both cases, the sink bundle (# 2) has a counter-flow arrangement, while the source bundle (# 1) has a parallel-flow arrangement in one case and a counter-flow arrangement in the other. The heating and cooling water is provided at constant flow rates and inlet temperatures, which are summarized in Table 1.5.8.

Table 1.5.8 Test conditions for the simulated cases

Case	Parallel	Counter
Heating water flow rate (kg/s)	0.168	0.070
Inlet temperature (°C)	49.12	49.07
Cooling water flow rate (kg/s)	0.055	0.054
Inlet temperature (°C)	14	14

The simulated results for the circulating water temperature at the source leg inlet and outlet are shown in Figs. 1.5.27 and 1.5.28 for the parallel- and counter-flow arrangements in the source leg, respectively, along with the experimental results obtained from the literature (Hallinan et al., 1986). As can be seen from the comparisons, the predicted source leg inlet and outlet temperatures agree well with the experimental data for both the transient and the quasi-steady state. The differences are within 7% for quasi-steady state and 15% for transient. The good agreement between the code results and the experimental data implies that the steady-state heat transfer and pressure drop correlations can be used to predict the transient behaviours of a natural circulation system. The main reason for this is that natural circulation is a slow process, and each moment during the transient can be treated as a quasi-steady state.

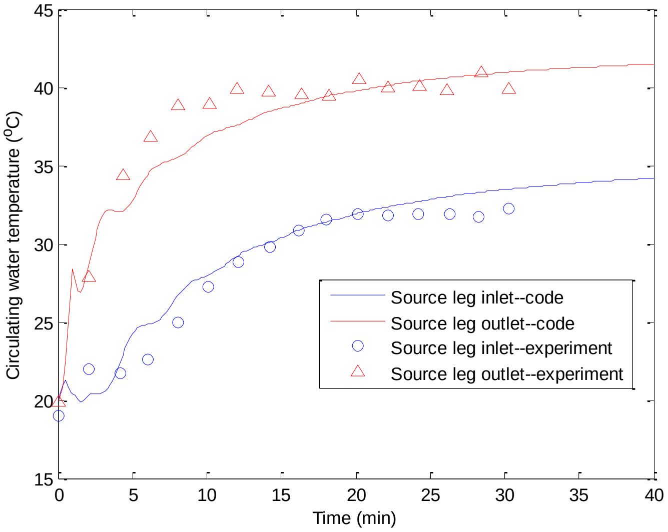

Fig. 1.5.27. Comparison of the code results with experimental data for parallel-flow arrangement in the source leg

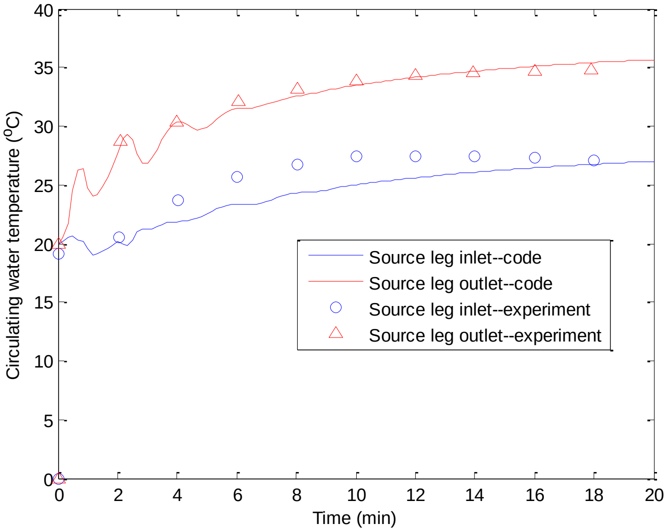

Fig. 1.5.28. Comparison of the code results with experimental data for counter-flow arrangement in the source leg

The flow rate of the circulating water has also been predicted. However, in the literature, the circulating water flow rate is not measured mainly because of the difficulty in finding a non-invasive way to measure the flow rate without disturbing the flow field. Therefore, a direct comparison in the flow rate of the circulation water is not available. However, we can still make an approximate comparison for the quasi-steady-state flow rate based on an energy balance. Based on the temperature and flow rate information for the heating water, and the temperate information for the circulating water from the literature, the circulating water flow rates at quasi-steady state are found to be approximately 0.092 and 0.106 kg/s for the parallel- and counter-flow arrangements, respectively. The predicted flow rates are 0.053 and 0.066 kg/s for the two cases, lower than the experimental results by 42% and 38%, respectively. There are a few reasons for the large discrepancies. First, the experimental flow rates are evaluated indirectly, and measurement errors in the heating water flow rate and the temperatures can be accumulated to cause larger error in the calculated circulating water flow rates. Second, at the quasi-steady state, the circulating water is still slightly absorbing energy, which can be seen from the increasing temperatures. Therefore, its flow rate should be smaller than estimated by applying the energy balance. Lastly, the heat transfer correlations for the tube side of the tube bundles could have relatively large errors. Based on the simulation results, it is found that heat transfer is more limited by the tube side in the two bundles. The adopted correlations have probably under-predicted the heat transfer coefficients for the tube side, leading to smaller heat addition rate to and removal rate from the loop, and correspondingly lower flow rate for the circulating water. Moreover, although the source bundle inlet (sink bundle outlet) and outlet (sink bundle inlet) temperatures have been predicted well by the code, the possible improper selection of the bundle tube-side heat transfer correlations has led to poor predictions of the local circulating water temperatures in the two tube bundles. Therefore, the buoyancy is not predicted correctly, leading to the discrepancies in the circulating water flow rates. As can be imagined, if the heat transfer correlations are properly benchmarked, the code should be able to reproduce the experimental results.

Thermal Performance Evaluation of the HTDF by the MATLAB Code

A high-temperature DRACS test facility (HTDF) is currently under construction at OSU, along with the LTDF. The HTDF employs FLiNaK and KF-ZrF_4 as the primary and secondary coolants, respectively. With the HTDF, the DRACS performance in terms of its capability of removing the decay heat under a similar condition to the prototypic can be evaluated. 1-1/2" and 1-1/4" Sch 40 pipes are used for the primary and secondary loops, respectively. The HTDF core is simulated with 7 cartridge heaters with a total nominal power of 10 kW. The DHX employs a shell-and-tube design containing 80 5/8" BWG 18 tubes at a length of 0.325 m. Due to the high temperature gradient from the secondary salt to the ambient air, plain tubes are used. A total of 36 1/2" BWG 16 tubes are adopted in a staggered array in two layers. A vortex diode design that would exhibit desired pressure drops for both the forward and reverse flow directions has been obtained via a parametric CFD study (Lv et al., 2013). The diode design employs converging/diverging nozzles and a disk-shape chamber with a diameter of 6.6 cm and thickness of 1.56 cm. A cantilever sump pump for high-temperature application has also been employed in the HTDF.

To evaluate the thermal performance of the HTDF, a MATLAB code is developed based on the code previously developed for the LTDF. The code principle is the same as before, i.e., to solve the energy balance equations and integral momentum equations. In addition to the changes in the geometric setup, the other main changes include coolant properties, and heat transfer and pressure drop models/correlations. Temperature-dependent coolant properties have been employed in the code. For the primary (FLiNaK) and secondary (KF-ZrF_4) salts, correlations to predict the properties are obtained from the reports by Williams et al. (2006), as summarized in Table 1.5.9. For the air, the idea gas law is used to predict the density. For the other properties, tabulated values (Engineering ToolBox) are utilized to obtain the best-fit correlations, as summarized in Table 1.5.9.

Table 1.5.9 Temperature-dependent properties of the coolants (T in Kelvin)

	Density (kg/m^3)	Specific heat (J/Kg-K)	Viscosity (cP)	Thermal conductivity (W/m-K)
FLiNaK	2530-0.73(T-273)	1883	0.04exp(4170/T)	0.0005T+32/41.3-0.34
KF-ZrF_4	3416-0.887(T-273)	1046	0.159exp(3179/T)	0.0005T+32/103.9-0.34
Air	353.186/T	1007	(0.343T+92.153)E-4	7E-5T+0.0242

For the three main heat-exchanging components, i.e., the core, DHX and NDHX, heat transfer models/correlations that have been selected in designing these components are used in the code. For the core in the HTDF, a bundle of 7 cartridge heaters are used. Sahoo and Mohanty (1987) have investigated the heat transfer for flows in a similar geometry. Their research shows that for laminar flow (Re < 2,300), the Nusselt numbers for the wall and interior sub-channels are constants of 6.704 and 13.95, respectively. An area-weighted average of the corresponding heat transfer coefficients of the two sub-channels is taken for the entire bundle for laminar flow. For turbulent flow (Re > 10,000), it is found by Sahoo and Mohanty (1991) that the Dittus-Boelter correlation should predict the heat transfer coefficient well, which is shown in Eq. (1.5.46). For transition flow, linear interpolation is made between the heat transfer coefficients predicted by the laminar and turbulent flow models.

The DHX and NDHX in the HTDF are designed by the same method as that for the LTDF, namely, the Delaware Method (Hewitt, 1992). Therefore, some of the heat transfer correlations previously used for the LTDF are still applicable. For the DHX shell side, the heat transfer coefficient is based on that for ideal cross flow over tube banks and then corrected by a series of correction factors. Eqs. (1.5.12) – (1.5.15), along with Table 1.5.1, are used to compute the DHX shell-side heat transfer coefficient. For the NDHX air side, since the flow is completely cross flow, Eqs. (1.5.13) – (1.5.15) and Table 1.5.1 are used without any correction factors. For the DHX and NDHX tube side, the Hausen correlation and Sieder-Tate correlation have been used for the laminar flow (Re < 2,300) and turbulent flow (Re > 10,000), respectively, as shown in Eqs. (1.5.16) and (1.5.17). For transition flow, a linear interpolation was made between Eqs. (1.5.16) and (1.5.17). When the flow is stagnant, a Nusselt number of value 2 is used, analogous to the heat conduction from a sphere to a stagnant fluid.

In the present code for the HTDF, energy storage in the core vessel, DHX shell, and the piping systems during the transient has also been considered. For the piping systems, the Hausen correlation and Sider-Tate correlation are used for the laminar and turbulent flow, respectively. For the core, an imaginary annulus between the core vessel and the rod bundle is assumed. For laminar flow, a constant Nusselt number of 7.52 suggested by Lee and Kuo (1998) is employed. For turbulent flow, the Dittus-Boelter correlation is adopted. For the DHX, because the clearance between the shell and tube bundle is much smaller than the shell inner diameter, and also the flow in the clearance is mainly along the periphery of the shell inner surface, a heat transfer model for flow between parallel plates is considered. Laminar flow is retained in the aforementioned clearance, and a constant Nusselt number of 7.54 (Todreas and Kazimi, 1990) corresponding to a constant boundary temperature condition is used.

Two inlets have been designed for the HTDF core vessel, both of which are on the side of the vessel near the bottom. One of the inlets directs the flow into the DRACS primary loop, while the other inlet is connected to the intermediate pump loop. When the flow is laminar (Re < 2,300), it develops into longitudinal flow over a short distance after the coolant enters the core and the main contributor to the pressure drop is due to the friction. In such a case, the friction factor correlation developed by Sahoo and Mohanty (1987) for rod bundles is used, which states that the product of the friction factor and the Reynolds number is a constant of 89.972. When the flow is in turbulent flow regime (Re > 4,000), the flow bounces back and forth on the side of the core vessel after it enters the core, in which case it is more reasonable to assume form loss as the main pressure drop contributor. In a previous CFD study (Lv et al., 2013) of vortex diodes for application to the HTDF, a CFD study is performed to obtain the pressure drop over the core corresponding to a turbulent mass flow rate of 5.30 kg/s, which is found to be 7,299 Pa. Part of this total pressure drop is due to the form losses when the flow enters and exits the core. By assuming a contraction loss coefficient of 0.5 and expansion loss coefficient of 1, and subtracting those losses from the total pressure drop, an equivalent form loss coefficient of 1.502 is found for the form loss inside the core only, which is used for turbulent flow in the present code. For transition flow, a linear interpolation is made between the laminar and turbulent models.

The way to deal with the DHX shell-side pressure drop is similar to that for the heat transfer coefficient. The DHX shell-side pressure drop is composed of three distinct parts: that in pure cross flow, Δp_c; that in the end zone (first and last baffle compartment), Δp_e; and that in the baffle window, Δp_w. The former two are based the pressure drop (Δp_{bi}) for the ideal cross flow over the tube banks in one baffle compartment with central baffle spacing, L_{bc}. The cross-flow pressure over $(N_b - 1)$ baffle compartments is obtained by correcting Δp_{bi} as:

$$\Delta p_c = \Delta p_{bi}(N_b - 1)R_b R_l \tag{1.5.69}$$

where N_b is the number of baffles. The end-zone pressure drop can be calculated from:

$$\Delta p_e = \Delta p_{bi}\left(1 + \frac{N_{tcw}}{N_{tcc}}\right)R_b R_s \tag{1.5.70}$$

where N_{tcc} is the number of effective tube rows crossed between the baffle tips while N_{tcw} is the number of effective rows crossed in the baffle window. The bundle bypass factor (R_b), leakage flow correction factor (R_l), and unequal baffle spacing correction factor (R_s) are detailed in the Heat Exchanger Design Handbook (Hewitt, 1992). The ideal cross flow pressure drop, by definition, is:

$$\Delta p_{bi} = 2 f_i N_{tcc} \frac{(G_s)^2}{\rho_s} \left(\frac{\mu_s}{\mu_{s,w}} \right)^{-0.14} \tag{1.5.71}$$

where G_s, ρ_s, μ_s are the shell-side mass flux, density, and viscosity, respectively. The tube wall effect is accounted for by considering $\mu_{s,w}$, which is the viscosity of the shell-side fluid at the tube wall temperature. The fanning friction factor is empirically correlated as:

$$f_i = b_1 \left(\frac{1.33}{L_{tp} / D_t} \right)^b (\mathrm{Re}_s)^{b_2} \tag{1.5.72}$$

$$b = \frac{b_3}{1 + 0.14(\mathrm{Re}_s)^{b_4}} \tag{1.5.73}$$

where L_{tp} and D_t are the tube pitch and outer diameter, respectively; and Re_s is the shell-side Reynolds number. The values of b_1, b_2, b_3, and b_4 corresponding to different Reynolds number Re are listed in Table 1.5.10 (Hewitt, 1992).

Table 1.5.10 Empirical coefficients for calculation of f_i (Hewitt, 1992)

Re	b_1	b_2	b_3	b_4
10^5 - 10^4	0.372	-0.123	7.00	0.500
10^4 - 10^3	0.486	-0.152		
10^3 - 10^2	4.570	-0.476		
10^2 - 10	45.100	-0.973		
< 10	48.000	-1.000		

The pressure drop over the N_b baffle widows for turbulent flow ($\mathrm{Re}_s \geq 100$) is calculated as:

$$\Delta p_w = N_b \left[(2 + 0.6 N_{tcw}) \frac{(G_w)^2}{2\rho_s} \right] R_l \tag{1.5.74}$$

and for laminar flow ($\mathrm{Re}_s < 100$) as:

$$\Delta p_w = N_b \left\{ 26 \frac{G_w \mu_s}{\rho_s} \left[\frac{N_{tcw}}{L_{tp} - D_t} + \frac{L_{bc}}{(D_w)^2} \right] + \left[2 \frac{(G_w)^2}{2\rho_s} \right] \right\} R_l \tag{1.5.75}$$

where D_w is the equivalent hydraulic diameter of a baffle window; and G_w is the mass flux based on the geometric mean of the cross flow area and the window net area.

On the NDHX air side, air flows across the tube banks. Therefore, Eqs. (1.5.70) - (1.5.73) and Table 1.5.10 are applicable to predict the pressure drop on the NDHX air side. For the DHX and

NDHX tube side, depending on the flow regime, Eqs. (1.5.47) – (1.5.49) can be used to calculate the Darcy friction factor.
The fluidic diode is the main contributor to the total pressure drop in the DRACS primary loop. In the previous CFD analysis of vortex diodes, correlations for the forward and reverse Euler numbers (similar to the form loss coefficient) are developed, as shown in Eqs. (2.4.25) and (2.4.26). These correlations have been adopted in the present code to calculate the pressure drops in the forward and reverse flow directions of the vortex diode.

Pressure drops in the pipes include the friction and form losses. For the frictional pressure drop in the pipes, Eqs. (1.5.47) – (1.5.49) have been selected to calculate the Darcy friction factor. For form losses, a loss coefficient of 0.9 is used for the elbows. In addition, form losses associated with flow entering and exiting the components have also been accounted for. Loss coefficients of 0.5 and 1 (Todreas, 1990) have been used for contraction and expansion, respectively.

Before we perform simulations of different scenarios, a grid-independence study is conducted to investigate the effect of the mesh size on the simulation results. For this study, a start-up scenario is assumed, in which the initial temperatures in the primary, secondary and pump loops are assumed to be 500°C while the initial temperatures in the air loop are assumed to be 40°C. There are no initial flows assumed for the secondary salt and air. For the primary and pump loops, the initial flows are assumed to be the same as that at the steady state of the core normal operation. In the previous CFD study of vortex diodes, a scaling analysis is performed for the steady state of the core normal operation, yielding flow rates of 0.120 and 5.301 kg/s for the initial upward flows in the DRACS branch and core branch, respectively.

The effects of the DHX and NDHX mesh size are first examined. For the first run, the core, DHX and NDHX are axially divided into 11, 5 and 5 pieces, respectively; and a mesh size of 0.2 m is used for all the pipes. The steady-state results predicted by the code are listed in Table 1.5.11, along with the nominal design conditions.

Table 1.5.11 Code results for nodalization case 1 (Nc = 11, ND = 5, NN = 5, and 0.2 m for pipes)

	Primary Salt		Secondary Salt		Air	
	Design	Code	Design	Code	Design	Code
T_{hot} (°C)	722.14	721.35	665.33	652.92	110	110.09
T_{cold} (°C)	677.86	676.97	589.67	577.54	40	40
ΔT (°C)	44.28	44.38	75.65	75.38	60	60.09
$\dot{m}$ (kg/s)	0.120	0.120	0.127	0.127	0.142	0.142

As can be seen, all the temperature differences and mass flow rates predicted by the code agree well with the design values. This is understandable because the temperature differences and the mass flow rates are coupled and are governed by the energy balance and integral momentum equations; as long as energy is balanced and the pressure drops in the loops are correctly simulated, the temperature differences and mass flow rates predictions should match the design values. However, the absolute temperatures of the coolants will be determined by the heat transfers in the two heat exchangers, i.e., the DHX and NDHX. As can also be seen, the predicted secondary salt temperatures deviate from the design value appreciably, although the percentage differences are small (less than 3%), which indicates that the two heat exchangers are not properly simulated. After reviewing the design processes of the DHX and NDHX, we realize that in order to reproduce the design results by the code, the mesh size for the DHX should be as small as possible, while the NDHX should be treated as an entire piece.

The DHX and NDHX are design based on the method of LMTD (logarithmic mean temperature difference) that is defined based on the inlet and outlet temperatures of the cold and hot sides. In the DHX, the flow arrangement is near-counter current, for which the LMTD can be obtained by integrating the temperature difference between the hot and cold sides along the flow directions. Therefore, in order to obtain the accurate LMTD and thus the inlet and outlet temperatures of the two sides, the axial discretization should be fine enough so that the temperature distributions along the flow direction are properly captured. However, for the NDHX, cross flow arrangement is encountered. Because the present code is based on one-dimensional formulation, the effect of the transversal temperature distribution is not considered; and if the NDHX is divided into subsections along the tube, due to the loss of the information on the air-side transversal temperature distribution, the temperature distributions of the tube and tube-side salt will not be simulated correctly, leading to inaccurate predictions of the inlet and outlet temperatures for the salt side. Therefore, the NDHX should be treated as an entire piece, the same as the way it is designed.

To prove our previous postulation, a second nodalization case is investigated, in which the NDHX is assumed as one piece while all other settings are the same as nodalization case 1. The simulation results are illustrated in Table 1.5.12.

Table 1.5.12 Code results for nodalization case 2 (Nc = 11, ND = 5, NN = 1, and 0.2 m for pipes)

	Primary Salt		Secondary Salt		Air	
	Design	Code	Design	Code	Design	Code
T_{hot} (°C)	722.14	731.73	665.33	664.01	110	110.09
T_{cold} (°C)	677.86	687.34	589.67	588.64	40	40
ΔT (°C)	44.28	44.38	75.65	75.38	60	60.09
$\dot{m}$ (kg/s)	0.120	0.120	0.127	0.127	0.142	0.142

As can be seen, the temperature differences and mass flow rates are not affected by changing the mesh size for the NDHX, which agrees with our previous conclusion. In addition, the temperatures of the secondary salt agree better with the design values by treating the NDHX as one piece. However, the temperatures of the primary salt are deviating from the design values, which based on our previous postulation is probably because the mesh for the DHX is too coarse. We therefore run two more nodalization cases, in which the DHX is first divided into 15 subsections and secondly 30 subsections while keeping all other settings the same as nodalization case 2. The code results for these two cases are summarized in Tables 1.5.13 and 1.5.14. As can be apparently seen, the predicted primary salt temperatures are getting closer to the design values as the mesh for the DHX is refined. In addition, it seems dividing the DHX into 30 subsections is enough to generate grid-independent solutions. In the meanwhile, the predicted secondary salt temperatures are not affected as long as the NDHX is treated as one piece.

Table 1.5.13 Code results for nodalization case 3 (Nc = 11, ND = 15, NN = 1, and 0.2 m for pipes)

	Primary Salt		Secondary Salt		Air	
	Design	Code	Design	Code	Design	Code
T_{hot} (°C)	722.14	724.17	665.33	663.99	110	110.09
T_{cold} (°C)	677.86	679.78	589.67	588.64	40	40
ΔT (°C)	44.28	44.40	75.65	75.35	60	60.09
$\dot{m}$ (kg/s)	0.120	0.120	0.127	0.127	0.142	0.142

Table 1.5.14 Code results for nodalization case 4 (Nc = 11, ND = 30, NN = 1, and 0.2 m for pipes)

	Primary Salt		Secondary Salt		Air	
	Design	Code	Design	Code	Design	Code
T_{hot} (°C)	722.14	722.28	665.33	663.98	110	110.09
T_{cold} (°C)	677.86	677.88	589.67	588.64	40	40
ΔT (°C)	44.28	44.40	75.65	75.35	60	60.09
$\dot{m}$ (kg/s)	0.120	0.120	0.127	0.127	0.142	0.142

The effect of the core mesh size on the simulation results is also examined. Two nodalization cases based on case 4 are studied, in which the core is divided into 5 and 22 subsections, respectively. The results for the two cases are listed in Tables 1.5.15 and 1.5.16. It is observed that the steady-state results are insensitive to the core mesh size.

Table 1.5.15 Code results for nodalization case 5 (Nc = 5, ND = 30, NN = 1, and 0.2 m for pipes)

	Primary Salt		Secondary Salt		Air	
	Design	Code	Design	Code	Design	Code
T_{hot} (°C)	722.14	722.28	665.33	663.98	110	110.09
T_{cold} (°C)	677.86	677.88	589.67	588.64	40	40
ΔT (°C)	44.28	44.40	75.65	75.35	60	60.09
$\dot{m}$ (kg/s)	0.120	0.120	0.127	0.127	0.142	0.142

Table 1.5.16 Code results for nodalization case 6 (Nc = 22, ND = 30, NN = 1, and 0.2 m for pipes)

	Primary Salt		Secondary Salt		Air	
	Design	Code	Design	Code	Design	Code
T_{hot} (°C)	722.14	722.28	665.33	663.99	110	110.09
T_{cold} (°C)	677.86	677.88	589.67	588.64	40	40
ΔT (°C)	44.28	44.40	75.65	75.35	60	60.09
$\dot{m}$ (kg/s)	0.120	0.120	0.127	0.127	0.142	0.142

Lastly, the influence of the mesh size for the pipes on the simulation results is investigated. Based on nodalization case 4, the mesh size for the pipes is changed from 0.2 m to 0.1 m, with the results shown in Table 1.5.17. As can be seen from the comparison between case 4 and case 7, further refining the mesh for the pipes will not affect the steady-state simulation results.

Table 1.5.17 Code results for nodalization case 7 (Nc = 11, ND = 30, NN = 1, and 0.1 m for pipes)

	Primary Salt		Secondary Salt		Air	
	Design	Code	Design	Code	Design	Code
T_{hot} (°C)	722.14	722.28	665.33	663.98	110	110.09
T_{cold} (°C)	677.86	677.88	589.67	588.63	40	40
ΔT (°C)	44.40	44.40	75.65	75.35	60	60.09
$\dot{m}$ (kg/s)	0.120	0.120	0.127	0.127	0.142	0.142

Based on the previous grid-independence study, we conclude that to obtain grid-independent results for the steady-state coolant temperatures and mass flow rates, the core and DHX can be axially divided into 11 and 30 subsections, respectively. The NDHX should be treated as one piece, and a mesh size of 0.2 m is fine enough for the pipes. These mesh settings are used in the transient simulations of an accident scenario that will be discussed shortly.

As an example, a scenario corresponding to a situation that will be experimentally simulated in our lab is examined. After the primary and secondary salts are transferred to the corresponding loops, the core heaters are turned on and a total power of 9 kW is provided. In the meanwhile, the pump is turned on to provide a targeted flow rate of 5.4215 kg/s. The system will continue running until a steady state is reached. By the time the steady state is reached, the pump is tripped and the total power from the core heaters is changed to 10 kW. The simulated scenario starts from the point of the pump tripping and core power change. The initial conditions, i.e., the steady state that is reached before the simulated scenario, are summarized in Table 1.5.18. The inlets and outlets are defined with respect to the initial flow directions. The temperature difference over the core is quite small mainly because of the large flow through the core. Because there is no heat sink in the pump branch, the coolant temperature is uniform along the pump branch.

Table 1.5.18 Initial conditions of the simulated scenario

Core Branch	Core Inlet (^oC)	Core Outlet (^oC)	Mass Flow Rate (kg/s)
	682.24	683.14	5.301
DRACS Branch	DHX Shell-side Inlet (^oC)	DHX Shell-side Outlet (^oC)	Mass Flow Rate (kg/s)
	682.24	642.51	0.120
Pump Branch	Uniform Temperature (^oC)		Mass Flow Rate (kg/s)
	682.24		5.422
Secondary Loop	DHX Tube-side Inlet (^oC)	DHX Tube-side Outlet (^oC)	Mass Flow Rate (kg/s)
	545.47	614.97	0.124
Air Loop	Inlet (^oC)	Outlet (^oC)	Mass Flow Rate (kg/s)
	40	105.22	0.137

The simulation results with above initial conditions are illustrated in Figs. 1.5.29 -1.5.33. The inlets and outlets here are defined with respect to the final flow directions. The transient starts at time point of 0. As can be seen, steady state is reached at approximately 1.2E5 seconds. The steady-state temperatures and mass flow rates are found to be exactly the same as those shown in Table 1.5.14 for nodalization case 4. This indicates that the steady state is independent on the initial conditions, which is understandable. As discussed earlier, the temperature differences and mass flow rates are governed by the energy balance and integral momentum equations while the absolute temperatures are determined by the heat exchanger designs. As long as the facility design is fixed (the loop height, heat exchangers), and the core power is identical, the final steady state reached will be the same, independent on the initial conditions.

As can be observed, the temperatures and mass flow rate of the primary salt vary more drastically than the secondary salt and air during the beginning phase of the transient. This is mainly because of the flow reversal in the DRACS branch that happens at around 40 seconds. Due to the lack of heat sink in the pump branch, the flow in this branch will eventually decrease to zero which occurs at around 1,000 seconds, as can be seen from Fig. 1.5.33. Before the pump flow dissipates completely, it bounces around zero for a while.

One thing that should be mentioned is that starting from around 4,000 seconds, the results are seen to exhibit some fluctuations. There does not seem to be any physical explanations to these fluctuations since the results right before and after this section of fluctuations are developing quite smoothly. Therefore we think that these fluctuations are associated with the numerical solver that has been used. Further investigations into this are being taken.

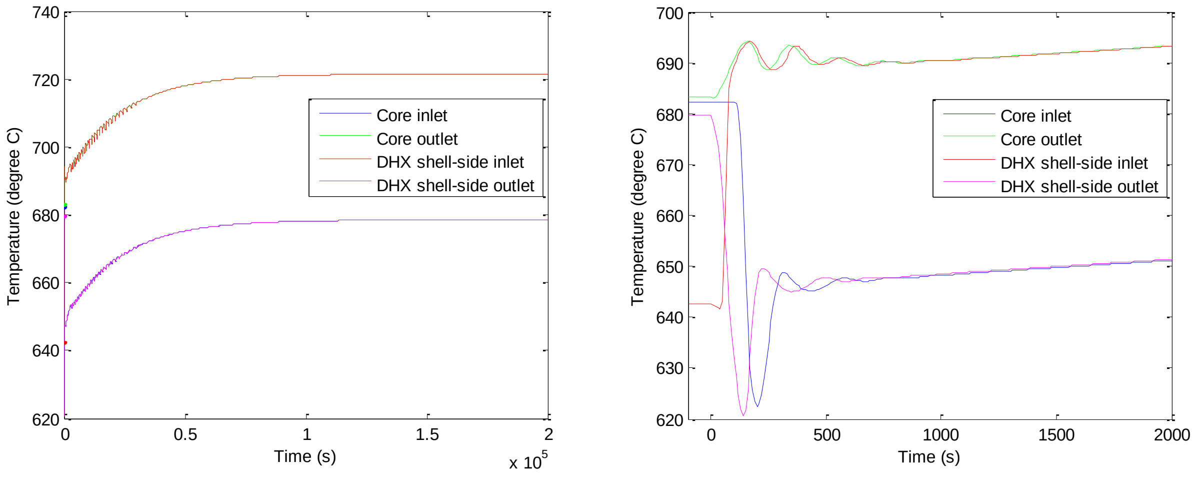

(a) (b)

Fig. 1.5.29. Temperatures in the primary loop during the transient with pump coastdown for up to: (a) t = 200,000 s and (b) t = 2,000 s

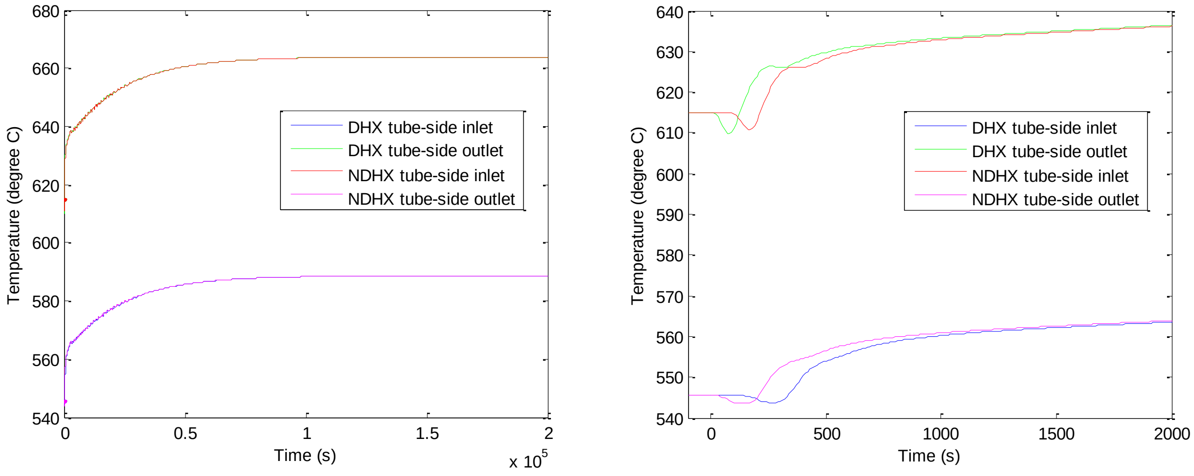

(a) (b)

Fig. 1.5.30. Temperatures in the secondary loop during the transient with pump coastdown for up to: (a) t = 200,000 s and (b) t = 2,000 s

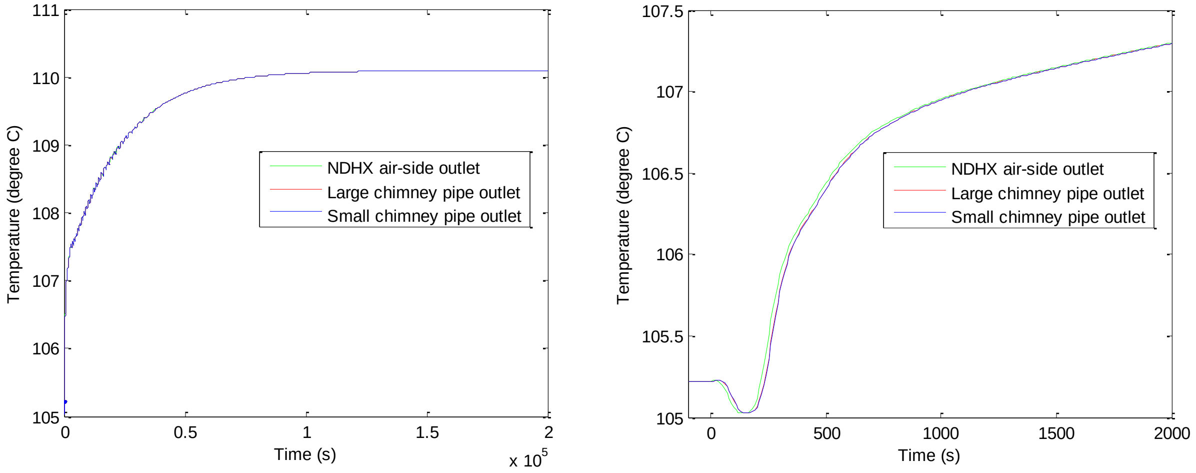

(a) (b)

Fig. 1.5.31. Temperatures in the air loop during the transient with pump coastdown for up to: (a) t = 200,000 s and (b) t = 2,000 s

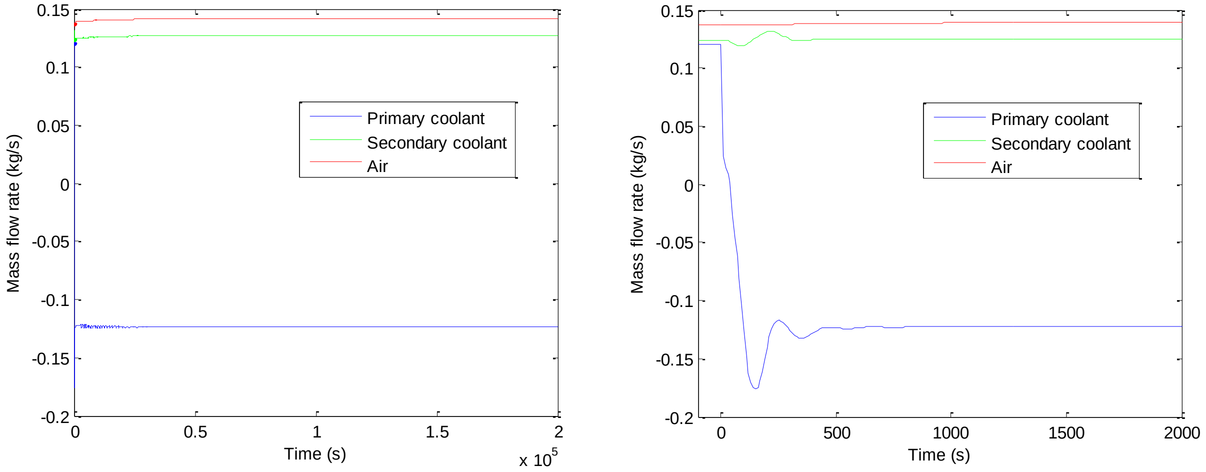

(a) (b)

Fig. 1.5.32. Mass flow rates in the primary, secondary and air loops during the transient with pump coastdown for up to: (a) t = 200,000 s and (b) t = 2,000 s

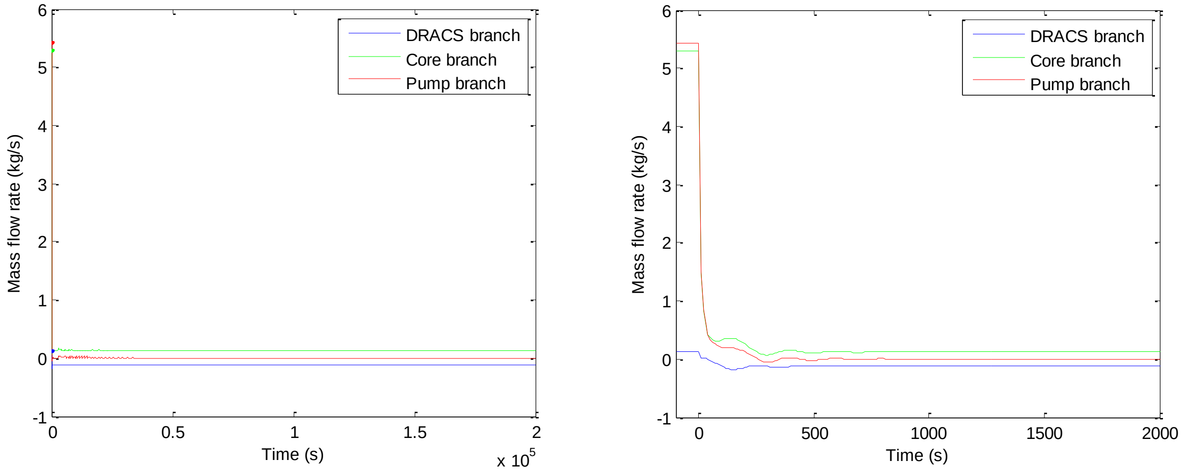

(a) (b)

Fig. 1.5.33. Mass flow rates in the DRACS, core and pump branches during the transient with pump coastdown for up to: (a) t = 200,000 s and (b) t = 2,000 s

In the above simulation, a total power of 9 kW has been provided to bring the system to a steady state before tripping the pump. There is a specific reason for choosing the power as such. Different powers have been tried and it is found that there will be the risk of overcooling the secondary salt if this power is too low. When the total power is lowered, the temperatures of the coolants as well as the NDHX tubes will decrease. At the point when the NDHX tube temperature is below the melting point of the secondary salt, it will start to solidify on the tube surface. To illustrate this, the steady state-state temperature of the NDHX tubes corresponding to three different powers of 7, 8, and 9 kW are shown in Figs. 1.5.34 – 1.5.36. As can be seen, when the total power is 8 kW, the NDHX tube temperature is only 18°C above the secondary salt melting point (390°C). To be safe, the total power has been determined to be 9 kW.

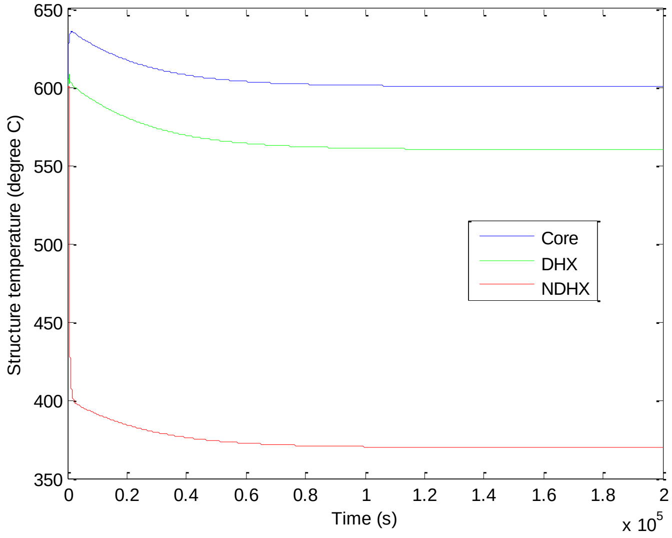

Fig. 1.5.34. Structure temperatures for power of 7 kW

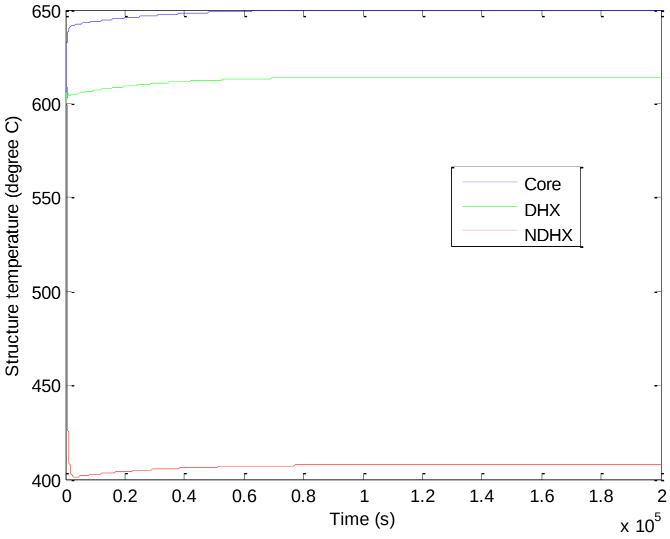

Fig. 1.5.35. Structure temperatures for power of 8 kW

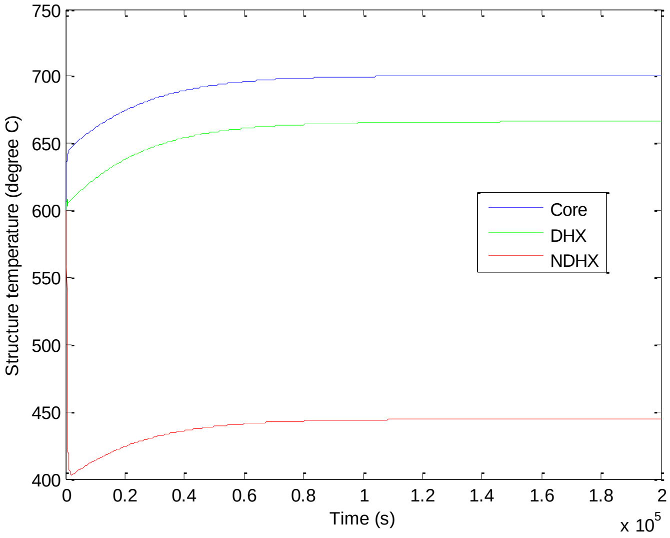

Fig. 1.5.36. Structure temperatures for power of 9 kW

References:

Engineering ToolBox, http://www.engineeringtoolbox.com

Gruszczynski, M. J. and Viskanta, R., “Heat Transfer to Water from a Vertical Tube Bundle under Natural Circulation Conditions”, *ANL-83-7*, Argonne National Laboratory, 1983.
Hewitt, G.F., *Handbook of Heat Exchanger Design*, chapter 3.3, Begell House, Inc., Wallingford, 1992.

Hallinan, K. P. and Viskanta, R., “Dynamics of a Natural Circulation Loop: Analysis and Experiments”, *Heat Transfer Eng*, **7**, pp. 43-52, 1986.

Hallinan, K. P. and Viskanta, R., “Heat Transfer from a Vertical Tube Bundle under Natural

Circulation Conditions”, *Int. J. Heat & Fluid Flow*, **6**, pp. 256-264, 1985.
Hewitt, G.F., *Handbook of Heat Exchanger Design*, chapter 3.3, Begell House, Inc., Wallingford, 1992.

Johns-Manville insulation pipe, http://www.jm.com.

Lee, Y. M. and Kuo, Y. M., “Laminar Flow in Annuli Ducts with Constant Wall Temperature”, *Int. Comm. Heat Mass Transfer*, **25**, pp. 227-236, 1998.

Lv, Q., Chen, M., Sun, X., Christensen, R.N., Blue, T., Yoder, G., Wilson, D., and Sabharwall, P., “Design of Fluidic Diode for a High-temperature DRACS Test Facility,” *The 21st International Conference on Nuclear Engineering (ICONE21)*, Chengdu, China, July 29-August 2, 2013, ICONE21-16902.

Mohanty, A. K. and Sahoo, K. M., "Laminar Convection in Wall Sub-Channel and Transport Rates for Finite Rod-Bundle Assemblies by Superposition", *Nuclear Engineering and Design*, **92**, pp. 169-180, 1986.

Morgan, V. T., “The Overall Convective heat Transfer from Smooth Circular Cylinders”, *Adv. Heat Transfer*, **11**, pp. 199-212, 1975.

Sahoo, K. M. and Mohanty, A. K., "Finite Element Analysis for Laminar Flow and Heat Transfer in Finite Rod Bundles", *Chem. Eng. Comm.*, **51**, pp. 129-140, 1987.

Sahoo, K. M. and Mohanty, A. K., "Turbulent Transport in Wall Subchannels and in Finite Rod Clusters," *Int. J. Heat and Fluid Flow*, **12**, pp. 142-149, 1991.

Todreas, N. E. and Kazimi, M. S., *Nuclear System I – Thermal Hydraulic Fundamentals*, Chapter 10, Taylor & Francis Group, LLC, New York, 1990.

Williams, D.F., “Assessment of Candidate Molten Salt Coolants for the NGNP/NHI Heat-Transfer Loop”, ORNL/TM-2006/69, Oak Ridge National Laboratory, Oak Ridge, TN, 2006.

Williams, D.F., Toth, L.M., Clarno K.T., “Assessment of Candidate Molten Salt Coolants for the Advanced High-Temperature Reactor (AHTR),” ORNL.TM-2006/12, Oak Ridge National Laboratory, Oak Ridge, TN, 2006.

Wolverine Engineering Data Book II, http://www.wlv.com/products/databook/databook.pdf.

2. Issues/Concerns
Improvements in the code formulation, heat transfer and pressure loss models have been made to the computer code that is being developed at Ohio State University. However, the pump trip process during the first stage of the DRACS transient has not been incorporated yet, which will be considered in our next work. In addition, we plan to further justify the code assumptions and also validate the code using a system analysis code, such as RELAP5. Currently, the code validation using the experimental data from the LTDF is ongoing.

Task 1.6: Design a scaled-down low-temperature DRACS test facility using surrogates (Ohio State Responsible).

1. Task Status: Completed

In the design of the low-temperature DRACS test facility, we initially considered Dowtherm A as the surrogate of the primary salt but found some difficulties in the core scaling due to the low thermal conductivity of Dowtherm A. Water with much higher thermal conductivity was thus selected as both the primary and secondary coolants in the new design.

Figure 1.6.1 shows the core design composing of three one-inch electric heaters that was proposed to model the reactor core. There are two types of sub-channels, namely, interior sub-channel of type I and wall sub-channel of type II. The dimensions of the core are summarized in Table 1.6.1. The pitch-to-diameter ratio and wall-distance-to-diameter ratio was 1.6 and 1.4, respectively.

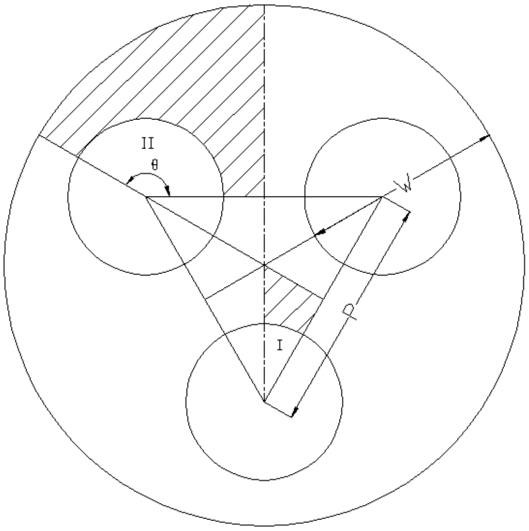

Fig. 1.6.1. Core design in the experiment

Table 1.6.1 Dimensions of the core design

P/*D*	1.6
W/*D*	1.4
Vessel diameter	9.26 cm
Heater diameter (*D*)	2.54 cm (1 inch)
Heater length	1 m

From a literature review, a number of studies on the heat transfer coefficient were performed in a 7-rod design, such as Mohanty and Sahoo (1986) and Sahoo and Mohanty (1987), and the related studies were also discussed by Todreas and Kazimi (1990). However, there was little study for a 3-rod design. The difference between the 3-rod design and 7-rod design is the wall sub-channel analysis, because the embraced angle θ has increased from 120 to 150° changing from the 7-rod to 3-rod design. In our analysis, it was assumed that this change will not considerably affect the Nusselt number of the wall sub-channel, and the same Nusselt number obtained from the 7-rod design study was therefore used in our 3-rod design analysis. As a result, the heat transfer coefficients for the wall sub-channel and the interior sub-channel are respectively 85.5 and 172.5 W/m^2-K, assuming the bulk temperature of the primary water in the core was 70 °C. As shown in Table 1.3.2, it is required to use a total power of at least a few kilowatts that would be significantly larger compared to the possible heat loss in the system. In view of this, the total power provided by the three electric heaters without considering the heat loss was assumed to be 2048 W, resulting in a temperature difference of 100 °C between the heater surface and the bulk water for the wall sub-channel. To avoid sub-cooled boiling on the heater surface, the primary system has to be pressurized to 10 bar (The saturate temperature of water at 10 bar is about 180 °C).

Stainless steel 304 was assumed as the sheath material of the three heaters. The scaling methodology developed in Task 1.3 was applied, with the some preliminary scaling results listed in Table 1.6.2. It was found that, although water yielded better scaling results than Dowtherm A, there was still a conflict between the core scaling and the loop scaling. Since the purpose of this low-temperature test facility is to study the couplings between the three natural circulations, we relaxed the core-scaling requirement and intentionally chose a convection time ratio of 1.14, which rendered reasonable loop scaling results. Based on the loop scaling results, the working conditions of the fluids were calculated, as summarized in Table 1.6.3.

Table 1.6.2 Scaling results with water

Fluence ($\times 10^{25}$ n/m^2)			0	0.1	0.2	0.5	1	3--8
Power (kW)			2.05					
Power ratio, %			1.02					
Primary loop	Time ratio		42.0	46.3	49.8	57.4	64.7	73.2
	Length ratio		0.75	0.75	0.75	0.75	0.75	0.75
	D_h ratio in Core	From Scaling	5.7	6.3	6.7	7.8	8.8	9.9
		From Design	3.0					
	δ ratio in core		3.9	4.3	4.6	5.3	6.0	6.8
	Velocity ratio		0.018	0.016	0.015	0.013	0.012	0.010
	Area ratio		3068	4125	5126	7863	11242	16266
	ΔT ratio		2.1×10^{-4}	1.7×10^{-4}	1.5×10^{-4}	1.1×10^{-4}	8.9×10^{-5}	6.9×10^{-5}

Table 1.6.3 Working conditions of the fluids

	Primary water (10 bar)	Secondary water (1 bar)	Air
T_{hot} (°C)	76.5	65.2	40
T_{cold} (°C)	63.7	34.8	20
$\dot{m}$ (kg/s)	0.038	0.016	0.102

Since the convection time ratio deviated from that yielded by core scaling, we examined how much distortion had been induced in the core scaling. The core scaling results are summarized in Table 1.6.4. The sheath thickness of the heater has been chosen as 0.13 inch so that the time ratio number in the prototype is similar to that in the model (our experiment). However, neither Stanton number nor Biot number was matched between the prototype and our model, which will lead to different boundary condition between the liquid and the heated surface. In addition, the ratio of heat source number is much larger than 1. However, the actual heat input rate in the experiments can be adjusted.

Table 1.6.4 Core scaling results

	Prototype	Model	Ratio
Conduction depth	0.436 cm	0.330 cm	0.757
St	2.26	0.12	0.052
T	15.0	18.7	1.24
Bi	0.173	0.019	0.11
Q	0.044	1.24	28.1
F/A^2	4.44	0.037	0.0083

With the working conditions of the fluids determined, we could proceed to complete the designs of the DHX and NDHX. A shell-and-tube heat exchanger with plain tubes was designed for the DHX, and a finned-tube heat exchanger for the NDHX. Stainless steel 304 was chosen for both the DHX and NDHX. The design of the DHX and NDHX follows the Delaware Method detailed in the Heat Exchanger Design Handbook (Hewitt, 1992). When designing the heat exchangers, the scaling results of the hydraulic diameter, the conduction depth, and heat transfer coefficient for both shell and tube sides have been used as references. The design parameters of the DHX and NDHX that would be used in our low-temperature experiment are summarized in Tables 1.6.5 and 1.6.6. The scaling results of these designed heat exchangers are summarized in Tables 1.6.7, 1.6.8, and 1.6.9.

Table 1.6.5 Design results of the DHX

Material	SS 304
Tube OD	12.09 mm
Tube thickness	1.23 mm
Tube number	49
Pitch to diameter ratio (Triangular pattern)	1.485
Tube length	325 mm
Shell ID	150 mm
Baffles	4
Baffle cut	20%

Table 1.6.6 Design results of the NDHX

Material	SS 304
Tube OD (D_t)	12.36 mm
Tube thickness	1.26 mm
Tube number	30 (1 row)
Pitch to diameter ratio	2.25
Tube length	1100 mm
Width	835 mm
Fin height	0.6 D_t
Fin thickness	0.5 mm
Fin spacing	0.5 mm

Table 1.6.7 Scaling results of DHX shell side

	Prototype	Model	Ratio
Conduction depth	1.25 mm	1.23 mm	0.98
Hydraulic diameter	12.4 mm	10.8 mm	0.87
Heat transfer coefficient	1499 W/m^2-K	891 W/m^2-K	0.594
St	4.40	3.84	0.87
T	125	125	1
Bi	0.0791	0.0691	0.87
F/A^2	43.3	4.00	0.093

Table 1.6.8 Scaling results of DHX tube side

	Prototype	Model	Ratio
Conduction depth	1.25 mm	1.23 mm	0.98
Hydraulic diameter	13.4 mm	9.64 mm	0.72
Heat transfer coefficient	339 W/m^2-K	293 W/m^2-K	0.866
St	0.187	0.238	1.27
T	21.3	21.3	1
Bi	0.0179	0.0227	1.27
F/A^2	7.91	0.17	0.021

Table 1.6.9 Scaling results of NDHX tube side

	Prototype	Model	Ratio
Conduction depth	1.25 mm	1.26 mm	1.01
Hydraulic diameter	13.4 mm	9.84 mm	0.74
Heat transfer coefficient	321 W/m^2-K	246 W/m^2-K	0.77
St	0.178	0.196	1.10
T	19.7	19.8	1
Bi	0.0181	0.0200	1.10
F/A^2	27.3	0.95	0.035

As seen in Tables 1.6.7, 1.6.8, and 1.6.9, the time ratio number matches between the prototype and the model because the conduction depth has been strictly scaled in our designs. There are some distortions in the Stanton number and Biot number. The reason is that it is difficult to control the heat transfer coefficients to be the same as scaled while maintaining the hydraulic diameter and the conduction depth the same as scaled because of the complexity of the heat transfer coefficient with respect to the geometry of the heat exchangers and the working conditions of the fluids. Since the distortions are reasonably small, the current designs of DHX and NDHX are considered to be acceptable and can guide us to choose appropriate heat exchangers available in the market for the low temperature test facility.

Finally, the scaling results of the primary and secondary loops have to be examined, respectively, as summarized in Tables 1.6.10 and 1.6.11, respectively. As can be seen, the ratio of $\sum_i L_i / A_i$ is not unit for either primary loop or the secondary loop, which, however, can be easily adjusted by changing the length of the horizontal pipes. Richardson numbers is matched for both the primary and secondary loops, which ensures the circulation of the loops. In addition, a needle valve will be used in our experiment to model the fluidic diode in the primary loop as well as to adjust the pressure loss in the loop. Pressure drop of 94.5 Pa introduced by the needle valve is called for to match $\sum \mathrm{F}_\mathrm{i} / A_i^2$ for the primary loop. Similarly, pressure drop of 36.1 Pa due to a needle valve is required in order to match $\sum \mathrm{F}_\mathrm{i} / A_i^2$ for the secondary loop. A schematic drawing of the low temperature test facility is shown in Fig. 1.6.2.

Table 1.6.10 Primary loop scaling results

	Prototype		Model		Ratio
Pipe ID	150.0 mm		37.0 mm		0.247
ΔT	45.0°C		12.9°C		0.29
Height	2,280 mm		1,710 mm		0.75
l_0/u_0	42.2 s		47.8 s		1.14
$\sum_i L_i / A_i$	3.82		2.67		0.70
R	87.1		87.0		1.0
Δp (Pa)	core	13.0	core	0.023	--
	Pipe	~16.0	Pipe	~8.4	--
	DHX shell side	122	DHX shell side	2.5	--
	Fluidic diode	330	Needle valve	**~94.5**	--
$\mathrm{F}_\mathrm{i} / A_i^2$	Total	174.6	Total	~174.6.0	~1.0

Table 1.6.11 Secondary loop scaling results

	Prototype		Model		Ratio
Pipe ID	150.0 mm		20.0 mm		0.133
ΔT	50.0°C		30.4°C		0.61
Height	420 mm		420 mm		1.0
l_0/u_0	7.15 s		8.12 s		1.14
$\sum_i L_i / A_i$	14.4		7.54		0.52
R	21.3		21.3		1.0
Δp (Pa)	DHX tube side	28.0	DHX tube side	0.2	--
	Pipe	~26.0	Pipe	~18.3	--
	NDHX tube side	96.0	NDHX tube side	1.25	--
	Needle valve	--	Needle valve	**~36.1**	--
$\mathrm{F}_\mathrm{i} / A_i^2$	Total	42.5	Total	~42.5	~1.0

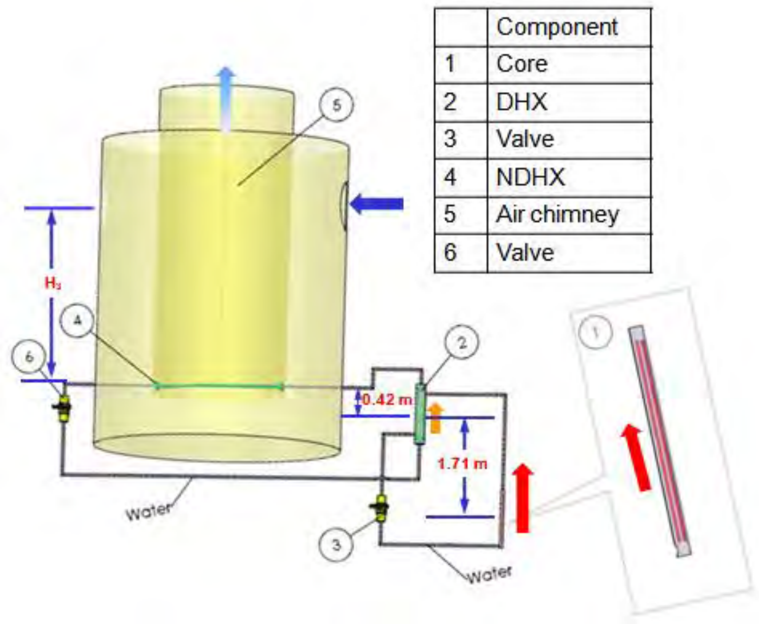

	Component
1	Core
2	DHX
3	Valve
4	NDHX
5	Air chimney
6	Valve

Fig. 1.6.2. Schematic drawing of the low temperature test facility

References

Hewitt, G.F., *Handbook of Heat Exchanger Design*, chapter 3.3, Begell House, Inc., Wallingford, 1992.

Mohanty, A. K. and Sahoo, K. M., "Laminar Convection in Wall Sub-Channel and Transport Rates for Finite Rod-Bundle Assemblies by Superposition", *Nuclear Engineering and Design*, **92**, pp. 169-180, 1986.

Sahoo, K. M. and Mohanty, A. K., "Finite Element Analysis for Laminar Flow and Heat Transfer in Finite Rod Bundles", *Chem. Eng. Comm.*, **51**, pp. 129-140, 1987.

Todreas, N.E. and Kazimi, M.S. " Systems: Vol. II, Elements of Thermal Hydraulic Design," Hemisphere, NY 1990.

2. Issues/Concerns
None

Task 1.7: Construct the scaled-down low-temperature DRACS test facility (Ohio State Responsible).

1. Task Status: Completed

The low temperature test facility that we are constructing is shown Fig. 1.7.1. The main components involved in such a test facility are the core, DHX, fluidic diode, NDHX, and air chimney. The air chimney is not shown here. Due to realistic constraints on the experiment environment, a special air chimney design that is quite different from the prototype has been considered and will be discussed later. With enough information obtained from Task 1.6, we started to purchase the components shown in Fig. 1.7.1 as well as related monitoring/measuring instruments.

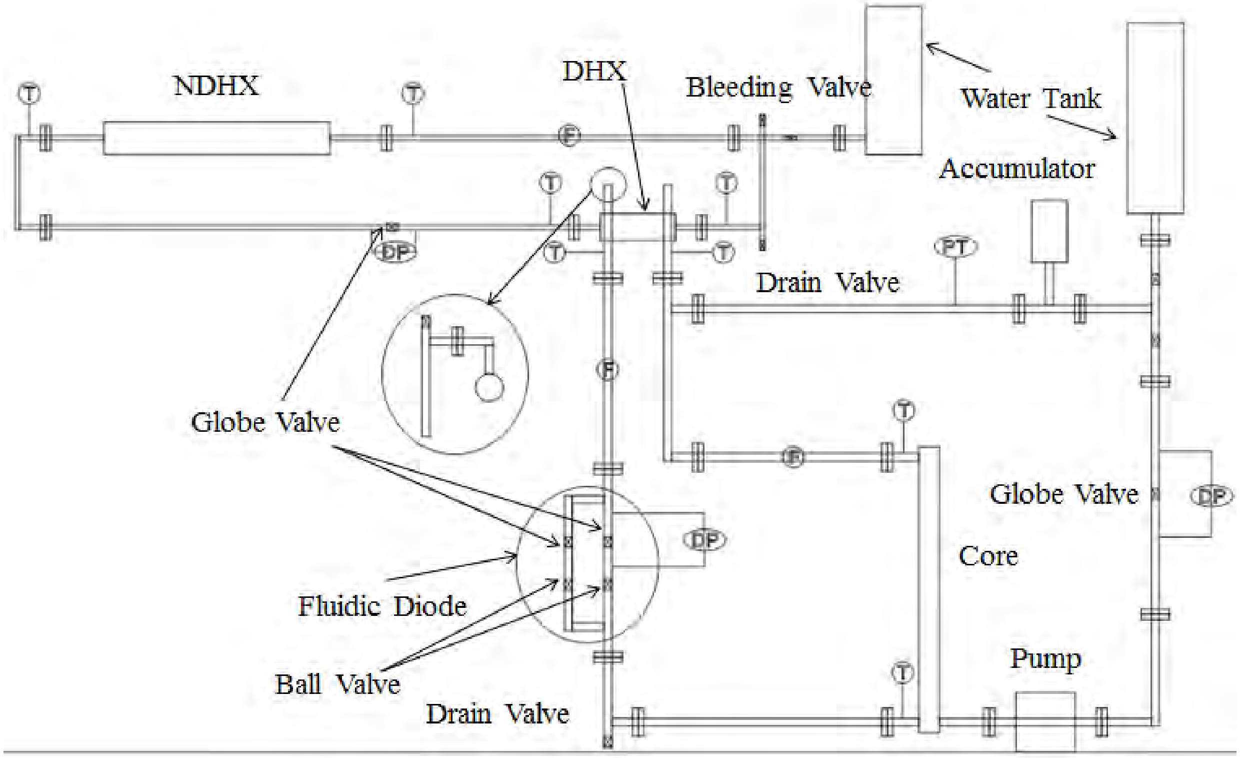

Fig. 1.7.1. Schematic of the low-temperature DRACS test facility

Figure 1.7.2(a) shows a picture of the heaters, of which some details are shown in Fig. 1.7.2(b). The dimensions of the heater to be used in our experiments are summarized in Table 1.7.1. As determined in the scaling analysis, the heater has diameter of 1 inch, and heated length of 1 m. A 1-inch NPT fitting is welded onto one of its ends, with which the heaters can be easily installed into the core. A preliminary CFD simulation of flow inside the core reveals that the developing flow length at the entrance is around 0.25 m. Accordingly, an unheated length of 0.25 m has been considered in front of the NPT fitting. There is another unheated section of 0.1 m at the tip of the heater, which is included for installing a spacer. The spacer ensures alignment of the heaters, and has a design similar to what is shown in Fig. 1.6.1. It is simply a circular stainless steel plate with three 1-inch bore-through holes for the heaters. The 1-inch NPT fitting corresponds to the outer diameter of the threads of 1.315 inch. Based on this information as well as our core design, the minimum space left between adjacent heaters is 0.285 inch (7.239 mm). A built-in type J thermocouple is located at the joint of unheated section 1 and the heated section, where the temperature of the heater is supposed to be the highest in longitudinal direction. Such a thermocouple, working together with a limit temperature controller, prevents the heaters from overheating. Each heater is able to provide 2.0 kW power, which is twice what is required to ensure the scalability. The power of each heater will be separately controlled by a combination of voltage transformer and power meter.

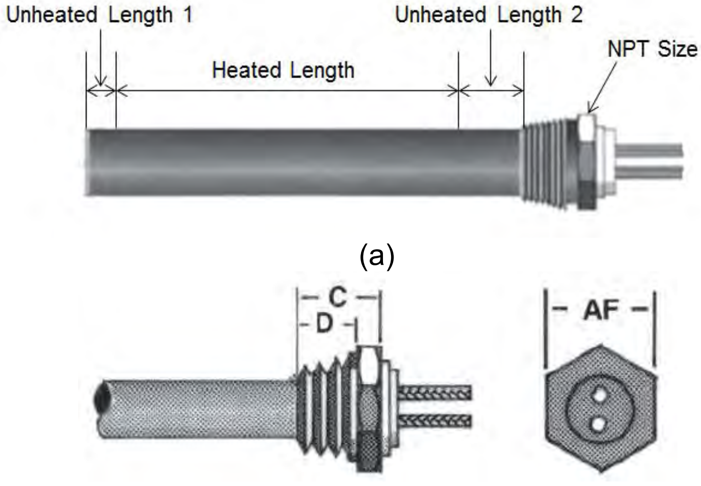

(a)

(b)

Fig. 1.7.2. (a) Picture of a Cartridge Heater and (b) its NPT fitting

Table 1.7.1 Dimensions of the heater in our experiment

Diameter	1 inch
Heated length	1 m
Unheated length 1	0.1 m
Unheated length 2	0.25 m
NPT size	1 inch
Thread OD	1.315 inch
AF	1.37 inch
C	1.13 inch
D	0.68 inch

As mentioned in the scaling analysis, the core is made of three aforementioned heaters surrounded by a circular vessel. A 4-inch schedule 80s stainless steel pipe is chosen as the core vessel, as it has an inner diameter of 9.72 cm, close to the design value of 9.26 cm. In addition, the selected pipe has a wall thickness of .0337 inch (0.86 mm), which is thick enough for the placement of the spacer. The side view of the core top portion, where the spacer is placed, is shown in Fig. 1.7.3. The inner wall of the pipe has been partially bored by 4.56 mm thick and 25.4 mm deep. The core top end is welded into a 4-inch slip-on flange, and sealed by a 4-inch blind flange.

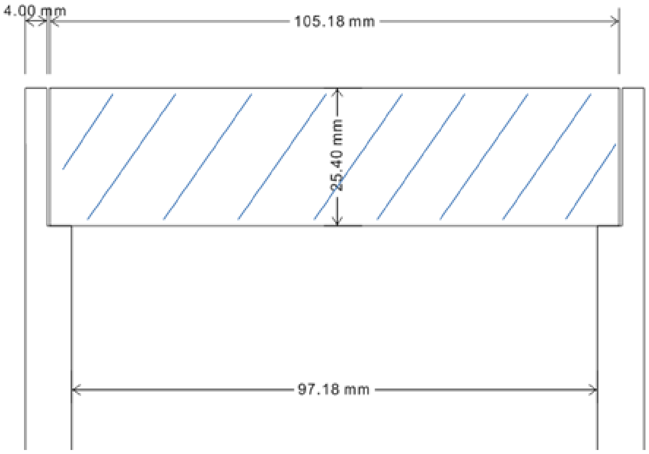

Fig. 1.7.3. Top portion of the core

The shell-and-tube heat exchanger Unit SSCF 05014 from ITT Standard is similar to the DHX designed in Task 1.6, and thus is adopted in our experiment. Comparisons between the two designs are summarized in Table 1.7.2. The Unit 05014 is also evaluated by the DHX design code developed at Ohio State University. When fouling is considered, the capacity estimated by our code is 1,999 W, which is about 3% different from the value provided by the heat exchanger vender. We then performed the scaling analysis of Unit 05014 based on the scaling methodology developed in Task 1.3, and the scaling results are summarized in Tables 1.7.3 and 1.7.4. As can be seen, although deviating from the designed DHX, the Unit 05014 still exhibits acceptable scaling results, especially for the time ratio number. The Stanton numbers for both sides and the Biot number for the tube side are not matched well, which will mainly affect the boundary temperatures.

Table 1.7.2 Comparisons between Unit 05014 and the DHX designed in Task 1.6

	Unit 05014	DHX designed in Task 1.6
Tube OD (inch)	0.375	0.476
Tube thickness (inch)	0.044	0.048
Tube number	80	49
Pitch to diameter ratio	1.208	1.485
Tube length (inch)	14	12.8
Total surface are (Sq Ft)	9.1	6.5
Shell ID (inch)	5	5.9
Baffles	4	4
Baffle cut	25%	20%
Material	SS 316	SS 304
Capacity (W)	2062	2048

Table 1.7.3 Scaling results of Unit 05014 shell side

	Prototype	Model	Ratio
Conduction depth	1.25 mm	1.12 mm	0.90
Hydraulic diameter	12.4 mm	3.8 mm	0.31
Heat transfer coefficient	1499 W/m^2-K	928 W/m^2-K	0.619
St	4.40	11.22	2.55
T	125	150	1.20
Bi	0.0791	0.0658	0.83

Table 1.7.4 Scaling results of Unit 05014 tube side

	Prototype	Model	Ratio
Conduction depth	1.25 mm	1.12 mm	0.90
Hydraulic diameter	13.4 mm	7.3 mm	0.54
Heat transfer coefficient	339 W/m^2-K	368 W/m^2-K	1.09
St	0.187	0.400	2.14
T	21.3	25.6	1.20
Bi	0.0179	0.0261	1.46

A finned-tube heat exchanger from Thermal Transfer Systems, Inc. that is similar to the NDHX designed in Task 1.6 has been purchased for our experiment. The comparisons between the two designs are summarized in Table 1.7.5**.** The capability of purchased unit, evaluated by the NDHX design code developed at Ohio State University, is 3199 W, which is higher than the required power, i.e., 2048 W. A scaling analysis was also performed for the purchased NDHX to identify any distortion that may have been caused in the scaling results, as listed in Table 1.7.6. As can be seen, the time ratio number is larger than 1, which denotes a much faster conduction process in the NDHX structure in experiment than in prototype. This should not be a source of concern since the conduction process is already much faster than the convection in the prototype. Again, the unmatched Stanton number and Biot number will distort the boundary temperatures.

Table 1.7.5 Comparisons between the purchased NDHX and the NDHX designed in Task 1.6

	NDHX purchased	NDHX designed in Task 1.6
Material	Copper tube + Aluminum fin	SS 304
Tube OD (inch)	0.625	0.49
Tube thickness (inch)	0.035	0.05
Tube number	52 (in 2 rows)	30 (in 1 row)
Pitch to diameter ratio	2.4	2.25
Tube length (inch)	39	43.3
Row width (inch)	39	32.9
Fin height (inch)	0.4375	0.3
Fin thickness (inch)	0.01	0.02
Fin spacing	10 fins/inch	25 fins/inch
Capacity (W)	3199	2048

Table 1.7.6 Scaling results of the purchased NDHX tube side

	Prototype	Model	Ratio
Conduction depth	1.25 mm	0.89 mm	0.71
Hydraulic diameter	13.4 mm	14.1 mm	1.05
Heat transfer coefficient	321 W/m^2-K	168 W/m^2-K	0.52
St	0.178	0.093	0.52
T	19.7	40.2	2.04
Bi	0.0181	0.0094	0.52

In the current low-temperature test facility, a combination of globe valves and ball valves is employed to simulate the fluidic diode, as shown in Fig.1.7.1. The two parallel branches, each of which consists of a globe valve and a ball valve, simulate the forward and reverse flow directions of the fluidic diode, respectively. The two globe valves are identical, and can provide resistance as desired by turning the stem. The two ball valves are motorized, and only one of them is open at a given flow direction. The globe valve in the forward direction of the fluidic diode should not exhibit large resistance when it is completely open, which is characterized by the flow coefficient:

$$C_v = 1.156\dot{Q}\sqrt{SG}\Big/\sqrt{\Delta P}\,, \tag{1.7.1}$$

where $\dot{Q}$, SG, and ΔP are the volumetric flow rate in m^3/hr, specific gravity of water, and the pressure drop over the valve in bar, respectively. By estimating the available driving force based on the loop scaling results, and the pressure drops over the core, the DHX shell side, and the primary pipes, the desired pressure drop over the globe valve is found to be around 92 Pa at the mass flow rate of 0.038 kg/s, which corresponds to a flow coefficient of 5.2. A globe valve with flow coefficient of 20 has been adopted.

To switch the fluidic diode simulator from the high flow resistance to low flow resistance upon flow reversal, a controlling system using voltage I/O modules from National Instruments has been developed. The controlling mechanism is illustrated in Fig. 1.7.4. The flow through the fluidic diode simulator will be monitored through the ultrasonic flow meter. When the flow is about to reverse, i.e., when the initial upward flow decreases to zero, the voltage output module will send out two 24-V signals to the fluidic diode simulator. One voltage signal closes the ball valve located in the branch with high flow resistance, and the other signal opens the ball valve located in the other branch with low flow resistance.

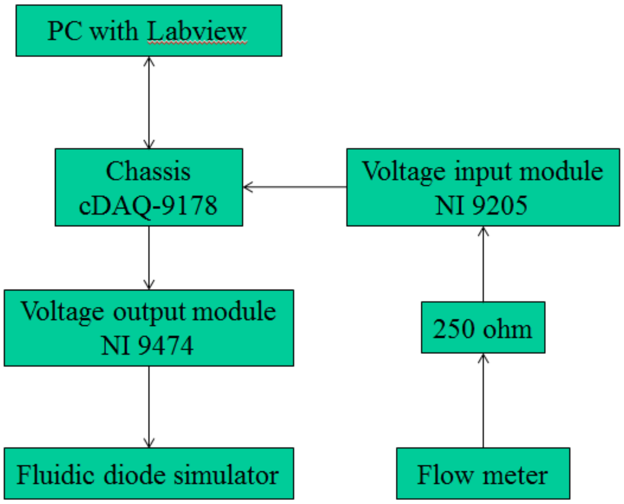
PC with Labview
Chassis cDAQ-9178
Voltage input module NI 9205
Voltage output module NI 9474
250 ohm
Fluidic diode simulator
Flow meter

Fig. 1.7.4. Controlling system for the fluidic diode simulator

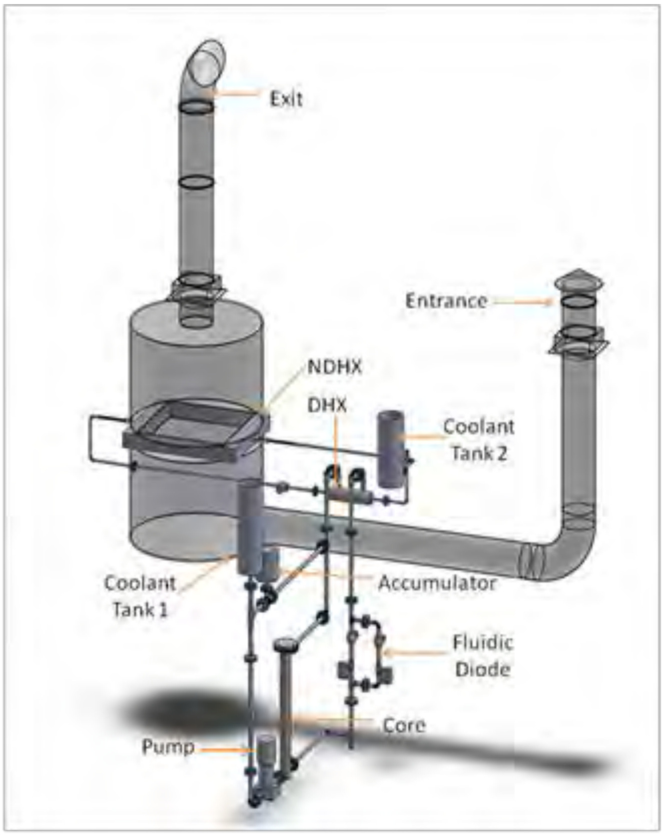
Exit
Entrance
NDHX
DHX
Coolant Tank 2
Coolant Tank 1
Accumulator
Fluidic Diode
Core
Pump

Fig. 1.7.5. Air chimney design

Because the facility will be built in a confined lab rather than an open space, a special air chimney design that is quite different from the prototype has been considered, as shown in Fig.1.7.5. There are two 14-inch openings in the ceiling in our lab, which are utilized as the entrance and the exit of the chimney. The NDHX, with a square face of 39 inch by 39 inch, is positioned in a plastic pipe with ID of 1.4 m. The area between the inner surface of the pipe and the edge of the NDHX will be blocked to confine the airflow to the NDHX. All the indoor ducts are made from galvanized steel while the outdoor ducts above the roof are made from stainless steel 304. The smaller duct inside the room, as well as that at the exit, are insulated with a 1.5-inch (38.1 mm) thick fiberglass blanket to maintain the incoming air temperature and inhibit heat loss from the hot leg where the hot air rises after passing through the NDHX. The big ducts are insulated with a layer of 1-inch (25.4 mm) ceramic fiber blanket before applying the fiberglass blanket, mainly due to the high temperatures that will be encountered later in the high-temperature test facility since the air chimney ducts will be shared with the HTDF.

As seen from the scaling results in Task 1.6, the primary and secondary pipes have ID of 1.457 and 0.787 inch, respectively. Two ASME standard stainless steel pipes, namely, 1-1/4-inch schedule 10s and 3/4-inch schedule 40s, respectively having ID of 1.442 and 0.824 inch which are close to the design values are used. The distance between the thermal centers of the DHX and the core is 1.71 m. The distance between the thermal centers of the NDHX and the DHX is 0.42 m. As mentioned in Task 1.6, the ratio of $\sum_i L_i / A_i$ showing in the non-dimensional momentum equation is not unit for either primary loop or the secondary loop, which, however, can be easily adjusted by changing the length of the horizontal pipes. Matching this ratio leads to width of 1.47 and 3.5 m for the primary and secondary loops, respectively. In addition, an extra pressure drop of 37.3 Pa is required in order to match $\sum \mathrm{F}_\mathrm{i} / A_i^2$ for the secondary loop, which can be provided by a globe valve. The same globe valve as in the primary loop is used so that only one valve calibration is needed.

As can be seen from Fig.1.7.1, there is another flow path connecting between the DHX inlet and the core inlet. The calibration of the globe valves used in the primary and secondary loops is performed in this extra branch by adding an identical globe valve. In addition, this branch provides the chance to model the pump trip process, which is the first stage of DRACS transient. The pump power can be estimated based on the working conditions of the primary water under normal operation of the core. It was assumed that the ratio of the flow through the core under normal operation to that under the accident keeps the same from the prototype to the experiment, which is found to be around 43.3. Correspondingly, the flow rate through the core under normal operation is 26.1 GPM, based on which the total pressure drop along the extra branch when the calibration valve is completely open is estimated to be around 0.25 bar, or equivalently 8.3 feet. The power desired from the pump to overcome the total pressure can be calculated as:

$$P_{output} = \dot{Q}\Delta P, \tag{1.7.1}$$

where $\dot{Q}$ and ΔP are the volumetric flow rate and pressure drop, respectively. The desired power is found to be 0.055 hp. Assuming a pump efficiency of 20% which is usually conservative, the total power of the pump is supposed to be 0.27 hp. The circulator pump B604T from Bell & Gossett can provide a head of 15 feet at 40 GPM of water, and thus is applicable to our test facility. A variable frequency drive is connected to the pump to control its speed.

The primary loop is pressurized by a bladder accumulator that is also connected to the aforementioned extra branch. A bladder accumulator mainly consists of a tank and a rubber bladder which separates the liquid side from the gas side. Clean nitrogen is charged into the gas side gradually to pressurize the primary system after water fills the system. The accumulator we are using is SB 330 from Hydac, and has water capacity of 1 gallon. When pressurized from 1 bar to 10 bar, the volume change of the primary water is around 5 cm^3, which is negligible compared to the capacity of the accumulator.

There is one drain valve and one bleeding valve which are simply ball valves for both the primary and secondary loops. The drain valves are located at the lowest elevation for both loops. The drain valves will be connected to vacuum pump to evacuate the system before feeding water in. The residual air can be expelled from the system through the bleeding valves, which are located at the highest elevation for either loop. A relief valve with scalable set pressure from 150 to 300 Psi is employed at the inlet of the DHX for safety concern.

The test facility is to be fully instrumented. For the flow rate measurement, Clamp-on ultrasonic flow meters are considered, as they will not cause physical intrusiveness to the flow. The flow rates in the primary and secondary pipes are summarized in Table 1.7.6. As seen, the flow rates are quite small, requiring sensitive flow meters. The Clamp-on ultrasonic flow meters from Flexim, capable of measuring flow as small as 9 mm/s, are used. Two flow meters are installed in the primary loop, in order to be able to measure both the main flow through the core and the parasitic flow through the fluidic diode during pump trip transient.

Table 1.7.6 Flow rates in the primary and secondary pipes

	Primary	Secondary
Velocity (m/s)	0.0358	0.0517
Volumetric flow rate (GPM)	0.603	0.254

Because of its non-intrusive feature, the clamp-on ultrasonic flow meter has also been considered for the measurement of the air flow rate. However, it was found out that the air has to be compressed when using an ultrasonic flow meter to measure the air flow rate, mainly due to the requirement on the density of the gas that carries the ultrasonic signal. This requirement eliminates the possibility of using the ultrasonic flow meter for our chimney system.

In the two DRACS test facilities, the air flow rates at the nominal conditions are quite small, as shown in Table 1.7.7. To measure such small flow rates, an insertion probe type thermal mass flow meter from Eldridge Products is adopted in our facilities, which will not cause significant pressure drop. A thermal flow meter utilizes a wire tip that dissipates heat to the flowing air. The air flow rate can be calculated based on the dissipated heat or the power consumed by the wire tip. For most thermal mass flow meters, there is a requirement on the minimum straight lengths upstream and downstream of the measuring location (usually, 10 and 5 pipe diameters, respectively), which cannot be met in our chimney system due to the large diameter and the fixed length of the air chimney. However, the model 9840MPNH that we purchased from Eldridge Products employs a special averaging tube that only requires 3 pipe diameters of straight run upstream and downstream of the measuring location (Eldridge Products). The averaging tube is a simple design that employs a series of holes on the upstream face, as shown in Fig. 1.7.6. When purchased, this unit has been calibrated to the desired range (0 – 1300 SCFM).

Table 1.7.7 Nominal air flow rates in the DRACS test facilities

	Velocity (m/s)	Vol. flow rate (SCFM)	Vol. flow rate (SCFH)
Low-temperature	0.853	179.5	10,768.4
High-temperature	1.187	249.9	14,991.3

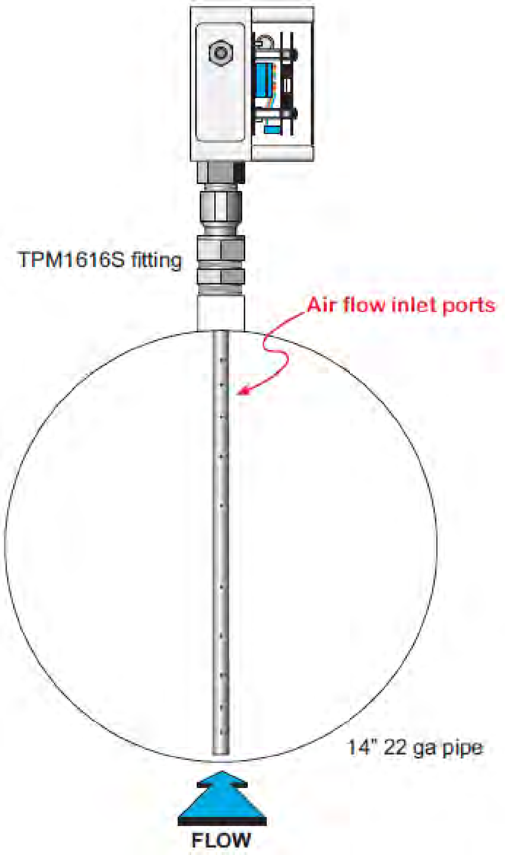

Fig. 1.7.6. The averaging tube design

The pressure drops over the main components are summarized in Table 1.7.8. As seen, except the globe valves, the pressure drops over all other components are too small to measure. A Honeywell STD 120 differential pressure transducer, which has range as small as 0-250 Pa is used to monitor the pressure drops caused by the globe valves in both the primary and secondary loops, as well as for the valve calibration. A Honeywell STG 140 gauge pressure transducer with range of 0-300 Psig is employed to monitor the pressure of the primary system when pressurizing it.

Table 1.7.8 Pressure drops over main components

	Pressure Drop (Pa)
Core	0.02
DHX shell side	4.5
Primary globe valve	~ 92.1
DHX tube side	0.5
NDHX tube side	0.2
Secondary globe valve	~ 37.3

The inlet and outlet temperatures of the core, the DHX, and the NDHX need to be measured in order to evaluate the heat transfer performance of the system. As observed from the scaling results in Task 1.6, all these temperatures, as well as the temperature differences are measurable. Therefore, generous-purpose T-type thermocouples can be applied. T-type thermocouples with a 1/8” diameter and a length of 6” from Omega are used.

The construction of the low-temperature DRACS test facility has been completed and it is currently under operation. A few snapshots of the assembled LTDF are shown in Figs. 1.7.7–1.7.12. As can be seen from the pictures, most of the components, including the core, DHX, pump and accumulator are supported using threaded rods so that the level is adjustable. There is a duct damper located the vertical pipe section, as shown in Fig. 1.7.11. This air damper gives us some flexibility in controlling the air flow. In some cases, e.g., during the initial filling of the salts into the system, we may consider closing the air duct to avoid salt freezing in the NDHX.

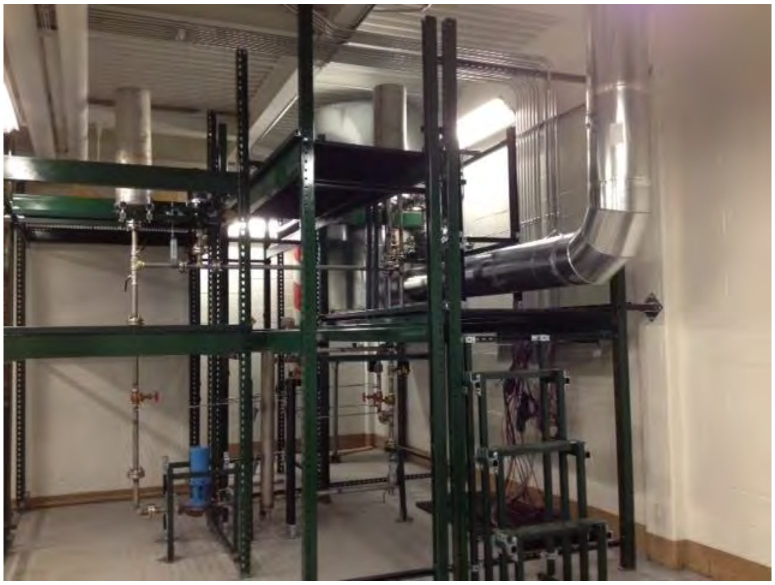

(a)

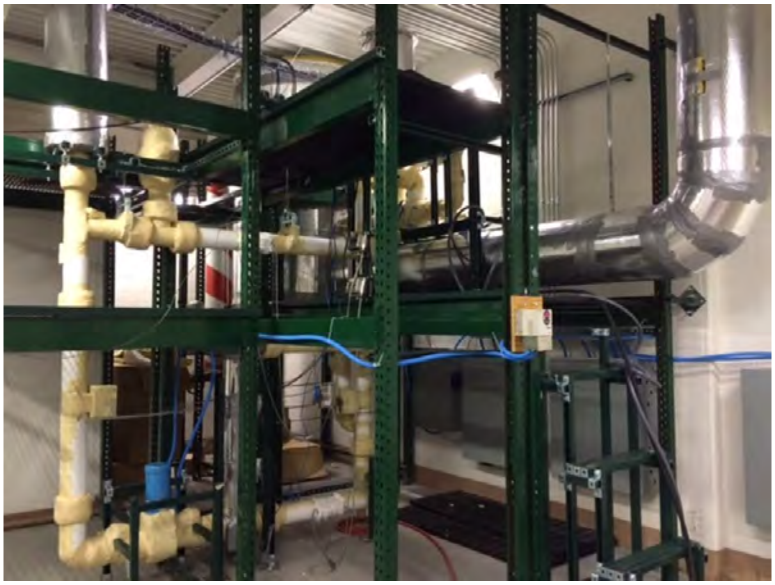

(b)

Fig. 1.7.7. Overview of the LTDF (a) without and (b) with thermal insulation

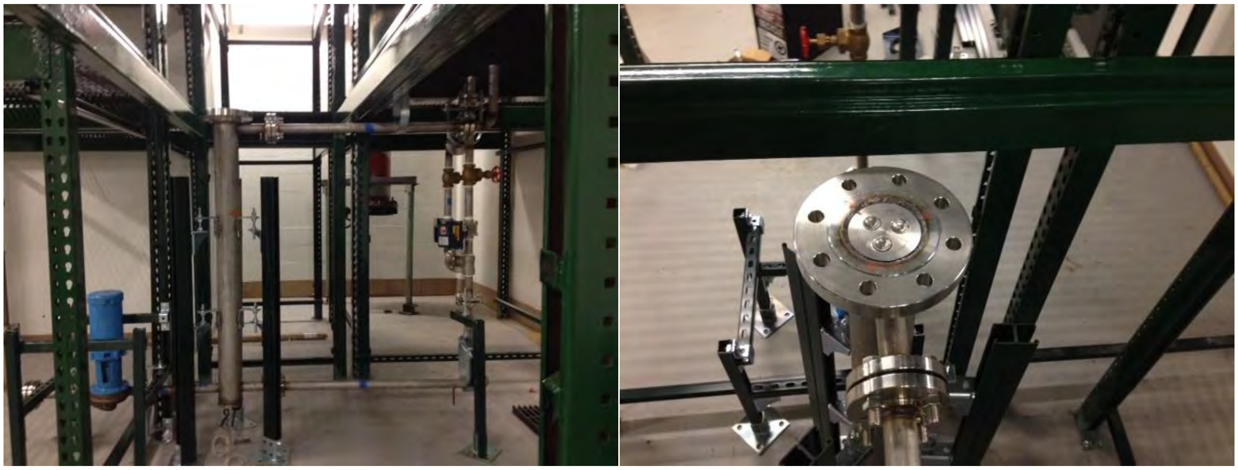

Fig. 1.7.8. Side view and top view of the core

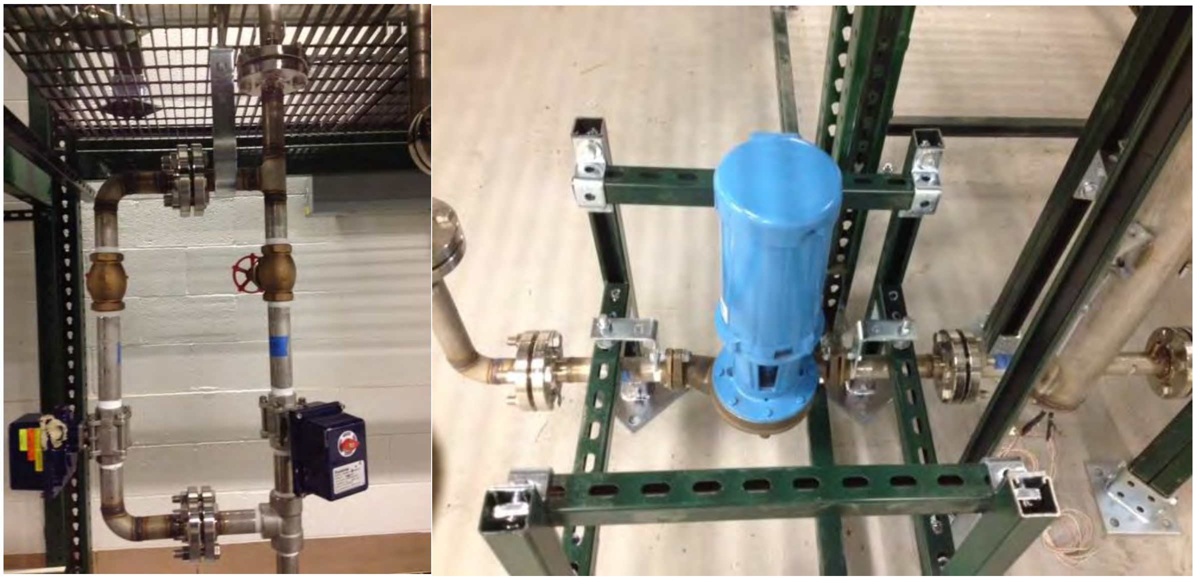

Fig. 1.7.9. The fluidic diode simulator and the pump

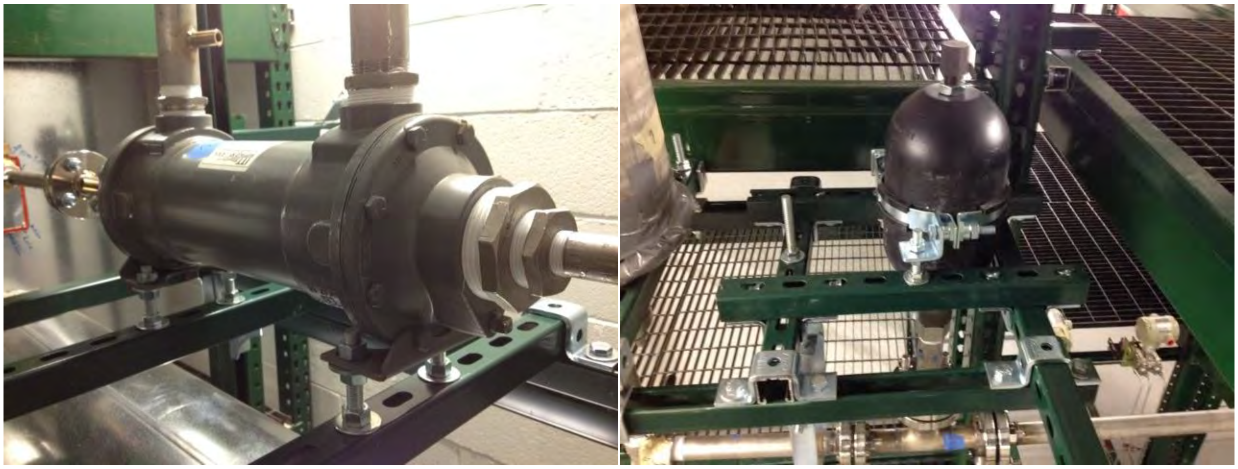

Fig. 1.7.10. The DHX and the accumulator

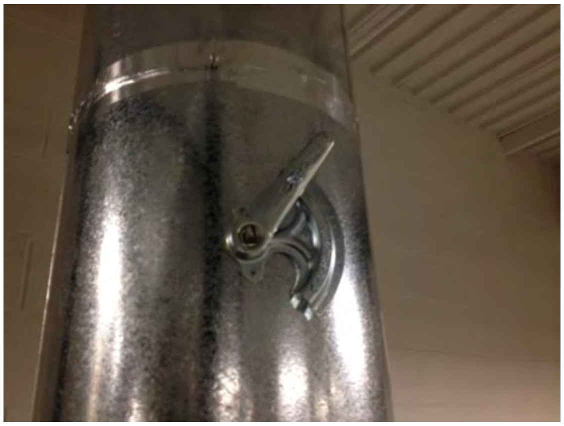
Fig. 1.7.11. The air damper in the chimney system

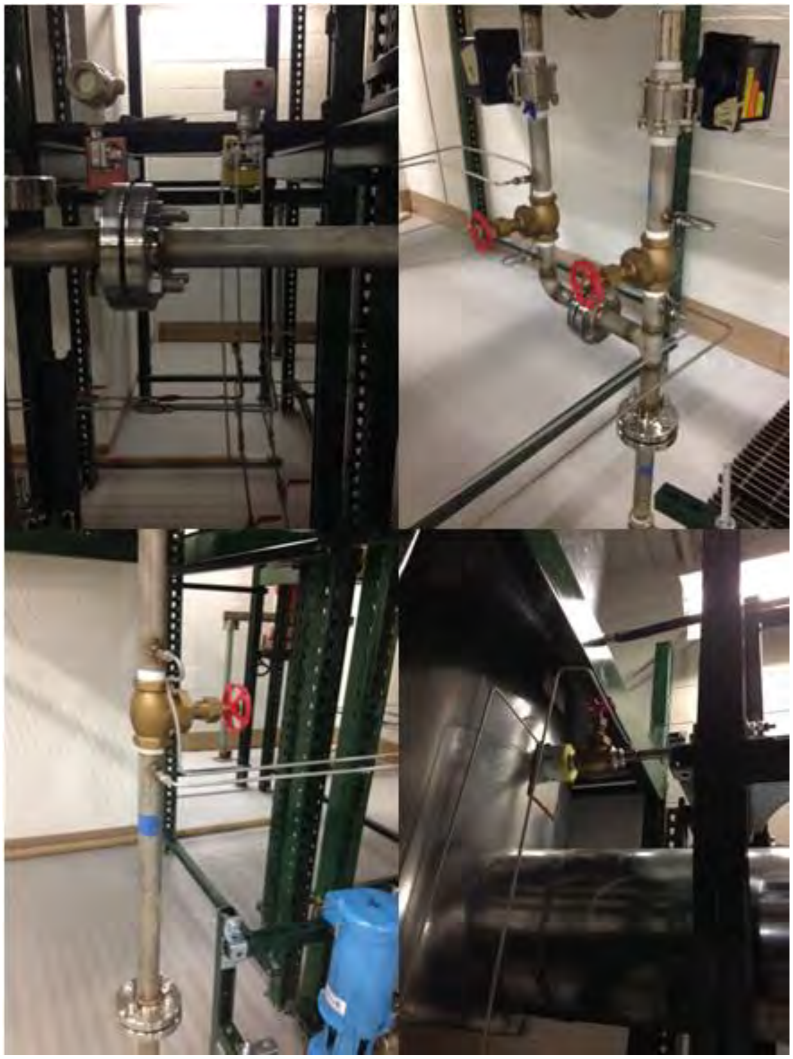
Fig. 1.7.12. The pressure measurement/monitoring system

The power provided to the LTDF core can be continuously controlled through a power controlling and monitoring system, as shown in Fig. 1.7.13. The power controlling system consists of five devices, namely, the temperature controller, fuse, SCR power controller, the watt transducer, and the contactor. The temperature controller receives temperature information from the thermocouple that is built into the core heater, and actuates the contactor to turn off the power when the heater interior temperature exceeds the limit. The SCR power controller, along with the protection fuse, controls the heater power in zero-crossing mode through a 4-20 mA input signal. The watt transducer monitors the actual power that is supplied to each of the heaters.

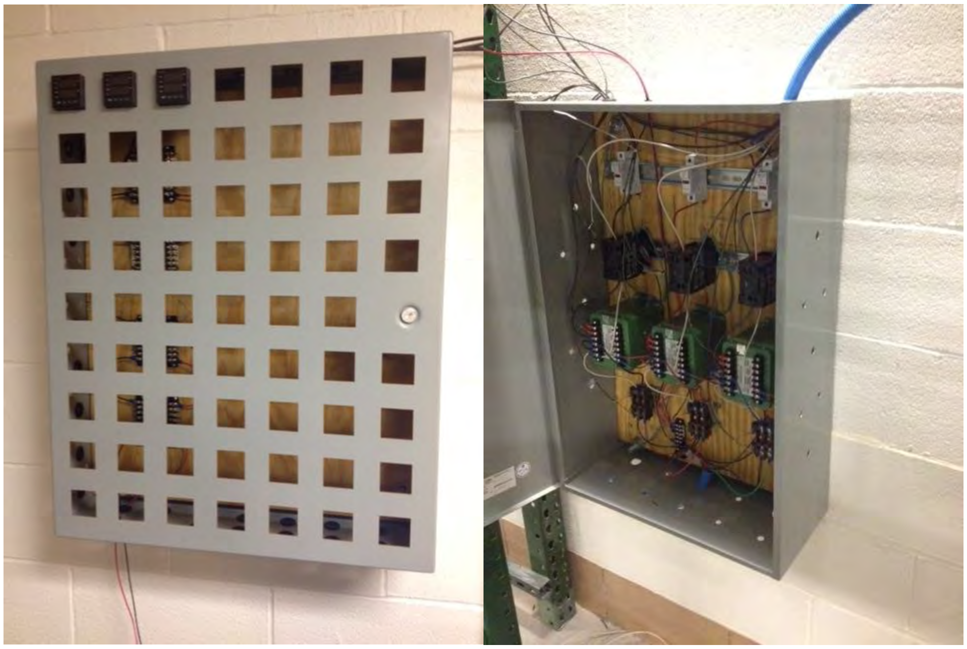

Fig. 1.7.13. Power controlling system for the low-temperature facility

The data acquisition system that will be shared between the LTDF and HTDF is shown in Fig. 1.7.14. This system is based on input/output modules from National Instruments. The small voltage signals from the thermocouples are directly acquired by the system. The 4-20 mA current signals from the pressure transducers, flow meters, and watt transducers will be first converted to 1-5 V voltages before being acquired. In addition, this system, controlled through Labview, will also generate the 4-20 mA controlling signal needed for the SCR controllers and the 12 V actuation signal needed for the automated ball valves in the fluidic diode simulator.

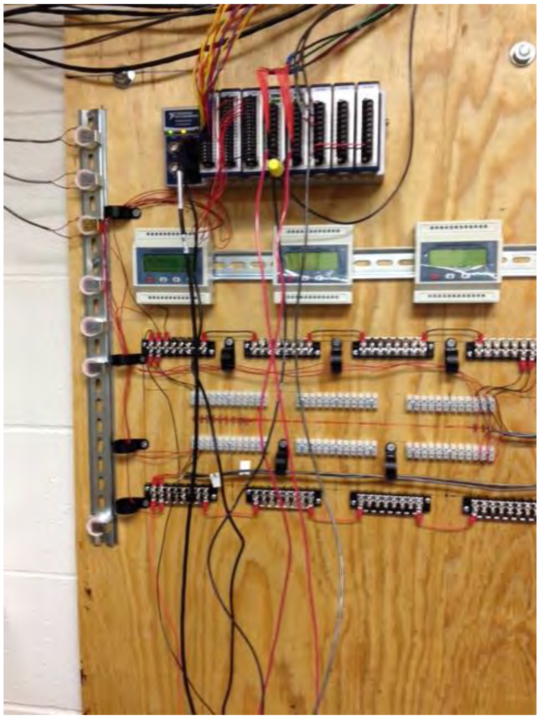

Fig. 1.7.17. Data acquisition system for the low-temperature facility

References

Eldridge Products, Inc., http://www.epiflow.com/Master-Touch%20FAT%20MPNH%20rev2.05.pdf

Flexim, http://www.flexim.com

2. Issues/Concerns
None.

Task 1.8: Design a scaled-down high-temperature liquid fluoride salt facility to simulate the DRACS performance (Ohio State Responsible).

1. Task Status: Completed

The same scaling process as applied to the low-temperature test facility has been followed to obtain a reference design for the high-temperature test facility, based on which an engineering design is being developed. Due to the high temperatures involved, as well as the corrosion issue exhibited by the fluoride salts, several engineering problems have to be addressed, which will be discussed in detail in Task 2.4.

Before starting the scaling analysis, the coolants must be identified. Based on previous experience with the scaling analysis of the low-temperature test facility, a fluoride salt with high thermal conductivity is preferred as the primary salt. In this regard, FLiNaK (LiF-NaF-KF, 46.5-11.5-42 in mol%) was selected as the primary salt. For the secondary salt, there is more concern with the potential issue of salt freezing caused by overcooling; accordingly, KF-ZrF_4 (58-42 in mol%) with low melting point has been chosen. The physical properties of FLiNaK and KF-ZrF_4 are summarized in Table 1.8.1

In the design, seven electric heaters in a triangular pattern are used to simulate the core. The cross-sectional view of the core is shown in Fig. 1.8.1. The dimensions of the core design are summarized in Table 1.8.2. The heaters, with a sheath diameter of 1 inch and a heated length of 0.8 m, are surrounded by a 141.7-mm ID vessel. The total power provided by the heaters is 10 kW, which corresponds to 5% of that in the prototypic design. The determination of the core was based on both heat transfer and engineering considerations.

Table 1.8.1 Summary of properties of FLiNaK and KF-ZrF_4 (T in Kelvin)

	Melting point (^oC)	Density (kg/m^3)	Specific heat (J/Kg-K)	Viscosity (cP)	Thermal conductivity (W/m-K)
FLiNaK	454	2530-0.73(T-273)	1883	0.04exp(4170/T)	0.0005T+32/41.3-0.34
KF-ZrF_4	390	3416-0.887(T-273)	1046	0.159exp(3179/T)	0.0005T+32/103.9-0.34

Heat transfer for a laminar flow parallel to a 7-rod bundle in a circular vessel has been studied by Mohanty and Sahoo (1986, 1987), who divided the flow channel into two categories, i.e., type I and II, as shown in Fig. 1.8.1. Out of the cases they studied, the case with pitch-to-diameter ratio *P/D* and wall-distance-to-diameter ratio *W/D* of 1.6 and 1.4, respectively, is found to give the best heat transfer in the core. However, due to the engineering concern, the pitch-to-diameter ratio and wall-distance-to-diameter ratio have been increased to 1.822 and 1.462, respectively, which will ease the fitting of the heaters. In addition, the heat transfer coefficient for both sub-channels has found to be inversely proportional to the heater sheath diameter; therefore small diameter heaters are preferred. However, as the heaters become smaller, the fitting of these heaters into the core becomes more difficult (as more heaters will be required to maintain the total heating power). As a result, the diameter of the heaters was determined to be 1 inch. The corresponding heat transfer coefficients for the wall and interior sub-channels are 141 and 190 W/m^2-K, respectively, at the nominal DRACS condition.

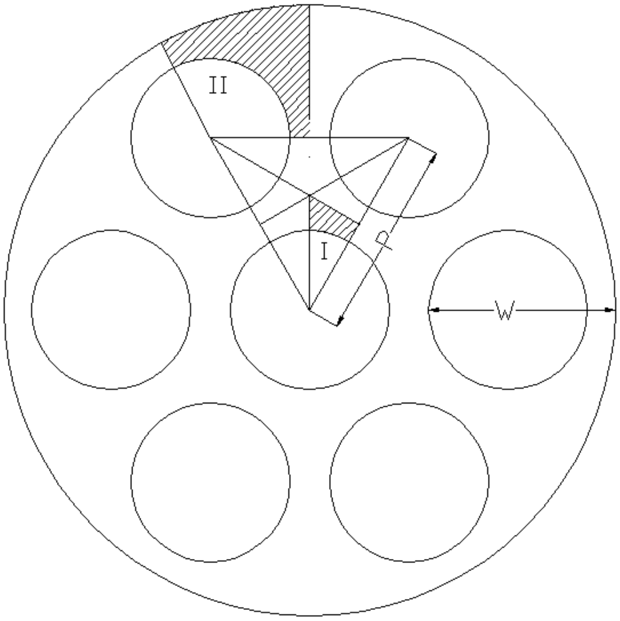

Fig. 1.8.1. The core design in the high-temperature test facility

Table 1.8.2 Dimensions of the core design

P/D	1.822
W/D	1.468
Vessel diameter	141.7 mm
Heater diameter (D)	25.4 mm (1 inch)
Heated length	0.8 m

In the core scaling analysis, an area-weighted average has been taken between the heat transfer coefficients of the aforementioned two sub-channels as the overall heat transfer coefficient, which is 162 W/m^2-K. Alloy N has been assumed as the heater sheath material, which may not be ultimately used in the engineering design due to the availability of Alloy N. However, this is not an issue for the scaling analysis since the thermal properties of Alloy N are close to those of the candidate sheath materials, i.e., Incoloy 800, Inconel 600, or SS 316. Our experience indicates that an almost perfect core scaling would lead to unacceptable results for the loop scaling. Therefore, a compromise has been made in the core scaling by intentionally adjusting the convection time ratio to 0.6, which will yield good loop scaling results. The resulting deviation in the core scaling has been examined as summarized in Table 1.8.3. As can be seen, the Stanton number and Biot number are not matched well. However, these two numbers mainly simulate the boundary layer temperature drop and the fluid-solid interfacial temperature (Ishii and Kataoka, 1984), which is not of our great concern as long as the failure temperature of the heater is not reached. The time ratio number has been perfectly matched by employing a sheath thickness of 2.34 mm, which may not be feasible for a 1-inch heater. By reducing the sheath thickness, the ratio of the time ratio number will be larger than 1, which signifies a faster conduction process over the convection process in the experiment than in the prototype. Nevertheless, this should not be an issue because the overall thermal performance is limited by the convection in the prototype since the absolute value of the time ratio number in the prototype is much larger than 1. Finally, the heat source number ratio is larger than 1, which may cause elevated temperature in the heater sheath in experiment. However, this problem can be mitigated by adjusting the power provided by the heaters.

Table 1.8.3 Core scaling results

	Prototype	Model	Ratio
Conduction depth	4.36 mm	2.34 mm	0.537
St	2.26	0.088	0.039
T	26.2	26.2	1.00
Bi	0.099	0.013	0.13
Q	0.044	0.39	8.9
F/A^2	4.44	7.13	1.61

Table 1.8.4 Working conditions of the salts and air

	FLiNaK	KF-ZrF$_4$	Air
T_{hot} (°C)	722	666	110
T_{cold} (°C)	678	590	40
$\dot{m}$ (kg/s)	0.120	0.127	0.142

With the convection time ratio determined, we were able to obtain the working conditions of the salts from the loop scaling, which are shown in Table 1.8.4. The working conditions of air were determined in the design of NDHX, which will be discussed later. The coolant working conditions, along with the scaling results for the DHX and NDHX, enables us to finalize the heat exchanger designs.

A shell-and-tube heat exchanger design for DHX has been obtained with a MATLAB code based on the Delaware Method (Hewitt, 1992). The DHX design is summarized in Table 1.8.5. SS 316 is considered as the construction material in the present design mainly due to the cost concern. 5/8-inch BWG gauge 18 standard tubes have been employed in the design, as well as the shell which corresponds to 8-inch Schedule 10 ASME standard pipe. The tube wall thickness is larger than what is suggested by the scaling analysis mainly due to the consideration of potential corrosions. In addition, the tube thickness based on scaling results does not correspond to any standard tubes, which will add to the cost. Since the tube dimensions are not exactly the same as what were suggested by the scaling analysis, there will be scaling distortions in the heat exchanger scaling. In addition, the heat transfer coefficients, especially that on the shell side, cannot be obtained as scaled owing to the complex dependence of the heat transfer coefficient on the heat exchanger geometry and fluids working conditions. This will also contribute to the distortion in scaling. Therefore, the scaling results of the DHX have been examined as shown in Tables 1.8.6 and 1.8.7. As can be seen, the Stanton and Biot numbers are not matched very well. This will mainly distort the simulation of the boundary layer temperature drop as stated before. The ratio of time ratio number is smaller than one for both the shell and tube sides because of the introduction of thicker tube wall than required. However, the heat transfer is still limited by the convection process if we pay attention to the absolute valve of the time ratio number.

Table 1.8.5 Design results of the DHX

Material	SS 316
Tube OD	15.88 mm
Tube thickness	1.25 mm
Tube number	80
Pitch to diameter ratio (Triangular pattern)	1.28
Tube length	325 mm
Shell ID	211 mm
Baffles	4
Baffle cut	20%

Table 1.8.6 Scaling results of DHX shell side

	Prototype	Model	Ratio
Conduction depth	1.25 mm	1.25 mm	1.00
Hydraulic diameter	15.88 mm	15.88 mm	1.00
Heat transfer coefficient	1499 W/m^2-K	1040 W/m^2-K	0.694
St	4.40	2.24	0.51
T	125	87.1	0.70
Bi	0.0791	0.0506	0.64
F/A^2	43.3	11.6	0.27

Table 1.8.7 Scaling results of DHX tube side

	Prototype	Model	Ratio
Conduction depth	1.25 mm	1.25 mm	1.00
Hydraulic diameter	13.4 mm	13.4 mm	1.00
Heat transfer coefficient	339 W/m^2-K	145 W/m^2-K	0.428
St	1.03	0.34	0.33
T	117	82	0.70
Bi	0.0179	0.0070	0.39
F/A^2	7.91	1.91	0.24

Table 1.8.8 Design results of the NDHX

Material	SS 316
Tube OD (D_t)	15.88 mm
Tube thickness	1.25 mm
Tube number	30 (2 rows)
Pitch to diameter ratio (Triangular pattern)	1.84
Tube length	438 mm
Width	438 mm

For the NDHX design, plain tubes have been used since the temperature gradient between the tube side and the shell/air side is much larger than that in the low temperature test facility. The design of NDHX is summarized in Table 1.8.8. SS 316 and 5/8-inch BWG gauge 18 standard tubes have been used. Thirty tubes with a length of 438 mm are placed in two layers in a staggered triangular pattern with a pitch-to-diameter ratio of 1.84.

One thing worth of mentioning is that thermal radiation is neglected in the NDHX design, which has been justified by our analysis. The NDHX design code gave us an average tube wall temperature of 502°C, at which the tubes will radiate energy intensively to the ambience. However, for the purpose of conservatism in our experiment, the air chimney where the NDHX will be installed will be thermally insulated. Although the tubes will emit radiation in all directions, the radiation that strikes the chimney wall will not be able to escape and will be absorbed by the wall. The chimney wall will consequently be heated up and radiate heat back to the tubes. Ultimately, a balance will be reached and the heat can only be removed mainly in terms of air convection. The only extra contribution to the heat removal will be the radiation that escapes directly from the top of the chimney. In this sense, a view factor must be taken into account when evaluating the extra heat removal by thermal radiation, which can be expressed as:

$$\dot{Q} = \varepsilon \sigma A F_{1\to 2}(T_1^4 - T_2^4), \tag{1.8.1}$$

where ε , σ , A , T_1, and T_2 are the emissivity of the tube material, the Stefan-Boltzmann constant, the tube radiating area, the tube wall temperature, and the ambience temperature, respectively. The emissivity of Inconel at 502°C is around 0.6 (from Omega). The Stefan-Boltzmann constant is 5.67E-8 kg/s^3-K^4. The ambient temperature has been assumed as 25°C. The view factor $F_{1\to 2}$ is defined as:

$$F_{1\to 2} = \frac{\cos\theta_1 \cos\theta_2}{\pi S^2} \mathrm{d}A_2, \tag{1.8.2}$$

which denotes the proportionality of the total radiation that leaves surface 1 and strikes surface 2, as shown in Fig. 1.8.2. For the high temperature test facility, a similar chimney design to that of the low temperature test facility will be employed, in which the NDHX will be located 0.75 m beneath the exit in the ceiling. In the present analysis the tubes have been collapsed onto a horizontal plane for simplicity. In addition, the circular exit through which the radiation will escape has been represented by an equivalent square with width of 0.315 m. By aforementioned simplifications, the total radiation that comes from the top layer of tubes and escapes into the ambience is around 71 W, which is merely 0.7% of the total power of the test facility. Due to the shielding effect of the top layer of tubes, the contribution to the escaping radiation from the bottom layer will be even smaller. Totally, the heat removed in terms of escaping thermal radiation will not exceed 1.4% of the total power, which justifies the fact that we have neglected the thermal radiation in the NDHX design.

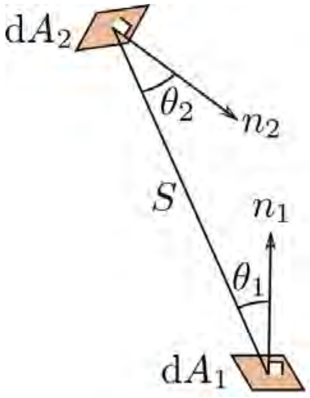

Fig.1.8.2. Schematic illustration of the view factor

Similar to the DHX design, the tubes used in the NDHX design have thicker walls than scaled due to corrosion consideration and cost concern. The deviation in the NDHX scaling is therefore examined, the results of which are shown in Table 1.8.9. Although the Stanton, time ration, and Biot numbers are not matched well, the same arguments as in the DHX design reveal that no severe issue will be caused in modeling the prototypic DRACS by using the high-temperature test facility, especially the heat transfer performance.

Table 1.8.9 Scaling results of NDHX tube side

	Prototype	Model	Ratio
Conduction depth	1.25 mm	1.25 mm	1.00
Hydraulic diameter	13.4 mm	13.4 mm	1.00
Heat transfer coefficient	321 W/m^2-K	148 W/m^2-K	0.46
St	0.97	0.34	0.35
T	108	80	0.74
Bi	0.0181	0.0076	0.42
F/A^2	27.3	3.2	0.12

Upon the completion of the DHX and NDHX design, we can close the loop scaling by matching $\sum_i L_i / A_i$ and $\sum \mathrm{F}_\mathrm{i} / A_i^2$ between the prototype and the test facility. The former summation is matched by varying the horizontal pipe length, which results in a loop width of 1 and 4 m for the primary and secondary loop, respectively. Matching the second summation calls for extra pressure loss of 303 and 622 Pa in the primary and secondary loop, respectively. The required pressure loss in the primary loop will be provided by the fluidic diode which will be investigated later on in Task 2.6. The required pressure loss in the secondary loop can be provided by a throttling valve. The loop scaling results are summarized in Tables 1.8.10 and 1.8.11.

Table 1.8.10 Primary loop scaling results

	Prototype		Model		Ratio
Pipe ID	150.0 mm		40.9 mm		0.273
ΔT	45.0°C		44.3°C		0.98
Height	2,280 mm		1,140 mm		0.5
l_0 / u_0	42.2 s		25.3 s		0.6
$\sum_i L_i / A_i$	3.82		3.93		1.03
R	87.1		87.1		1.0
Δp (Pa)	core	13.0	core	14.8	--
	Pipe	~16.0	Pipe	~19.5	--
	DHX shell side	122	DHX shell side	24.1	--
	Fluidic diode	330	Fluidic diode	**~303**	--
$\mathrm{F}_\mathrm{i} / A_i^2$	Total	175	Total	~175	~1.0

Table 1.8.11 Secondary loop scaling results

	Prototype		Model		Ratio
Pipe ID	150.0 mm		35.0 mm		0.233
ΔT	50.0°C		75.7°C		1.51
Height	2,300 mm		1,081 mm		0.47
l_0 / u_0	7.15 s		4.29 s		0.6
$\sum_i L_i / A_i$	9.4		9.4		1.0
R	116.8		116.8		1.0
Δp (Pa)	DHX tube side	28.0	DHX tube side	5.8	--
	Pipe	~26.0	Pipe	~73.2	--
	NDHX tube side	96.0	NDHX tube side	9.7	--
	Globe valve	~630	Globe valve	**~622**	--
F_i / A_i^2	Total	221	Total	~221	~1.0

As mentioned previously, the chimney design in the high-temperature test facility is quite similar to that in the low-temperature facility. For the high-temperature facility, the extended pipe outside the lab, which is required to provide enough buoyancy is around 2.06 m, close to that in the low-temperature facility. In addition, as described in the NDHX design, a thermal radiation balance between the NDHX tubes and the chimney wall will be reached when they have the same temperature, which can be as high as 502°C. Therefore, high temperature metal will need to be used for the chimney to withstand the high temperatures.

References

Hewitt, G.F., *Handbook of Heat Exchanger Design*, chapter 3.3, Begell House, Inc., Wallingford, 1992.

Ishii, M. and Kataoka, I., “Scaling Laws for Thermal-Hydraulic System under Single Phase and Two-Phase Natural Circulation,” *Nuclear Engineering and Design*, **81**, pp. 411-425, 1984.

Mohanty, A. K. and Sahoo, K. M., "Laminar Convection in Wall Sub-Channel and Transport Rates for Finite Rod-Bundle Assemblies by Superposition", *Nuclear Engineering and Design*, **92**, pp. 169-180, 1986.

Sahoo, K. M. and Mohanty, A. K., "Finite Element Analysis for Laminar Flow and Heat Transfer in Finite Rod Bundles", *Chem. Eng. Comm.*, **51**, pp. 129-140, 1987.

SS 316 emissivity by Omega, http://www.ib.cnea.gov.ar/~experim2/Cosas/omega/emisivity.htm.

2. Issues/Concerns

None

Task 2.1: Complete the construction of the low-temperature test facility (Ohio State Responsible).

1. Task Status: Completed
Refer to Task 1.7

2. Issues/Concerns
None

Task 2.2: Develop an extensive test matrix (Ohio State Responsible).

1. Task Status: Completed

2. Issues/Concerns
None

Task 2.3: Complete the design of the high-temperature fluoride salt test facility (Ohio State Responsible).

1. Task Status: Completed
Refer to Task 1.8

2. Issues/Concerns
None

Task 2.4: Construct the scaled-down high-temperature salt DRACS test facility (Ohio State Responsible).

1. Task Status: In progress

A reference design of the high temperature test facility through scaling analysis has been obtained in Task 1.8. With this reference design, we proceeded to identify the major components, including instruments available commercially that could be used in the facility. Various engineering problems were encountered mainly due to the high temperature and the corrosion issue in our application. In addition, the cost issue has affected, and will continue affecting, our final decision on the design. Figure 2.4.1 shows a preliminary 3D drawing of the high-temperature test facility under construction. Some details, e.g., the inert gas supply and vent lines are not shown, which will be added after final decision is made on everything.

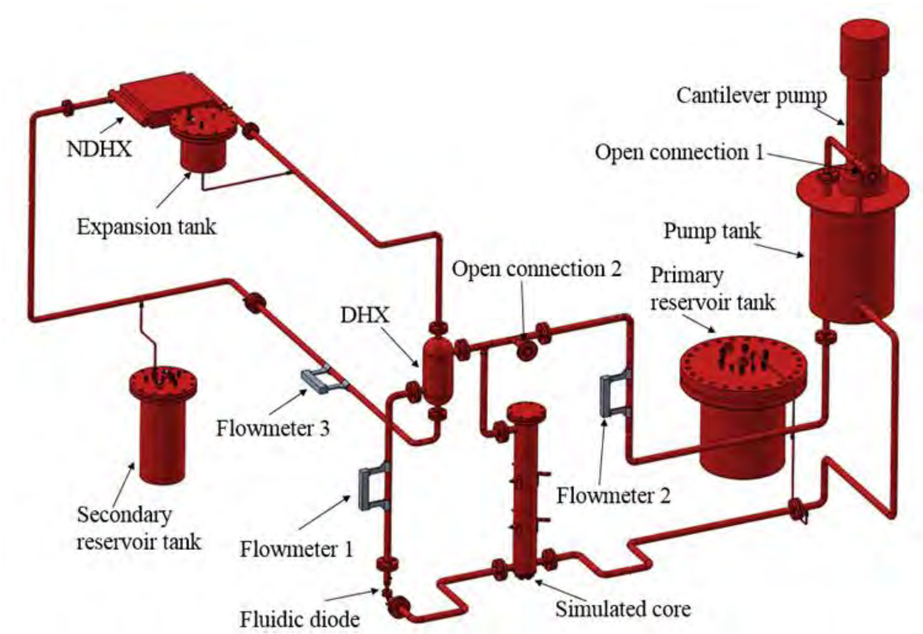
Cantilever pump
Open connection 1
NDHX
Expansion tank
Pump tank
Open connection 2
Primary reservoir tank
DHX
Flowmeter 3
Flowmeter 2
Secondary reservoir tank
Flowmeter 1
Fluidic diode
Simulated core

Fig. 2.4.1. Preliminary 3D drawing of the high temperature test facility

Core

The core is simulated by cartridge heaters in staggered array, as shown in Fig. 1.8.1. The cartridge heaters that will be used in our experiment are illustrated in Fig. 2.4.2. The heaters have a diameter of 1 inch and a heated length of 0.8 m. An unheated section of 0.1 m at the end of the heaters is designed for the use with a spacer to assure good alignment of the heaters. The spacer design is the same as the one used in the low-temperature facility except that there are seven 1-inch holes instead of three 1-inch ones. The unheated section at the end of the heater is included for the developing flow at the entrance of the core, as well as the fitting of these heaters into the bottom plate of the core. A CFD simulation of the flow development at the core entrance has been performed, with the results illustrated in Fig. 2.4.3. The velocity profile at the inlet was assumed to be parabolic. As can be seen, after the flow enters the core by 0.3 m, the velocity profile already becomes quite uniform, signifying that complete longitudinal flow has almost been reached. Therefore, unheated length of 0.4 m has been added to the end of the heater, with 0.1 m for the purpose of fitting. A type-J thermocouple is located at the joint between the unheated section 1 and the heated section for monitoring heater temperature. Each heater can provide a power of 10 kW, larger than the nominal design value of 1,430 W, so that we will be able to operate the system at higher power levels in the future if necessary. Also, with the power of each heater being 10 kW, the total power of the core can reach 70 kW, enabling us to simulate the decay power profile that is approximately 60 kW in the beginning of the DRACS transient. Heater vendors, including Watlow, have been contacted for a quote.

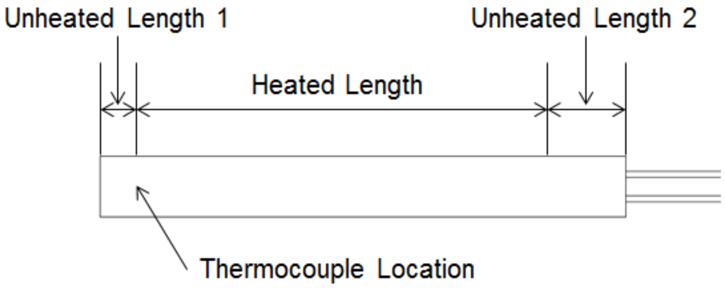
Unheated Length 1
Unheated Length 2
Heated Length
Thermocouple Location

Fig. 2.4.2. Schematic drawing of the heaters used in our experiment

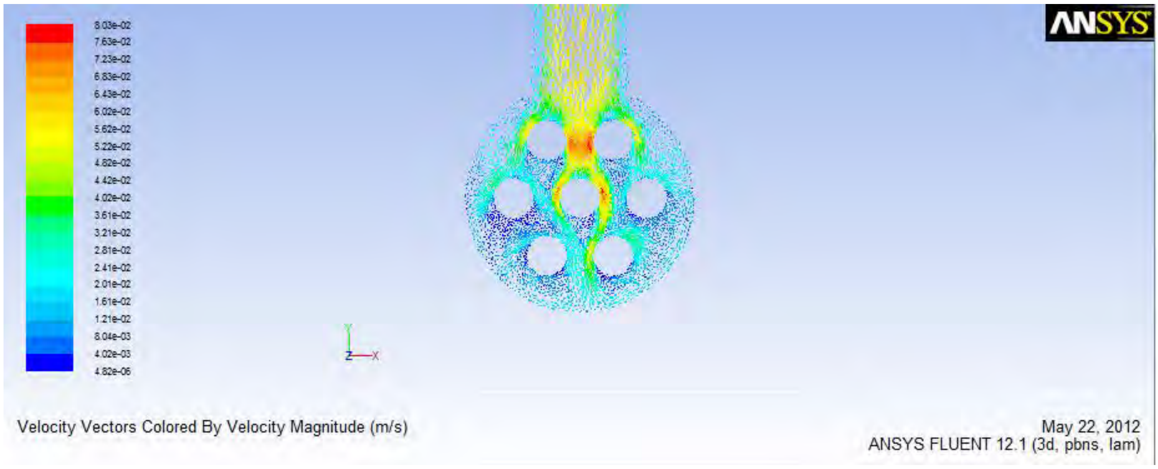

(a)

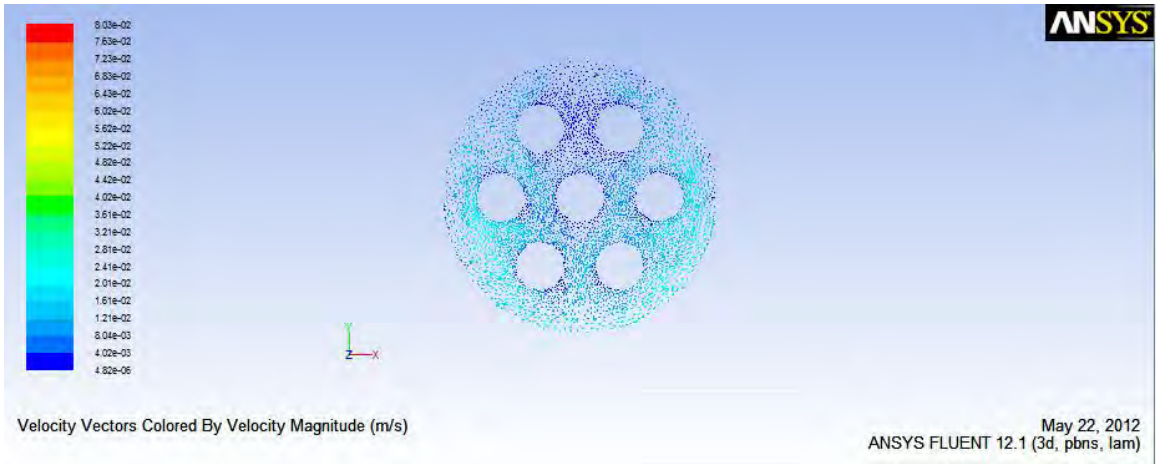

(b)

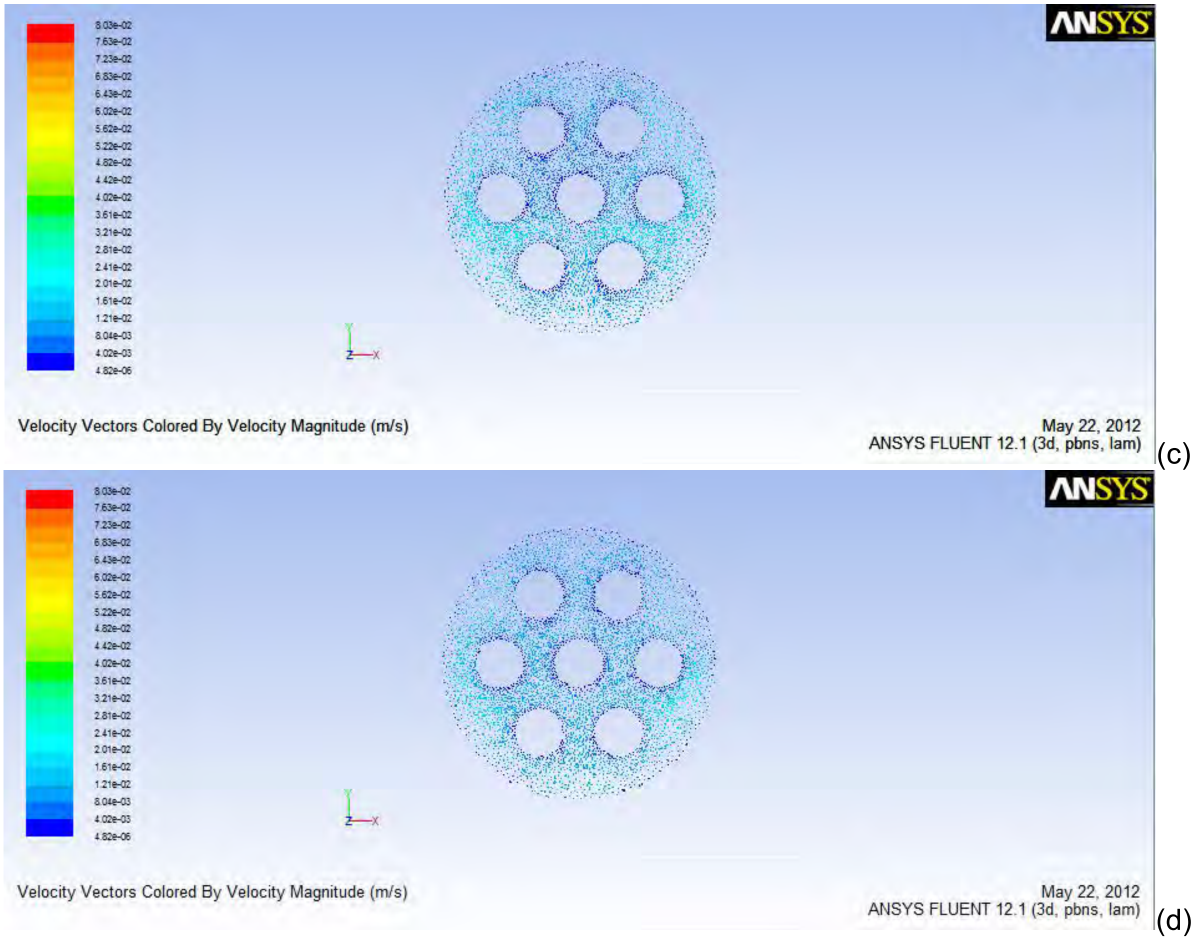

Fig. 2.4.3. Velocity profile on planes at (a) Z = 0; (b) Z = 0.1 m; (c) Z = 0.2 m; (d) Z = 0.3 m

The core is composed of 7 such heaters fitted into a 6-inch schedule 80 standard pipe which has the closest inner diameter to the design value. The heaters will be fitted into the core using Swagelok compression fitting, the working principle of which is illustrated in Fig. 2.4.4. The male connector will be welded onto the bottom plate of the core directly with the heaters tightened by screwing the hexagonal nut.

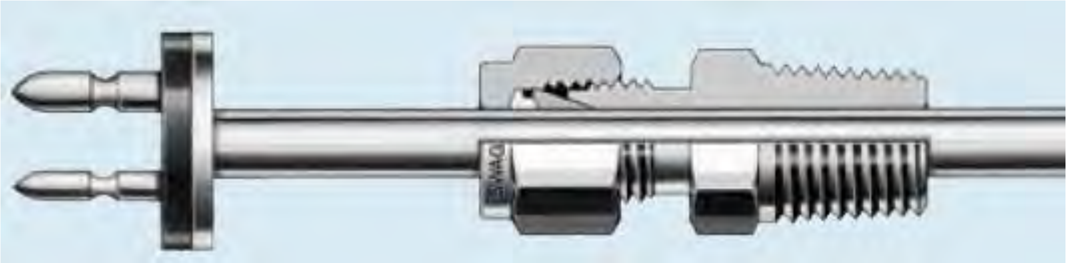

Fig. 2.4.4. Swagelok compression fitting for the fitting of the heaters

In the present design, the heater diameter has been determined to be 1 inch mainly due to the concern of heater fitting. With 1 inch heater and the Swagelok fitting, the spacing between adjacent heaters is shown in Fig. 2.4.5. As clearly seen, the minimum spacing between two hexagonal nuts can be as small as 5.95 mm, which is barely enough for the fitting tools to get in. Although reducing the heater diameter is beneficial to the scaling, the difficulty of fitting the heaters forces us to use larger heaters.

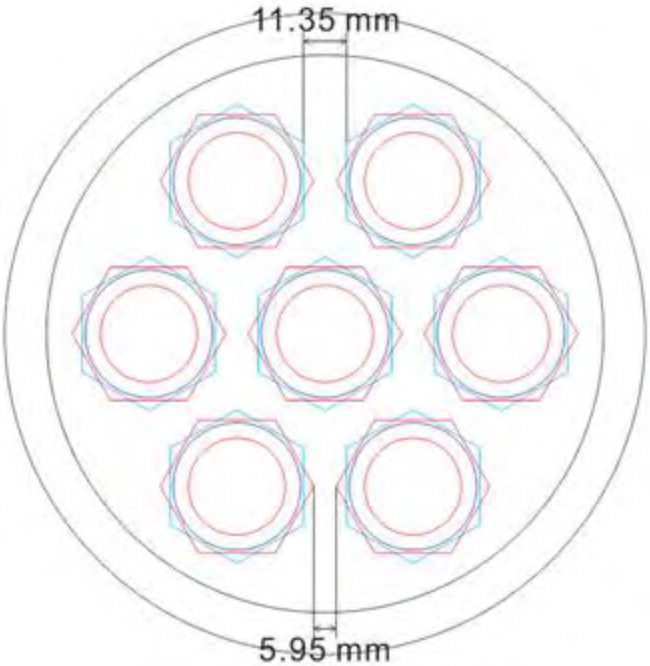

Fig. 2.4.5. Spacing between the Swagelok compression fittings

DHX and NDHX

For the DHX, we contacted a few vendors for some special alloys as the material, including Nickel 200/201 and Inconel 600. It seems the price of the heat exchangers in such special alloys is prohibitively high, because of which we decided to use SS 316 as the construction material. There exists the potential problem of plugging with SS 316 tubes, which was observed in ORNL test loops (Brian and et al., 1952). However, as the tubes used in our design are not very small, this problem will probably not happen. The DHX was manufactured by a local vendor called Gaspar, and was ASME stamped to 750°C at 30 psi. For the NDHX, SS 316 has been selected as the material due to the same concern. Exact Exchanger Inc., who provided the finned tube NDHX for our low-temperature test facility has been contacted to provide high-temperature NDHX. This NDHX is certified to 704°C at 60 psi. In the initial design of the NDHX, 5/8" BWG 18 SS 316 tubes were used. However, at the time when we placed the purchased order to the vendor, we were informed that to meet the design requirements SS 316H has to be used. The vendor could only find 1/2" BWG 16 tubes made from SS 316H. We therefore modified the NDHX design slightly, which is summarized in Table 2.4.1.

Table 2.4.1 Modified design of the NDHX

Material	SS 316
Tube OD (D_t)	12.7 mm
Tube thickness	1.65 mm
Tube number	36 (2 rows)
Pitch to diameter ratio (Triangular pattern)	1.9
Tube length	434 mm
Width	434 mm

Fluidic Diode

The conventional vortex diode as shown in Fig. 2.4.6 will be adopted in the high-temperature facility. The fluidic diode adopted should exhibit desired pressure drops at prescribed flow rates for both the forward and reverse directions. Therefore, prior to the design of the fluidic diode, the design parameters, i.e., the desired pressure drops and flow rates should be determined. For the forward flow direction, the desired pressure drop and mass flow rate of the salt can be obtained from the scaling analysis of the DRACS during its normal operation. The scaled nominal working conditions for the DRACS high-temperature test facility can be found from Table 1.8.4. The pressure drops over the various components in the primary loop at the DRACS nominal state are summarized in Table 2.4.2. Based on the scaling results, this vortex diode is supposed to cause a pressure loss of around 303 Pa at the salt flow rate of 0.12 kg/s.

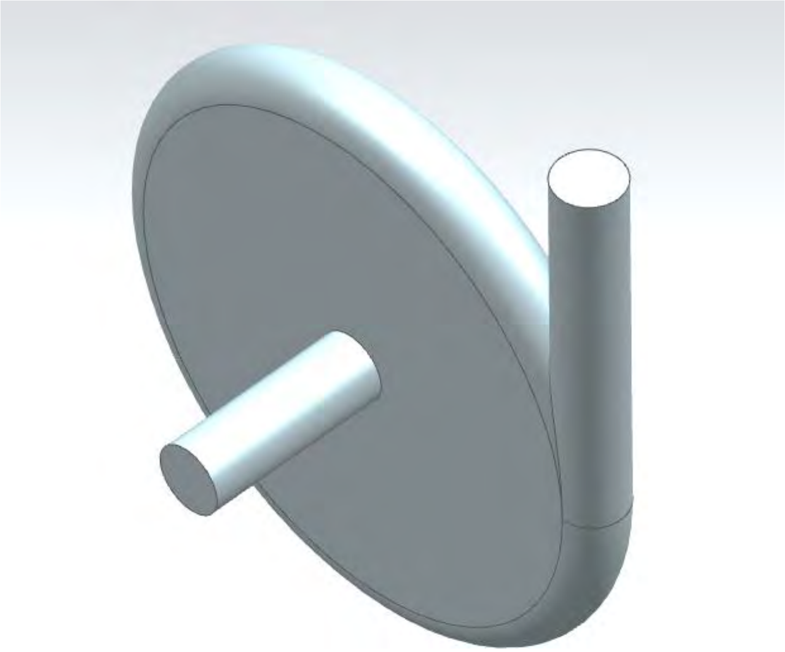

Fig. 2.4.6. The vortex fluidic diode design

Table 2.4.2 Nominal working conditions of the DRACS high-temperature test facility

	Pressure Drop (Pa)
Core	14.8
DHX shell side	24.1
Pipe	10.3
Form loss	9.2
Fluidic diode	~ 303

For the reverse flow direction of the diode, the desired pressure drop and salt flow rate are related to the determination of the initial conditions for the DRACS transient, i.e., the nominal conditions of core normal operation. To correctly simulate the initial conditions of the DRACS transient in experiment, a simplified scaling analysis has been performed for core normal operation, which is similar to the scaling analysis for DRACS normal operation. At the steady state during core normal operation, the main flow through the core and the parasitic flow through the fluidic diode are in parallel, as illustrated in Fig. 2.4.7. Here, $\dot{m}_c$, $\dot{m}_D$, and $\dot{m}$

denote the mass flow rates of the main flow through the core, the bypass flow through the DRACS, and the total flow during core normal operation, respectively. The total power provided by the core is $\dot{Q}_c$, while the heat loss to DRACS due to the parasitic flow is $\dot{Q}_D$. Most of the flow that enters the core (lower plenum) at temperature of T_i will go through the core, being heated up to T_{oc}. A small fraction of the total flow is diverted to the DHX, transferring heat to the DRACS secondary salt to prevent it from freezing. The hot salt from the core and the cold salt from the DHX (T_{oD}) are well mixed in the core upper plenum, resulting in a salt temperature of T_o.

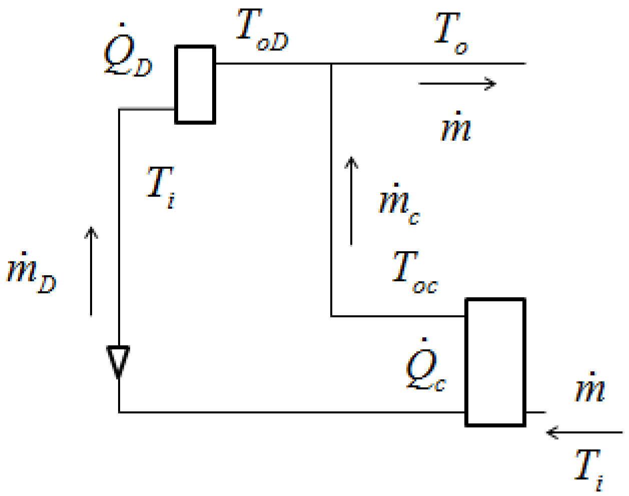

Fig. 2.4.7. Operating conditions during core normal operation

At steady state, the simplified conservation equations for the two parallel loops shown in Fig. 2.4.7 can be expressed as:

Mass conversation:

$$\dot{m}_D + \dot{m}_c = \dot{m}, \tag{2.4.1}$$

Energy balance:

$$c_p \dot{m}_c (T_{oc} - T_i) = \dot{Q}_c, \tag{2.4.2}$$

$$c_p \dot{m}_D (T_i - T_{oD}) = \dot{Q}_D, \tag{2.4.3}$$

$$c_p \dot{m} (T_o - T_i) = \dot{Q}, \tag{2.4.4}$$

$$\dot{m}_c T_{oc} + \dot{m}_D T_{oD} = \dot{m} T_o, \tag{2.4.5}$$

Integral momentum:

$$\beta g \rho (T_{oc} - T_i)\left(\frac{l_c}{2} + \frac{l_D}{2} + l\right) + \beta g \rho (T_{oc} - T_{oD})\frac{l_D}{2} + \sum_i \frac{\dot{m}_D^2}{2\rho a_i^2}\left(f_i \frac{l_i}{d_i} + K_i\right) = \sum_i \frac{\dot{m}_c^2}{2\rho a_i^2}\left(f_i \frac{l_i}{d_i} + K_i\right), \tag{2.4.6}$$

where c_p, β, ρ, and g are the specific heat, thermal expansion coefficient and density of the primary salt, and the gravitational acceleration, respectively. l_c, l_D, and l denote the height of the core, height of the DHX, and the vertical distance between DHX inlet and core outlet, respectively. It should be noted that the thermal centers of the DHX and the core have been assumed to be located at their geometric centers. a_i, l_i, d_i, f_i, and K_i are the flow area, length, hydraulic diameter, friction factor, and form loss coefficient for a specific component in the two parallel loops shown in Fig. 2.4.7. The heat removed through the intermediate heat exchanger that is shown here is assumed to be $\dot{Q}$.

Table 2.4.3 Reference values and dimensionless parameters

	Reference values	Dimensionless parameters
Mass flow rate	$\dot{m}_0$: nominal mass flow rate through the core during core normal operation	$\dot{M}_k = \dot{m}_k / \dot{m}_0$ $k = c, D, or\ none$
Length	l_0 : vertical distance between thermal centers of DHX and core	$L_i = l_i / l_0$
Area	a_0 : cross-sectional area of the primary piping	$A_i = a_i / a_0$
Temperature	ΔT_0 : nominal temperature increase over the core during core normal operation	$\theta_k = (T_k - T_0) / \Delta T_0$ $k = oc, oD, o, and\ i$

As before, the conservation equations are non-dimensionalized by introducing appropriate dimensionless parameters, which are summarized in Table 2.4.3, along with the reference numbers. The conservation equations are non-dimensionalized as:

$$\dot{M}_D + \dot{M}_c = \dot{M}, \tag{2.4.7}$$

$$\dot{M}_c(\theta_{oc} - \theta_i) = \frac{\dot{Q}_c}{c_p \dot{m}_0 \Delta T_0}, \tag{2.4.8}$$

$$\dot{M}_D(\theta_i - \theta_{oD}) = \frac{\dot{Q}_D}{c_p \dot{m}_0 \Delta T_0}, \tag{2.4.9}$$

$$\dot{M}(\theta_o - \theta_i) = \frac{\dot{Q}}{c_p \dot{m}_0 \Delta T_0}, \tag{2.4.10}$$

$$\dot{M}_c \theta_{oc} + \dot{M}_D \theta_{oD} = \dot{M}\theta_o, \tag{2.4.11}$$

$$\begin{aligned}(\theta_{oc} - \theta_i)\frac{\beta g \rho^2 \Delta T_0 l_0 a_0^2}{\dot{m}_0^2} + (\theta_{oc} - \theta_{oD})\frac{L_D}{2}\frac{\beta g \rho^2 \Delta T_0 l_0 a_0^2}{\dot{m}_0^2} + \frac{\dot{M}_D^2}{2}\sum_i \frac{1}{A_i^2}(f\frac{l}{d} + K)_i \\ = \frac{\dot{M}_c^2}{2}\sum_i \frac{1}{A_i^2}(f\frac{l}{d} + K)_i.\end{aligned} \tag{2.4.12}$$

Based on above non-dimensional conservation equations, the similarity criteria for core steady-state normal operation are proposed as:

$$\left(\frac{\dot{Q}_c}{c_p \dot{m}_0 \Delta T_0}\right)_R = 1, \tag{2.4.13}$$

$$\left(\frac{\dot{Q}_D}{c_p \dot{m}_0 \Delta T_0}\right)_R = 1, \tag{2.4.14}$$

$$\left(\frac{\dot{Q}}{c_p \dot{m}_0 \Delta T_0}\right)_R = 1, \tag{2.4.15}$$

$$L_{D\;R} = 1, \tag{2.4.16}$$

$$\left(\frac{\beta g \rho^2 \Delta T_0 l_0 a_0^2}{\dot{m}_0^2}\right)_R = 1, \tag{2.4.17}$$

$$\left(\sum_i \frac{1}{A_i^2}\left(f\frac{l}{d} + K\right)_i\right)_R = 1. \tag{2.4.18}$$

Here, the subscript *R* denotes the ratio between the model and the prototype. Equations (2.4.13), (2.4.16), and (2.4.17) can be used together to scale the main flow through the core during core normal operation. One thing worth of mentioning is that the scaling for DRACS normal operation performed previously results in a value of 0.54 for $L_{D\;R}$. Because of this, Eq. (2.4.17) was violated intentionally and a value of 1.3 was selected for the ratio on the left hand side to relieve the distortion in the second term (buoyancy term) in Eq. (2.4.12). In the DRACS prototypic design, its capability was assumed as 1% of the core nominal power, which was also adopted for the high-temperature test facility, leading to a core nominal power of 1 MWth. The scaling results for the core flow during core normal operation are summarized in Table 2.4.4.

Table 2.4.4 Scaling results for the core flow during core normal operation

	Model	Prototype	Ratio
$\dot{Q}_c$	1 MW	20 MW	5%
ΔT_0	100°C	104°C	0.96
$\dot{m}_0$	5.30 kg/s	79.66 kg/s	0.0665

The bypass flow through the DRACS during core normal operation can be scaled using Eqs. (2.4.13) and (2.4.14), which can be expressed in a more straightforward way:

$$\left(\dot{m}_D \Delta T_D\right)_R = \left(\dot{m}_0 \Delta T_0\right)_R, \tag{2.4.19}$$

$$\left(\frac{\dot{Q}_D}{\dot{Q}_c}\right)_M = \left(\frac{\dot{Q}_D}{\dot{Q}_c}\right)_P, \tag{2.4.20}$$

where ΔT_D is the temperature decrease on the DHX shell side during core normal operation. Equation (2.4.20) implies that heat loss to the DRACS during core normal operation in the experiment should account for the same proportion of the total core power as in the prototypic. Equation (2.4.18) only imposes constraint on the product of the mass flow rate ratio and the temperature decrease ratio for the bypass flow, leaving some flexibility in determining the bypass flow. In our high-temperature test facility, a preliminary value of 0.1203 kg/s has been selected for the mass flow rate of the bypass flow (the flow in the vortex diode reverse direction), which is same as the primary salt flow rate during DRACS normal operation (the flow in the diode forward direction). There is some reasoning behind selecting the bypass flow rate as such. In our DRACS prototypic design, the flow in the vortex diode forward direction accounts for around 2.3% of the core flow during core normal operation. Although we did not perform a detailed calculation of the bypass flow through the DRACS (vortex diode reverse direction) during core normal operation for our DRACS prototypic design, it should usually not exceed 2.5% of the main core flow (Yoder, 2011). Therefore, as a rough estimation, the flow in the reverse direction of the vortex diode should be close to that in the forward direction. In a nutshell, for the vortex diode in the high-temperature test facility, the flow rates in both the forward and reverse directions have been determined as 0.1203 kg/s. It should be noted that, later on, if the reverse mass flow rate of 0.1203 kg/s leads to difficulty in designing the vortex diode, the reverse flow rate should be varied since we have some flexibility in it according to the previous scaling analysis.

After determining the desired flow rate in the reverse direction of the vortex diode, we still need to determine the desired pressure drop over it, which will be related to pressure drop over the core. The strategy used to calculate the desired pressure drop over the vortex dido in its reverse direction is illustrated in Fig. 2.4.8. Since, the main flow through the core is in parallel with the bypass flow through the vortex diode, the pressure drops caused in the two parallel loops should be the same between points A and B. We first calculated the pressure drop between points A and B from the core loop, which was then used to determine the desired pressure drop over the vortex diode in reverse direction. In the core loop, most of the pressure drop is due to the core, the accuracy of the pressure drop in which is quite important. Also, the flow in the core is complicated, which will undergo cross flow, longitudinal flow, as well as the transition in between. We therefore decided to perform a CFD analysis for the pressure drop in the core.

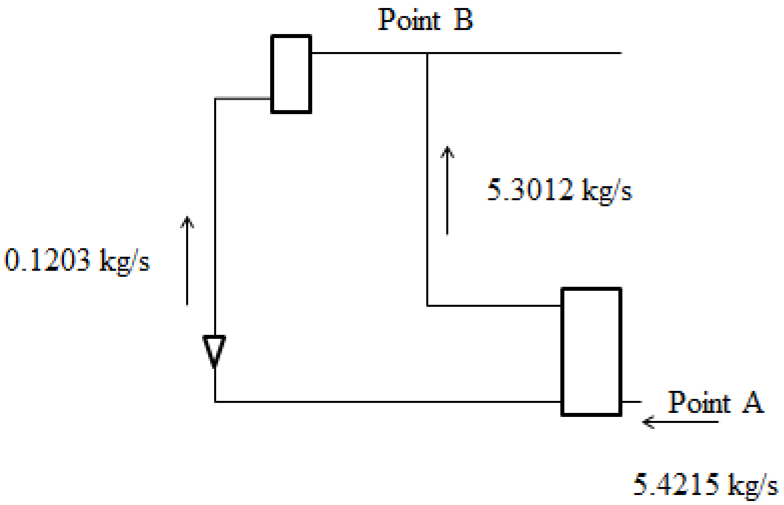

Fig. 2.4.8. Calculation of the desired pressure drop in the vortex diode reverse direction

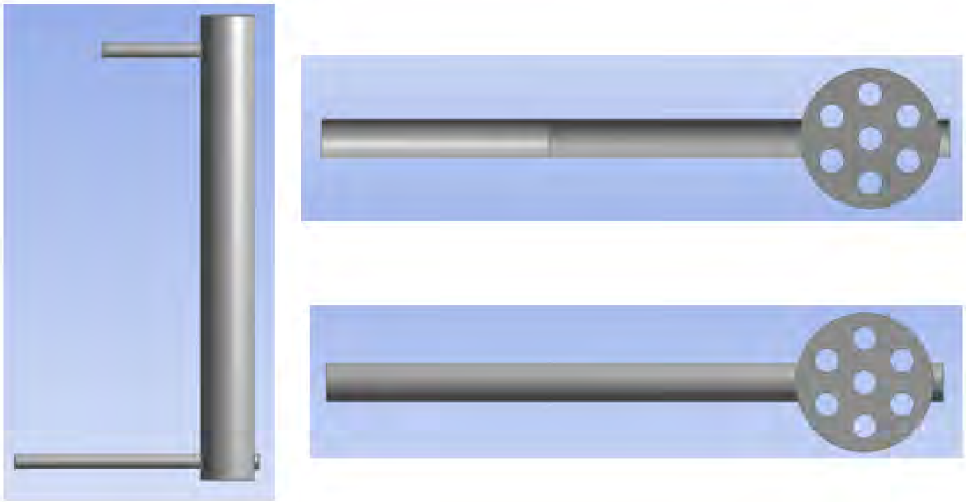

Fig. 2.4.9. Geometry of the core model used in CFD calculation

The geometry of the core model is illustrated in Fig. 2.4.9. The solid-looking part is actually the fluid region, while the seven hollow-looking cylinders denote the seven heaters. A short inlet pipe of 1 cm is attached to the core on the right side, and two outlet pipes are on the left side, one of 26.3 cm and the other of 50 cm. The top outlet is the core outlet, while the bottom one is connected to the DRACS bypass loop. Turbulent flow is expected inside the core, and the standard k-ε model has been used. Turbulence at the inlet is specified in terms of the turbulence intensity and hydraulic diameter. The turbulence intensity can be calculated as:

$$I = 0.16(\mathrm{Re})^{-1/8}. \tag{2.4.21}$$

The Reynolds number at the inlet is found to be 41,255, resulting in turbulence intensity of 4.24%. The inlet pipe inner diameter of 4.09 cm is used as the hydraulic diameter. Boundary condition of constant mass flow rate is specified for the inlet, and boundary condition of outflow is specified for the two outlets. The calculated pressures at the inlet and outlets are listed in Table 2.4.5. It should be noted that the gravitational pressure drop is not included in the CFD calculation. As can be seen, from the inlet to the bottom outlet, pressure increases which is mainly because of the abrupt velocity decrease when the salt exits the core into the bottom outlet pipe.

Table 2.4.5 Pressures at the inlet and outlets of the core

	Inlet	Top outlet	Bottom outlet
Pressure (Pa)	-141	-7,440	1,239

The other pressure drops in the core loop are the friction in the pipe and the form loss at the elbow, which are found to be 2,195 and 2,520 Pa, respectively. Thus, the total pressure drop between points A and B calculated from the core loop is 12,015 Pa. The pressure drops in the DRACS bypass loop are subsequently calculated, which are mainly the pressure drop on DHX shell side, friction in the pipe, form loss. The results are summarized in Table 2.4.6. Because pressure increases from the core inlet to bottom outlet, the corresponding pressure drop is denoted as negative. As noted, the gravity difference of the salt between the two loops has also been accounted for. The desired pressure drop over the fluidic diode in reverse direction is therefore found to be 12,463 Pa.

Table 2.4.6 Pressure drop between points A and B

Pressure drop between points A and B: 12,015 Pa	DRACS bypass loop	Core inlet to bottom outlet (Pa)	-1,380	Gravity difference between the two loops (buoyancy): 881 Pa
		DHX shell side (Pa)	30	
		Pipe (Pa)	16	
		Form loss (Pa)	5	
		Fluidic diode (Pa)	12,463	
	Core loop	Core inlet to top outlet (Pa)	7,299	
		Pipe (Pa)	2,195	
		Form loss (Pa)	2,195	

After determining the design parameters of the vortex diode, i.e., the desired flow rates and pressure drops for both directions, we proceed by performing a parametric CFD study of multiple vortex diodes in different size and geometry. Many researchers have studied the pressure drop characteristics in the vortex diodes with water (Zobel, 1936; Kulkarni et al., 2008 and 2009). It is found that the performance of vortex diode is dependent on the diode geometry, diode size, nozzle configuration, and Reynolds number. Usually, vortex diodes with inlet and outlet nozzles being of the same size as the chamber height exhibit higher diodicity which is defined as the ratio of reverse pressure drop to forward pressure drop at the same flow rate. Therefore, all the vortex diodes we are studying fulfill the aforementioned condition. In addition, studies with water have also shown that higher diodicity can be achieved at aspect ratio of 6 which is the ratio of chamber diameter to chamber height. In our studies, we have covered a range of 4 to 10 for the aspect ratio. Figure 2.4.10 illustrates the geometry of the vortex diodes that are under investigation. As can be seen, the both the axial and tangential nozzles consist of three sections, which are a small pipe section, a large pipe section and a pipe reducer in between. The large pipe section is the same as the DRACS primary pipe in size, i.e., ASME 1.5" pipe. Four different sizes have been considered for the small pipe section, namely, ASME 1.25", 1", 0.75" and 0.5", as standard pipes reducers can only reduce 1.5" to these sizes. Therefore, there are totally 16 vortex diodes being studied.

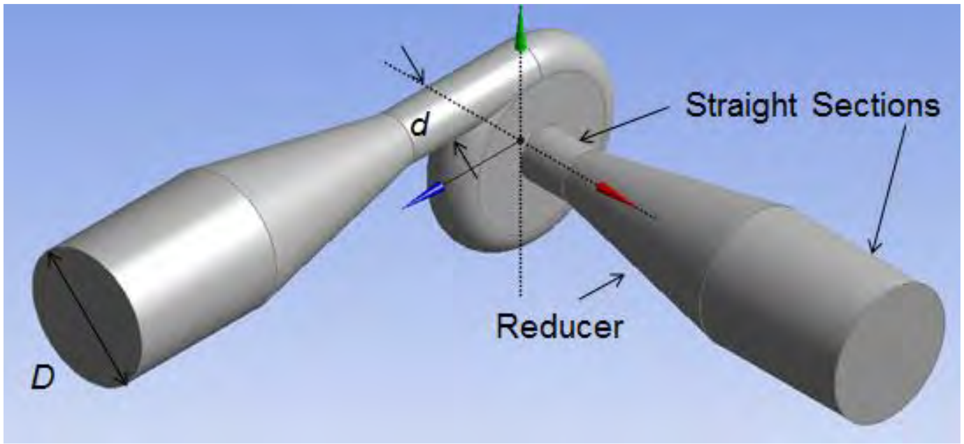

Fig. 2.4.10. Geometry of the studied vortex diodes

As discussed previously, the desired flow rate in the forward flow direction is 0.12 kg/s, while the desired flow rate in the reverse flow direction is in the vicinity of that. Four different inlet flow rates for both the forward and reverse directions have been examined, namely, 0.6, 0.12, 0.18, and 0.24 kg/s, corresponding to the port Reynolds number in the range of 711 to 4,789. Table 2.4.7 summarizes the cases that have been investigated, i.e., the design matrix.

Table 2.4.7. Design matrix of the vortex diodes

Chamber Height (inch)	Aspect Ratio	Port Size (inch)	Inlet Flow Rate (kg/s)
0.5	4, 6, 8, 10	0.5	0.6, 0.12, 0.18, 0.24
0.75		0.75	
1		1	
1.25		1.25	

FLUENT (ANSYS) by ANSYS has been used for CFD calculations. Each vortex diode model was meshed using the incorporated ICEM mesher. Tetrahedral and triangular cells were used for the volume and surface, respectively. Although mesh sensitivity study was not performed for all the diode designs, for the smallest diode it was found that total mesh number of above 1 million yielded grid-independent results. In addition, studies by Kulkarni et al. (2008) show that for a vortex diode with similar size to the smallest one in Table 5, 3×10^5 cells are enough to generate grid-independent results. Therefore, around 10^6 cells were used for the smallest diode, and for larger diodes the number of cells was increased according to their total volume.

As stated earlier, the Reynolds number based on the smaller pipe size of the nozzle is in the range of 711 to 4,789, in the laminar and laminar-to-turbulent transition regimes. However, if the Reynolds number is defined based on the large pipe size of the nozzle, only laminar regime will be encountered. In addition, after the fluid enters the diode chamber, the stretching of the fluid is likely to lead to relaminarization of the flow (Kulkarni et al., 2008; Ragab et al., 1995; Narasimha et al., 1979). CFD and experimental studies by Kulkarni et al. (2008, 2009) have also shown that the laminar flow model predicts results with better agreement with experiments than the k-ε model even for higher flow Reynolds number. In view of all these findings, we have selected the laminar model for all the calculations presented in this paper.

Since four different inlet mass flow rates have been studied, the boundary condition at the inlet has been specified as constant mass flow rate. For the outlet, boundary condition of pressure outlet has been used, which assumes zero gauge pressure at the outlet. In addition, pressure-based solver has been selected for all the calculations.

Typical flow patterns in the diode under the forward flow condition are illustrated in Figs. 2.4.10 and 2.4.11. Figure 2.4.10 shows the flow streamlines in the diode, while Fig 2.4.11 shows the vector plot of the fluid velocity on a cut plane that is through the centerline of the axial nozzle and perpendicular to the centerline of the tangential nozzle. In the forward flow direction, the fluid enters the diode through the axial nozzle. After entering the diode chamber, the fluid first impinges onto the back wall of the chamber and then distributes radially over the chamber. When the fluid reaches the periphery of the chamber, swirls are generated, as can be clearly seen in Fig 2.4.11. These small swirls then proceed toward the tangential nozzle along the periphery of the chamber, forming a spiral trajectory as shown in Fig 2.4.10.

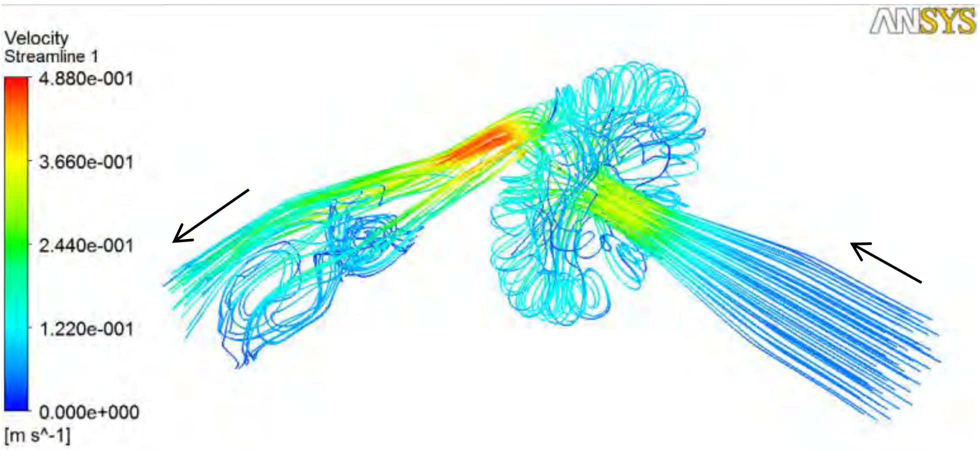

Fig. 2.4.10. Typical flow streamlines in the forward flow direction (port size of 0.5”, aspect ratio of 6, and inlet mass flow rate of 0.12 kg/s)

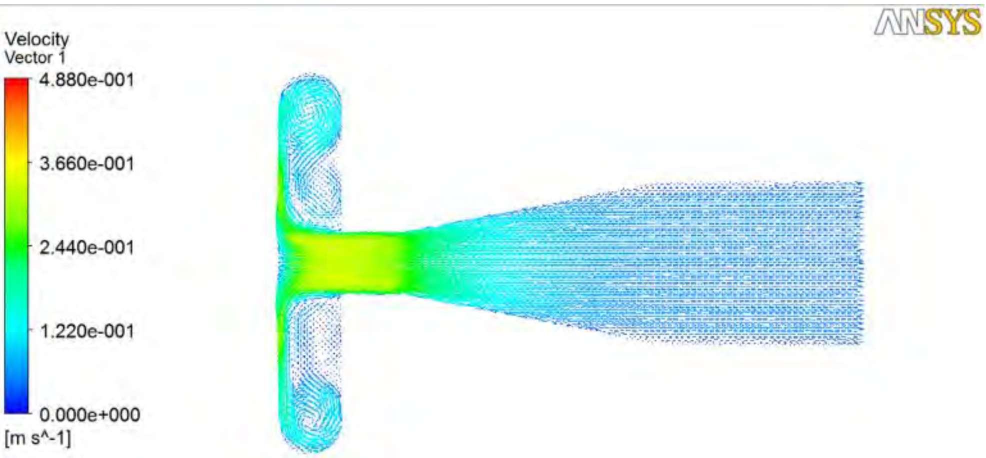

Fig. 2.4.11. Vector plot of the fluid velocity on the cut plane through the centerline of the axial nozzle (port size of 0.5", aspect ratio of 6, and inlet mass flow rate of 0.12 kg/s)

In the reverse flow direction, the flow patterns inside the diode are illustrated in Figs. 2.4.12 and 2.4.13. In this case, the fluid enters the diode through the tangential nozzle. Strong swirl flows are formed in the chamber, which can be clearly seen from the flow streamlines in Fig. 2.4.12 or the fluid velocity plot on the chamber middle plane in Fig. 2.4.13. The swirl flows are the main origin of the high flow resistance in the reverse flow direction. It can also been seen from Fig. 2.4.12 that after exiting the diode chamber, there is still a swirling component for the flow through the nozzle. This swirling component will dissipate gradually as the fluid flows along the nozzle.

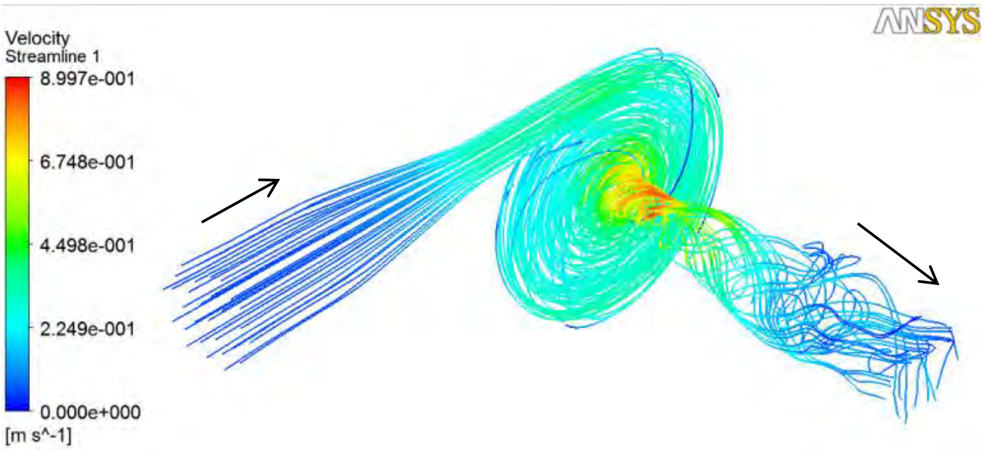

Fig. 2.4.12. Typical flow streamlines in the reverse flow direction (port size of 0.5", aspect ratio of 6, and inlet mass flow rate of 0.12 kg/s)

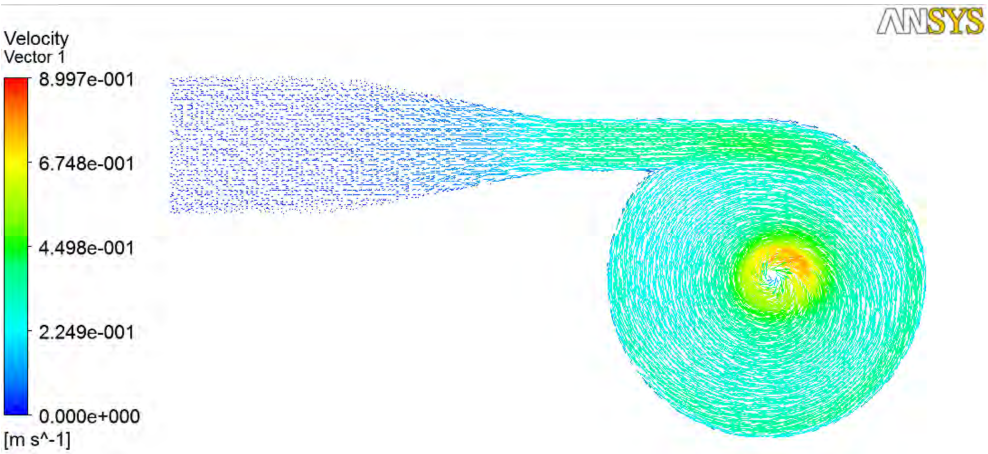

Fig 2.4.13. Vector plot of the fluid velocity on the chamber middle plane (port size of 0.5”, aspect ratio of 6, and inlet mass flow rate of 0.12 kg/s)

The performance of a vortex diode can be characterized by the forward and reverse Euler numbers and the diodicity that are defined as:

$$\mathrm{Eu}_f = \frac{\Delta p_f}{0.5 \rho v^2} \tag{2.4.22}$$

$$\mathrm{Eu}_r = \frac{\Delta p_r}{0.5 \rho v^2} \tag{2.4.23}$$

$$\mathrm{D} = \left(\frac{\Delta p_r}{\Delta p_f} \right)_{\textit{same flow rate}} \tag{2.4.24}$$

where Δp_f and Δp_r are the pressure drops in the forward and reverse flow directions, respectively; ρ is the density of the fluid; and v is the fluid mean velocity at the inlet port (small pipe section of the nozzle).

The effect of the Reynolds number on the Euler numbers and diodicity are shown in Figs. 2.4.14-2.4.16, which are for the diodes with a 0.5”-diameter port. It should be noted that the Reynolds number has also been defined based on the fluid mean velocity in the port. As can be seen, the Euler number in the forward direction decreases with increased Reynolds number, while the Euler number in the reverse direction exhibits the opposite trend, leading to an increased diodicity with increased Reynolds number. As discussed in the previous section, flow in the forward direction will distribute radially inside the chamber. The major mechanism of the forward pressure drop is the friction exerted by the chamber wall and periphery. Although the boundary layer at the chamber wall and periphery and thus the specific dependence of the friction factor on Reynolds number is not clear, the friction factor should have a decrease trend with the increase of the Reynolds number.

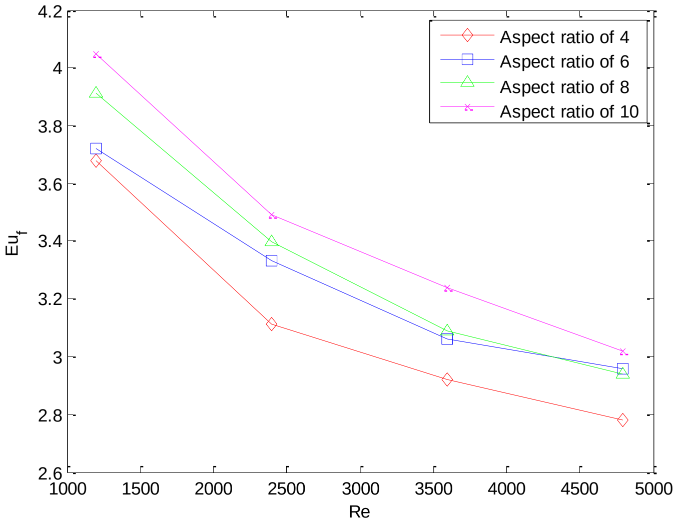

Fig. 2.4.14. Effect of Re on Eu_f (0.5” port)

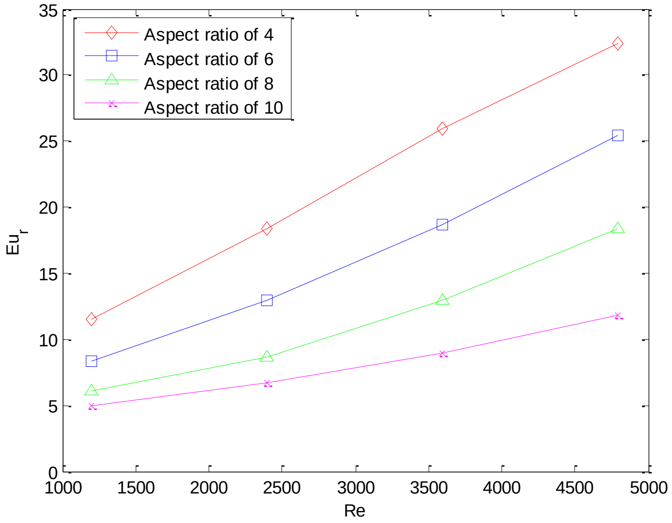

Fig. 2.4.15. Effect of Re on Eu_r (0.5” port)

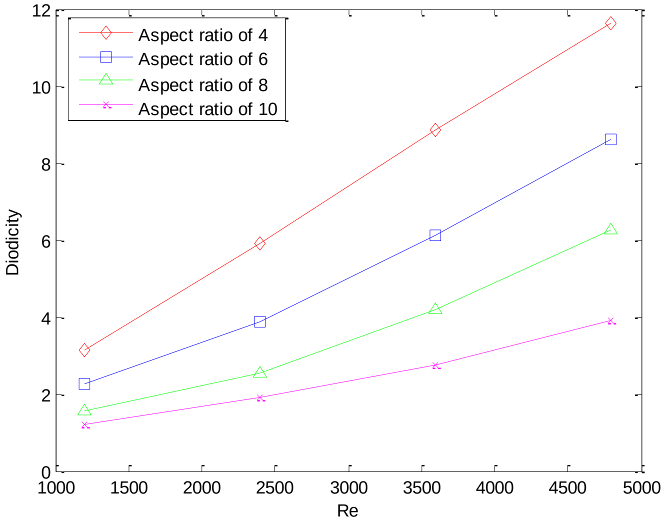

Fig. 2.4.16. Effect of Re on diodicity (0.5” port)

For the reverse flow, the vortex formed inside the diode chamber can be divided into two regions, namely, the free vortex region and the forced vortex region. The free vortex region extends from the chamber periphery to a critical radius, and the forced vortex region extends from the critical radius to the center of the chamber (Stairmand, 1990; Kulkarni, 2008). In the free vortex region, the angular momentum of the flow is conserved for negligible friction by the chamber wall. Therefore, flow velocity (mainly the tangential velocity) increases with decreased radius in the free vortex region. The kinetic energy of the flow in the free vortex region increases correspondingly, causing the main pressure drop in the reverse flow direction. In the forced vortex region, the fluid tangential velocity decreases gradually to zero at the chamber center. The tangential component of the flow velocity in the forced vortex region is partially converted to the axial velocity component when the flow exits the diode chamber, leading to partial pressure recovery. The pressure drop in the reverse flow direction is mainly determined by the pressure drop in the free vortex region. As will be discussed later, the free vortex region has a positive dependence on the Reynolds number, which explains the increase trend of the reverse Euler number with the increase of the Reynolds number. For all other diodes with different port sizes, similar trends have been observed for the Euler numbers and diodicity.

The influence of the chamber aspect ratio on the diode performance can also be seen from Figs 2.4.11-2.4.16. The Euler number in the forward flow direction exhibits positive dependence on the aspect ratio, while the Euler number in the reverse flow direction and the diodicity have negative dependence on the aspect ratio, i.e., decrease with the increase of the aspect ratio. The observed opposite trends for the forward and reverse flows are again related to the different pressure drop mechanisms in the two flow directions. With larger aspect ratio, the length over which the forward flow will experience friction is longer, leading to higher Euler numbers. For the reverse flow direction, as will be seen later, the free vortex region decreases as the chamber aspect ratio increases, resulting in lower Euler numbers.

The effect of the port size on the diode performance has also been examined, which is found not significant. To demonstrate this, the Euler numbers and diodicity at a fixed chamber aspect ratio of 4 and a fixed Reynolds number of 1,500 are plotted against the ratio of the port diameter (small pipe section of the nozzle) to that of the main pipe (large pipe section of the nozzle), as shown in Fig. 2.4.17. The Reynolds number that is defined based on the port size may have accounted for some effect of it. The week dependence of the diode performance on the port size seen from Fig. 2.4.17 is mainly due to the contributions of the two nozzles to the total pressure drops, which will be seen in the subsequent discussion.

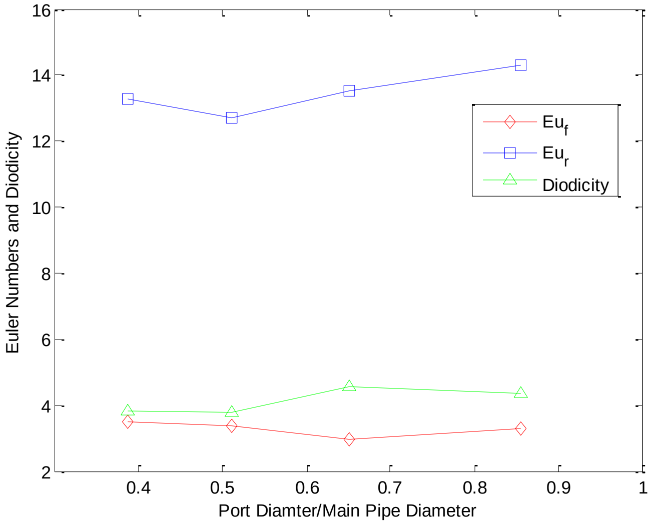

Fig. 2.4.17. Effect of port size on diode performance at aspect ratio of 4 and Re of 1,500

The calculated Euler numbers in both the forward and reverse flow directions have been correlated with the Reynolds number at the port, the chamber aspect ratio (denoted as α), and the ratio of the port diameter to the main pipe diameter (denoted as d^*). WOLFRAM MATHEMATICA (WOLFRAM) which has the built-in function for multiple nonlinear regressions has been used to correlate the CFD results. Correlations that mathematically fit well with the calculated forward and reverse Euler numbers are obtained as following:

$$\mathrm{Eu}_f = \left[(41.42 - 117.37d^* + 95.46d^{*2}) + \frac{9.7\alpha}{\mathrm{Re}^{0.53}}\right] \times \mathrm{Re}^{-0.57+1.58d^*-1.3d^{*2}} \tag{2.4.25}$$

$$\mathrm{Eu}_r = \left(\frac{0.055}{\alpha} - \frac{0.099}{\alpha^2}\right)^2 \mathrm{Re}^{1.53} + \left(\frac{80.9}{\alpha} - \frac{128.6}{\alpha^2}\right) + (24.8 - 142.9d^* + 230.3d^{*2} - 117.5d^{*3}) \tag{2.4.26}$$

The maximum deviations with the CFD results for the above two correlations are 6% and 20%, respectively.

In the forward flow direction, as discussed previously, the main pressure drop is due to the friction in the diode chamber, which is accounted for by the second term in the bracket in Eq. (2.4.25). A closer look at this friction term reveals that the forward Euler number increases with increased chamber aspect ratio, which is consistent with previous observations. In addition, the port size and correspondingly the Reynolds number at the port will affect the boundary layer development inside the chamber and thus the format of dependence on the Reynolds number. This is the reason why d^* appears in the power of the Reynolds number. The first braced term in the bracket along with the Reynolds number term outside of the bracket in Eq. (2.4.25) accounts for the form loss in the two nozzles. According to Crane (1982), the pressure loss coefficient in converging and expansion nozzles should be a polynomial function of d^*, which agrees with Eq. (2.4.25) if we expand the Reynolds number term outside of the bracket in Taylor series as:

$$\mathrm{Re}^{-0.57+1.58d^*-1.3d^{*2}} = 1 + \ln(\mathrm{Re})(-0.57 + 1.58d^* - 1.3d^{*2}) + \cdots. \tag{2.4.27}$$

For the reverse flow, as discussed earlier, the main pressure drop is due to that in the free vortex region, which is accounted for by the first term in Eq. (2.4.26). Wormley (1969) and Stairmand (1990) have defined a modified boundary layer coefficient (BLC) to determine the range of the free vortex region (i.e., the critical radius, r_c), which can be written as:

$$\mathrm{BLC} = \frac{2\alpha f S}{\mathrm{Re}_r^{\ 0.25}}, \tag{2.4.28}$$

where α is the aspect ratio; f is the friction factor of the flow at the chamber wall; and S is the ratio of the fluid tangential velocity to its radial velocity near the chamber periphery. The Reynolds number, Re_r , is defined based on the fluid radial velocity near the chamber periphery, which is proportional to the Reynolds number based on the fluid velocity at the port (Priestman, 1987). It was found by Stairmand (1987) that the critical radius increases with the BLC.

As an approximate estimation, S is proportional to the aspect ratio (Priestman, 1987). In addition, if a laminar flow on flat plate is assumed for calculation the friction factor, f , it will depend on the Reynolds number as $1/\mathrm{Re}^{0.5}$ (Priestman, 1987). Therefore, in approximation the BLC (i.e., r_c) varies with the aspect ratio and Reynolds number as:

$$\mathrm{BLC} \propto \frac{\alpha^2}{\mathrm{Re}^{0.75}} \tag{2.4.29}$$

From Eq. (2.4.29), it can be clearly seen that the free vortex region increases with increased Reynolds number and decreased aspect ratio, which explains the previously observed trend of the reverse Euler number with the Reynolds number and aspect ratio.

The pressure drop in the free vortex region can be estimated using Bernoulli's equation as:

$$\Delta p_{free} = \frac{1}{2}\rho v^2 \left[\left(\frac{r_0}{r_c}\right)^2 - 1\right] \tag{2.4.30}$$

where r_0 is the chamber radius. With Eq. (2.4.29), the contribution of the pressure drop in the free vortex region to the Euler number in the reverse direction can be approximated as:

$$\frac{\Delta p_{free}}{0.5\rho v^2} \propto \frac{\mathrm{Re}^{1.5}}{\alpha^4} - 1 \tag{2.4.31}$$

which is close to the first term in Eq. (2.4.26).

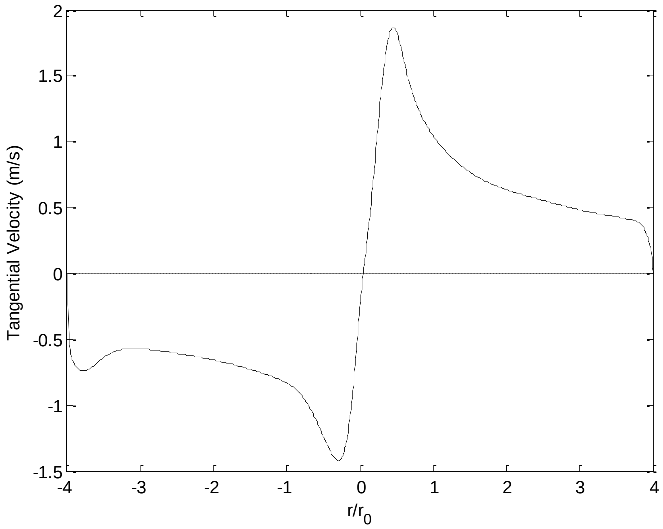

Fig. 2.4.18. Tangential velocity profiles over the chamber cross-section

The second term in Eq. (2.4.26) is probably due to the form loss associated with the recirculation flow along the chamber periphery. Actually, the free vortex region does not start from the chamber periphery, as can be seen from Fig. 2.4.18, which shows the fluid tangential velocity profiles over the chamber cross-section for the diode with a port diameter of 0.5", an aspect ratio of 8, and an inlet mass flow rate of 0.24 kg/s. The fluid seems to recirculate along the chamber periphery once before entering the free vortex region, which causes addition pressure loss that can be accounted for by the second term in Eq. (2.4.26). With similar argument to that for the forward flow direction, the last term in Eq. (2.4.26) is mainly due to the pressure drop in the two nozzles.

With the correlations for the forward and reverse Euler numbers determined, the diodicity for the vortex diodes can be obtained based on its definition in Eq. (2.4.24). However, this will lead to complex formulation and large combined error. Alternatively, the diodicity obtained from the CFD calculations can be correlated in a similar way as the reverse Euler number, which yields:

$$\mathrm{D}=\left(\frac{0.081}{\alpha}-\frac{0.141}{\alpha^2}\right)^2\mathrm{Re}^{1.33}+\left(\frac{14.8}{\alpha}-\frac{17.4}{\alpha^2}\right)+(12.1-69.0d^*+116.7d^{*2}-62.2d^{*3}) \quad (2.4.32)$$

Based on above analysis, Eqs. (2.4.25), (2.4.26) and (32) can be used to predict the Euler numbers and diodicity for cases with Re, α , and d^* not significantly deviating from the ranges of 711-4,789, 4-6, and 0.39-0.86, respectively.

Equations (2.4.25) and (2.4.26) are used to predict the port diameter and chamber aspect ratio that will meet the design parameters discussed earlier, i.e., the desired flow rates and pressure drops for both flow directions. It was found that if the desired reverse flow rate is 0.12 kg/s, the predicted aspect ratio will be negative, indicating that the desired pressure drop in the reverse direction cannot be achieved at such low flow rate. Since we have freedom in the desired reverse flow rate, as discussed earlier, we have changed it to 0.24 kg/s, which yield a reasonable design with a port diameter of 1.56 cm and a chamber diameter of 6.6 cm, respectively. A CFD simulation is subsequently performed for this diode design to calculate the pressure drops in the forward and reverse directions, which were found to be 299 and 12,500 Pa, respectively. The differences between the calculated and desired pressure drops are only 1.3 and 0.3% for the forward and reverse flow directions, respectively, which confirms the validity of Eqs. (2.4.25) and (2.4.26) within their applicable ranges. The vortex diode design with a port diameter of 1.56 cm and a chamber diameter of 6.6 cm has been selected for the HTDF.

Pump

A vertical cantilever sump type pump as shown in Figs. 2.4.19 and 2.4.20 has been adopted in our test facility. This pump provides the forced flow through the core, enabling us to model the pump trip transient. The pump consists of the motor, shaft, volute chamber where the blade is located, and the discharger. Except the motor, the entire pump will be submerged in a sump tank. As in the low temperature test facility, the same process of estimating the pump power has been performed which reveals that a 4-hp pump should be sufficient, even with only 10% pump efficiency. A standard model, CWO-HS-80, from Nagle will be used in our test facility. This pump contains a 5-hp motor which allows us the run our facility at heavier duty if necessary. The pump has a maximum capability of 120 gpm flow at a 20-ft head. All wetted parts in the pump will be SS 316. Purchase order for this pump has been addressed to Nagle, who is now manufacturing this pump.

Since the pump is submerged in a tank during operation, the problem of connecting the pump discharger to the main pipe line has been identified. Although there is flange connection at the end of the pump discharger, as shown in Fig. 2.4.19, we will not be able to get access to it and fasten the connection due to the pump mounting plate. One solution we have found is to pre-fasten the pair of the flanges at the end of the discharger, while keeping the bottom half not welded to the pipe line that penetrates through and is welded to the bottom plate of the pump tank. Therefore, when the pump is installed, the discharger will be simply slided onto the main pipe line. Inevitably, there will some leakage flow from the discharger back to the pump tank. However, based on our estimation, this leakage flow is insignificant compared with the total pumped flow (0.53 GPM vs. 41 GPM) when the pump is operated in the nominal condition.

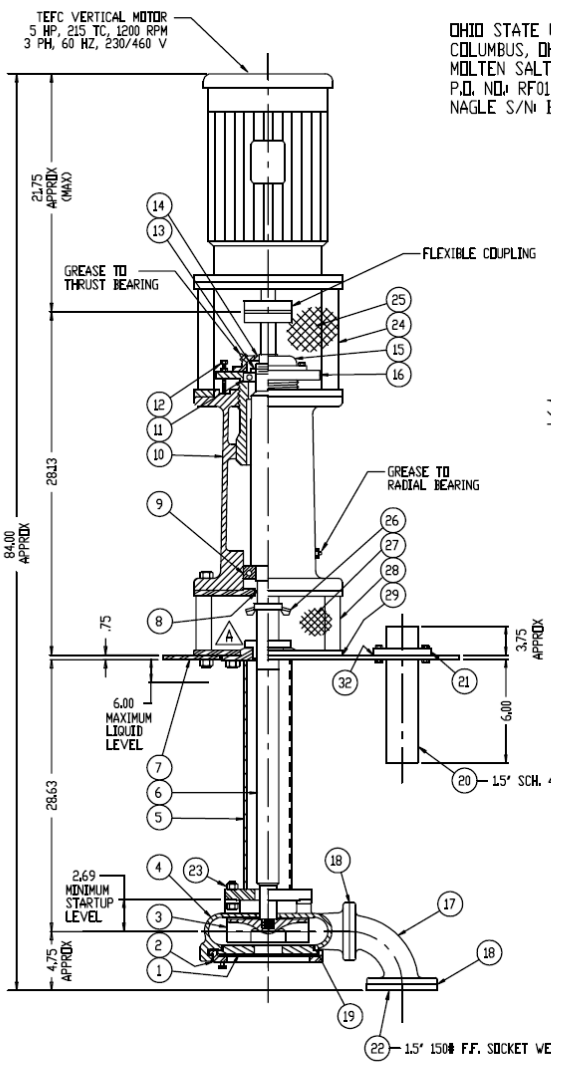
TEFC VERTICAL MOTOR
5 HP, 215 TC, 1200 RPM
3 PH, 60 HZ, 230/460 V
OHIO STATE
COLUMBUS, O
MOLTEN SALT
P.O. NO. RF01
NAGLE S/N
21.75 APPROX (MAX)
84.00 APPROX
28.13
.75
28.63
4.75 APPROX
3.75 APPROX
6.00
GREASE TO THRUST BEARING
FLEXIBLE COUPLING
GREASE TO RADIAL BEARING
6.00 MAXIMUM LIQUID LEVEL
2.69 MINIMUM STARTUP LEVEL
A
14
13
12
11
10
9
8
7
6
5
4
3
2
1
25
24
15
16
26
27
28
29
32
21
20
1.5' SCH.
23
18
17
18
19
22
1.5' 150# F.F. SOCKET WE

Fig. 2.4.19. The vertical cantilever sump type pump to be used in the experimental facility

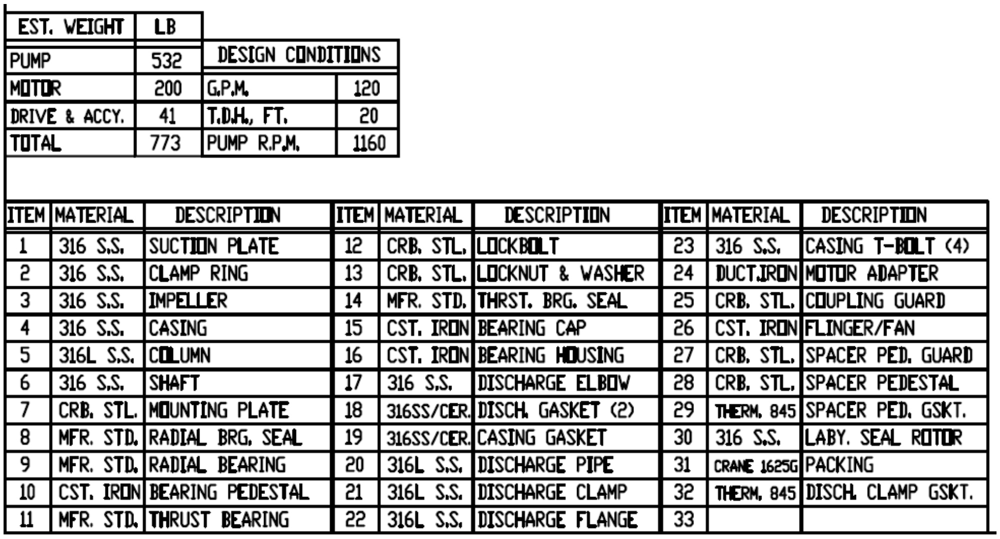

EST. WEIGHT	LB
PUMP	532
MOTOR	200
DRIVE & ACCY.	41
TOTAL	773

DESIGN CONDITIONS	
G.P.M.	120
T.D.H., FT.	20
PUMP R.P.M.	1160

ITEM	MATERIAL	DESCRIPTION	ITEM	MATERIAL	DESCRIPTION	ITEM	MATERIAL	DESCRIPTION
1	316 S.S.	SUCTION PLATE	12	CRB. STL.	LOCKBOLT	23	316 S.S.	CASING T-BOLT (4)
2	316 S.S.	CLAMP RING	13	CRB. STL.	LOCKNUT & WASHER	24	DUCT.IRON	MOTOR ADAPTER
3	316 S.S.	IMPELLER	14	MFR. STD.	THRST. BRG. SEAL	25	CRB. STL.	COUPLING GUARD
4	316 S.S.	CASING	15	CST. IRON	BEARING CAP	26	CST. IRON	FLINGER/FAN
5	316L S.S.	COLUMN	16	CST. IRON	BEARING HOUSING	27	CRB. STL.	SPACER PED. GUARD
6	316 S.S.	SHAFT	17	316 S.S.	DISCHARGE ELBOW	28	CRB. STL.	SPACER PEDESTAL
7	CRB. STL.	MOUNTING PLATE	18	316SS/CER.	DISCH. GASKET (2)	29	THERM. 845	SPACER PED. GSKT.
8	MFR. STD.	RADIAL BRG. SEAL	19	316SS/CER.	CASING GASKET	30	316 S.S.	LABY. SEAL ROTOR
9	MFR. STD.	RADIAL BEARING	20	316L S.S.	DISCHARGE PIPE	31	CRANE 1625G	PACKING
10	CST. IRON	BEARING PEDESTAL	21	316L S.S.	DISCHARGE CLAMP	32	THERM. 845	DISCH. CLAMP GSKT.
11	MFR. STD.	THRUST BEARING	22	316L S.S.	DISCHARGE FLANGE	33		

Fig. 2.4.20. Specifications and main components of the pump

Throttling in Secondary Loop

Based on the scaling results for the HTDF, throttling was found necessary to provide an extra pressure drop of 596.5 Pa in the secondary loop, as shown in Table 2.4.8, along with the pressure drops in other components at the nominal steady state condition. A long square-edged orifice plate has been considered for the needed throttling, which features simplicity and easy maintenance.

Table 2.4.8 Pressure drops in the HTDF secondary loop at the nominal steady state

Component	Pressure Drop (Pa)
DHX tube side	5.8
NDHX tube side	21.5
Pipe	65.2
Form loss	21.8
Globe valve	~ 596.5

For a long square-edged orifice plate, as illustrated in Fig. 2.4.21, the pressure loos coefficient can be evaluated from (Chowdhury and Fester, 2012):

$$K = \frac{170.5\beta^{-3.17}}{\mathrm{Re}} + \left[-17\beta + 5\left(\frac{t}{d}\right)^{\left[(53.77\beta^2 - 71.23\beta + 26.23)(t/d)^{-0.92}\right]} \right] \tag{2.4.33}$$

where Re is the Reynolds number; β is defined as the ratio of the orifice diameter (d) to that of the pipe (D); t is the thickness of the orifice; and d is the diameter of the orifice. Based on the desired pressure drop that is found to be 596.5 Pa, an orifice plate design with thickness of 25.4 mm and diameter of 10.8 mm is obtained. This orifice design can be easily fabricated from a 1-inch thick plate and will be sandwiched between a pair of flanges in the secondary loop.

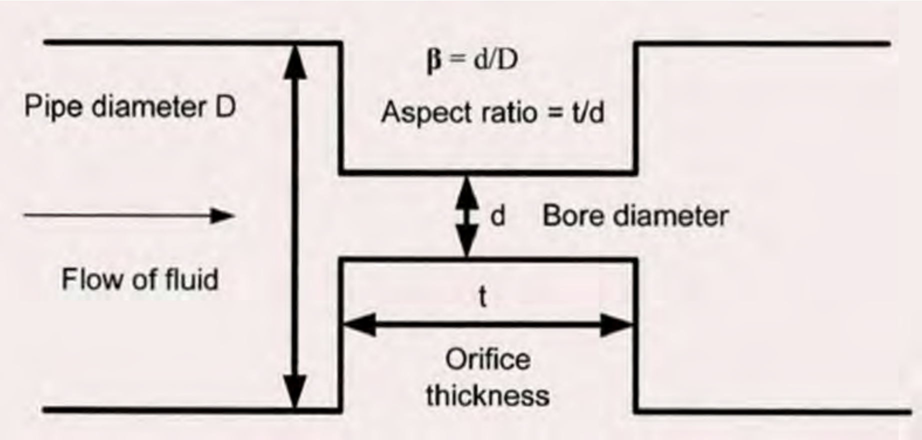

Fig. 2.4.21. Long square-edged orifice plate

Vacuum Pump

To alleviate the corrosion in the high-temperature facility, the entire system should be kept as inert as possible. Before salts are fed into the system, it should be vacuumed with vacuum pumps. With idea gas law, it is easy to derive that:

$$\frac{V_{residual}}{V_{total}} = \frac{P_{vacuum}}{P_{atm}} \tag{2.4.34}$$

where $V_{residual}$ and V_{total} denote the volume of the residual air and the total volume of the loop, respectively. P_{vacuum} is the final vacuum pressure the system can reach, while P_{atm} denotes the atmospheric pressure. The total volumes in the primary and secondary loops (or salt inventory) are 111 and 32 liters, respectively. From McMaster, vacuum pumps that can reach vacuum of 0.1 microns are readily available. In principle, the higher the vacuum we can reach, the less the air that will remain in the system. However, there is the potential problem of salt boiling when the system is vacuumed to a certain extent. The vapour pressure of the salts that are used in our facility at different temperatures is thus examined, which is shown in Fig. 2.4.22. Since the primary and secondary salts will be melted at 550 and 500°C, respectively, it would be safe to vacuum the system to 1 micron. The residual airs were therefore found to be 0.14 and 0.04 cm^3 in the primary and secondary loops, respectively. In reality, the volume of the residual air can be further reduced if the evacuation process is continued when the salts are fed into the system.

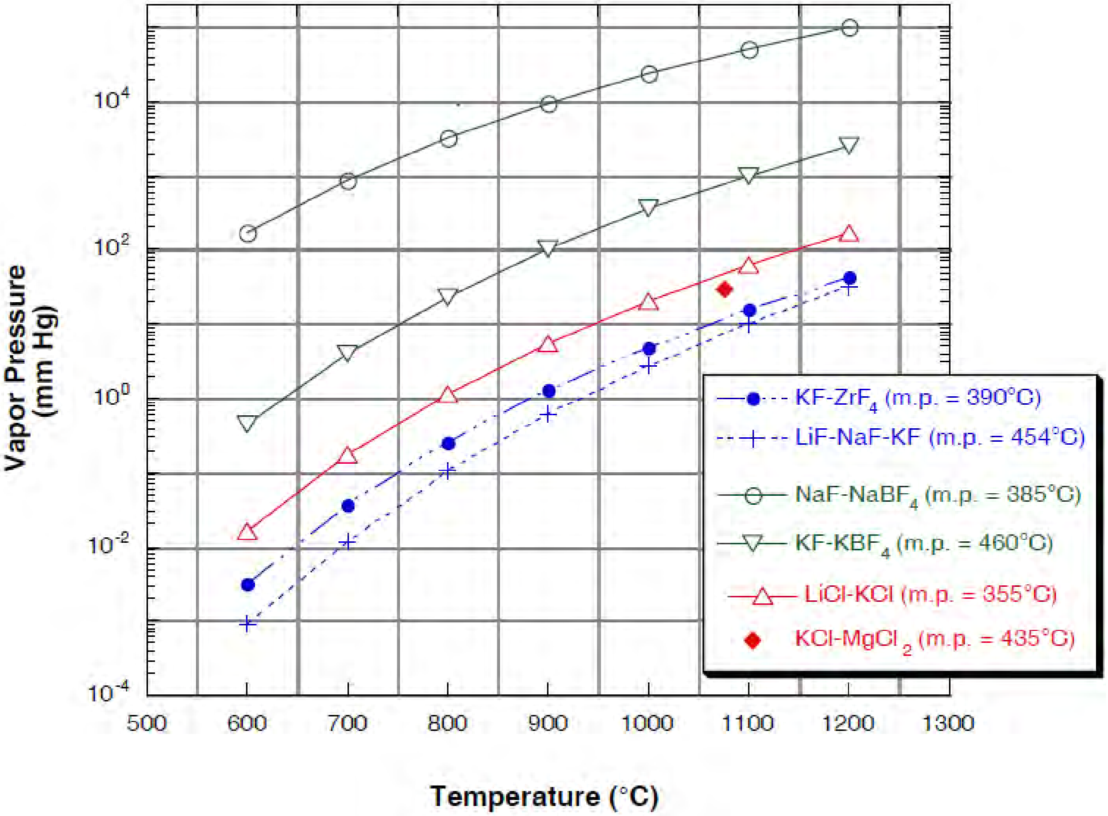

Fig. 2.4.22. Vapor pressure of the salts (Williams, 2006)

Salt Feeding

Because the salts are in solid state at the room temperature, they must be melted before filling the entire system. The salts will be first melted in the reservoir tanks which are wrapped with tape heaters. After the salts are completely melted, they will be transferred to the loops by pressuring the reservoir tanks with Argon. The studies conducted by Blander (1958) and Grimes (1958) suggest that Argon will be barely dissolved into FLiNaK or $NaF-ZrF_4$. Because the secondary salt used in our experiment, $KF-ZrF_4$, has close composition to $NaF-ZrF_4$, we assumed that they will exhibit comparable Argon solubility. In addition, Argon will also be used as the cover gas to prevent oxidation of the facility. After the experiment is completed, the salts will be drained back into the reservoir tanks. A side view of the reservoir tank is shown in Fig. 2.4.23.

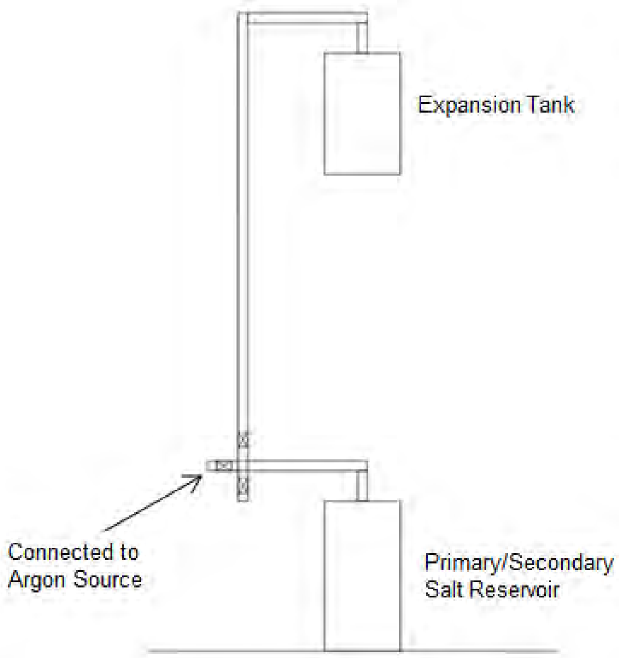

Fig. 2.4.23. Side view of the reservoir tank connecting the expansion tank

Pipe Flexibility Analysis

Due to the high temperature property of present facility, thermal expansion will be significant. Thermal stress will be accumulated and ultimately lead to leakage if the piping system is not flexible enough. Therefore, a pipe flexibility study has been performed to make sure that failure will not happen in any position in the test facility, especially the flange fitting. To make sure no leakage would occur at any location of the flange connections, the maximum allowable bending moment for a pair of flanges is examined which can be expressed as (Blick, 1950):

$$M \le \frac{GA_B S_{op}}{4} - p\frac{\pi G^2}{2}\left(\frac{G}{8} + bm\right) \tag{2.4.35}$$

where M is the maximum allowable bending moment without causing leakage; G is the mean gasket diameter; A_B is the total bolting area; S_{op} is the operating bolt stress; p is the internal hydraulic pressure; b is half of the effective operating width of the gasket; and m is the gasket coefficient which is defined as the ratio of the required gasket pressure to the internal hydraulic pressure. For most applications, the gasket coefficient can be selected as 2.5 (Blick, 1950), which is conservative for the present analysis mainly because the spiral wound gaskets used in the HTDF require lower bolt load compared with other gaskets.

As can be seen from Eq. (2.4.35), the maximum allowable bending moment for flanges will be smaller with increased internal hydraulic pressure. In the primary loop of the HTDF, the maximum internal hydraulic pressure will be encountered at the lower horizontal pipe between the core and the pump tank when the core is in normal operation. The maximum internal hydraulic pressure is found to be approximately 27 psia, which is the summation of the overhead gas pressure in the pump tank, the hydraulic head of the salt, and the pump head corresponding to the nominal flow rate of 5.4 kg/s. With the above maximum internal hydraulic pressure and a safety factor of 4 for the bolt operating stress (i.e., the bolt operating stress is assumed to be a quarter of the maximum allowable stress of the bolt material, SS 316), the maximum allowable bending moment is determined to be 1,005 ft-lbs.

The thermal stress is caused by the anchors that restrict the free expansion of the pipes when they are heated. In this regard, a completely floating loop will not have the issue of thermal stress. Therefore, our principle of designing the piping system is to make it floating wherever it is possible. The component that must be anchored in the facility is the pump tank, mainly due to the vibrations that may be caused when the pump is in operation. The DHX which is almost at the same elevation as the pump tank will also be anchored to avoid bending stress being accumulated in the connecting pipe between the DHX and the pump tank. With these two components anchored, the primary and secondary loops have some freedom to expand downward and upward, respectively.

The thermal expansion of a heated pipe can be calculated as:

$$\Delta = \alpha L(T_f - T_i) \tag{2.4.36}$$

where α is the thermal expansion coefficient of the pipe material; L is the total length of the pipe; T_i and T_f are the initial and final temperatures of the pipe, respectively. As can be seen, the thermal expansion is proportional to the length of the pipe. Therefore, any long run of pipes may cause over stress and should be analysed.

In the primary loop, flexibility should be provided to the two vertical legs to avoid over stress in the DHX shell-side inlet and outlet nozzles. Using Eq. (2.4.36), it is found that the thermal expansions in the two vertical legs are 1.8 cm (left leg in Fig. 2.4.1) and 2.2 cm (right leg in Fig. 2.4.1), respectively. Load springs readily available from McMaster will be used to accommodate these thermal expansions. For the fluidic diode, 4 load springs with a total spring rate of 124 lbs/inch are installed. Similarly, the core will be equipped with 4 load springs that have a total spring rate of 200 lbs/inch. These springs are stiff enough to accommodate the weights of the two vertical legs, which are roughly 62 and 324 lbs, respectively. With the thermal expansions accommodated in the load springs, the bending fore that will be caused in the DHX shell-side nozzles can be estimated as:

$$F = K\Delta \tag{2.4.37}$$

where K is the spring rate of the springs, and Δ is the thermal expansion that needs to be accommodated. The bending forces in the DHX shell-side inlet and outlet nozzles were found to be 173 and 88 lbs, respectively. Correspondingly, the bending moment in the two nozzles will be 114 and 58 ft-lbs, respectively, which are within the capability of the flange fittings.

The flexibility analysis of the piping between the fluidic diode outlet and the core inlet is simplified as illustrated in Fig. 2.4.24. Two anchor points were assumed at the fluidic diode outlet and the core inlet, respectively. Based on the guided cantilever method (Kellogg, 1956), the required total length of the U-shape loop (in unit of ft) is:

$$L = \sqrt{\frac{3ED\Delta}{144 S_A}} \tag{2.4.38}$$

where E, S_A, D, and Δ, are the Young's modulus of the piping material in psi, maximum allowable stress for the piping in psi, nominal pipe size in inch, and the thermal expansion to be absorbed in inch. The maximum allowable stress for the pipe should be evaluated using:

$$S_A = f(1.25S_c + 0.25S_h) \tag{2.4.39}$$

where S_c and S_h are the maximum allowable stress for the pipe at cold and hot temperatures, respectively. The correction factor f can be estimated based on the number of operation cycles, as shown in Table 2.4.9. Our facility will not be operated for more than 7,000 cycles, thus correction factor of 1 has been used. The thermal expansion to be absorbed, Δ, should be evaluated based on the direct distance between the two anchor points. With Eq. (2.4.38), the required length for the U loop was found to be 1.22 m, shorter than what existed, i.e., 1.64 m. The bending force and moment at the anchor points can be estimated as (Kellogg, 1956):

$$F = 10^6 A_1 \left(\frac{I\Delta}{L^3} \right) \tag{2.4.40}$$

$$M = 10^5 A_2 \left(\frac{I\Delta}{L^2} \right) \tag{2.4.41}$$

where Δ is the thermal expansion to be absorbed, and L is the distance between the anchor points. A_1 and A_2 are two constants, which can be looked up from the so-called M. W. Kellogg charts (Kellogg, 1956). The moment of inertia, I, can be calculated as:

$$I = 0.78(r_o^4 - r_i^4) \tag{2.4.42}$$

where r_o and r_i denote the inner and outer diameter of the pipe, respectively. With Eqs. (2.4.40) and (2.4.41), the bending force and moment at the anchor points were found to be 847 lbs and 668 ft-lbs, respectively. As can be seen, the bending moment is within the bending capacity of the flange fittings. Therefore, no failure is expected even if the flange fittings are welded to the fluidic diode and the core directly.

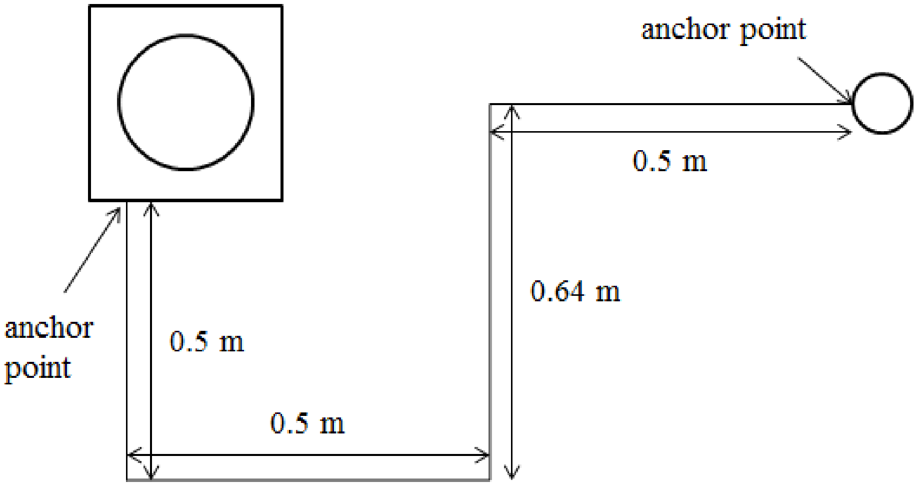

Fig. 2.4.24. Piping between the fluidic diode and the core

Table 2.4.9 Correction factor for the maximum allowable stress

Cycles N	Factor f
7,000 and less	1.0
Over 7,000 to 14,000	0.9
Over 14,000 to 22,000	0.8
Over 22,000 to 45,000	0.7
Over 45,000 to 100,000	0.6
Over 100,000 to 200,000	0.5
Over 200,000 to 700,000	0.4
Over 700,000 to 2,000,000	0.3

In the loop where the pump is located, there are two long pipe runs, one between the DHX and pump tank, the other between the core and the pump tank. For the former pipe run, the flexibility analysis is simplified as shown in Fig. 2.4.25. Using Eq. (2.4.38), the required length for the U loop was found to be 2 m. The layout shown in Fig. 2.4.25 ensures the pipe flexibility. As seen, a pipe guide is located at 1 m to the left of the U loop, which guides the thermal expansion in desired direction. With the pipe guide present, the bending moment will be exerted on the guide instead of the left anchor point. Eqs. (2.4.40) and (2.4.41) can still be used to estimate the bending force and moment, however, L will be the distance between the pipe guide and the right anchor point in this case. The bending force and moment were found to be 277 lbs and 441 ft-lbs, respectively. As seen from Fig. 2.4.1, there is a pair of flange fitting at the inlet of the pump tank. Based on above analysis, failure will not happen in this flange. It should be noted that, the above analysis is conservative. The right anchor point should be assumed on the bottom of the pump tank rather than what is shown in Fig. 2.4.25. Therefore, the pump tank has also participated in providing the flexibility, which has yet been neglected.

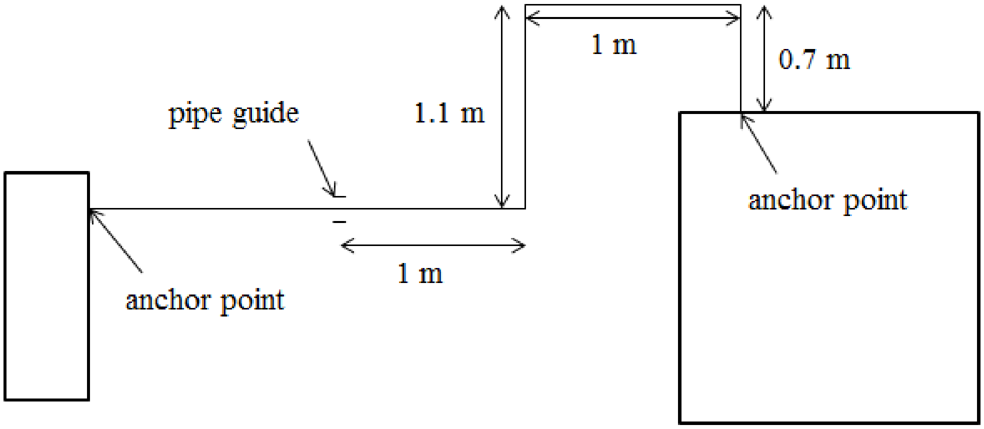

Fig. 2.4.25. Piping between the DHX and the pump tank

For the piping between the core and the pump tank, the flexibility analysis is simplified as shown in Fig. 2.4.26. Although two anchor points have been assumed in the present calculation, the left one is virtually not fixed. As discussed earlier, the vertical leg where the core is located can expand downward freely, which will counteract part of the thermal expansion in the vertical pipe beneath the pump tank. The net thermal expansion in vertical direction is 0.31 cm. The thermal expansion in the horizontal direction was calculated to be 2.38 cm. For an L-shape expansion loop that is similar to what is encountered here, the required length of either leg to absorb the thermal expansion in the other leg is also estimated by Eq. (2.4.38). To absorb the 0.33-cm thermal expansion in the vertical direction, the required length of the horizontal pipe is 0.64 m, smaller than existed, i.e., 2 m. However, the vertical pipe beneath the pump tank is not sufficient to absorb the expansion in the horizontal pipe which is 2.38 cm. An extra piping length of 0.15 m is needed, which can be obtained from the U loop shown in Fig. 2.4.26. The total length of the U loop has been selected to be longer than needed mainly because of engineering concern, as it will be difficult to form a small U loop of 0.15 m. The U loop was neglected when the bending moment at the two anchor points was calculated, which would be conservative. The bending moment at the anchor points can be estimated as (Kellogg, 1956)

$$M = \frac{6EI}{L^2}\Delta \tag{2.4.43}$$

where L is the length of the absorbing leg, and all other parameters have the same meanings as before. The bending moments at the core anchor point and pump tank anchor point are 85 and 1,037 ft-lbs, respectively. Therefore, no failure will happen in the two flange fittings in the horizontal pipe. The flange fitting in the vertical pipe will also survive if it is not welded directly onto the bottom of the pump tank.

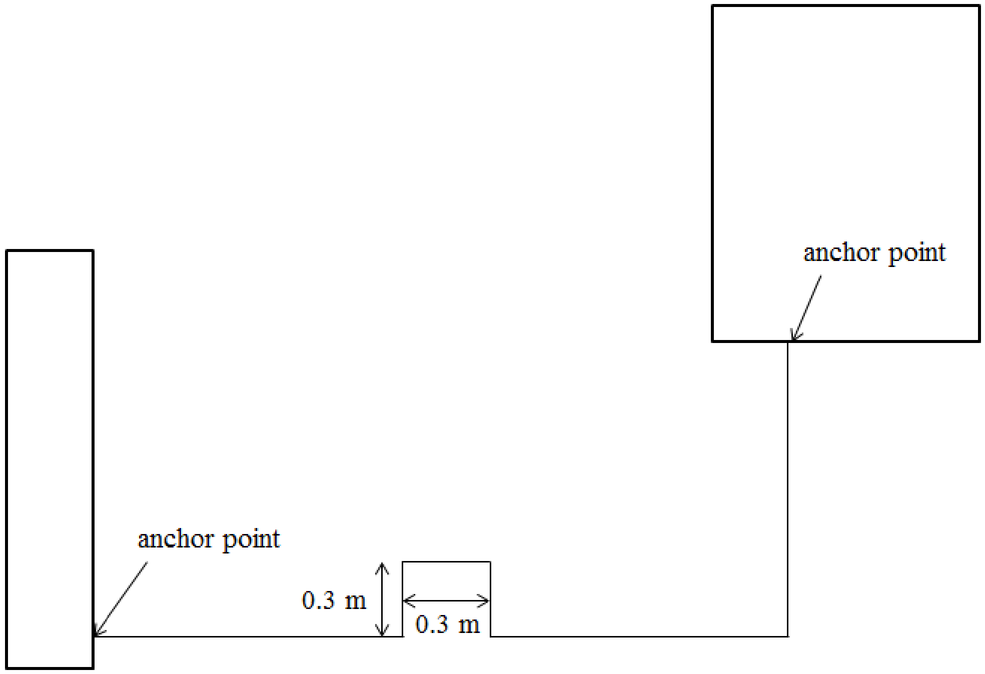

Fig. 2.4.26. Piping between the core and the pump tank

In the secondary loop, all horizontal pipe runs will be supported from bottom, which enables the loop to expand upward freely. No constraints will be exerted on the vertical pipe connecting to the NDHX outlet, which enables the loop to freely expand away from the DHX in horizontal direction. Therefore, the secondary loop is overall more flexible than the primary loop. No failures are expected to happen in the piping unless in the flange fittings. To evaluate the bending moment at each flange fitting, the secondary loop was divided into two parts along the diagonal line between the corner above the DHX and the corner beneath the NDHX. The part containing the NDHX was first analyzed, as shown in Fig. 2.4.27. A pipe support is located in the middle point of the pipe connected to the NDHX inlet, which will accommodate the weight of this horizontal pipe as well as the salt inside it. The force F is caused by the thermal expansion in the vertical pipes, which can be estimated using guided cantilever method. With two anchor points assumed at the ends, the force F can be calculated using (Kellogg, 1956):

$$F = \frac{12EI}{L^3}\Delta \tag{2.4.44}$$

where all the parameters have the same interpretations as in Eq. (2.4.43). A net expansion of 0.39 cm should be used in the calculation of F, which was found to be 3 lbs. Considering the moment and force balance, forces F_1, W_1, W_2, and F_3 were found to be 45, 49, 45, and 1 lbs, respectively. The bending moments at the NDHX inlet and outlet nozzles are approximately 10.5 and 2 ft-lbs, respectively, which are well within the bending capacity of the flange fittings.

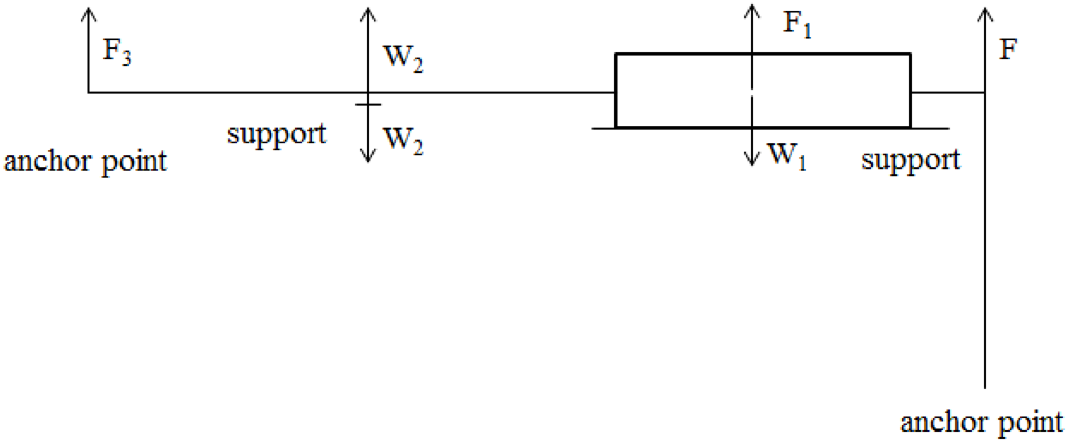

Fig. 2.4.27. Flexibility analysis for secondary loop part 1

For the second part in secondary loop, the flexibility analysis was simplified as shown in Fig. 2.4.28. Two pipe supports are installed beneath the horizontal pipe. One support is located in the middle point of the pipe to accommodate the weight of the pipe and the enclosed salt. The other support is to the left of the right end by 0.4 m. The force exerted at the right end comes from the thermal stress which has been calculated in previous step, and the weight of the vertical pipe (including the salt) connected to the NDHX outlet. The net force at the right end was calculated to be 23 lbs. With force and moment balance, F_1, W_2, and F_3 were found to be 26, 56, and 3 lbs, respectively. The bending moment at the flange fitting near the right end is approximately 15.1 ft-lbs, signifying no failure in the fitting.

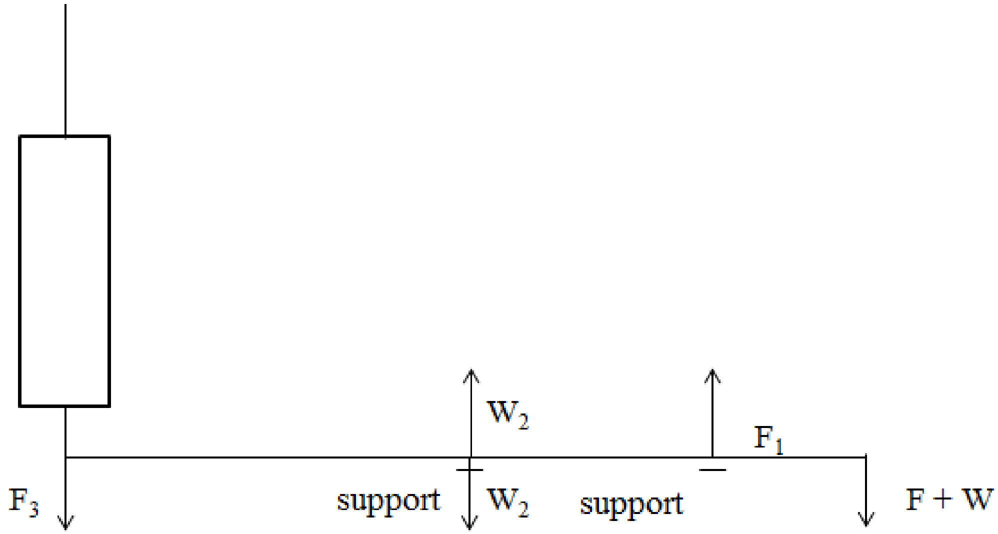

Fig. 2.4.28. Flexibility analysis for secondary loop part 2

When the horizontal pipes and the NDHX expand horizontally, friction between them and the supports will lead to bending stress in the DHX tube-side nozzles. The bending moment in the nozzles can be calculated as:

$$M = F_{fri} L \tag{2.4.45}$$

where L is the distance between the nozzle and the corresponding horizontal piping, and the friction force F_{fri} can be obtained from:

$$F_{fri} = \mu F_{per} \tag{2.4.46}$$

Here, μ is the friction coefficient between the contacting surfaces, and F_{per} is the net force between the contacting surfaces in perpendicular direction. With Eqs. (2.4.45) and (2.4.46), the bending moments at the DHX tube-side inlet and outlet nozzles were found to be 32.8 and 165 ft-lbs, respectively, which would not cause any failure in the flange fitting.

Salt Melting and Pre-processing

The salts will be melted and pre-processed in the salt reservoir tanks. It is found that melting the salts will consume a lot of energy and time. During the scaling analysis, pipe sizes have been decreased as much as possible to reduce the inventory for both the primary and secondary salts. The pump tank and the expansion tank have also been carefully designed to reduce the salt inventory. Despite these efforts, we still need around 266 kg primary salt and 113 kg secondary salt. To estimate the time needed to melt and heat the salts to a specific temperature (550°C for FLiNaK, 500°C for KF-ZrF_4), their specific heat capacity in both solid and liquid states and heat of fusion should be known. For FLiNaK, its specific heat capacity is a function of temperature:

Liquid (Williams, 2006):

$$c_p(\text{J/kg-K}) = 976.13 + 1.063T(\text{K}) \tag{2.4.47}$$

Solid (Rogers, 1983):

$$c_p(\text{J/kg-K}) = 1298.9 - 0.978T(\text{K}) + 1.533\times10^{-3}T^2(\text{K}) \tag{2.4.48}$$

The heat of fusion for FLiNaK is found from Powers's (1956) study, which is 397 kJ/kg. For KF-

ZrF_4, its specific heat capacity only for liquid at 700°C is found, which is 1,050 J/kg-K (Williams, 2006). Its specific heat in solid state has been assumed to be the same as that in liquid state. No literature has been found containing the heat of fusion for KF-ZrF_4, but its constituent salts. The constituent salts, KF and ZrF_4, have heat of fusion of 486 and 384 kJ/kg (Misra, 1987; Mcdonald, 1962), respectively. Mass-weighted average is taken to estimate the heat of fusion for KF-ZrF_4, resulting in a value of 417 kJ/kg. The specific heat and heat of fusion that are used to estimate the salt melting time are summarized in Table 2.4.10. If heating power of 30 and 10 kW are available to the primary and second salts, it will take around 2.8 and 2.9 hours to melt them, respectively.

Table 2.4.10 Specific heat and heat of fusion for the salts

	FLiNaK	KF-ZrF_4
Melting point (°C)	454	390
Average specific heat (solid) (J/kg-K)	1,271	1,050
Average specific heat (liquid) (J/kg-K)	1,800	1,050
Heat of fusion (kJ/kg)	397	417

The commercial grad fluoride salts usually contain some impurities, which will accelerate the corrosion to the structure alloy if not pre-processed. As suggested by ORNL (Shaffer, 1971), three steps should be taken in the pre-processing process, which will remove the oxide, sulfur and structure metal (Fe) consecutively. There are usually two sources for the oxide impurities, the starting salt materials or incomplete evaporation of the absorbed water in the salts. If the oxides are not removed, they will deposit onto the heaters, causing deteriorated heat transfer. The oxides can be eliminated by purging HF-H_2 mixture through the salts. Sulfur usually comes from the sulfates in the starting salts, which will cause attack on Ni if not removed. Purging the salt with HF-H_2 mixture can also remove the sulfur in the salts. The structure metal, usually Fe, can come from either the starting salts or the vessels. Severe corrosion to vessels can be caused if the structure metal is not pre-removed. The way to remove the structure metal is to add Zr or Li to the salts, or to purge H_2 through the salts. Building a salt pre-processing equipment will be too costly and time consuming for us. Therefore, we are now contacting ORNL about providing processed salts for us since they have the salt pre-processing equipment and capability.

Instrumentation

To evaluate the thermal performance of the HTDF system and the heat exchangers, the temperatures at the inlet and outlet of the core and the heat exchangers need to be measured. Experimental data on the temperature, flow rates and pressure drops over the variant components are also necessary to benchmark the heat transfer and pressure drop correlations/models used in the prototypic DRACS design, as well as the MATLAB code. In addition, salt levels in the pump tank and reservoir tanks should be monitored. Challenges have been encountered in identifying the instrumentation for the HTDF mainly due to the high temperature, the corrosion, and the required accuracy.

Flow Meter

In the HTDF, at the nominal steady state, the salt flow rates and the available buoyance are small. Usually intrusive flow meters, like the venturi flow meters, will cause extra pressure drop which is not desirable in the HTDF. Therefore, clamp-on ultrasonic flow meter without intrusion to the flow has been considered. In addition, without direct contact with the salts, the corrosion problem is ruled out for ultrasonic flow meter. However, the high temperatures in the HTDF have caused some challenges in identifying the proper ultrasonic flow meter. Usually, the piezoelectric material used in the transducers of the ultrasonic flow meter is susceptible to high temperature, implying that the transducers cannot be clamped onto the hot pipes in the HTDF directly. One solution that has been adopted by industries to push the temperature limit is to use an injector isolate the hot pipes from the transducers, as illustrated in Fig. 2.4.29. The injector must be carefully designed so that the temperature is brought down enough when it gets to the transducers. In addition, the design of the injector will also need to take into account the propagation of the ultrasonic wave in the injector.

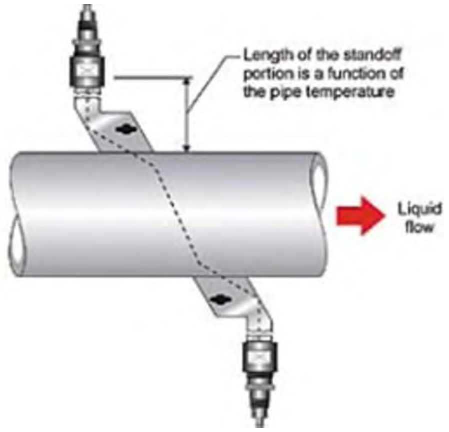
Length of the standoff portion is a function of the pipe temperature
Liquid flow

Fig. 2.4.29. Injector used in the ultrasonic flow meters for high temperature application

We have identified one company called Flexim (Flexim) who can provide a solution to our application. They once invented an injector for ORNL for their application with temperature up to 700°C. In our HTDF, the primary salt will reach higher temperature, which calls for modification to the injector design employed by ORNL. The flow meter obtained from Flexim will be demonstrated in our HTDF to see if it is applicable to a temperature of 750°C.

Pressure Transducer

For the pressure and differential pressure measurements, three challenges have been identified, namely, the high temperature, the corrosion issue, and the required accuracy. NaK filled pressure transducers are commercially available for high temperature application up to 1000°F (538°C) (ONEhalf20). Since this temperature limit is well above the melting points of the salts, which are 454 and 390°C (Williams, 2006) for the primary and secondary salts, respectively, these models can be applied if cooling tubes are added between the measuring locations and the pressure transducers. In addition, SS 316 or Incoloy 800 diaphragms that are the physical interfaces between the salts and the transducers are available. With Ni-plating, the diaphragms can be made quite resistant to the salt corrosion (Sabharwall et al., 2010). However, the models found so far are not capable of measuring the small pressure drops encountered in the HTDF, as summarized in Table 2.4.11. The NaK filled pressure transducers identified thus far have a minimum range of 0 to 500 psig, and a full scale error of 0.5% (2.5 psi) (ONEhalf20). The small pressure drops encountered in the HTDF are not measurable with these NaK filled pressure transducers.

Table 2.4.11 Nominal steady-state pressure drops in primary and secondary loops in the HTDF

Component	Pressure Drop (Pa)	Component	Pressure Drop (Pa)
Core	14.8	DHX tube side	5.8
DHX shell side	24.1	NDHX tube side	21.5
Pipe	13.0	Pipe	65.2
Form loss	11.2	Form loss	21.8
Fluidic diode	~ 298.3	Throttling	~ 596.5

Currently, efforts in finding NaK filled pressure transducers with much higher accuracy are still ongoing. Besides that, we are also considering two custom pressure transducer designs which may provide the desired measurement accuracy. The first design is a kind of manometer design based on salt level measurement. To measure the differential pressure across a test section, taps at the bottom and top of a test section are connected to sealed pressure cans, which will be filled with Argon gas. The salt levels in the two salt cans will be measured using different level sensoring technologies, like laser, ultrasonic and magnetostrictive level sensors. By measuring the salt levels, and knowing the salt densities, the differential pressure can be determined. This type of custom pressure transducer design has been used by University of Wisconsin in their salt test loops, which achieved an accuracy of 0.9 Pa during preliminary tests (Sabharwall et al., 2010). The drawback of this design is that the salt inventories will be increased significantly, which will lead to even longer pre-melting time as discussed earlier.

The second custom design that is being investigated is based on pressure transducers for gas measurement. Usually, pressure transducers for gas have high accuracies, but low temperature limit. DPTM50 is such a transducer from Honeywell that has a minimum range of 50 Pa and a full scale error of 0.2% (0.1 Pa) (Honeywell). However, the operating temperature limit of this model is only 50°C. The basic idea of the custom design is to isolate the hot measuring point from the gas pressure transducer by Argon gas encapsulated in small tubes. The pressure at the measuring point is propagated to the transducer and measured therein. The connecting tubes should be long enough so that the temperature is sufficiently reduced when it gets to the transducer. One challenge of this custom design is to accurately control the salt-Argon interface. During the transient in the HTDF, the pressures at the measuring locations will vary, meaning that the salt-Argon interface will shift. The amount of the encapsulated Argon gas should be carefully controlled so that no gas can get into the system. Fused quartz tubes that can work at high temperatures have been considered to monitor the salt-gas interface. The monitoring quartz tubes will be connected to the stainless steel sensing tubes with compressing tube fittings. Quartz tubes (Technical Glass Products) for compression type fittings have been identified. It should be noted that graphite ferrules (Chromalytic Technology) should be used for the quartz tube side and that close attention should be paid to avoid over-tightening the tube.

Thermocouple

For the thermocouples, the main concern will be the corrosion issue. Hastelloy N has excellent corrosion resistance to the salts, but its availability is questionable. Corrosion studies performed at University of Wisconsin (Sabharwall et al., 2010) indicated that Ni-plated Incoloy 800 has corrosion resistance comparable to Hastelloy N. Therefore, it is suggested that Ni-plated Incoloy 800 be used for the thermocouple probes.

Level Sensor

In the HTDF, level sensor for continuous level monitoring is needed for the salt reservoir tanks.

For the pump tank, a level switch is needed so that when the salt level reaches a set point (slightly above the starting level of the pump) the salt feeding process is ceased. Magnetostrictive level sensors/switches are being investigated. These sensors are based on measuring the traveling time of electromagnetic waves reflected by the metal float at the salt surface, and usually have high accuracies (Babbitt International). However, corrosion to the metal float may affect the accuracies of the sensors. If this is really the case, the probe and the float that have direct contact with the salts will be plated with Ni.

Magnetostrictive level sensors usually feature high accuracy. However, all commercial Magnetostrictive sensors found so far are suitable for temperature only up to 400°C, much lower than those encountered in the HTDF. Despite the efforts of finding a custom solution for the magnetostrictive level sensor, we have not found any vendor who is interested.

The only level sensors that are found capable of withstanding high temperature are the RF (radio frequency) admittance level sensors from two companies, Ametek Drexelbrook and Delta Controls. The RF admittance level sensor is based on the principle of measuring the admittance of the circuit that is formed between the sensor probe and the salt tank. When the salt level changes, the measured circuit admittance will change accordingly. Ametek Drexelbrook and Delta Controls have models that can work at temperature up to 1,500^{o}F, sufficient for the use in the HTDF. However, the RF admittance level sensors exhibit relatively lower accuracy, typically of around 1.5 mm, depending on the probe design. Such accuracy is good enough for monitoring the salt levels in the pump tank, reservoir tanks, and expansion tank. The level sensors were purchased from Delta Controls after a bidding process.

Layout of the Test Facilities and the Support Platform

Effort has been made to lay out the two test facilities without them interfering with each other. The secondary loop of the HTDF has to be modified to avoid interference with a wind tunnel, a small portion of which is currently housed in our lab, as shown in Fig. 2.4.30. The box shown in the figure denotes the wind tunnel, and the low- and high-temperature test facilities are shown in grey and red, respectively. As can be seen, the two test facilities are deployed such that they can coexist. However, the chimney system is shared by the two facilities, implying that only one NDHX can be put in position and only one test facility can be at operation at one time.

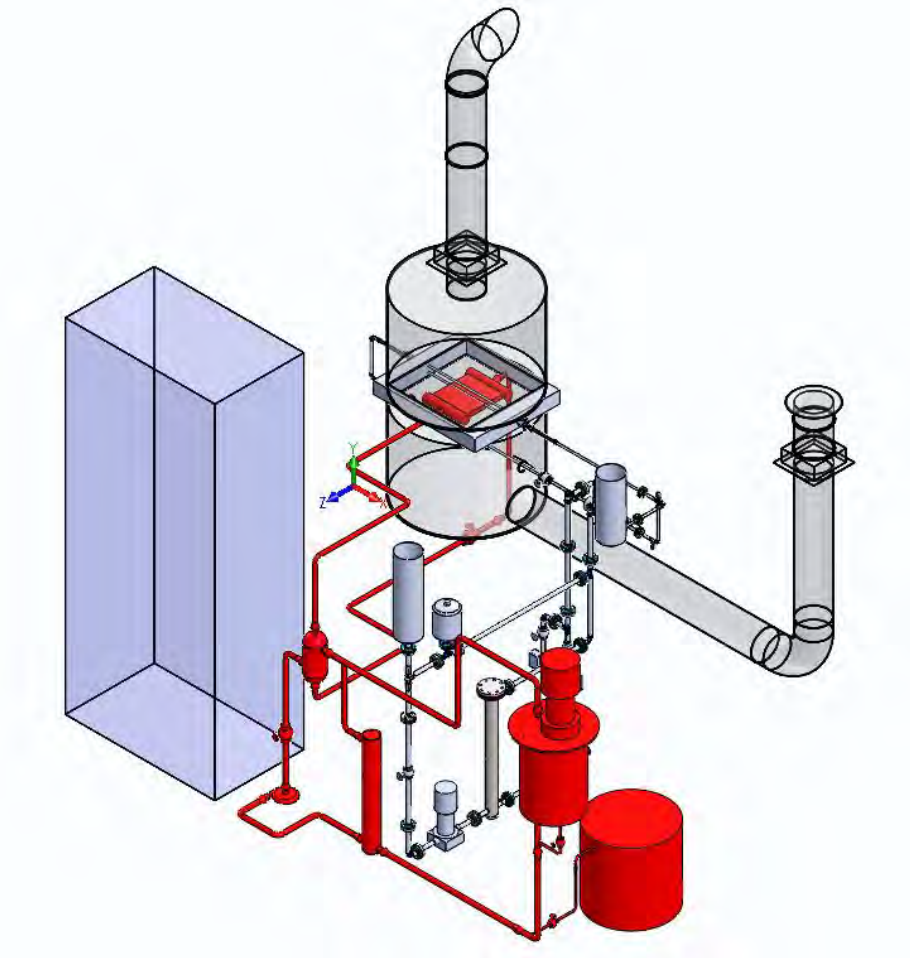

Fig. 2.4.30. Layout of the DRACS test facilities

Since the secondary loop of the HTDF was modified, the piping flexibility was rechecked. Using Eq. (2.4.35), the thermal expansion in the vertical leg on top of the DHX is around 0.34 cm, which can be absorbed by a perpendicular leg of 0.92 m, based on Eq. (2.4.37). The top horizontal pipe is 2.39 m (without including the Z bend), long enough to absorb the thermal expansion. Similarly, the thermal expansion in the vertical leg that is connected to the NDHX can be completely absorbed by the bottom horizontal pipe. For the bottom horizontal pipe, the thermal expansion is found to be 1.35 cm, requiring a perpendicular absorbing leg of 1.83 m. The vertical leg that is connected to the NDHX is only 1.54 m, which seems not sufficient to accommodate the expansion. However, the 0.8-m Z bend in the bottom horizontal pipe is adequate to make up the remaining required length. Actually, it has been found that Z bends are 40% more effective than L bends in absorbing thermal expansions (ASHRAE Handbook, 2008). Similarly, the thermal expansion of 1 cm in the top horizontal pipe can be absorbed by the Z bend and the vertical leg above the DHX.

To support the components in the DRACS test facilities that are at high elevations, a platform has been designed. The platform is supposed to be able to withstand the loads exerted by these components, which are summarized in Table 2.4.12. The weights of the chimney pipes were estimated based on a wall thickness of 1/8th inch.

Table 2.4.12 Loads exerted onto the platform by the test facility components

Component	Weight (lbs)
Salt pump	2,151
High-temperature DHX	151
High-temperature NDHX	49
Secondary salt expansion tank	258
Low-temperature DHX	44
Low-temperature NDHX	126
Primary water tank	182
Secondary water tank	144
Accumulator	34
Chimney bottom	126
Chimney top	284
Chimney small pipe	98

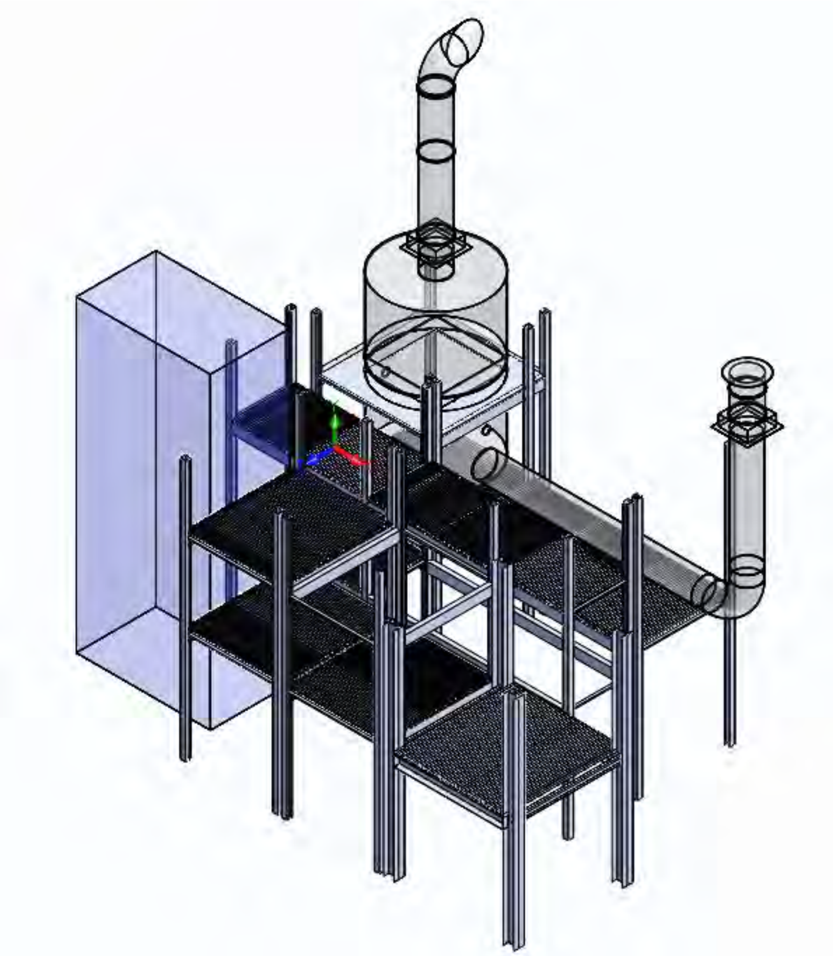

Fig. 2.4.31. Supporting platform for the DRACS test facilities

As can be seen from Table 2.4.12, the load exerted by the salt pump is considerable. To ensure safety steel beams (I beam and H beam) have been selected as the main support structure for the salt pump. For all other components, pallet ranks, which are pre-engineered framings, are strong enough to support the loads. A platform that has been designed for the support of the DRACS test facilities is illustrated in Fig. 2.4.31. Pallet racks from UNIRAK have been considered in the current design. The uprights and the load beams that are adopted are UFH37 and SB552, respectively, the capabilities of which are summarized in Tables 2.4.13 and 2.4.14. In the present platform design, the spacing between floorings will not exceed 70 inches and the maximum length for the load beam is 108 inches, indicating that the adopted pallet racks will survive for the loads other than the salt pump.

Table 2.4.13 Capabilities of the pallet rack uprights

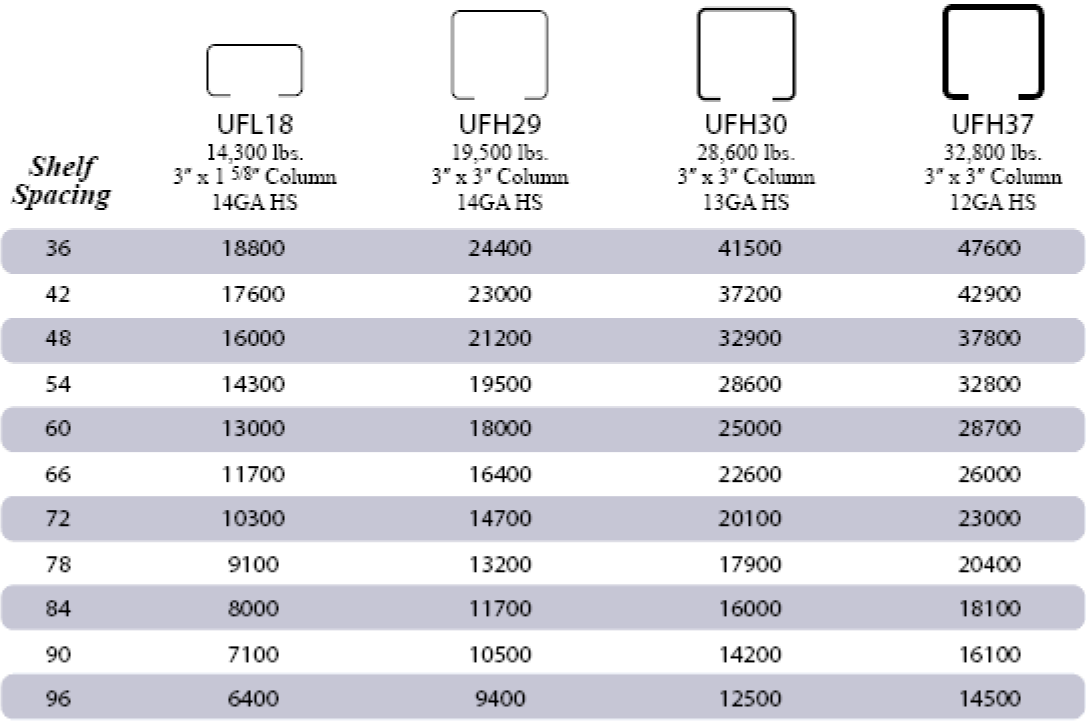

Shelf Spacing	UFL18 14,300 lbs. 3" x 1 5/8" Column 14GA HS	UFH29 19,500 lbs. 3" x 3" Column 14GA HS	UFH30 28,600 lbs. 3" x 3" Column 13GA HS	UFH37 32,800 lbs. 3" x 3" Column 12GA HS
36	18800	24400	41500	47600
42	17600	23000	37200	42900
48	16000	21200	32900	37800
54	14300	19500	28600	32800
60	13000	18000	25000	28700
66	11700	16400	22600	26000
72	10300	14700	20100	23000
78	9100	13200	17900	20400
84	8000	11700	16000	18100
90	7100	10500	14200	16100
96	6400	9400	12500	14500

Table 2.4.14 Capabilities of the pallet rack load beams

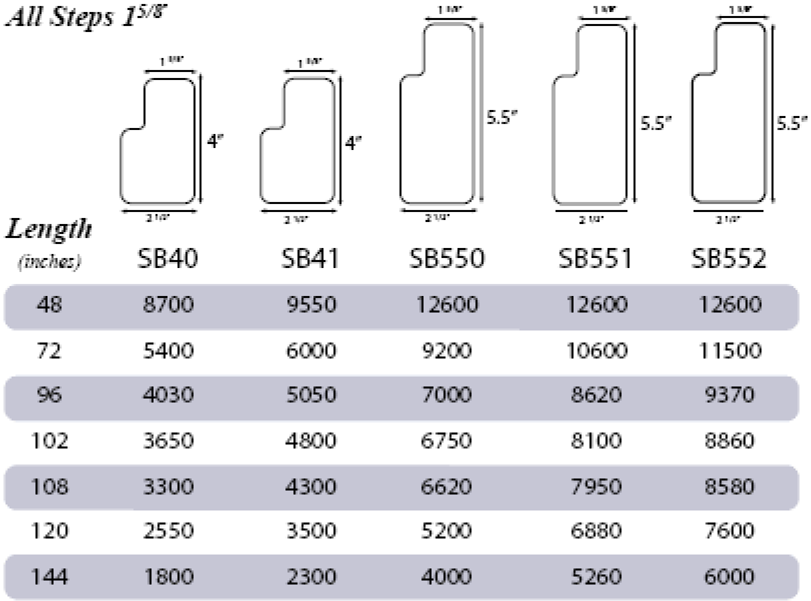

All Steps 1 5/8"

Length (inches)	SB40	SB41	SB550	SB551	SB552
48	8700	9550	12600	12600	12600
72	5400	6000	9200	10600	11500
96	4030	5050	7000	8620	9370
102	3650	4800	6750	8100	8860
108	3300	4300	6620	7950	8580
120	2550	3500	5200	6880	7600
144	1800	2300	4000	5260	6000

Steel bar gratings have been selected for the floorings, as illustrated in Fig. 2.4.31. When the bar gratings are subject to external loads, the main stress that may cause the failure is the bending stress. To identify the proper size for the bar gratings, the bending stress resulted from external loads were estimated as (Clark Engineers, Inc.):

$$\sigma = \frac{Fab}{a+b}\frac{h/2}{I} \tag{2.4.49}$$

where *F* is the external load, and *a* and *b* are the distances from the two anchor points to the point where the load is applied, respectively, as shown in Fig. 2.4.32. *I* denotes the moment of inertia of the grating, which can be estimated as:

$$I = \frac{wh^3}{12}N \tag{2.4.50}$$

where w and h are the bar width and height, respectively; N is the total number of the bars. The steel bar gratings (Metal Depot) adopted have a yield strength of 42,000 psi, which should not be exceeded by the resulted bending stress from the loads. Using Eqs. (2.4.49) and (2.4.50), it is found that gratings with bar size of 1.5” tall and 0.25” wide and bar spacing of 19/16” are needed to support the salt pump, while smaller gratings with bar size of 1” tall and 0.125” wide and spacing of 19/16” are sufficient for other components. The resulted maximum bending stress lies in the gratings for the pump, which is approximately 15,480 psi, smaller than the yield strength of the gratings.

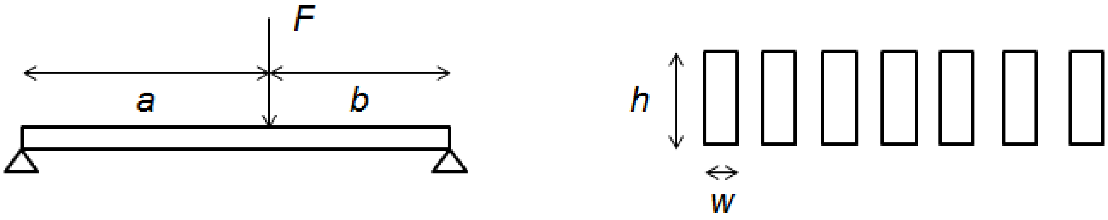

Fig. 2.4.32. Bar gratings subject to external load

As mentioned earlier, steel beams are used as the supporting frame for the salt pump to ensure safety. 6-inch H beams (5.99” by 0.23” web by 5.99”) are used for the supporting columns and the loading beams and 3-inch I beams (3” by 0.17” web by 2.33”) are used for the bracing beams. The caused stress in the supporting structure for the salt pump was analysed through a CFD simulation, the result of which is shown in Fig. 2.4.33. A direct conclusion that can be drawn from the simulation is that no failure is expected in the supporting structure. As also can be seen, most of the stress is accumulated in the gratings that have direct contact with the pump tank, and the loading beams. The maximum stress is located in the gratings, which is smaller than estimated by Eqs. (2.4.49) and (2.4.50). The main reason is that a point load is assumed for those two equations, which will lead to larger estimated bending stress.

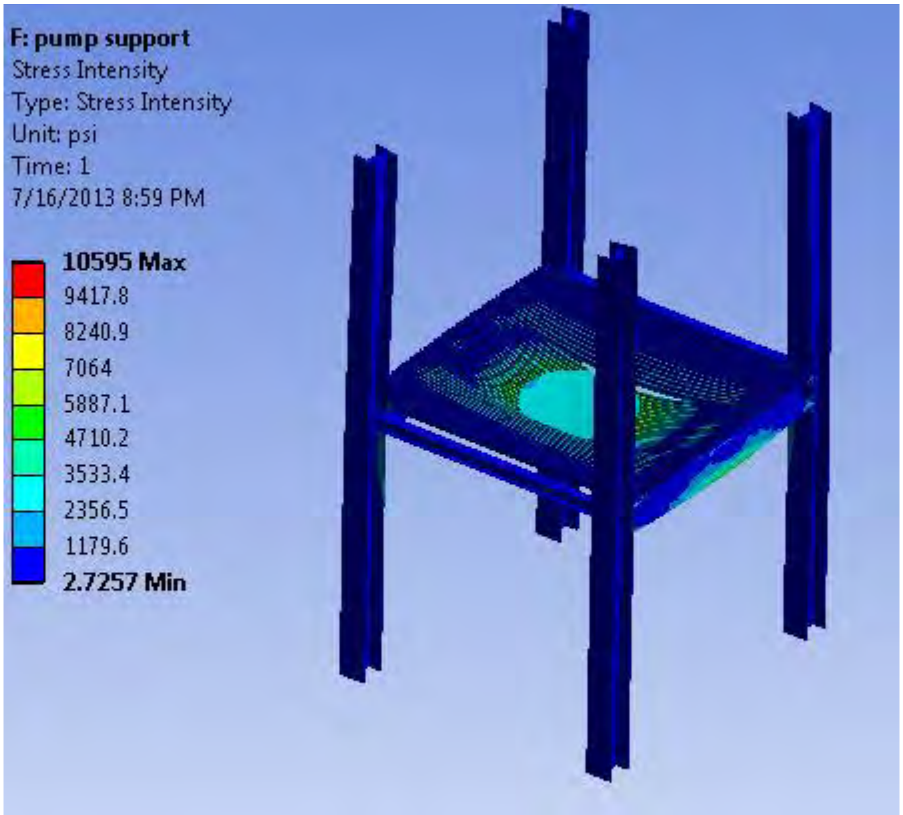
F: pump support
Stress Intensity
Type: Stress Intensity
Unit: psi
Time: 1
7/16/2013 8:59 PM
10595 Max
9417.8
8240.9
7064
5887.1
4710.2
3533.4
2356.5
1179.6
2.7257 Min

Fig. 2.4.33. Stress caused in the supporting structure for the salt pump

Data Acquisition System and Power Controlling System

To acquire the data on the temperature, pressure/differential pressure, salt level, and flow rate, a data acquisition has been designed as shown in Fig. 2.4.34. This data acquisition is based on input modules from National Instruments. The cDAQ-9178 chassis is a basis that provides connection between the input modules and the PC. This chassis contains 8 slots and supports up to 256 channels. Signals from the thermocouples are voltage signals in the order of a few tens of mV, which can be measured directly by the voltage input module NI 9213. Signals from the flow meters, pressure transducers, and level sensors are current signals in the range of 4-20 mA. These current signals will be converted to 1-5 V voltage signals using 250-ohm resistors before they are measured by the voltage input module NI 9205. This data acquisition system will be shared by both the LTDF and HTDF.

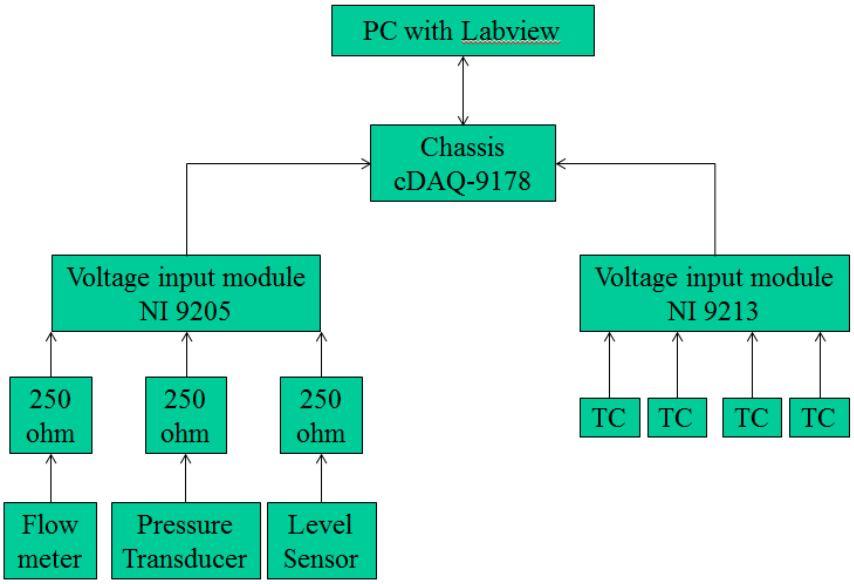
PC with Labview
Chassis cDAQ-9178
Voltage input module NI 9205
Voltage input module NI 9213
250 ohm
250 ohm
250 ohm
TC
TC
TC
TC
Flow meter
Pressure Transducer
Level Sensor

Fig. 2.4.34. Data acquisition system for the two test facilities

For the two test facilities, the total power available from the core heaters is larger than the nominal design power, which enables to simulate the decay power profile. To simulation the decay power profile, a power controlling system has been designed as shown in Fig. 2.4.35. The SCR power controller is controlled by Labview to modulate the power. Due to the built-in thermocouple in the heater, the heater internal temperature can be monitored by the limit controller. When the heater internal temperature exceeds the set point, the limit controller will trigger the 1-pole contactor to turn off the heater, which prevents the heater from overheating.

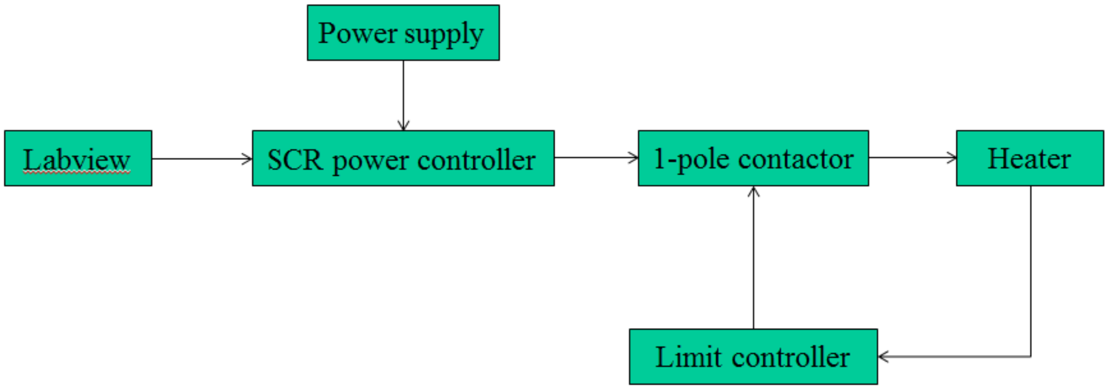
Power supply
Labview
SCR power controller
1-pole contactor
Heater
Limit controller

Fig. 2.4.35. Power controller for the core heaters

The actual power that is supplied to the heaters will be monitored using watt transducers from Ohio Semitronics. The watt transducers will be connected following the SCR power controllers and measure the current and voltage simultaneously, producing a 4-20 mA output current signal that is proportional to the power. Because the SCR controllers are operated in zero-crossing mode (the mode in which the power is modulated by adjusting the number of fired cycles over a fixed time period), a 5-second filter has to be added to the watt transducers to smooth out the output signal.

General CFD Study of Vortex Diodes

Previously, a parametric CFD study was performed to obtain a vortex diode design for the HTDF. However, the vortex diodes examined therein employed converging/diverging nozzles, not general for other applications. In addition, only a narrow Reynolds number range (711-4,789) was covered in the previous study. In regard of this, a more general CFC study of vortex diodes, covering wider Reynolds number range (Re < 30,000), was performed. Correlations for the forward and reverse Euler numbers were developed, which would be useful for any design purposes.

For the new set of vortex diodes that have been studied, straight inlet and outlet nozzles, and a disk-shape chamber with curved periphery are employed, as shown in Fig. 2.4.36. The dimensions of the investigated vortex diodes are summarized in Table 2.4.15. The inlet and outlet nozzles have same inner diameter, which is also identical to the chamber height. The examined chamber ratio (ratio of the chamber diameter to chamber height) ranges from 4 to 10. Three different inlet/outlet sizes have been studied, including 0.5", 1", and 1.5" nominal pipe size (Schedule 40). In addition, the inlet and outlet nozzles are extended, with a length of 3 times of the chamber diameter for the axial nozzle and a length of 2 times of the chamber diameter for the tangential nozzle. One of the main reasons to employ extend inlet/outlet nozzles is to eliminate any reverse flows at the inlet/outlet boundaries. In addition, in either the forward or the reverse flow direction, the flow field and correspondingly the pressure drop characteristics in the exit pipe following the chamber will be significantly affected by the flow in the chamber. Therefore, it is more reasonable to investigate the pressure drop in the exit pipe as an integral part of the total pressure drop in the vortex diode.

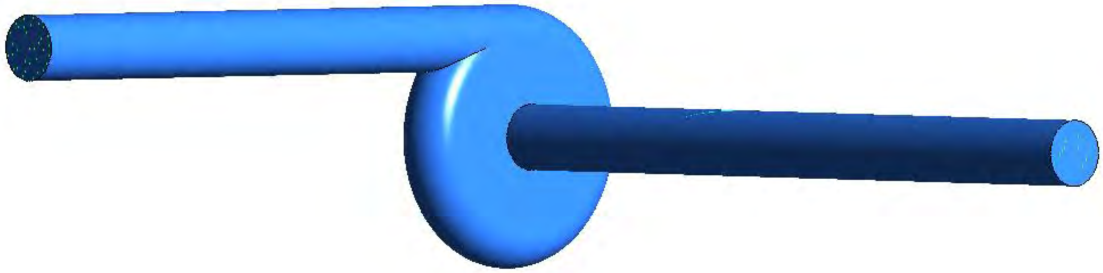

Fig. 2.4.36. Geometry of the vortex diode

Table 2.4.15 Dimensions of the studied vortex diodes

Chamber Height (inch/cm)	Aspect Ratio	Inlet/Outlet Size (inch/cm)
0.5/1.58	4, 6, 8, and 10	0.5/1.58
1/2.66		1/2.66
1.5/4.09		1.5/4.09

There have been preceding numerical studies of vortex diodes performed in different Reynolds number ranges. Figs. 2.4.37 and 2.4.38 show the calculated pressure drops/diodicity compared with the experimental results by Kulkarni et al. (2008) and Yoder et al. (2011), respectively. The study by Klukarni et al. indicates that for Reynolds number less that around 30,000, laminar model will predict better results than k-epsilon model. In the study by Yoder et al. (2011), k-epsilon model is used for high Reynolds number (Re > ~ 20,000) and predicts the result well. Based on these findings, we decided to divide the entire Reynolds number range into two, Re < 30,000 and Re > 30,000. For our study, we focused on the range of Re < 30,000, and selected laminar model for all the calculations.

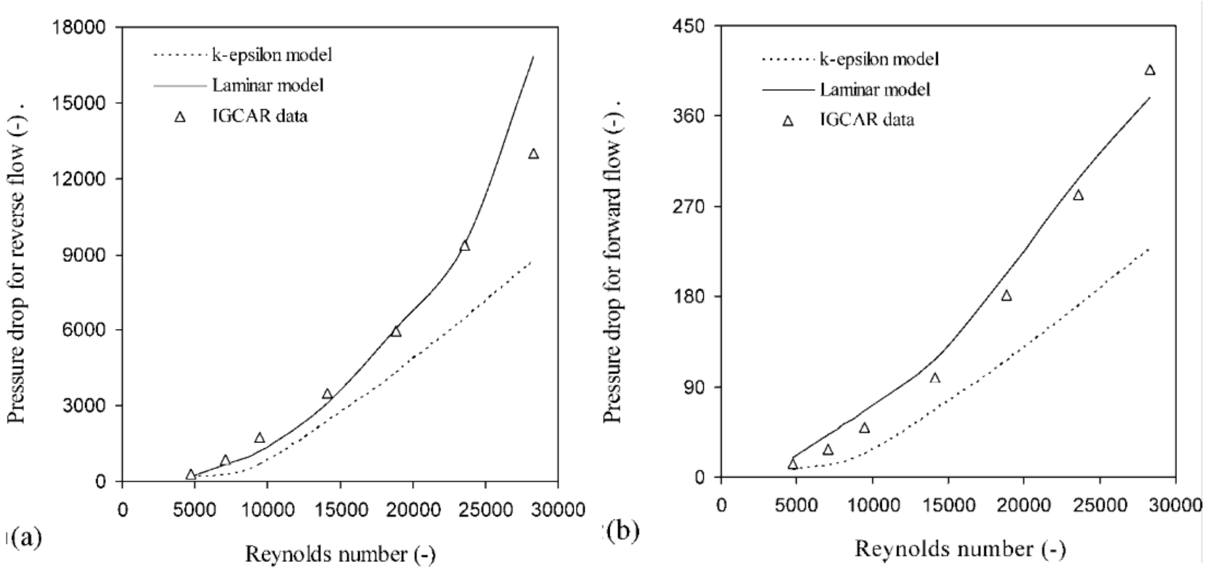

Fig. 2.4.37. Comparison of calculated pressure drops with experimental data (Klukarni et al., 2008)

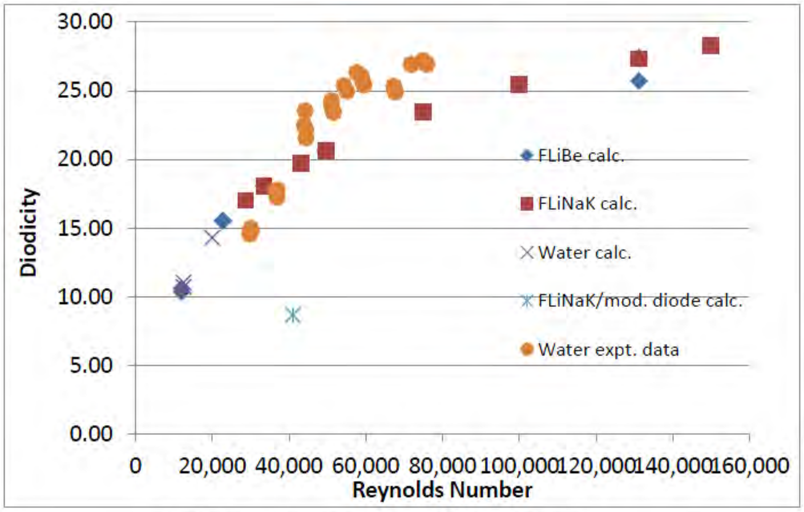

Fig. 29. Comparison of experimental data and CFD predictions.

Fig. 2.4.38. Comparison of calculated diodicity with experimental data (Yoder et al., 2011)

For numerical simulations, the results (pressure, temperature, et al.) are usually dependent on the mesh size. As the mesh size decreases, the simulation results will approach to values corresponding to infinitesimal mesh size, which are called the grid-converged solutions. The grid-converged solutions can be derived from three solutions based on three different meshes through Richardson extrapolation (Schwer, 2008):

$$f_{h=0} \cong f_1 + \frac{f_1 - f_2}{r^p - 1} \qquad (2.4.51)$$

where h is a measure of the mesh size; *f's* are the solutions based on different meshes; r is refinement ratio, defined as the ratio of the smaller mesh size to larger mesh size; and p is the order of convergence, which denotes how fast the solutions are approaching the grid-converged solutions as the mesh is refined. The order of convergence p is defined based on the difference between the solution corresponding to mesh size of h and the exact solution as:

$$E = f(h) - f_{exact} = Ch^p + H.O.T \tag{2.4.52}$$

where C is a constant, and *H.O.T* are the higher order terms. For three meshes of $h_1 < h_2 < h_3$ with constant refinement ratio of r, the order of convergence can be calculated as:

$$p = \frac{\ln\left(\dfrac{f_3 - f_2}{f_2 - f_1}\right)}{\ln r} \tag{2.4.53}$$

If the mesh refinement ratio is not constant, the order of convergence can be solved for from the following equations:

$$p = \frac{\left|\ln\left|f_{32} / f_{21}\right| + q(p)\right|}{\ln r_{21}} \tag{2.4.54}$$

$$q(p) = \ln\left(\frac{r_{21}^p - s}{r_{32}^p - s}\right) \tag{2.4.55}$$

$$s = sign\left(f_{32} / f_{21}\right) \tag{2.4.56}$$

where r_{ij} and f_{ij} are defined as:

$$f_{ij} = f_i - f_j \tag{2.4.57}$$

$$r_{ij} = h_j / h_i \tag{2.4.58}$$

The solutions obtained from Eq. (2.4.51) are actually approximations to the grid-converged solutions, as it is impossible to use mesh vanishing mesh size. There is an error band associated with the solutions obtained from Eq. (2.4.51), which is dictated by the so-called grid convergence index (GCI):

$$GCI_{21} = \frac{F_s}{r^p - 1}\left|\frac{f_2 - f_1}{f_1}\right| \tag{2.4.59}$$

where Fs is the safety factor. If three meshes have been used for the evaluation of the GCI, 1.25 can be used for the safety factor.

For numerical simulations, usually the mesh has to be refined until the corresponding solutions are within the range determined by Eqs. (2.4.51) and (2.4.59), i.e., $(1 - GCI)f_{h=0}$ to $(1 + GCI)f_{h=0}$. In the present parametric CFD study, a grid convergence study has been performed to determine the appropriate mesh size. Due to the large quantity of cases involved in the present study, it is unrealistic to perform the grid convergence study for each case. Therefore, one selective case with inlet size of 1 inch, aspect ratio of 4, and inlet mass flow rate of 0.1203 kg/s was examined to determine the mesh size which was applied to all other cases.

In the present study, the mesh was generated using the ICEM mesher, in which a global maximum surface mesh size and maximum volume mesh size can be specified. The mesh can be refined by decreasing the scale factor, which will scale down both the surface and volume mesh size. In the grid convergence study, a maximum surface mesh size of 2 mm and a maximum volume mesh size of 6 mm were applied. Four different meshes were examined by decreasing the scale factor from 1 to 0.7692, 0.5917, and 0.4552, which would yield a constant refinement ratio of 0.7692. The calculated forward and reverse pressure drops are summarized in Table 2.4.16. Based on the results for the first three meshes, the predicted ranges for the grid-converged forward and reverse pressure drops are 64.08-70.25 Pa and 122.48-129.80 Pa, respectively. As can be seen, the results for mesh 3 lie in the predicted ranges, indicating that mesh 3 is fine enough for present study. Therefore, for all the cases involved, a maximum surface mesh size of 2 mm and volume mesh size of 6 mm, and scale factor of 0.5917 have been applied.

Table 2.4.16 Results of the grid convergence study

Scale Factor	Cell Number	Forward Pressure Drop (Pa)	Reverse Pressure Drop (Pa)
1	516,675	71.22	112.52
0.7692	871,911	70.39	120.11
0.5917	1,502,154	69.74	123.26
0.4552	2,738,145	67.33	127.58
Converged solution based on first three meshes		67.17	126.14
GCI		0.046	0.029
Range		64.08-70.25	122.48-129.80

Typical flow patterns in the diodes in the forward and reverse directions are shown in Figs. 2.4.39 and 2.4.40. In the forward flow direction, majority of the flow in the chamber is in the radial direction. When the flow approaches the chamber periphery, secondary recirculation flow is formed. After the flow exits the chamber, the secondary recirculation flow dissipates quickly and majority of the flow becomes longitudinal. In the reverse flow direction, strong swirling flow is formed after the flow enters the chamber. The swirling component remains after the flow exits from the chamber, extending over the entire outlet nozzle. This swirling component alters the friction characteristics in the outlet pipe significantly.

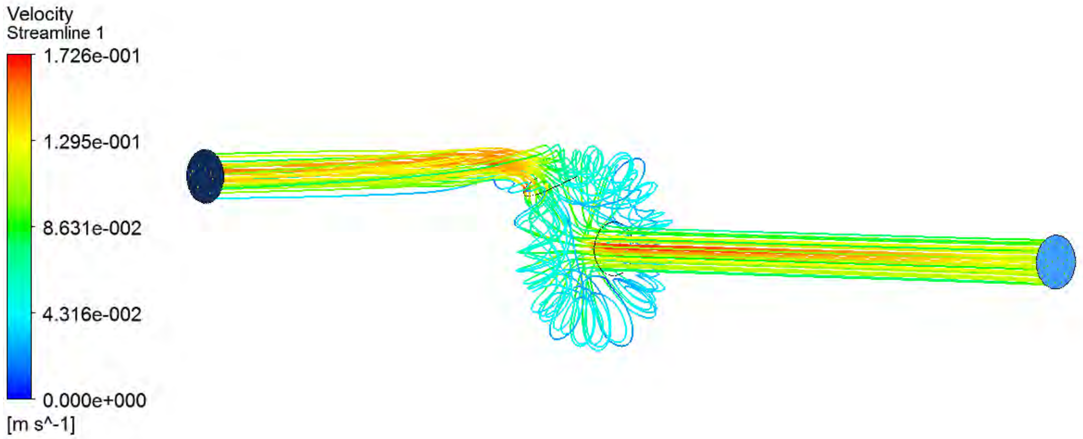

Fig. 2.4.39. Flow pattern in the forward flow direction

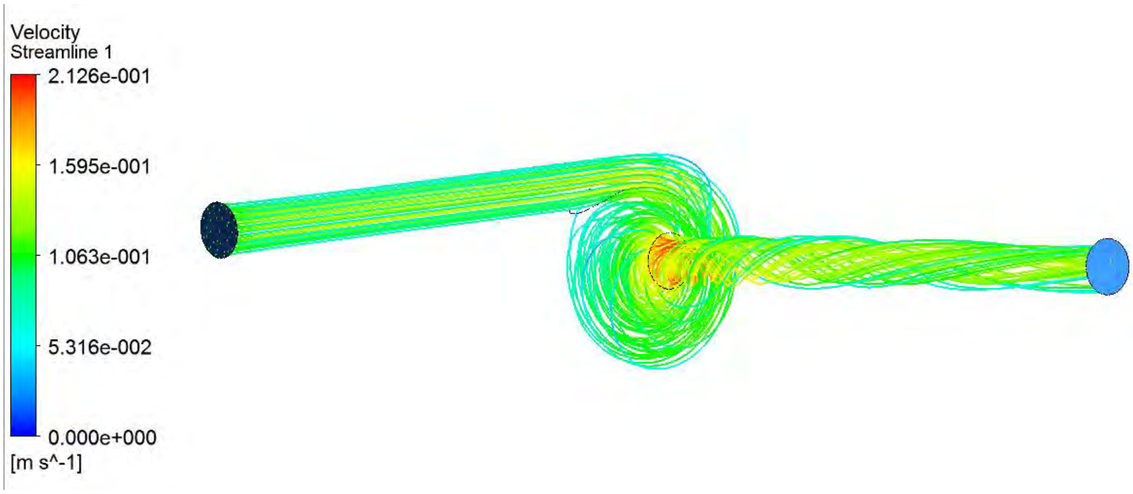

Fig. 2.4.40. Flow pattern in the reverse flow direction

The effects of the Reynolds number and aspect ratio on the forward and reverse Euler numbers are illustrated in Figs. 2.4.41-2.4.46. In the forward flow direction, the Euler number has a negative dependence on the Reynolds number, and a positive dependence on the aspect ratio. This is related to the pressure drop mechanism in the forward flow direction, which is mainly the friction in the nozzles and the chamber, and the form loss. For friction pressure drop, the pressure drop coefficient has a negative dependence on the Reynolds number. In addition, the friction pressure drop is proportional to the ratio of the flow length to the hydraulic diameter, which in present case is represented by the aspect ratio. Another characteristic observed is that the forward Euler number approaches a constant as the Reynolds number increases, which is due to the form loss when the flow enters and leaves the chamber.

In the reverse flow direction, the Euler number increases with the Reynolds number for Re > 10,000. However, for Re < 10,000, the Euler number is flat or even shows a decreasing trend with the Reynolds number. The above features are again related to the pressure drop mechanism in the reverse flow direction. In the reverse flow direction, the pressure drop is due to the accelerational pressure drop in the chamber, friction in the nozzles, and form loss. As found in the previous CFD study of vortex diodes for the HTDF, the accelerational pressure drop in the chamber has a positive dependence on the Reynolds number, while the friction pressure drop in the nozzles has a negative dependence on the Reynolds number. At low Reynolds number, the friction pressure drop dominates, making the overall Euler number show a flat and even decreasing trend. However, at higher Reynolds number, the accelerational pressure drop is dominant, making the overall Euler number shown an increasing trend with the Reynolds number.

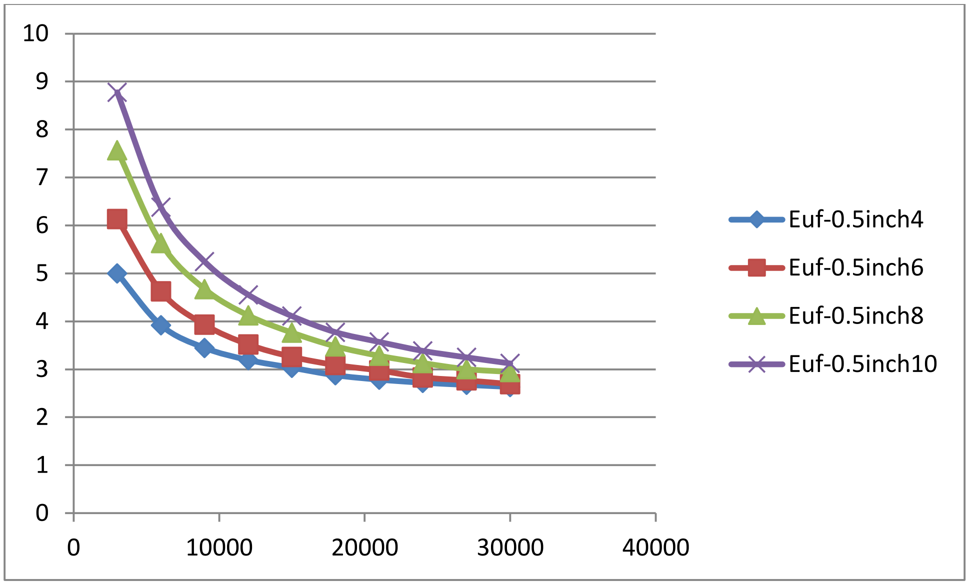

Fig. 2.4.41. Forward Euler number for vortex diode with 0.5-inch inlet/outlet

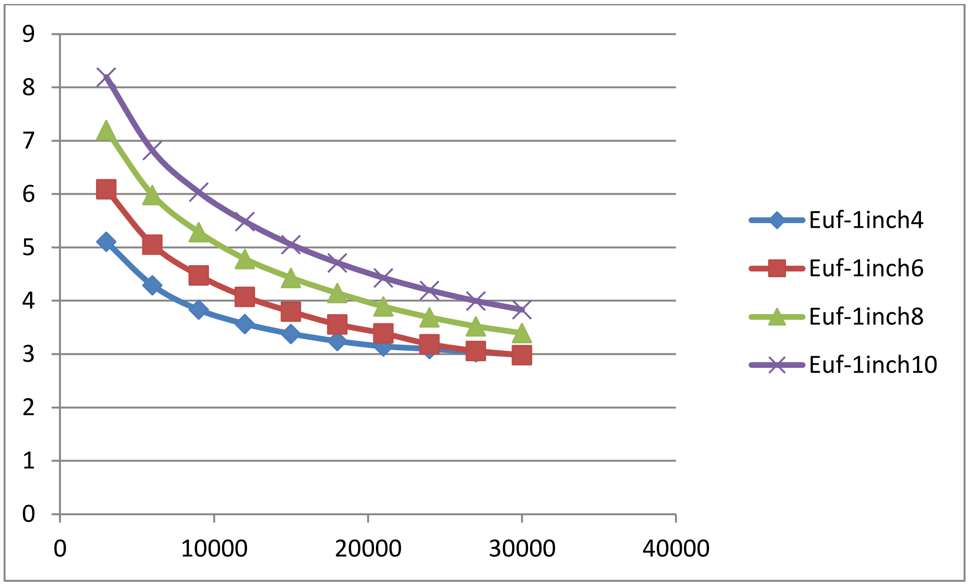

Fig. 2.4.42. Forward Euler number for vortex diodes with 1-inch inlet/outlet

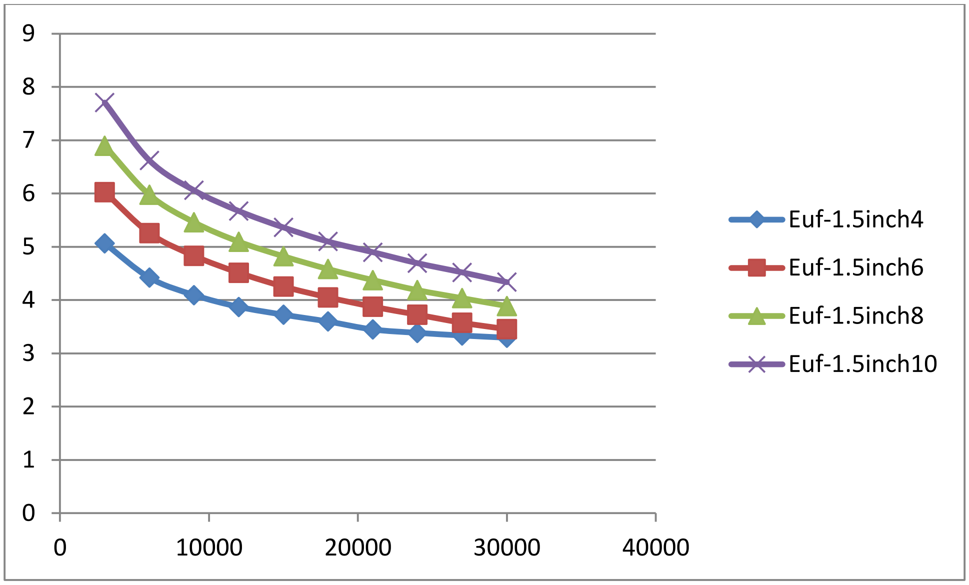

Fig. 2.4.43. Forward Euler number for vortex diodes with 1.5-inch inlet/outlet

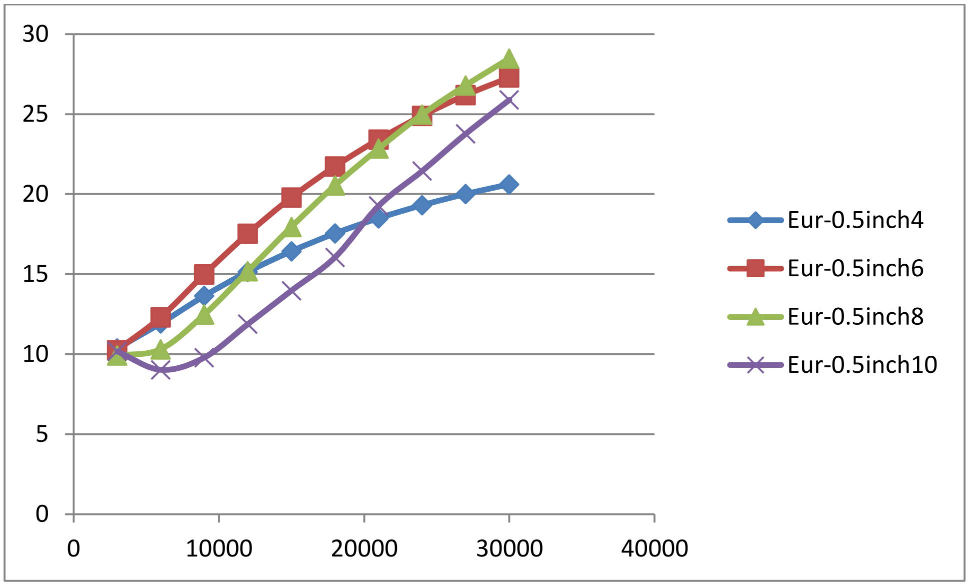

Fig. 2.4.44. Reverse Euler number for vortex diode with 0.5-inch inlet/outlet

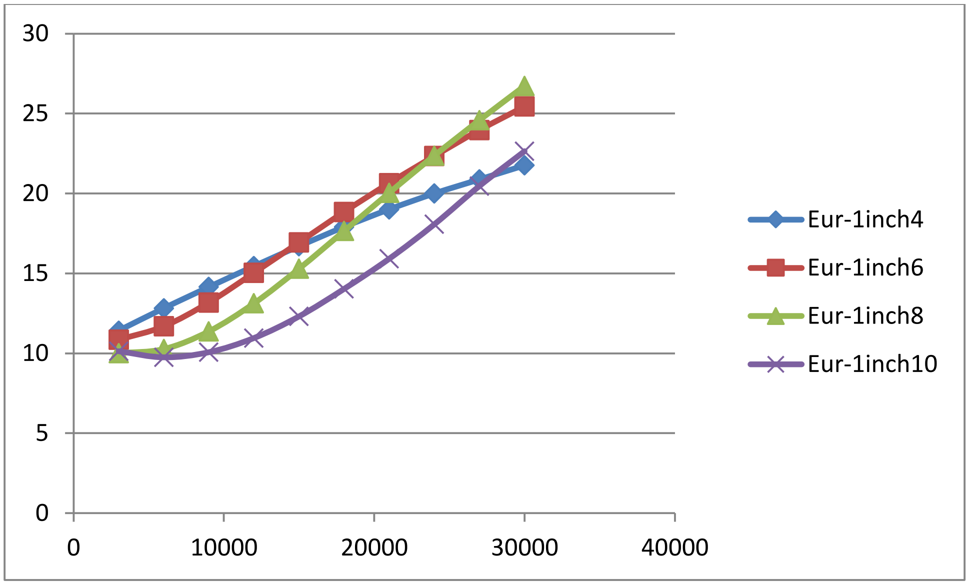

Fig. 2.4.45. Reverse Euler number for vortex diode with 1-inch inlet/outlet

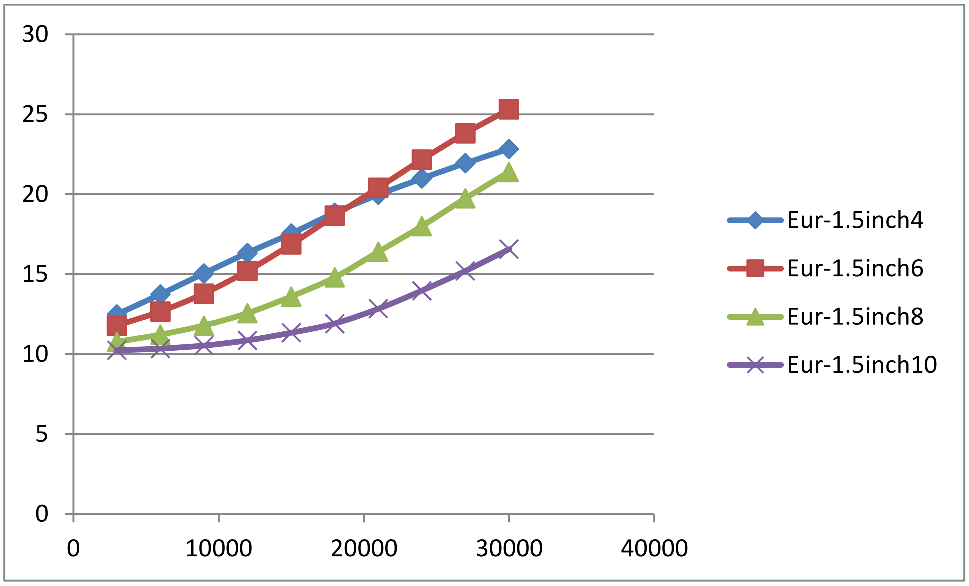

Fig. 2.4.46. Reverse Euler number for vortex diode with 1.5-inch inlet/outlet

The calculated forward and reverse Euler numbers were correlated with the Reynolds number and the aspect ratio. As discussed earlier, the pressure drop in the forward flow direction is due to the friction and form loss, the former of which is proportional to the aspect ratio. Therefore, the forward Euler number can be correlated with the Reynolds number and aspect ratio in the following format:

$$\mathrm{Eu}_{\mathrm{f}} = A + \frac{B\alpha}{\mathrm{Re}^{C}} \tag{2.4.60}$$

For the reverse flow direction, as discussed in previous CFD study, the accelerational pressure drop coefficient in the chamber has the format similar to Eq. (2.4.31). Taking into account of the friction in the nozzles and the form loss, it is found that a good correlation for the reverse Euler number can be expressed as:

$$\mathrm{Eu}_r = \left(-\frac{D}{\alpha^2}+\frac{E}{\alpha}\right)^2 \mathrm{Re}^F + \frac{G\alpha}{\mathrm{Re}^H} + I \tag{2.4.61}$$

The correlational coefficients shown above are summarized in Table 2.4.17. These coefficient are valid in the Re range of 3,000-30,000, and aspect ratio range of 4-10.

Table 2.4.17 Coefficients in the forward and reverse Euler number correlations

	0.5" Inlet/Oulet	1" Inlet/Oulet	1.5" Inlet/Oulet
A	2.1	2.2	2.6
B	313.7	52.8	23.1
C	0.764	0.550	0.467
D	1.388	0.670	7.622
E	0.487	0.253	3.192
F	0.928	1.025	0.518
G	156.4	30.0	13.6
H	0.705	0.504	0.428
I	4.48	5.17	1.61

Trace Heating

Due to the high melting points of the salts, salt solidification may occur during the operation of the HTDF, especially in some stagnant points. To compensate for the heat loss and/or over-cooling, and to re-thaw the solidified salt, trace heaters have been considered for the HTDF. In addition, due to the high temperatures, heat loss from the HTDF to the ambience is severe, and accounts for a significant percentage of the total power from the core. The best insulation material for the HTDF identified so far is the WDS Ultra from Porextherm, which features low thermal conductivity of almost half of that of fiberglass. However, even with such an insulation material of 5 inch thick, the total heat loss from the HTDF is still approximately 849 W, accounting for 8.5% of the total core power. Therefore, the trace heaters are also intended to compensate for the heat losses.

Heat losses from the different sections in the primary and secondary loops are calculated, as summarized in Tables 2.4.18 and 2.4.19. Also listed are the corresponding temperature drops of the salts based on the nominal salt flow rates. The temperature drop of the salt over each section is not significant, implying that the locations of the trace heaters are not critical as long as correct amount of heat loss is compensated for. Four tape heaters with a total capability of 2.5 kW are adopted for the primary loop; 3 tape heaters with a total capability of 2.5 kW are adopted for the secondary loop; and 5 tape heaters with a total power of 3.0 kW for the pump loop. As can be seen, the total power from these tape heaters is larger than needed for the heat losses, which is mainly due to the consideration of re-thawing the salts in case of severe salt solidification upon complete loss of electricity for hours. During the operation of the HTDF, the heat losses will be carefully compensated for by using the variable transformers.

Table 2.4.18 Heat losses in the primary loop

	Heat Loss (W)	Temperature Drop (°C)
Core->DHX	66.6	0.29
DHX	46.3	0.20
DHX->Fluidic Diode	90.6	0.40
Fluidic Diode->Core	105.2	0.46
Core	112.7	0.50
Total	421.4	1.85

Table 2.4.19 Heat losses in the secondary loop

	Heat Loss (W)	Temperature Drop (°C)
DHX->NDHX	185.7	1.40
NDHX->DHX	242.4	1.82
Total	428.1	3.22

High-temperature Insulation

To inhibit the heat loss from the high-temperature facility to the ambience as much as possible, an insulation material with low thermal conductivity and capability of withstanding high temperature is desired. Based on the broad search, the best insulation material found so far is the WDS series from Porextherm, the thermal conductivity of which is shown in Table 2.4.20. The low thermal conductivity is achieved by the microporous structure in this type of material, and its maximum application temperature is 950°C (Porextherm). From the thermal conductivity point of view, it is desired to use this type of material for all the 5-inch thick insulation. However, due to the cost concern, we come up with a special design for the thermal insulation that consists of a 1-inch thick interior layer of WDS material and a 4-inch thick exterior layer of Pyrogel XT material. The Pyrogel XT has a lower temperature limit of 650°C, and higher but still comparable thermal conductivity to that of the WDS material at temperatures less than ~ 400°C, as shown in Fig. 2.4.47 (Aspen Aerogels). Based on our analysis, the 1-inch interior insulation is thick enough to reduce the temperature to less than 500°C that is acceptable for the Pyrogel XT. With this two-layer insulation design, the performance is still satisfactory, but the cost is lowered significantly.

Table 2.4.20 Thermal conductivity of the WDS series (Porextherm)

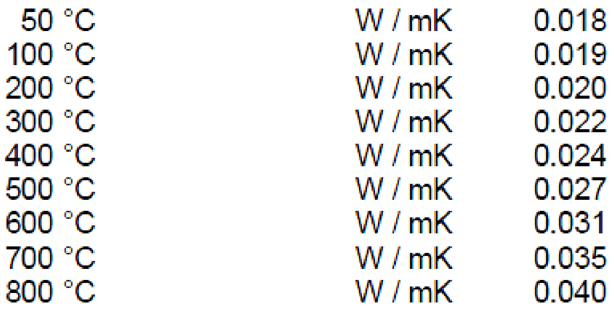

50 °C	W / mK	0.018
100 °C	W / mK	0.019
200 °C	W / mK	0.020
300 °C	W / mK	0.022
400 °C	W / mK	0.024
500 °C	W / mK	0.027
600 °C	W / mK	0.031
700 °C	W / mK	0.035
800 °C	W / mK	0.040

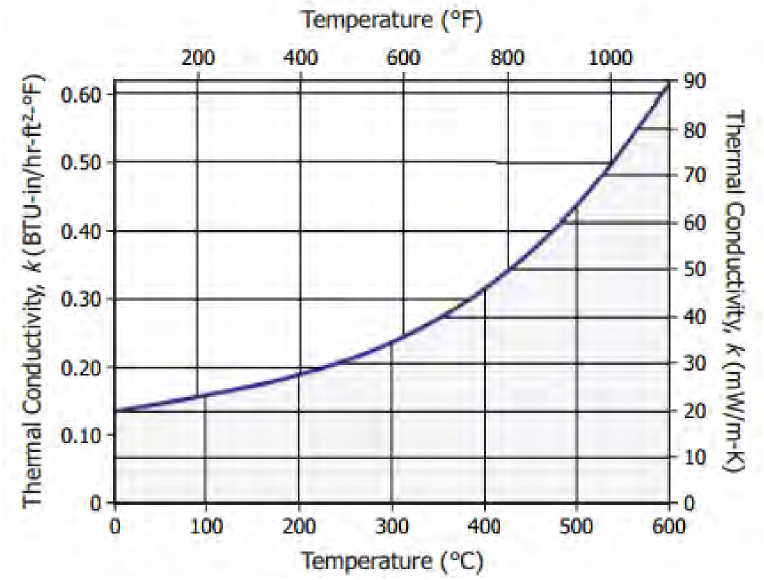

Fig. 2.4.47. Thermal conductivity of the Pyrogel XT (Aspen Aerogels)

High-temperature Bolting

To prevent leakage from occurring at any flange connections, the flanges need to be properly bolted. This contains two aspects, namely, the use of appropriate bolting materials (bolts, nuts and washers) and carefully following the correct bolting rules. Per ASME code, ASTM A193 B8 (equivalent to AISI SS304) bolts are recommended for high-temperature application up to 1500°F, and are thus selected for the HTDF. It should be noted that there are 2 classes for the ASTM 193 B8 material, namely, class 1 and 2. Class 2 has higher strength (tensile and yield) than class 1, and is selected. ASTM A194 Grade 8 hex nuts and SS304 washers are used with the aforementioned bolts per ASME code.

To properly bolt the flanges, the following rules should be followed:

1. Tighten the bold following specific pattern;
2. Apply preload torque of 40% to 70% of the bolt yield strength, which should be:
   2.1. sufficient to guarantee correct gasket seating stress;
   2.2. and less than the flange and gasket stress limit;
3. Apply the preload torque in steps, e.g., 30%, 60%, and 100% of the needed preload.

For the spiral wound gaskets used in the HTDF, sufficient preload is very important. The initial compressive load should make gasket conform to the flange surface and sufficiently compressed to compensate for internal voids or spaces that could be detrimental to a seal. In addition, the recommended upper limit of 70% of the bolt yield strength should be based on that at the elevated application temperature. Lastly, one common problem encountered with the bolts in high-temperature application is the stress relaxation. Shown in Fig. 2.4.48 are the typical stress relaxation curves for a few bolting materials. As can be seen, the remaining stress in the SS304 bolt material after 1,000-hour continuous operation decreases significantly as the temperature exceeds 600°C. In the HTDF, the salt temperatures are above 600°C, and it is highly recommended to retighten the bolts after every running of the facility (~ 50 hours).

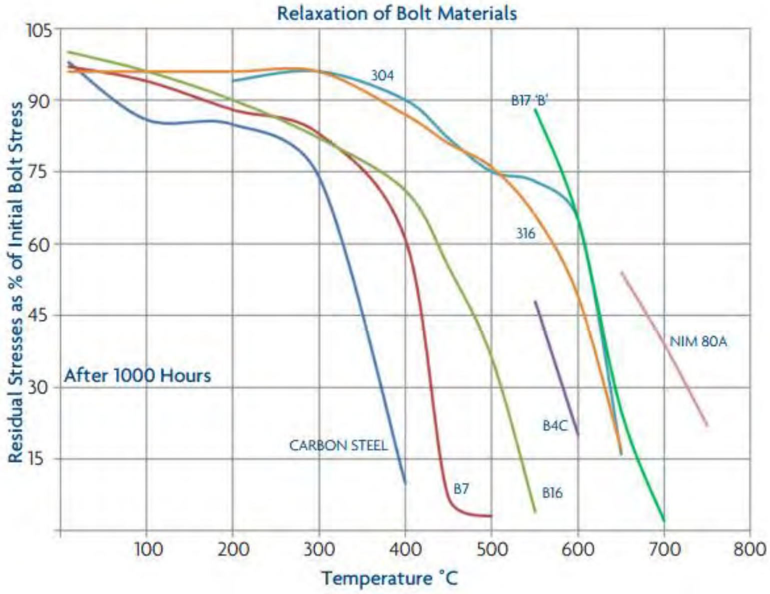

Fig. 2.4.48. High temperature stress relaxation (BOLTIGHT)

Pump Support Platform

A platform made from steel I-beams and bar gratings is designed to support the pump along with the pump tank. Previously, a stress analysis was performed based on the total weight of the pump, tank, and salt, with the results shown in Fig. 2.4.33. It was concluded that most of the stress was accumulated in the bar gratings and no failure would occur in the support platform. It should be noted that this analysis was based on the assumption that all the I-beams would be welded together. However, due to the size limit of the entrance to our lab, this platform has been redesigned with bolt connections adopted between the I-beams. The two horizontal loading I-beams that the bar gratings will directly sit on are connected to the main column beams with totally sixteen ½”-13 bolts. Based on the shear strength (approximately 60% of the ultimate tensile strength) of the bolts, a maximum weight of approximately 131,947 lbs can be supported, which is much bigger than the actual weight (~ 2,594 lbs).

In the previous stress analysis, it was also assumed that the total load was applied to a circular area that was equivalent to the area of the pump tank bottom surface (24” in diameter). However, the actual pump tank design, as shown in Fig. 2.4.52, employs three 5” by 5” footing plates. Because of the reduced contact area, the maximum stress in the bar gratings can be increased by six times, exceeding the yield strength of the steel bar gratings (~ 30 ksi). Due to this concern, a 24” circular steel plate with a thickness of 0.5” has been added between the tank and the bar gratings to distribute the load over a bigger area and avoid local failure in the bar gratings. In addition, to have the flexibility of adjusting the pump tank elevation, the pump tank will be supported from the bar gratings (with the 24” circular plate on top) with totally eight 7/8”-9 bolts. Both the compression limit and the thread stripping limit of these bolts have been examined, which are approximately 14,829 and 68,271 lbs/per bolt, respectively. These limits are significantly bigger than the total load that will be encountered, indicating that the tank along with the pump can be safely supported. Lastly, as can be seen from Fig. 2.4.49, there are four (one plate on the back can’t been seen from the current view) small rectangular plates with two holes welded onto the side of the tank. These plates not only work as the stoppers for the lap-joint flange but also provide additional support to the pump tank from the side.

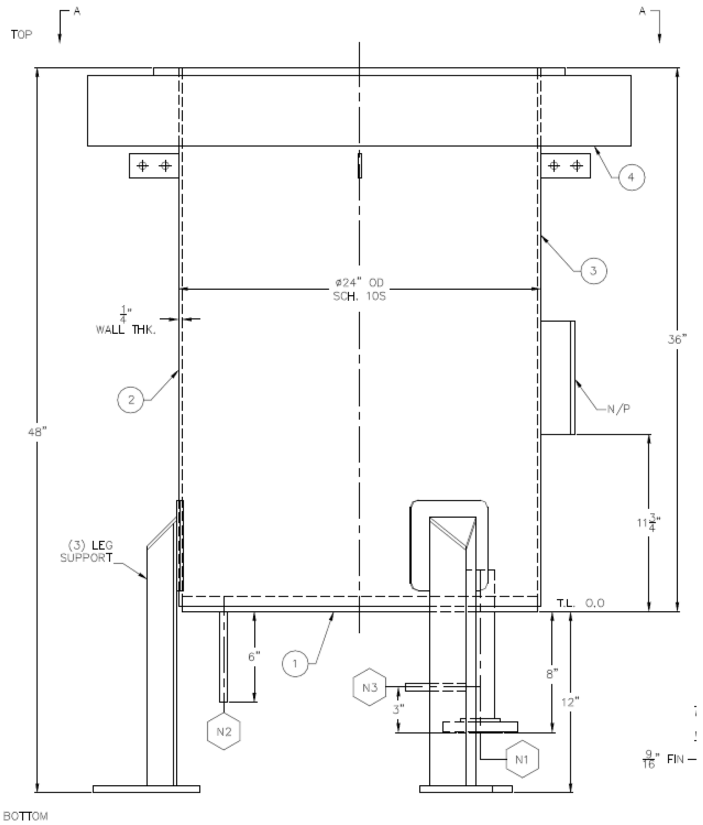

Fig. 2.4.49. Drawing of the pump tank

Power Controlling and Monitoring System

During the last quarter, we have completed the majority of the power controlling and monitoring system for the HTDF. A few snapshots of the system can be found from Fig. 2.4.50 to Fig. 2.4.52. The power control mechanism for the seven core heaters in the HTDF is similar to that for the LTDF. The only difference is that additional current transformers have been adopted to reduce the high electric currents through the HTDF core heaters before they are fed into the watt transducers for measurement. For the heaters used to melt the primary and secondary salts, on-off type control is needed, which only requires the temperature controllers and electric contactors, but not SCR controllers. As discussed earlier, the compensation for the heat loss in the HTDF is provided by the trace heaters and is adjusted through four variable transformers, which are shown in Fig. 2.4.51. All the temperature controllers are housed in a separate electric enclosure located in the control room for convenience.

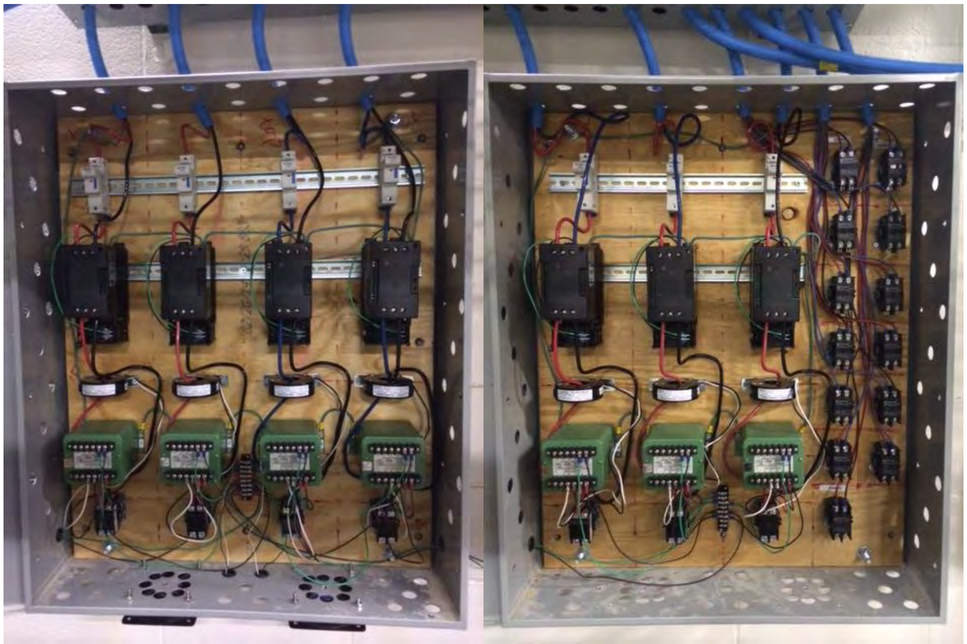

Fig. 2.4.50. Controllers for the core heaters and salt melting heaters

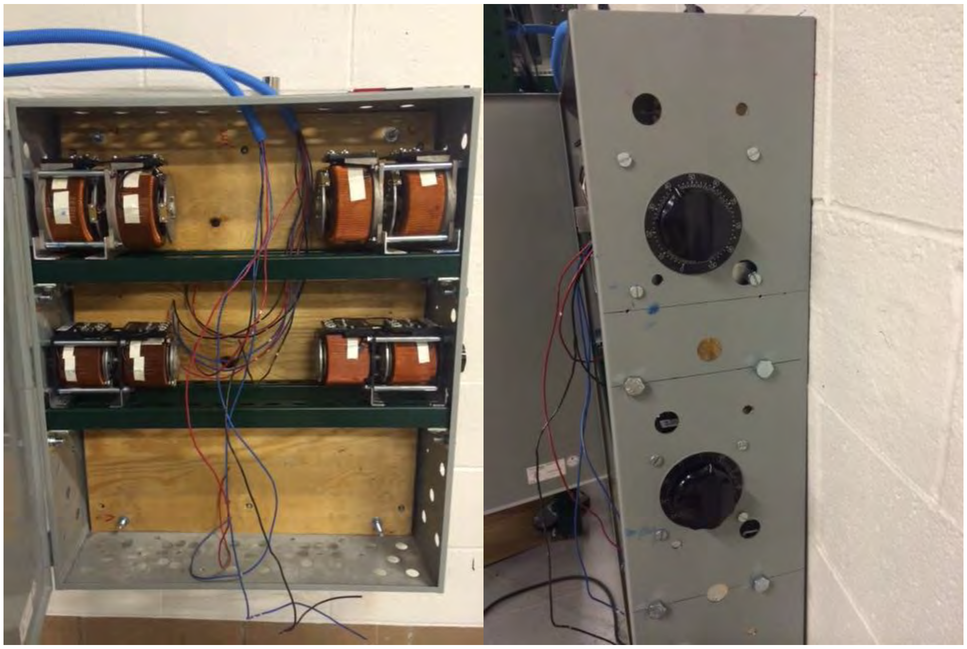

Fig. 2.4.51. Variable transformers for the trace heaters

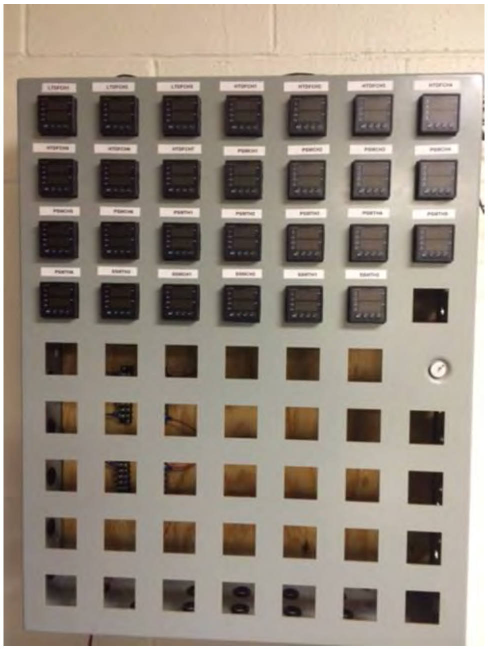

Fig. 2.4.52. Temperature controllers located in the control room

References

American Society of Heating, Refrigerating and Air-Conditioning Engineers, Inc, *ASHRAE Handbook – HVAC Systems and Equipment*, 2008.

ANSYS, http://www.ansys.com/Products/ANSYS.

Aspen Aerogels, http://www.aerogel.com/_resources/common/userfiles/file/Data%20Sheets/Pyrogel_XT_DS.pdf

Babbitt International, http://www.babbittlevel.com/LTM-4.pdf

Blander, M., Grimes, W.R., Smith, N.V., and Watson, G.M., “Solubility of Nobel Gases in Molten Fluorides. II. in the LiF-NaF-KF Eutectic Mixture”, *Journal of Physical Chemistry*, **63**, pp. 1164-1167, 1958.

Blick, R.G., “Bending Moments and Leakage at Flanged Joints,” *A Gulf Publishing Company Publication*, 1950.

BOLTIGHT Data Sheet, http://www.boltight.com/resources/Data-Sheets/DS-90-High-Temperature-Stress-Relaxation.pdf, accessed on August 26th, 2014.

Briant, R.C., and et.al., Aircraft Nuclear Propulsion Project Quarterly Progress Report, ORNL-1294, Oak Ridge National Laboratory, Oak Ridge, TN, 1952.

Chowdhury, M.R., and Fester, V.G., “Modeling Pressure Loses for Newtonian and Non-Newtonian Laminar and Turbulent Flow in Long Square Edged Orifices,” *Chemical Engineering Research and Design*, **90**, pp. 863-869, 2012.

Chromalytic Technology, http://www.chromtech.net.au/, accessed on April 28th, 2014.

Crane Co., “Flow of Fluids through Valves, Fittings, and Pipe”, New York, N.Y., 1982.

DPTM50 from Honeywell, http://www.honeywell-cooling.com/pdfs/products/Electronic_Controls/5_Equipment_for_SHC/4_DPTM/DB/de/DPTM50-500%20Druckdifferenztransmitter%20FEMA_GE0B-0466GE51%20R1007.pdf

Flexim, http://www.flexim.com/us

Grimes, W.R., Smith, N.V., and Watson, G.M., “Solubility of Nobel Gases in Molten Fluorides. I. in Mixtures of NaF-ZrF$_4$ (53-47 Mole %) and NaF-ZrF$_4$-UF$_4$ (50-46-4 mole %)”, *Journal of Physical Chemistry*, **62**, pp. 862-866, 1958.

John Miltion Clark Engineers, Inc., *Beam Theory Drivation*.

Kulkarni, A.A., Ranade, V.V., Rajeev, R., and Koganti, S.B., “CFD Simulation of Flow in Vortex Diodes”, *AIChE Journal*, **54**, pp. 1139-1152, 2008.

Kulkarni, A.A., Ranade, V.V., Rajeev, R., and Koganti, S.B., “Pressure Drop across Vortex Diodes: Experiments and Design Guidelines,” *Chemical Engineering Science*, **64**, pp. 1285-1292, 2009.

Metal Depot, https://www.metalsdepot.com

McDonald, R.A., Sinke, G.C., and Stull, D.R., “High Temperature Enthalpy, Heat Capacity, Heat of Fusion, and Melting Point of Zirconium Tetrafluoride,” *J. Chem. Eng. Data*, **7**(1), pp. 83-83, 1962.

Misra, A.K., and Whittenberger, J.D., “Thermal Energy Storage Applications in the Temperature Range 973 to 1400 K,” AIAA-87-9226, 22nd Intersociety Energy Conversion Engineering Conference, August 10-14, 1987, Philadelphia, PA.

Narasimha, R., and Sreenivasan, K.R., “Relaminarization of Fluid Flows,” *Adv Appl Mech*, **19**, pp. 221-309, 1979.

ONEhalf20, http://www.onehalf20.com/pdf/datasheets/nak_filled_melt_pressure_transducers_model_RTNAK_data_sheet.pdf

Porextherm, http://www.jrsuk.com/downloads/wds/Ultra.pdf, accessed on April 28th, 2014.

Powers, W.D., and Blalock, G.C., “Enthalpies and Heat Capacities of Solid and Molten Fluoride Mixtures,” ORNL-1956, Oak Ridge National Laboratory, Oak Ridge, TN, 1956.

Priestman, G.H., “A Study of Vortex Throttles Part 1: Experimental,” *Proc Inst Mech Eng*, **21**(C5), pp. 331-336, 1987.

Priestman, G.H., “A Study of Vortex Throttles Part 2: Viscid Flow Analysis,” *Proc Inst Mech Eng*, **21**(C5), pp. 337-345, 1987.

Ragab, S., and Sreedhar, M., “Numerical Simulation of Vortices with Axial Velocity Deficits,” *Phy*

Fluids, **7**(3), pp. 549-558, 1995.

Rogers, D.J., Yoko, T., and Janz, G.J., “Fusion Properties and Heat Capacities of the Eutectic LiF-NaF-KF Melt,” *J. Chem. Eng. Data*, **27**, pp. 366-367, 1982.

Sabharwall, P., Ebner, M., Sohal, M., Sharpe, P., Aderson, M., Sridharan, K., Ambrosek, J., Olson, L., and Brooks, P., “Molten Salts for High Temperature Reactors: University of Wisconsin Molten Salt Corrosion and Flow Loop Experiments – Issues Identified and Path Forward,” INL/EXT-10-18090, Idaho National Laboratory, Idaho Falls, ID, 2010.

Schwer, L.E., “IS YOUR MESH REFINED ENOUGH? Estimating Discretization Error using GCI,” LS-DYNA Anwenderforum, Bamberg, 2008.

Shaffer, J.H., “Preparation and Handling of Salt Mixtures for the Molten Salt Reactor Experiment,” ORNL-4616, Oak Ridge National Laboratory, Oak Ridge, TN, 1971.

Stairmand, J., “Flow Patterns in Vortex Chambers for Nuclear Duties,” *Nucl Energy*, **29**(6), pp. 413-418, 1990.

Technical Glass Products, http://www.technicalglass.com/cfq0-5.html, accessed on April 28th, 2014.

Todreas, N.E. and Kazimi, M.S., *Nuclear Systems I Thermal Hydraulic Fundamentals*, pp. 67, Taylor & Francis, 1990.

Yoder, G.L., Elkassabgi, Y., Leon, G.D., Fetterly, C., Ramos, J., Robbins, J., and Cunningham, R.B., “Vortex Diode Analysis and Testing for Fluoride Salt-Cooled High-Temperature Reactors,” ORNL/TM-2011/425, Oak Ridge National Laboratory, Oak Ridge, TN, 2011.

Williams, D.F., “Assessment of Candidate Molten Salt Coolants for the NGNP/NHI Heat-Transfer Loop”, ORNL/TM-2006/69, Oak Ridge National Laboratory, Oak Ridge, TN, 2006.

WOLFRAM, http://www.wolfram.com/.

Wormley, D.N., “An Analytical Model for Incompressible Flow in Short Vortex Chambers,” *J. Fluids Eng*, **91**(2), pp. 264-272, 1969.

Zobel, R., “Experiments on a Hydraulic Reversing Elbow”, *Mitt Hydr Inst Munich*, **8**, pp. 1-47, 1936.

2. Issues/Concerns

The design of the high-temperature facility has been completed, and it is currently under construction. In addition, the instrumentations have also been finalized. However, the feasibility and performance of the instruments (or instrument designs) cannot be determined until we start running the facility. As can be expected, the harsh environment will cause difficulty in operating the high-temperature test facility.

Task 2.5: Perform experiments with the low-temperature DRACS test facility to examine its thermal performance and reliability (Ohio State Responsible).

1. Task Status: In progress

Experiments have been performed in the low-temperature DRACS test facility (LTDF), which are divided into two categories, namely, the DRACS start-up scenario and pump trip scenario. The results for two representative experiments of the two scenarios are presented in the following discussions.

Scenario 1

In Scenario 1, the accident transient is initiated with no initial flows in both the DRACS primary and secondary loops. A step change of power from 0 to 2.1 kW is triggered at time point of 0 through the SCR power controllers controlled by a program written in Labview. Before the power is turned on, the pump is turned on to circulate the primary water so that a nearly uniform temperature is obtained in the primary loop. The pump is subsequently turned off and the pump loop is isolated from the remaining of the LTDF by closing the globe valve in the pump loop. Without a pump in the secondary loop, a nearly uniform initial temperature is realized by flushing the loop with fresh water from the secondary water tank where the temperature is uniform. For the air loop, as will be seen in the following discussion, there is an initial temperature variance along the loop and correspondingly a non-zero initial flow, due to the heating induced by the temperature gradient from the secondary water (at the room temperature) to the ambient air (at the outside ambient temperature, lower than the room temperature at the time when the experiment is carried out). The initial temperatures and flow rates are controlled with care so that the initial conditions can be correctly characterized when the experimental data are used for future code validation/benchmarking.

The development of the coolant temperatures and flow rates following the initiation of the transient is shown in Figs. 2.5.1 and 2.5.2. As can be seen, natural circulation/convection is successfully developed in all three loops, and a steady state is reached at approximately 35,000 seconds. After the heater power is turned on, due to the relatively fast heat conduction through the heater sheath, the primary water in the core is heated up almost immediately, which is the reason why an immediate temperature increase is seen at the core outlet, as shown in Fig. 2.5.1(b). Because of this, buoyance also starts to build up in the primary loop from the beginning, leading to the development of the primary flow, as seen from Fig. 2.5.2(a). The heated primary water therefore flows toward the DHX, leading to subsequent temperature increases at the DHX shell-side inlet and outlet, and core inlet, as shown in Fig. 2.5.1(b). The secondary water starts being heated up when the hot primary water gets to the DHX shell-side inlet at approximately 300 seconds. However, as shown in Fig. 2.5.2(a), the secondary flow stays as almost zero until approximately 650 seconds. This is mainly because the DHX is located in the bottom horizontal leg in the secondary loop, and there is a horizontal section between the DHX tube-side outlet and the vertical leg, as can be seen from Fig. 1.7.3. Heat has to be transferred to the vertical leg through heat conduction in water, which is a slow process, before the secondary flow starts to develop. For the air, as mentioned earlier, there is a small initial flow due to the heating by the secondary water, which can be seen from Fig. 2.5.2(b). This is the cause for the temperature decrease at the NDHX tube-side outlet, and subsequently the DHX tube-side inlet, as shown in Fig. 2.5.1(b). As the hot secondary water arrives at the NDHX tube-side inlet at approximately 1,000 seconds, the heat transferred to the air increases, causing an abrupt increase in the air flow rate, as seen from Fig. 2.5.2(b).

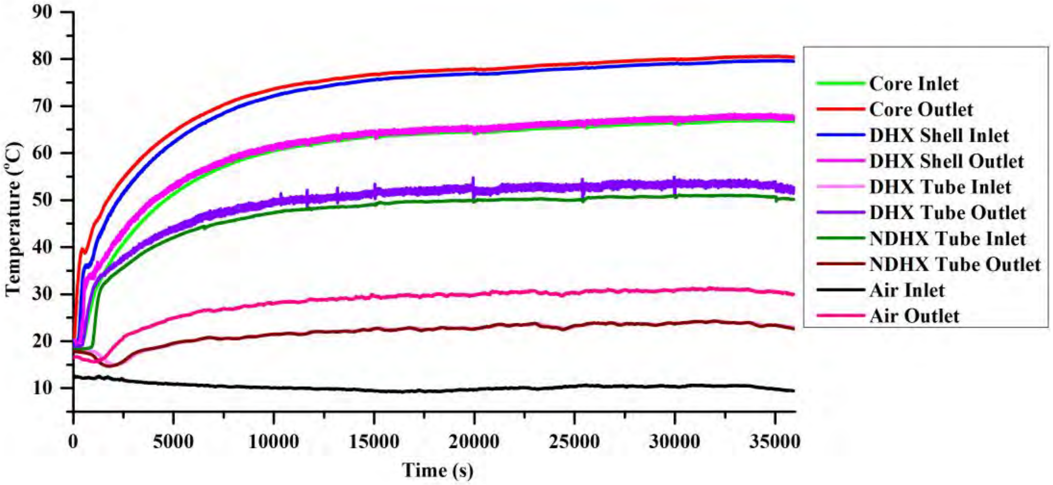

(a) Fluid temperature over 35,000 s (9.7 hours)

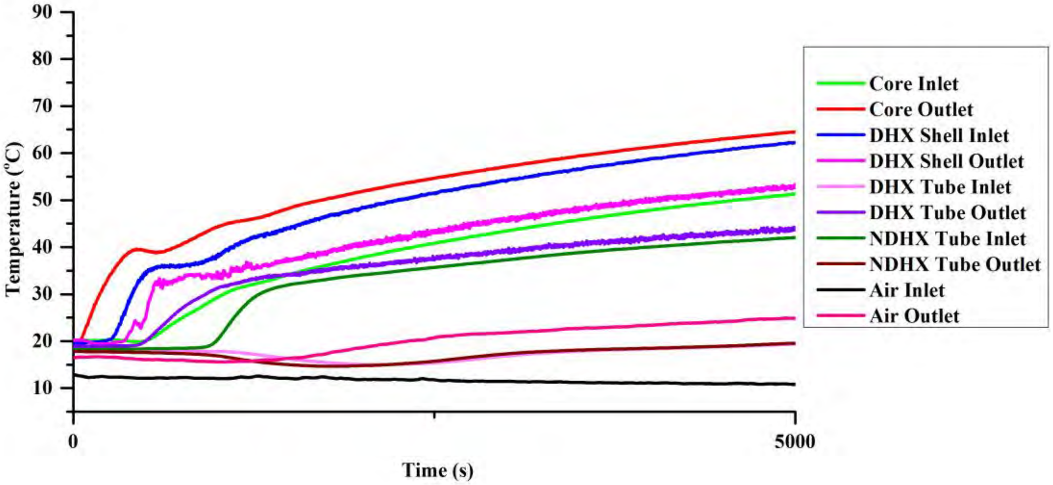

(b) Fluid temperature for the first 5,000 s

Fig. 2.5.1. Fluid temperature evolution during the startup transient (a) over 35,000 s and (b) for the first 5,000 s

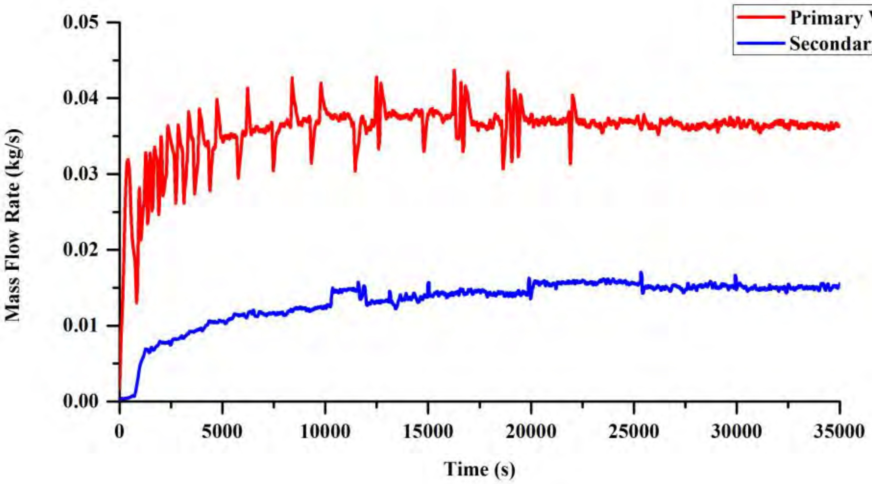

(a) Primary and secondary water

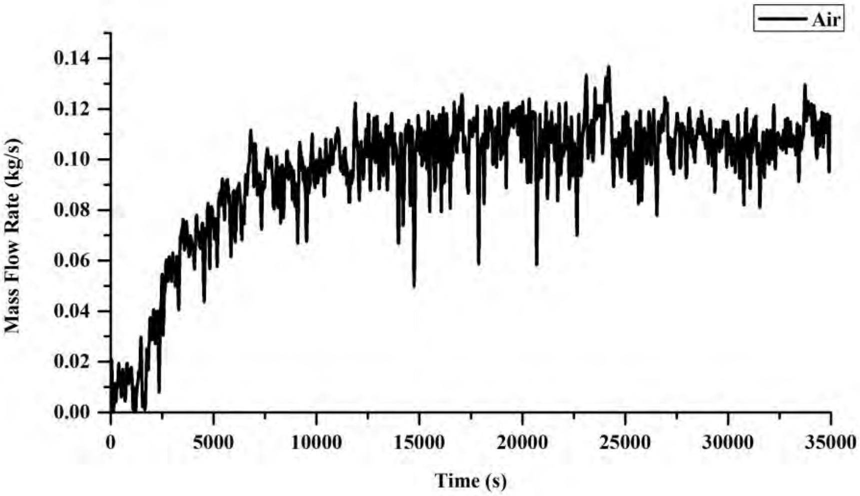

(b) Air

Fig. 2.5.2. Mass flow rates during the startup transient for (a) primary and secondary water and (b) air

The conditions of the steady state reached near the end of the transient are summarized in Table 2.5.1, along with the nominal conditions of the LTDF scientific design and the rating results of the as-built LTDF using the design code earlier developed for the LTDF. The as-built LTDF differs from the scientific design mainly in the DHX and NDHX (Lv et al., 2012). The rating process is based on the actual core operating power and air inlet temperature measured in the experiment, and assumes no heat loss. Uncertainties associated with the experimental results are analyzed using the root sum square method and are also given in Table 2.5.1. The uncertainties include both the random uncertainties associated with the measurements and the systematic uncertainties associated with the instruments, the latter of which are summarized in Table 2.5.2. The random uncertainties have been estimated to 95% confidence level. It is noted that the uncertainties of the flow rates are relatively big compared to the others. For the primary and secondary flow rates, this is mainly due to the minimum uncertainty of 9 mm/s of the clamp-on ultrasonic flow meters that have been used. Actually, this minimum uncertainty is typical for all the industrial ultrasonic flow meters that can be found so far. For the air flow rate, the uncertainty is mainly due to the random measurement uncertainty, which theoretically can be reduced by taking multiple measurements.

It should also be noted that, due to the heat loss along the pipes connecting the components of interest as well as the measurement uncertainties, there is a difference in temperature between the core outlet and DHX shell-side inlet, DHX shell-side outlet and core inlet, and so forth. The hot leg and cold leg temperatures of the primary and secondary loops, as well as the temperature differences given in Table II are averaged values over from 32,500 to 33,500 s. As can be seen from Table 2.5.1, the experimental flow rates and temperature differences between the hot and cold sides match the rating results well, indicating that the loop height and flow resistance in each of the LTDF loops have been properly scaled. In the present experiment, the primary throttling valve in the fluidic diode simulator and the secondary throttling valve are opened to positions yielding flow coefficients of 5.25 and 20, respectively (Lv et al., 2012). As can also be seen, the hot leg and cold leg temperatures of the secondary and air loops from the experiment match the rating results well, but not for the primary loop. This indicates that in the LTDF design code, the NDHX is correctly modeled, but the DHX is not. Another possible reason leading to the discrepancy could be the fouling resistance in the DHX, which is neglected in the LTDF design code. Effort in diagnosing the cause of the discrepancy is ongoing.

Table 2.5.1 Steady-state results and comparisons with the nominal LTDF design conditions and rating results of the as-built LTDF

	Design	Rating	Experiment
Power (W)	2,048	2,109	2,109 ± 21
Primary T_{hot} (^{o}C)	76.5	65.1	79.5 ± 0.4
Primary T_{cold} (^{o}C)	63.7	51.9	66.8 ± 0.4
Primary ΔT (^{o}C)	12.8	13.2	12.7 ± 0.5
Primary Water Flow (kg/s)	0.0376	0.0381	0.0365 ± 0.0086
Secondary T_{hot} (^{o}C)	65.2	54.1	52.2 ± 0.4
Secondary T_{cold} (^{o}C)	34.8	23.1	24.0 ± 0.4
Secondary ΔT (^{o}C)	30.4	31.0	28.3 ± 0.6
Secondary Water Flow (kg/s)	0.0161	0.0163	0.0150 ± 0.0034
Air T_{hot} (^{o}C)	40	30.8	31.0 ± 0.5
Air T_{cold} (^{o}C)	20	10.4	10.4 ± 0.6
Air ΔT (^{o}C)	20	20.4	20.6 ± 0.8
Air Flow (kg/s)	0.102	0.103	0.103 ± 0.017

Table 2.5.2 Measurement errors of the instruments

	Instrument Uncertainty
Ultrasonic Flow Meter	1% of reading + 9 mm/s
Thermal Mass Flow Meter	1% of reading + (0.5% + 0.05%/^{o}C) of full scale (ref: 21°C)
Differential Pressure Transducer	0.0525% of full scale
Gauge Pressure Transducer	0.075% of full scale
Thermocouple	0.5^{o}C or 0.4% of full scale
Watt Transducer	0.5% of full scale

A heat balance analysis has also been performed based on the steady-state results, as summarized in Table III. Due to the relatively large measurement uncertainties in the flow rates, large uncertainties are also encountered in the heat transfer rates due to the uncertainty propagation since the heat transfer rate is a function of the fluid mass flow rate. The implication learned here is that, for a natural circulation/convection system with small coolant flow rates, the large uncertainties in the measurements of the flow rates can cause large uncertainties in the heat balance calculations, making it difficult to quantify and model the heat loss. This issue will become more critical to any prototypic DRACS system, where heat loss would be significant due to the high temperatures of fluoride salts. Therefore, efforts in developing instruments capable of measuring small flows would deem necessary.

Table 2.5.3 Heat balance results

	Heat Transfer Rate (W)
Watt Transducer Reading	2,109 ± 21
Core	2,112 ± 504
DHX Shell Side	1,823 ± 442
DHX Tube Side	1,864 ± 426
NDHX Tube Side	1,700 ± 388
NDHX Air Side	2,144 ± 360

Scenario 2

In Scenario 2, a steady-state core normal operation is first simulated before initiating the accident transient. This simulated core normal operation is different from the prototypic core normal operation in that there is no intermediate heat exchanger (IHX) in the LTDF. Therefore, the LTDF simulated core will not provide the nominal core power but instead a power representing the parasitic heat loss to the DRACS during core normal operation. For the simulated core normal operation, a constant power of 1.6 kW is provided to the LTDF core. The pump speed is adjusted in conjunction with the opening of the globe valve in the reverse flow direction of the fluidic diode simulator so that the parasitic flow through the fluidic diode and the main flow through the core are approximately 0.072 and 0.894 kg/s, respectively. The system is maintained in operation until a steady-state is reached, following which the accident is initiated by shutting down the pump and step increasing the core power to 2.1 kW that represents the decay heat. The initial parasitic flow through the fluidic diode simulator is constantly monitored, and when it decreases to zero, the branch representing the forward flow direction is opened and the other branch closed.

The evolution of the coolant temperatures and flow rates following the pump trip is shown in Figs. 2.5.3 and 2.5.4. As can be seen from Fig. 2.5.3, following the pump trip, temperatures in the primary loop experience an abrupt change due to the flow reversal, and then gradually approach a steady state. The flow reversal in the primary loop causes a small perturbation in the secondary loop temperatures (NDHX tube-side inlet and DHX tube-side outlet), which then decays away over a short period of time. After that, the secondary temperatures increase slowly until a new steady state is reached. No immediate effect of the pump trip or flow reversal is observed on the air temperatures. The same characteristics are observed on the secondary water flow rate and air flow rate, as shown in Fig. 2.5.4(a). It can be seen from Figs. 2.5.4(b) and 2.5.4(c) that, after the pump trip, the residual pump flow and the parasitic flow through the primary loop decrease to zero very quickly, mainly due to the large flow resistance in the loop and relatively small inertia of the pump. The primary water flow is seen to decrease to zero over approximately 3 seconds and start to develop in the reverse direction immediately. No significant period of time during which the primary flow is stagnant is observed during the flow reversal process, mainly due to the existing temperature gradient and correspondingly buoyancy in the primary loop when the pump is shut down. Lastly, compared to the startup scenario discussed earlier, it takes much less time (~ 17,500 seconds) to reestablish the new steady state.

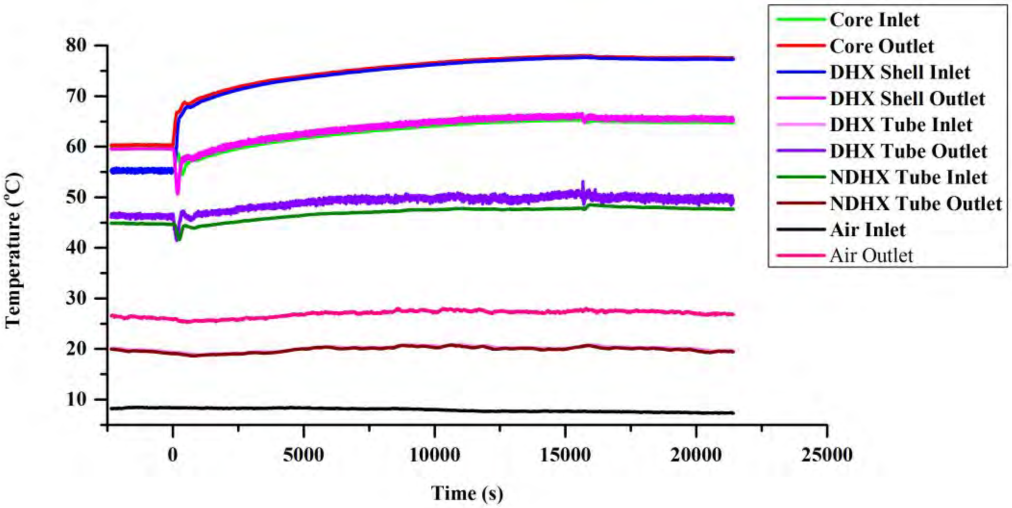

Fig. 2.5.3. Fluid temperature development during the pump trip transient

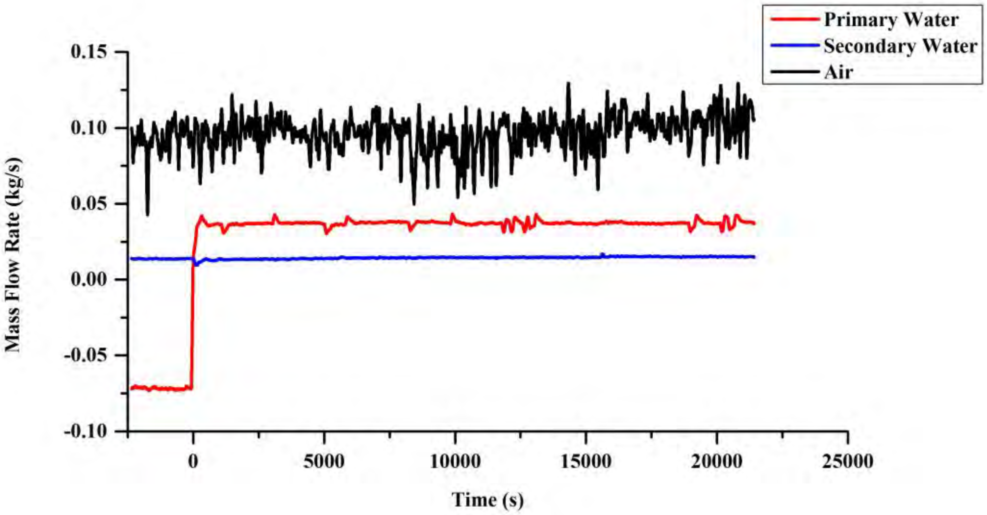

(a)

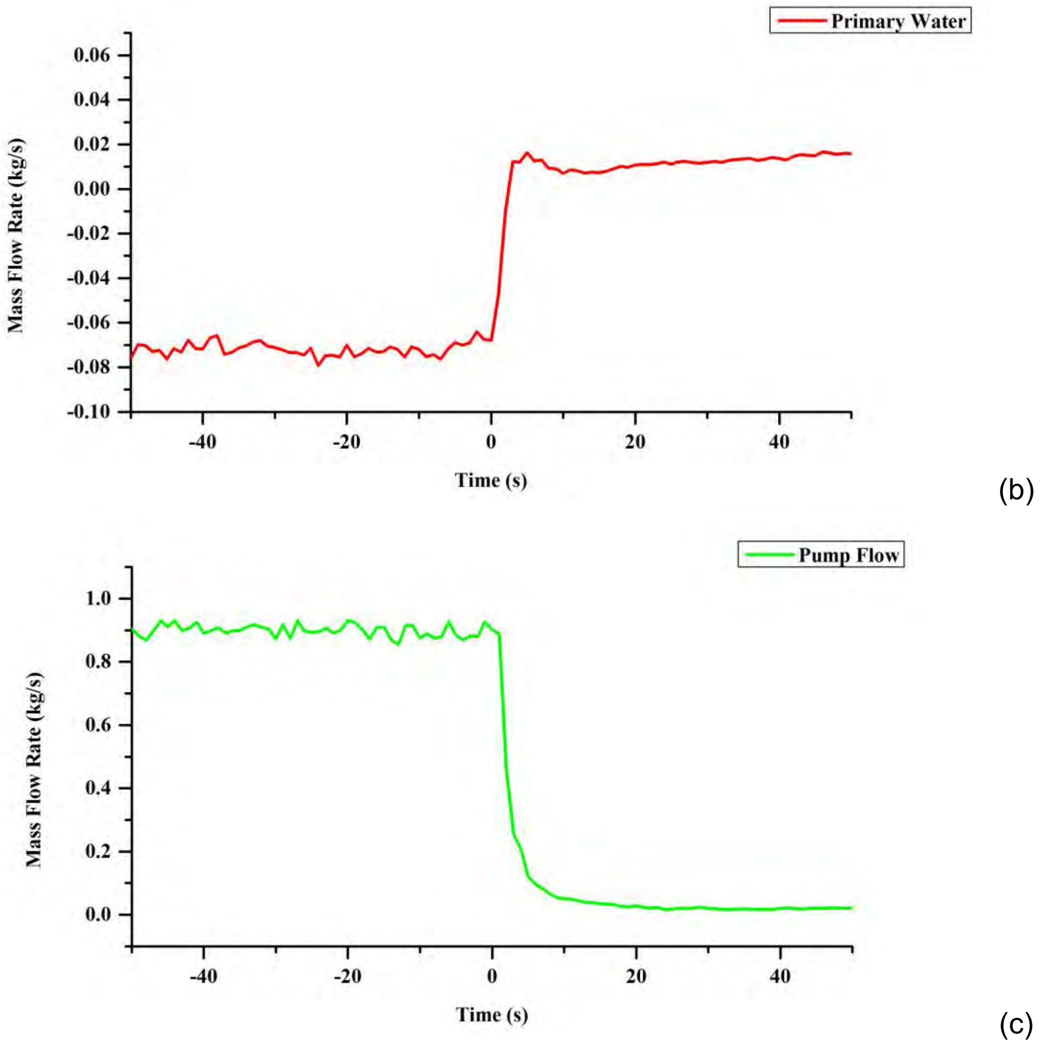

Fig. 2.5.4. Mass flow rates during the pump trip transient

References

Lv, Q., Wang, X., Adams, I., Sun, X., Christensen, R.N., Blue, T.E., Yoder, G., Wilson, D., and Sabharwall, P., "Design of a Scaled-down Low-temperature DRACS Test Facility for an AHTR," *Transaction of the American Nuclear Society*, American Nuclear Society 2012 Annual Meeting, Chicago, IL, June 24-28, 2012, Vol. 106, pp. 1071-1074.

2. Issues/Concerns
None

Patents/Publications/Presentations:

Patents:
None

Publications:
Q. Lv, H.C. Lin, X. Sun, R.N. Christensen, T.E. Blue, G. Yoder, D. Wilson, and P. Sabharwall, "Experimental Study of DRACS Thermal Performance in a Low-temperature

Test Facility," submitted to *NURETH16*, Chicago, IL, August 30-September 4, 2015.

Q. Lv, X. Wang, I.H. Kim, X. Sun, R.N. Christensen, T.E. Blue, G. Yoder, D. Wilson, and P. Sabharwall, "Scaling Analysis for the Direct Reactor Auxiliary Cooling System for FHRs," Nuclear Engineering and Design, Vol. 285, pp. 197-206, 2015.

Q. Lv, H.C. Lin, I.H. Kim, X. Sun, R.N. Christensen, T.E. Blue, G. Yoder, D. Wilson, and P. Sabharwall, "DRACS Thermal Performance Evaluation for FHR," *Annals of Nuclear Energy*, Vol. 77, pp. 115-128, 2015.

X. Wang, Q. Lv, X. Sun, R.N. Christensen, T.E. Blue, G. Yoder, D. Wilson, and P. Sabharwall, "A Modular Design of a Direct Reactor Auxiliary Cooling System for AHTRs," *Transaction of the American Nuclear Society*, Vol. 104, pp. 1077-1080, 2011 American Nuclear Society Annual Meeting, Hollywood, FL, June 26-30, 2011.

X. Wang, Q. Lv, X. Sun, R.N. Christensen, T.E. Blue, G. Yoder, D. Wilson, and P. Sabharwall, "Scaling Analysis for the Direct Reactor Auxiliary Cooling System for AHTRs," *Transaction of the American Nuclear Society,* Vol. 105, pp. 1027-1030, 2011 American Nuclear Society Winter Meeting, Washington, DC, October 30-November 3, 2011.

X. Wang, Q. Lv, X. Sun, R.N. Christensen, T.E. Blue, G. Yoder, D. Wilson, and P. Sabharwall, "Design of a Scaled-down DRACS Test Facility for an AHTR," *Transaction of the American Nuclear Society*, Vol. 105, pp. 1031-1034, 2011 American Nuclear Society Winter Meeting, Washington, DC, October 30-November 3, 2011.

Q. Lv, X. Wang, I. Adams, X. Sun, R.N. Christensen, T.E. Blue, G. Yoder, D. Wilson, and P. Sabharwall, "Design of a Scaled-down Low-temperature DRACS Test Facility for an AHTR," *Transactions of the American Nuclear Society*, Vol. 106, pp. 1071-1074, 2012 American Nuclear Society Annual Meeting, Chicago, IL, June 24-28, 2012.

Q. Lv, I. Adams, X. Wang, X. Sun, R.N. Christensen, T.E. Blue, G. Yoder, D. Wilson, and P. Sabharwall, "A MATLAB Code for Thermal Performance Evaluation of a Low-Temperature DRACS Test Facility," *Transaction of the American Nuclear Society*, Vol. 107, pp. 1374-1377, 2012 American Nuclear Society Winter Meeting, San Diego, CA, November 11-15, 2012.

Q. Lv, X. Wang, X. Sun, R.N. Christensen, T.E. Blue, G. Yoder, D. Wilson, and P. Sabharwall, "Scaling Analysis for the Direct Reactor Auxiliary Cooling System for AHTRs," *The 15th International Topical Meeting on Nuclear Reactor Thermal-hydraulics (NURETH-15)*, NURETH 15-592, Pisa, Italy, May 12-15, 2013.

Q. Lv, M. Chen, X. Sun, R.N. Christensen, T.E. Blue, G. Yoder, D. Wilson, and P. Sabharwall, "Design of Fluidic Diode for a High-temperature DRACS Test Facility," *The 21st International Conference on Nuclear Engineering (ICONE21)*, ICONE21-16902, Chengdu, China, July 29-August 2, 2013.

Q. Lv, I. Kim, X. Sun, R.N. Christensen, T.E. Blue, G. Yoder, D. Wilson, and P. Sabharwall, "Validation of A MATLAB Code for DRACS Thermal Performance Evaluation," *Transaction of the American Nuclear Society*, Vol. 109, pp. 1374-1377, 2013 American Nuclear Society Winter Meeting, Washington, DC, November 10-14, 2013.

Presentations:

X. Wang, Q. Lv, X. Sun, R.N. Christensen, T.E. Blue, G. Yoder, D. Wilson, and P. Sabharwall, “A Modular Design of a Direct Reactor Auxiliary Cooling System for AHTRs,” American Nuclear Society Annual Meeting, Hollywood, FL, June 26-30, 2011.

X. Wang, Q. Lv, X. Sun, R.N. Christensen, T.E. Blue, G. Yoder, D. Wilson, and P. Sabharwall, “Scaling Analysis for the Direct Reactor Auxiliary Cooling System for AHTRs,” 2011 American Nuclear Society Winter Meeting, Washington, DC, October 30-November 3, 2011.

X. Wang, Q. Lv, X. Sun, R.N. Christensen, T.E. Blue, G. Yoder, D. Wilson, and P. Sabharwall, “Design of a Scaled-down DRACS Test Facility for an AHTR,” 2011 American Nuclear Society Winter Meeting, Washington, DC, October 30-November 3, 2011.

Q. Lv, X. Wang, I. Adams, X. Sun, R.N. Christensen, T.E. Blue, G. Yoder, D. Wilson, and P. Sabharwall, “Design of a Scaled-down Low-temperature DRACS Test Facility for an AHTR,” 2012 American Nuclear Society Annual Meeting, Chicago, IL, June 24-28, 2012.

Q. Lv, I. Adams, X. Wang, X. Sun, R.N. Christensen, T.E. Blue, G. Yoder, D. Wilson, and P. Sabharwall, “A MATLAB Code for Thermal Performance Evaluation of a Low-Temperature DRACS Test Facility,” 2012 American Nuclear Society Winter Meeting, San Diego, CA, November 11-15, 2012.

Q. Lv, X. Wang, X. Sun, R.N. Christensen, T.E. Blue, G. Yoder, D. Wilson, and P. Sabharwall, “Scaling Analysis for the Direct Reactor Auxiliary Cooling System for AHTRs,” *The 15th International Topical Meeting on Nuclear Reactor Thermal-hydraulics (NURETH-15)*, Pisa, Italy, May 12-15, 2013.

Q. Lv, M. Chen, X. Sun, R.N. Christensen, T.E. Blue, G. Yoder, D. Wilson, and P. Sabharwall, “Design of Fluidic Diode for a High-temperature DRACS Test Facility,” *The 21st International Conference on Nuclear Engineering (ICONE21)*, Chengdu, China, July 29-August 2, 2013.

Q. Lv, I. Kim, X. Sun, R.N. Christensen, T.E. Blue, G. Yoder, D. Wilson, and P. Sabharwall, “Validation of A MATLAB Code for DRACS Thermal Performance Evaluation,” 2013 American Nuclear Society Winter Meeting, Washington, DC, November 10-14, 2013.